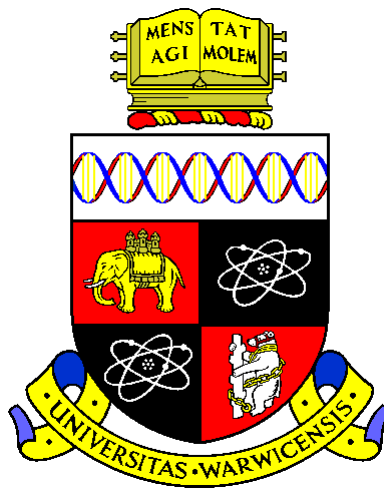# A Silicon Micromachined Lateral Resonant Strain Gauge Pressure Sensor

Christopher J. Welham
Department of Engineering
University of Warwick

April 1996

A thesis submitted to the University of Warwick in partial fulfilment of the requirements for the degree of Doctor of Philosophy

Summary

This thesis details the design, fabrication and testing of a new type of silicon resonant pressure sensor that comprises a single crystal silicon diaphragm and surface micromachined resonant strain gauge. A novel aspect of the pressure sensor is that the resonant strain gauge is designed to oscillate in a mode that is parallel to the plane of the diaphragm. The strain gauge is driven electrostatically and its motion sensed either capacitively or using an integrated piezoresistive pick-up.

Expressions for the resonant frequency and the relative pressure sensitivity of the pressure sensor are derived using Rayleigh's energy method and linear elastic theory. Electromechanical transfer functions are derived using an energy approach to describe the response of the resonator when operated in either the one-port or two-port mode.

Various pressure sensor designs and process test structures were fabricated by combining a surface micromachining process (sacrificial oxide and structural polysilicon) with a standard bulk anisotropic etching process.

The performance of the pressure sensors was determined experimentally by the visual inspection of the vibrating strain-gauge. The (unloaded) resonant frequencies of each sensor were measured and found to be within 20 kHz of the design values (50 and 130 kHz). Using a novel optical technique, the Q-factor of the resonator was measured to be 51 in air at atmospheric pressure and 26 000 in high vacuum (< 1 Pa). Relative pressure sensitivities were also determined experimentally and found to have values of between 0.5 and 3.44 ppm/Pa, which are in good agreement with the theory. The maximum pressure range and linear temperature dependence of the sensor were typically 4×10^5 Pa and -240 ppm/^{o}C, respectively. Finally, it has been demonstrated that the strain gauge can be electrostatically driven and capacitively sensed provided electrical cross-talk is minimised via an electrostatic shield.

As a result of this work, an alternative fabrication process is proposed that should lead to a superior design of lateral resonant pressure sensor.

Contents

Acknowledgements

I would like to acknowledge the help and support of many friends and colleagues in the work described in this thesis, and in preparation of the thesis itself. Firstly, I would like to thank my academic supervisors, Dr. J. W. Gardner of the University of Warwick and Mr. J. Greenwood of Druck Ltd., for their guidance and for giving me the benefit of their considerable experience. Secondly, I would like to thank all those in the micromechanical group at the University of Twente, The Netherlands. In particular I would like to thank Mr. H. Jansen and Dr. M. Elwenospoek. I am grateful for their generous assistance, patience and support with the practical work described in this thesis.

Many other friends and colleagues in the Engineering Department have been helpful. Although to numerous mention individually, I would like to thank Mr. F. Courtney for his practical assistance. I am also grateful to my colleagues at Druck Ltd., especially those in the semiconductor processing facility, for their help and support.

I would also like to thank the Engineering and Physical Science Research Council and Druck Ltd. with whose financial support this work was undertaken.

The help of other friends and family should also be acknowledged. I am grateful for their patience and support during the production of this thesis.

Declaration

The work described in this thesis is entirely my own and has not been published elsewhere unless indicated.

I have presented a paper entitled 'A laterally driven micromachined resonant pressure sensor' at the 8th International Conference on Solid-State Sensors and Actuators, (Transducers '95), Eurosensors IX, June 1995, Sweden. This paper has been accepted for publication in Sensors and Actuators A.

List of symbols

Roman Symbols	Designation	Units[1]
a	comb finger overlap	m
a_d	diaphragm side length	m
A_f	cross-sectional area of a flexure truss	m^2
b	flexure truss width	m
c	viscous damping factor	Nsm^{-2}
C	capacitance	F
C	parameter coupling electrical and mechanical energy domains	Vsm^{-1} (Csm^{-1})
d	comb finger gap	m
D	wafer diameter	m
e_i	generalised effort variable	-
E	parameter coupling electrical domains	Ω (S)
E_f	Young's modulus of flexure truss	GPa
E_D	Young's modulus of diaphragm	GPa
E_{SCS}	Young's modulus of single crystal silicon	GPa
f_i	generalised flow variable	-
f	generalised force	Nm^{-1}
f, F_R	frequency	Hz
g	one half of the diaphragm side-length	m
G_D	transduction factor	NPa^{-1}
G_N	gauge factor	N^{-1}
G_P	relative pressure sensitivity	Pa^{-1}
h	structural polysilicon thickness	m
i	current	A
I	area moment of inertia	m^4
k_{xl}	linear (small displacement) spring rate	Nm^{-1}
k_{xnl}	non-linear spring rate	Nm^{-3}
K_0, K_1, K_2	second-order polynomial coefficients	-
l	length	m
L	inductance	H
M_i	inertial mass	kg
M_t	flexure truss mass	kg
M	parameter coupling mechanical domains	Nm^{-1}
n	number of comb capacitor plates	-
N	load	N
O	pointer support offset	m
P	pressure	Pa
p_i	generalised momentum	-
q_i	generalised displacement	-
q	electrical charge	F
Q	Q-factor	-R
	correlation coefficient	-
t	diaphragm thickness	m
	time	s
T	kinetic energy	J
	temperature	^{o}C
u	velocity	ms^{-1}
U	energy	J
v	voltage	V
V	potential energy	J
V_p	polarisation voltage	V

[1] Alternative units are bracketed.

V_s	sense comb bias	V
x	displacement	m
Y	pointer-tip displacement	m
z	resonator image displacement	m
z_0	diaphragm-resonator separation	m
Z	diaphragm centre deflection	m

Greek Symbols	Designation	Units
α	diaphragm aspect ratio coefficient	-
ε	residual strain	ε
ε_0	residual strain	Fm^{-1}
	permittivity of free space	Fm^{-1}
Γ	transformer turns coupling ratio	-
φ	phase error	rads
κ	electromechanical coupling factor	-
λ	axial elongation	m
ν	Poisson's ratio	-
θ	flexure anchor rotation	deg.
ρ	resistivity	Ωm
$\theta_{i,r}$	angle incidence, reflection	deg.
ω	angular frequency	rads/s
ω_p	angular parallel resonant frequency	rads/s
ω_s	angular series resonant frequency	rads/s
ω_1	angular unloaded resonant frequency	rads/s

1. Introduction

Chapter 1
Introduction

This chapter provides an overview of silicon pressure sensors. The chapter begins by highlighting the current demand for highly accurate pressure sensors that possess an excellent stability and describes the role played by micromachining in the development of the modern pressure sensor. Following a description of the operation of piezoresistive and capacitive pressure sensors, the discussion focuses on the subject of this thesis; the resonant pressure sensor. A historical review of these devices is then given. At the end of the chapter the objectives of my research are stated and an outline of this thesis presented.

1.1 General introduction

Today, there is a common need in the industrial world to measure pressure. This is evident from the numerous technological fields that use pressure sensors. Some examples of these fields include: the petrochemical, aerospace, defence, marine and water industries, meteorology, control systems and process control [1.1]. Over the last ten years the annual sales of silicon based-pressure measuring equipment to these fields has grown to a figure of some 14.9 million units in Europe alone, a figure which is forecast to rise to 35.7 million units by 1997 [1.2].

The current growth of the pressure sensor market is fuelled by a general need to improve both the performance and efficiency of pressure measurement systems and instrumentation. As part of the resulting silicon-led advances, new applications are being created and many older electromechanical technologies are being displaced from the market. Two emerging markets are the automotive and biomedical industries, both of which require low cost, (prices of $1 to $7 each in high volume) medium performance pressure sensors. Applications for these sensors in the automotive sector include active suspension, braking systems and engine management. The latter is mostly stimulated by environmental emission regulations, whilst in the biomedical industry, there is great interest disposable blood pressure sensors. Another area of growth is the market for high accuracy pressure measurement. This is because of the increasing demands of high performance, high integrity, applications such as the calibration of pneumatically driven avionic systems, meteorology and the provision of portable secondary pressure standards. While this market is relatively small, the sensors are priced at between $400 to $1500, and thus potentially more lucrative than the low cost (high volume) pressure sensor market [1.2,1.3].

Currently a wide range of pressure sensors and pressure instrumentation is available, so that it is usually possible to find a model which is appropriate for almost any application. The majority of applications require a level of accuracy and stability that can be met by the conventional piezoresistive silicon strain-gauge or capacitive based pressure sensors [1.1]. However, these devices do not meet the needs of the high performance applications, which require extremely stable pressure measurements with an accuracy of 100, 10, or even 1 ppm full scale (FS). In these applications an excellent long term stability is required because it reduces the need for re-calibration, typically against bulky laboratory based pressure standards. Frequent re-calibration is also costly and may be impractical for certain applications, such as the provision of barometric pressure data from oceanographic weather stations (moored ships and buoys). When the sensor must operate under adverse environmental conditions, e.g. such as the high temperatures of a gas field or the vibrations that arise in meteorological survey aircraft the difficulty of attaining this accuracy is compounded. Small size, low weight and low power consumption are additional requirements [1.4].

A technology capable of fulfilling these requirements is the resonant pressure sensor. These sensors are able to achieve an accuracy of at least ± 0.01% FS and long term stability of < 100 ppm/year, see Table 1.1. Although silicon based pressure sensors have been under continuous development for over twenty years, the resonant pressure sensor is one technology that is still mostly based upon precision machined electromechanical sensing mechanisms. Indeed, silicon-based resonant pressure sensors with an accuracy and stability comparable to traditional precision machined devices have only recently become

commercially available [1.1]. The silicon-based resonant pressure sensor is attractive because, like the majority of today's piezoresistive and capacitive pressure sensors, it is produced using micromachining, which offers the potential for improved performance, greater portability and lower manufacturing costs.

1.2 Micromachined silicon pressure sensors

The rapid evolution of pressure sensor technology over the last decade can be directly attributed to the introduction of microelectronics, semiconductor (especially silicon) diaphragm technology, and the parallel development of *micromachining*, that began in the early 1960's and accelerated rapidly in the early 1980's. Micromachining allows the fabrication of mechanical devices with very small dimensions (in the micrometre range) and is based on the application of the conventional semiconductor processing techniques used to make microelectronic circuits. A wide range of sensors and actuators are now being produced using this technology, including accelerometers, gyroscopes, micropumps, AFM tips, inkjet nozzles, micromotors and micropumps [1.5-1.10].

Until the development of micromachining most pressure sensors were assembled from individually machined metal components and, as a consequence, tended to suffer from poor resolution, reliability and reproducibility. Diaphragms, for example, were fabricated by mechanical drilling and/or isotropic chemical etching [1.11]. The advantage of micromachining is that it overcomes these limitations because it retains the advantages of semiconductor processing. These advantages are the precise control of device dimensions and material composition, reproducibility and batch processing techniques, the latter of which can reduce unit production costs. Furthermore, as the term micromachining implies, it is possible to produce miniature devices on a scale that would be impossible using conventional precision machining techniques.

Within micromachining two technologies can be distinguished, namely, bulk micromachining and surface micromachining. Bulk micromachining is the 3-D sculpting of single crystalline materials (usually silicon) using various etching and bonding techniques. Surface micromachining, on the other hand, utilises the deposition and selective etching of thin films to form a free-standing microstructure on the surface of a (silicon) wafer, e.g. a diaphragm, beam or cantilever [1.10]. These two processes are shown schematically in Figure 1.1.
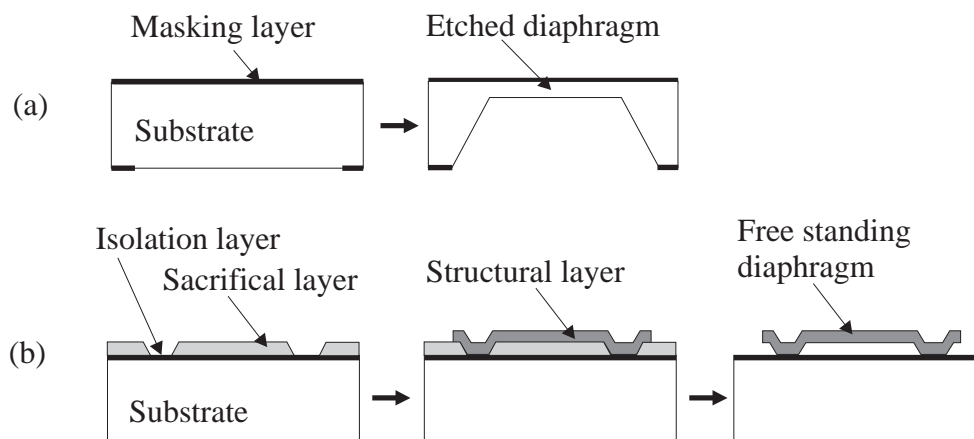
Figure 1.1 General method of fabricating a simple diaphragm using (a) bulk, and (b), surface micromachining; (a) The silicon substrate is patterned with a passivation mask and the diaphragm anisotropically etched. (b) An isolation layer and sacrificial layer are grown and patterned. A structural layer is then deposited and the diaphragm shape defined. The diaphragm is released by etching away the sacrificial layer.

Silicon is widely used as a base material for micromechanical devices. The reason is partly historic because the technology developed directly from the microelectronics industry, where silicon was, and still is, the dominant base material. A further reason is that single crystal silicon (SCS) is an ideal material to use for the fabrication of micromechanical devices; it is a high strength material, available at low cost and its material characteristics are well understood [1.12]. One (small) drawback of using silicon is that it reacts with corrosive media.

The modern silicon pressure sensor is composed of three elements, namely; a pressure-sensitive structure, a transduction mechanism[1] and signal conditioning/data acquisition electronics. These three elements are housed in a package which is compatible with the sensor's application. The pressure-sensitive structure is usually a diaphragm that deforms under an applied pressure. The purpose of the transduction mechanism is to convert the mechanical deformation of the pressure-sensitive structure into a measurable (electrical) signal. The primary function of the electronics is to amplify this signal. Further signal conditioning and electronic processing, e.g., temperature compensation, A/D conversion and calibration may then be performed, according to the sensor architecture and the needs of the end user.

By the beginning of the 1980's at least 5 different transduction mechanisms had been investigated for use in solid-state silicon pressure sensors, *viz*.; the stress effect on a *p-n* junction, the piezoelectric effect of thin films, optical deflection techniques, the piezoresistance of silicon, the capacitive effect of a deformable diaphragm and the frequency shift of a resonant structure [1.13]. Of these five, the piezoresistive, capacitive and resonant transduction mechanisms form the basis of silicon pressure sensor technology today.

1.2.1 Piezoresistive strain-gauge pressure sensors

The silicon piezoresistive strain-gauge pressure sensor is currently the most widely used pressure sensor because of its high sensitivity, good linearity, reliability and ease of manufacture [1.3]. This type of pressure sensor has been on the market for over twenty years and uses the stress induced change in silicon resistivity to measure pressure. Typically, a number of piezoresistors are diffused or ion-implanted into a SCS diaphragm, in a single, half or full-bridge arrangement. The diaphragm is formed by bulk anisotropic etching and its thickness accurately controlled with an etch stop. In a full bridge arrangement the piezoresistors are embedded near the edge of the diaphragm where the deflection induced strain is highest, see Figure 1.2. A pressure difference across the diaphragm induces a deflection, so modifying the piezoresistor values and changing the balance point of the resistance bridge. More recently, piezoresistive pressure sensors have been produced by surface micromachining. Here, in contrast to bulk etched devices, a polysilicon diaphragm is fabricated on the surface of a silicon substrate and deposited piezoresistors used to form the sensing bridge [1.14].

Although piezoresistive pressure sensors are well established, they suffer from several disadvantages which preclude their use in precision measurements and/or where a good long-term stability is needed. These disadvantages are include: a limited pressure sensitivity, a relatively high uncompensated temperature sensitivity (≈ 0.2 %/^{o}C) and a poor long-term stability. The pressure sensitivity is limited by the small fractional change in resistance of the piezoresistors, which is typically about 1% FS. Diffused piezoresistive devices are known to exhibit at least six temperature drift mechanisms, which all contribute to the high temperature sensitivity of the device [1.15]. The high temperature sensitivity of the diffused piezoresistive pressure sensor is usually avoided electronically using an (on chip) temperature sensor and a calibration circuit. However, a good stability is difficult to obtain because the piezoresistor values change by 1% to 2% over the lifetime of the sensor and are also sensitive to packaging induced stress [1.13,1.14].

---

[1] Strictly, the pressure-sensitive structure is also a transduction mechanism because it converts pressure into a mechanical deformation.

Contact pads

Diffused piezoresistors

Diaphragm

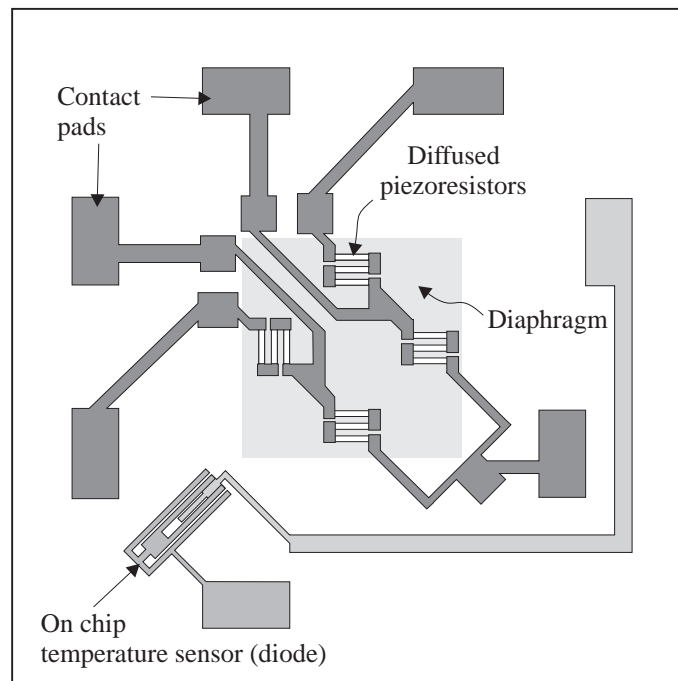On chip temperature sensor (diode)

Figure 1.2 3-D schematic of a diffused piezoresistor strain pressure sensor [1.1].

1.2.2 Capacitive pressure sensors

A capacitive pressure sensor is formed from two electrodes, one of which is attached to a diaphragm. Under an applied pressure the diaphragm deforms, so changing the capacitance of the two electrodes, which is measured by an external circuit.

In contrast to the piezoresistive mechanisms, pressure is determined by measuring the displacement of the diaphragm rather than its stress, and this leads to several advantages. Firstly, the intrinsic pressure sensitivity can be much higher than the piezoresistive pressure sensor. This is because the changes in capacitance are between 10% - 20%, compared to changes in resistance of less than 2 % seen in piezoresistive pressure sensors. Secondly, these devices are less susceptible to packaging stress and so have a better stability than piezoresistive sensors. Thirdly, the power requirements of a capacitive pressure sensor can be very small, in some cases less than 25 µW continuous power. In fact, this type of pressure sensor was initially developed because of the need for miniature low-power devices, particularly in biomedical applications where a low power consumption is a major design criterion [1.6].

One disadvantage of the capacitive pressure sensor is that the static capacitance of the sensing element is small, typically less than 1 pF. It is therefore important to minimise parasitic capacitance that will reduce the magnitude and quality of the output signal. This is achieved by placing the detecting circuit as close as possible to the sensing element, by using either a hybrid arrangement, where the sensing chip and electronics circuit are fabricated separately and then assembled next to each other, or a monolithic device where both elements are on the same chip [1.16,1.17].

1.2.3 Resonant pressure sensors

The resonant pressure sensor employs a much more advanced sensing scheme than its piezoresistive or capacitive counterparts. A resonant pressure sensor is based upon a mechanical resonator that is integrated with a pressure-sensitive structure, such as a diaphragm. Under an applied pressure the structure deforms, so inducing a shift in the natural frequency of the mechanical resonator. The resonant pressure sensor is only one of a number of sensors whose transduction mechanism is based on the modulation of a mechanical resonant frequency. These sensors are known as *resonant sensors*.

Resonant sensors possess a magnitude and phase of vibration which are sensitive to an applied measurand, such as a force, pressure, acceleration, temperature, or mass. Resonant sensors are attractive because they offer a high sensitivity, high resolution, excellent long term stability and low hysterersis, all of which lead to a high accuracy. The reason that a resonant sensor can attain a high sensitivity lies in the fact that an oscillating structure is generally more sensitive to a change internal state than a stationary

(analogue) structure [1.3]. For example, a vibrating string may easily double its frequency on the application of an external force, but the same force extends its length by only a fraction. A resonant sensor has the potential for a high resolution because its resonant frequency can be measured with an (almost) arbitrary precision, that is only limited in practice by the resolution of the frequency measurement system [1.3]. A further benefit of the resonant sensor is its frequency output signal. A frequency output signal has the advantages of a high immunity to noise and interference. Moreover, a frequency output can be handled directly by digital circuitry and by-passes the drift associated with analogue signals [1.18-1.26].

The stability of a sensor is determined by the effects of both internal and external influences. Resonant sensors have the potential for excellent stability because these influences can be minimised. Internal influences are minimised by fabricating the resonator from a material that possesses stable properties over time. External influences are minimised by careful design to reduce the effect of packaging stress, and by hermetically sealing the resonator to protect it from the environment.

Resonant sensors can be categorised into three groups, according to the nature of the mechanical vibrations of the sensing element [1.27],

(1)   Bulk acoustic wave (BAW) sensors. These devices are based on thin piezoelectric discs that are driven into a thickness or shear mode of resonance. The frequency of the resonant mode is normally in the MHz region. These sensors are well established as a standard means of measuring the thickness of vacuum evaporated thin films and have also been used to measure pressure [1.28].

(2)   Surface acoustic wave (SAW) sensors. These are usually based on the propagation of Rayleigh waves across the surface of a suitable solid medium, e.g. quartz. The propagation characteristics of SAWs, and hence their frequency, is influenced by surface conditions which are in turn altered by the measurand. These sensors normally operate at a frequency in the GHz range. A similar sensor also exists that utilises Lamb waves. These propagate in a plate whose thickness is comparable to the ultrasonic wavelength, with a frequency in the low MHz region. In this respect they are more convenient to use than SAW devices [1.29].

(3)   Resonant sensors based upon the vibration of a dedicated micromechanical structure. This type of resonator operates in frequency range 10 kHz to 1 MHz and is commonly referred to as a micromechanical resonant sensor. The resonant pressure sensor described in this thesis belongs in this category.

The sensitivity of a micromechanical resonant sensor arises because the fundamental (and harmonic) frequencies are a function of the energy stored by the resonant element. In this respect two mechanisms can be distinguished, namely, a change in kinetic energy and/or a change in the potential energy. A change in the kinetic energy is caused by a mass loading, a well known implementation of this mechanism being the quartz crystal microbalance or film thickness monitor. The sensitivity of a resonant pressure sensor, on the other hand, arises from a change in potential energy. A change in potential energy is induced by applying a mechanical force or strain to the resonant element of the sensor.

Generally, a resonant pressure sensor can be categorised into one of two types. The first is formed by integrating the mechanical resonator and pressure sensitive structure into a single element. An example of such a configuration is the resonant diaphragm pressure sensor shown in Figure 1.3. Here, the action of a differential pressure stretches the diaphragm, so increasing the level of potential energy and inducing a resonant frequency shift.
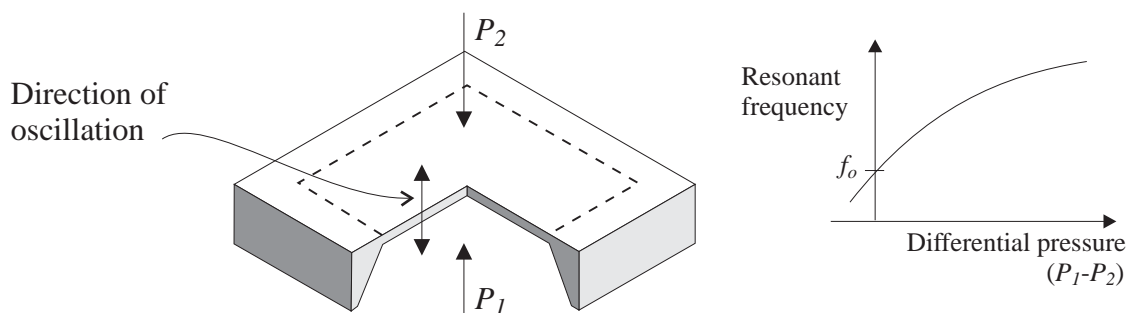
Figure 1.3 Schematic showing a resonant pressure sensor based upon a resonant diaphragm. The sensor is shown in a differential mode; for an absolute device one side of the diaphragm is enclosed and the cavity created evacuated. A typical pressure frequency response is shown.

Unfortunately this type of pressure sensor has two drawbacks. The first is that the resonant frequency is sensitive to the density of the surrounding gas. Consequently, pressure measurement in gases different to the calibration gas will result in an error in the pressure reading. The second is that at least one side of the resonator is exposed to the environment. This means that the resonator is susceptible to kinetic energy based frequency-shifts, induced by environmental effects e.g. condensation, dust and corrosion.

In the second type of resonant pressure sensor, a dedicated mechanical resonator is used to sense the deformation of the pressure-sensitive structure, as shown in Figure 1.4. Here, a frequency-shift is induced by applying a mechanical force to the end points of the resonator. Typically, the end points of the resonator are attached to a diaphragm through a supporting structure, although it is possible to embed the resonator within the diaphragm itself. The advantage of this configuration is that is allows the resonator to be completely enclosed within an evacuated cavity. This protects the resonator from the environment and bypasses problem of gas density sensitivity associated with vibrating diaphragm type pressure sensors. Moreover, it maximises the Q-factor of the mechanical resonator. The Q-factor of a vibrating mechanical resonator is a measure of its energy loss. A high (> 35 000) Q-factor is desirable because it leads to an improvement in both the measurement precision of the resonant frequency and the long term stability of the sensor [1.3].
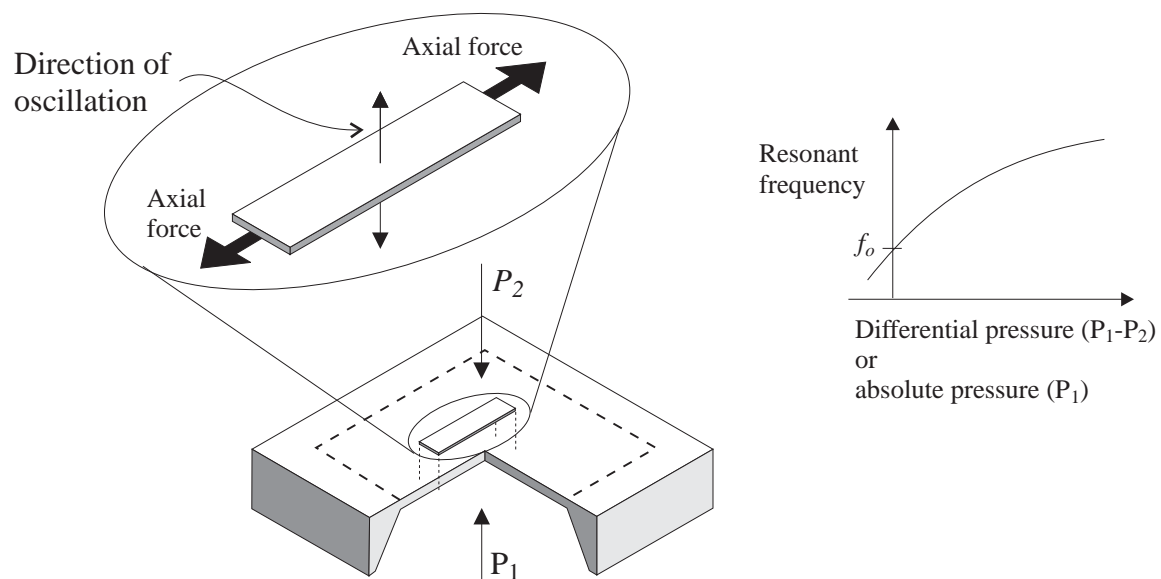

Figure 1.4 Resonant strain gauge or force transducer integrated onto the surface of a diaphragm (or force producing structure). A mechanical force is applied to the gauge by the deflection of the diaphragm, inducing a shift in resonant frequency of the gauge.

Note that if the relative stiffness of the mechanical resonator depicted in Figure 1.4 is low compared to that of diaphragm (or force producing structure), then the contribution of the stiffness of the resonator to the overall stiffness of the device will be small. In this instance, an axial force is induced in the resonator as a direct result of a displacement of its end points. The resonator is therefore referred to as a *resonant strain gauge* to emphasise the origin of the axial force. On the other hand, if the stiffness of the resonator is high, then the contribution of the diaphragm stiffness to the overall stiffness of the device will be small. Here, the mechanical resonator is referred to as a *resonant force transducer*, because the force applied to the resonator is the independent variable, which induces an axial elongation of the resonator [1.30].

In practice, the mechanical element of a resonant sensor will oscillate in a direction that is determined by its design and the location and shape of drive (and sense) electrodes, used to determine the resonant frequency. For example, the resonant strain gauge shown in Figure 1.4 is designed to possess a fundamental mode of oscillation whose displacement is perpendicular to the plane of the substrate. In 1990 Tang *et al.* [1.31,1.32] presented a new type of resonator that moved laterally, i.e., parallel to the substrate,

see Figure 1.5. This type of micromechanical resonator, commonly known as a lateral resonator, is realised by suspending a shuttle mass above the substrate on a micromechanical flexure. The microflexure also acts as spring and provides an elastic force for motion parallel to the plane of the silicon substrate.

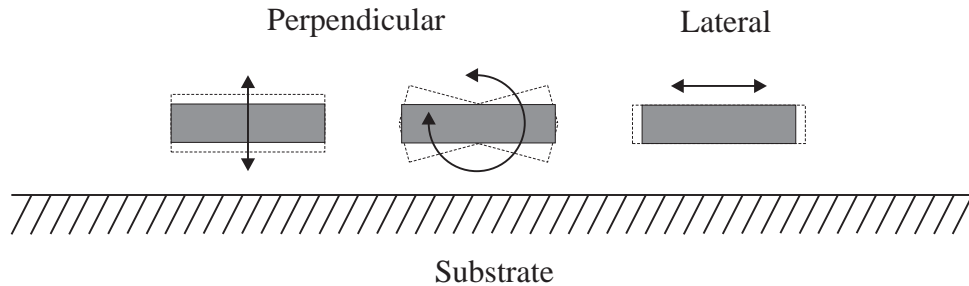Perpendicular   Lateral

Substrate

Figure 1.5 Schematic showing the, (a) perpendicular, and (b) lateral modes of oscillation. The direction of oscillation of each fundamental mode is indicated in each case.

Lateral resonators are employed as the sensing elements in various microsensor applications including microaccelerometers, gyroscopes, shear sensors and frequency selective microfilters [1.33]. However, their use as the sensing element of a resonant pressure sensor has yet to be investigated. One question that is addressed in this thesis is whether there is an advantage in producing a pressure sensor based upon a lateral resonator, rather than a resonator which oscillates in a more conventional perpendicular mode. The key technology in the production of lateral devices is surface micromachining [1.34-1.37]. This technology has been developed over the last 5 years to a point where it is becoming a standard process in many institutions. A large part of the research described in this thesis is dedicated to the fabrication of a surface micromachined lateral resonator and the reader is directed to the references at the end of chapter 4 for further information on this subject.

1.3 Resonant sensor electronics

To operate a resonant sensor it is necessary to excite a resonant mode and measure the frequency (or phase) shift of this mode as the measurand changes. To excite a resonant mode an excitation mechanism is used, while a detection mechanism is used to measure the resulting motion of the resonator. The frequency of the resonant mode is determined by comparing the relative magnitudes (or phases) of the excitation and detection signals. There are several different types of excitation/detection mechanism, where each type is characterised by the transduction principle employed. One well known example is based on the direct and indirect piezoelectric effect used in quartz crystal resonators [1.21]. Other types included electrostatic and magnetic based mechanisms [1.25].

Excitation and detection mechanisms are usually operated in a two-port mode or one-port mode. In the two-port mode, two separate elements are used to determine the resonant frequency, one for excitation and one for detection. Here, the response of the resonator resembles that of a band-pass filter. Currently the majority of resonant sensors are designed to operate in a two-port mode, see Table 1.1. An alternative approach, the one-port mode, is to employ a single element for both excitation and detection. In this case the response of the resonator is similar to that of a quartz crystal resonator [1.38].

For continuous operation a resonator is usually integrated with a feedback loop so that it forms the frequency determining element of an electronic oscillator. This mode of operation is shown schematically in Figure 1.6. In practice the configuration of the feedback loop depends on whether the resonator is operated in a one-port or two-port mode. However, in both cases the feedback loop is usually formed by an impedance matching network, buffer amplifier and automatic gain control. The electronic oscillator usually forms the primary stage of the sensor electronics, providing a pressure dependant resonant frequency. A further point to note from Figures 1.3 and 1.4 is that the pressure-frequency relationship is non-linear, and also temperature dependent (not shown). As with all sensors, to be of use the resonant pressure sensor must be calibrated to determine the relationship between the resonant frequency, pressure and temperature. Once the relationship is known the pressure can be computed from the measured resonant frequency and ambient temperature.

The resonant frequency is usually measured by using a known time base and the ambient temperature measured using a resistor or diode. Note that the non-linear relationship between the resonant frequency, applied pressure and ambient temperature means that conventional analogue electronics is ill-

suited to the task of calibration. Instead, the non-linear dependencies are determined numerically using standard polynomial curve fitting algorithms. Typically, the polynomial coefficients are stored in a ROM. The pressure is calculated by a microprocessor using the polynomial coefficients from a resonant frequency and temperature reading. One interesting method of improving the performance of a resonant (pressure) sensor is to use structural compensation [1.22]. Here, two (or more) resonators are employed to provide a difference signal and the pressure determined by comparing the resonant frequency of each.
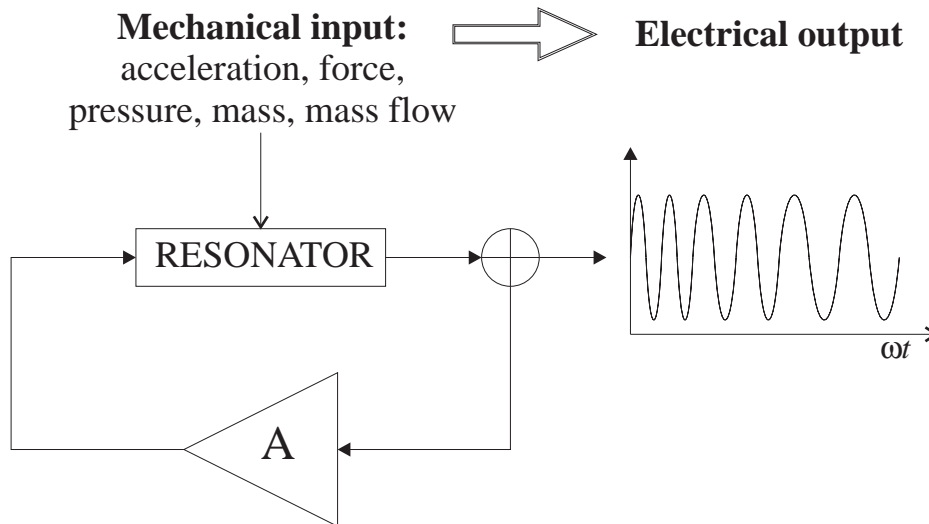

Figure 1.6 Schematic showing the operation of a resonant sensor. A change in the measurand, e.g. an acceleration, force, or pressure, induces a change in the mechanical resonant frequency. With the addition of a feedback loop the resonator forms the frequency determining element of an electronic oscillator.

1.4 Historical review

I have restricted this review to cover resonant pressure sensors. For a general review of resonant sensors and their applications, the reader is referred to the following references and references therein [1.19-1.26].

One of the first portable resonant pressure sensors was based on a vibrating metal cylinder. This technology dates backs to the 1950's where it was first developed in Sweden, and later transferred to the Solatron Electronic Group[2] in the UK. Its success led to the development of a line of vibrating cylinder pressure sensors which are commercially available today. The sensor consists of two metallic cylinders, one mounted inside the other. The space between the two cylinders is evacuated. The inner cylinder is excited into a hoop resonance mode using two electromagnetic coils. Two more coils are used to measure the response. The resonant frequency of the inner cylinder varies as a function of the stress created by the differential pressure and the reference vacuum. The drawback of this design is that resonant element, i.e. the inner cylinder, is exposed to the gas whose pressure is to be measured. It therefore suffers from the same disadvantages as resonant diaphragm pressure sensors explained earlier. Nevertheless, this sensor is used extensively as a portable pressure standard, though its future is uncertain as micromachined resonant pressure sensors come to the market [1.39].

One of the first commercially available pressure sensors to employ a separately machined mechanical resonator was produced in 1976 by Paros [1.40] using a quartz crystal resonant force sensor. The resonant force sensor consists of a clamped-clamped beam attached to an isolator spring whose purpose is to de-couple the clamped-clamped beam from the force producing structure. The conversion of a pressure input to a stress load on the force sensor is achieved using a set of bellows and a pivot mechanism, see Figure 1.7. To increase the Q-factor of the quartz resonator the complete assembly is mounted in an evacuated housing case. A range of resonant pressure sensors based on this mechanism are currently produced by Paroscientific[3]. A similar resonant pressure sensor, consisting of three doubled-ended tuning

---

[2] The Solatron Electronic Group Ltd., Farnborough, Hamphshire, England.
[3] Paroscientific, Inc. 4500 148th Avenue N.E. Redmond, WA 98052, USA.

forks and a bellows mechanism was produced by Ueda [1.41] and also Miller [1.42] in 1985 and 1988, respectively.
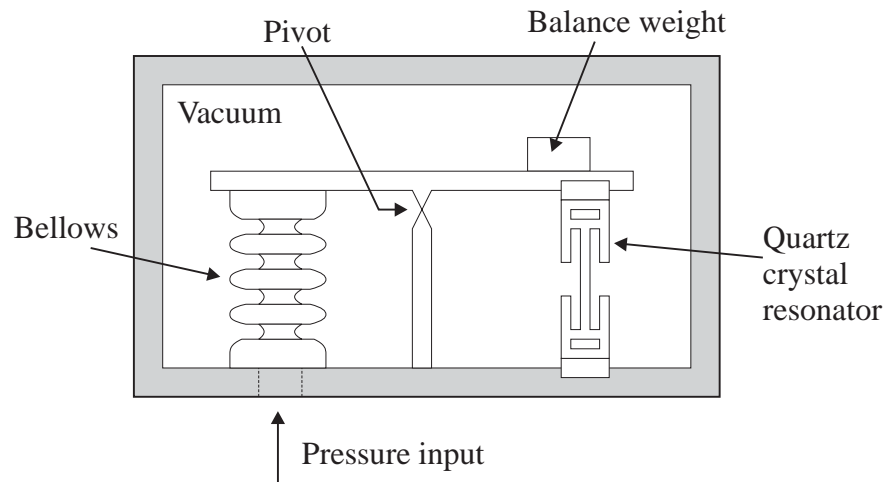
Figure 1.7 Schematic showing the design of an absolute pressure sensor produced by Paroscientific[3]. A pressure input is converted to a load on a quartz crystal resonator via a set of bellows and a pivot mechanism. The position and mass of the balance weight is adjusted to ensure the sensor is insensitive to linear accelerations.

At the beginning of the 1980's the increasing interest and development of (silicon) micromachining lead to a new generation of resonant pressure sensors. The first sensors were produced by Smits [1.43] and Greenwood [1.44] using silicon anisotropic etching and boron etch stops. The latter device is based on an electrostatically operated vibrating 'butterfly' resonator mounted on silicon pedestals that are connected to a diaphragm, see Figure 1.8. Upon the application of a pressure the diaphragm deforms rotating the silicon pedestals, so stressing the resonator and inducing a frequency shift. The resonator is enclosed with a silicon cap and the air evacuated through a vacuum tube which is then sealed.

Figure 1.8 SEM showing the bulk micromachined resonant pressure sensor based upon a vibrating butterfly structure developed by Greenwood et al. This sensor is commercially available[4].

Towards the end of the 1980's several other pressure sensors were developed, see Table 1.1. The design of these sensors was enabled by advances in micromachining, notably the development of silicon fusion bonding [1.45], the reactive sealing technique [1.46] and surface micromachining [1.34]. In general,

---

[4] Druck Ltd., Fir Tree Lane, Groby, Leicester, England, LE6 OFH.

these pressure sensors consist of resonant strain gauges mounted upon SCS diaphragms. Of these, the differential pressure sensor produced by the Yokogawa Corporation, see Figure 1.9, is commercially available [1.47]. The sensor consists of an 'H' shaped resonator which is fabricated into the surface of a SCS diaphragm using a combination of boron doping, silicon epitaxy and electrochemical etching. The resonator is driven with a magnetic excitation/detection mechanism and housed in an integrated silicon cap. The chamber created between the cap and diaphragm is evacuated and sealed using reactive sealing. One advantage of using an integrated silicon cap is that a differential pressure can be measured because each side of the diaphragm can be exposed to the pressure medium. In fact, this pressure sensor is designed to measure small differential pressures between two mediums, both of which are at a high pressure. This type of pressure measurement is often required in the Petrochemical industries.
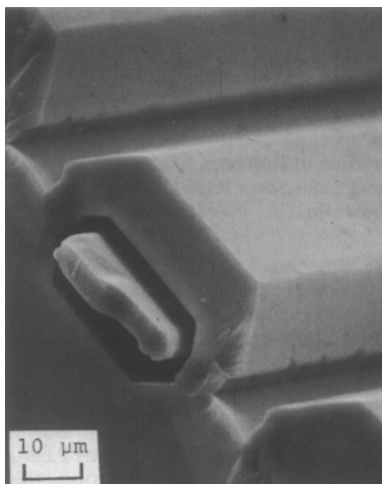
Figure 1.9 A SEM showing a cross section of the resonant pressure sensor developed by Ikeda et al. The resonant element is housed in an integrated 'corrugated' silicon cap. This resonant pressure sensor is commercially available[5].

Currently there are two research programmes aimed at developing *surface micromachined* resonant strain gauge (pressure) sensors. Guckel, Zook *et al.* [1.52] have reproduced a resonant pressure sensor whose design is similar to that of Ikeda described above. The resonator is fabricated from polysilicon using a combination of surface micromachining and silicon fusion bonding, a process that is reported to be simpler than the method used by Ikeda. Two different resonator drive schemes have been used namely, magnetic drive/sense and electrostatic drive and piezoresistive sensing. Tilmans has realised a resonant strain-gauge which is based on a single clamped-clamped beam [1.30]. Encapsulation is also via an integrated silicon cap and reactive sealing. The resonator, which has been fully tested, is driven electrostatically and the motion sensed capacitively. A resonant pressure sensor design based on this resonant strain gauge is proposed [1.53].

---

[5] Yokogawa Electric Corporation, 2-9-32, Nakacho, Musashino, Tokyo 180 Japan.

Table 1.1 Review of past, current and proposed pressure resonant pressure sensors. Shading indicates commercial availability; italics indicate predicted values only. For further information on sensor performance, i.e., repeatability, hysteresis and acceleration sensitivity, the reader is directed to the included references.

Refs.	Authors	Affiliation	Year	Sensitivity	Range (Bar)	Temp. Sensitivity	Stability
1.39	Love	Pressure Systems Inc.	1950-1988	-	0.03-1.3 a 0.3-34.5 a	±0.15 %/^{o}C	0.01% FS (12 mnths)
1.40	Paros	Paroscientific (USA)	1976	9%/bar	≤ 2.0 a	47 ppm/^{o}C	0.003 % FS (12 mnths)
1.41	Ueda *et al.*	Yokogawa Corporation	1985	-	-	-	-
1.43	Smits *et al.*	Univ. Twente	1983	37 %/bar	0-0.02 d	-	-
1.44	Greenwood	STL/Druck.	1984-1992	1.7-3.5 Hz/bar	0.75-1.15 a 0.35-3.52 a	-	0.02 % FS (12 mnths)
1.47	Ikeda et al.	Yokogawa	1990	-	-	-40 ppm/ C	<0.01% FS (12 mnths)
1.48	Stemme and Stemme	Chalmers University, Sweden	1990	19 %/bar	≥0.6 d	-16 ppm/^{o}C	-
1.49	Dufour *et al.*	LETI	1991	-	-	-20 ppm/^{o}C (SCS)	-
1.50	Buser and De Rooij	Neuchatel University/ ABB	1991	8 Hz/bar (Torsional mode)	15 a	-0.7 Hz/ ^{o}C	-
1.51	Kvisteroy *et al.*	Sensor Nor	1992	52 Hz/bar	1000 d	-	-
1.53	*Tilmans and Bouswtra*	*University Twente*	*1993*	*175 Hz/Pa*	*0.01 d*	-	-
1.52	Zook Guckel Burns *et al.*	Honeywell/ University Wisconsin	1991-1994	25 %/bar	0.7 a	-	-
1.54	Mandle e*t al.*	Sextant Avionique	1995	-	-	-	-

Key: BMM=Bulk micromachining; SMM=Surface micromachining; PM=Precision machining; GE=Global encapsulation; LE=Local Encapsulation; a=Absolute; d=Differential; FS=Full-Scale; - information not available.

Excitation mechanism	Detection mechanism	Mode	Resonator/ Mode of vibration	Res. Freq. (kHz)	Q-factor in vacuum (1000's)	Fabric- ation	Electronics
Electro- magnetic	Electro- magnetic	2-port	Dual cylinder	-	N/A	PM	Discrete
Piezoelectric	Piezoelectric	2-port	DETF/ Transverse	40	> 40 GE	PM	Off-Chip
Piezoelectric	Piezoelectric	2-port	DETF/ Transverse	1.2	-	PM	Off-Chip
Piezoelectric	Piezoelectric	2-port	Diaphragm/ Transverse	1.3	N/A	BMM	Integrated
Electrostatic	Capacitive	2-port	Torsional/ Complex	35	>30	BMM	Off Chip
Magnetic	Magnetic	2-port	'H shaped beam'/ Transverse	25	50 LE	BMM	Off Chip
Electrostatic	Electrostatic	2-port	Double diaphragm/ Torsional	17	80 GE	BMM	Off Chip
Piezoelectric	Piezoelectric	2-port	Beam/ perpendicular	20	43-120 GE	BMM	Off Chip
Electrostatic	Capacitive	2-port	'Paddle'/ Torsional & complex	20	43-120 GE	BMM	Off Chip
Optothermal	Optical	2-port	'Butterfly'/ Torsional & complex	83	20-40 GE	BMM	None
Electrostatic	*Capacitive*	*1-port*	*Beam/ Perpendicular*	*576*	*10 LE*	*SMM*	-
Electrostatic	Piezo- resistive	2-port	Beam/ Perpendicular	223	>25 LE	SMM	-
-	-	-	Beam/ Perpendicular	50	-	BMM	-

1.5 Research aims and objectives

The research described in this thesis is driven by the need to develop further the high performance resonant pressure sensor. The objectives are to attain an increased range over and above that of current devices, whilst retaining, or improving upon pressure sensitivity and long term stability. The fabrication process used to produce the sensor must be straightforward and have a high yield, to minimise production effort and cost. A potential way of reaching these objectives is to produce the pressure sensor using surface micromachining. The advantage of surface micromachining is that it offers a design flexibility above that of conventional bulk micromachining techniques and, as a consequence, the opportunity to improve both the architecture and performance of the pressure sensor. Following this rationale, the research in this thesis describes the design, fabrication and testing of a silicon micromachined lateral resonant strain-gauge pressure sensor. The term 'silicon micromachined' refers to the technology used to produce the pressure sensor, whilst the term 'lateral resonant strain-gauge' describes the configuration of the pressure sensor's mechanical resonator.

1.6 Outline of this thesis

Chapter 2 begins with a description of the resonant pressure sensor design. The factors that influence the performance of a resonant pressure are discussed and the potential advantages of the lateral resonant strain-gauge pressure sensor design are described. The remainder of the chapter is devoted to developing a model of the mechanical operation of the pressure sensor. The model is used to predict both the resonant frequency and gauge factor of the lateral resonator, and the relative pressure sensitivity and pressure resolution of the pressure sensor.

Chapter 3 describes the operation and response of the lateral resonator. Following a review of resonator excitation and detection mechanisms the operation of the lateral resonator and its (linear and non-linear frequency) response is described. An energy approach is used to derive expressions for the linear response of the resonator when operated in a one port and two port mode. Electrical equivalent circuits are constructed to illustrate how the external circuit used to drive and sense the motion of the resonator can influence the measured resonant frequency. Finally, the phenomenon of electrical cross-talk is described.

Chapter 4 is devoted to the fabrication of the resonant pressure sensor. Several areas are covered including: the important processing issues in surface micromachining; the physical and material structure of the pressure sensor; its encapsulation and mounting, and the geometry of photolithographic masks used to produce the sensor. The fabrication process is then described. To illustrate the flexibility of the process several variations on the basic pressure sensor design are shown. Finally, an investigation is made of the material properties of the resonator with the aid of test microstructures.

Chapter 5 describes the testing of the resonant pressure sensor and presents my results. First, the methods used to characterise the performance of the pressure sensor are described and measurements of the pressure sensitivity and temperature sensitivity presented. A novel optical detection technique is then described and used to measure the Q-factor variation of the lateral resonator with cavity pressure. The onset of non-linear behaviour is also illustrated. At the end of the chapter the first stages in integrating the pressure sensor into a closed loop mode of operation are described.

Finally, general conclusions are drawn in chapter 6 and future research is proposed.

References

[1.1]   Druck Holdings plc., UK Company Profile 1995.

[1.2]   Bogue R. W., Silicon sensors in Western Europe, *Proc. Sensors VI: technology, systems and applications*, IOP publishing, London (1993) 119-127.

[1.3]   Gopel W., Hesse J., Zemel J. N. (eds.), *Sensors a comprehensive survey,* Mechanical sensors, Vol. 7, Weinham, New York (1994) 513-556.

[1.4]   Busse D. W., Digital differential pressure transducer for air data applications, 1980 air data

         symopsium, *U.S. Air Force Academy*, Colorado Springs, Colorado, U.S.A. (1980).

[1.5]   Frank R., Pressure sensors merge micromachining and microelectronics, *Sensors and Actuators,*

         A28 (1991) 93-103.

[1.6]   Puers R., Capacitive pressure sensors: when and how to use them, *Sensors and Actuators,* A37-38

         (1993) 93-105.

[1.7]   Kaminsky G., Micromachining of silicon mechanical structures, *J. Vac. Sci. Technology*, B3

         (1985) 1015-1024.

[1.8]   Delapierre G., Micromachining: A survey of the most commonly used processess, *Sensors and

         Actuators*, 17 (1989) 123-138.

[1.9]   Howe R. T., Muller R. S., Gabriel J. and Trimmer S. N., Silicon micromechanics: sensors and

         actuators on a chip, *IEEE Spectrum*, July 1990.

[1.10]   Benecke W., Silicon micromachining for microsensors and microactuators, *Microelectonics

         Engineering*, Vol. 11 (1990) 73-82.

[1.11]   Bao M-H., Yu L.-Z. and Wang Y., Micromachined beam-diaphragm structure improves

         performance of pressure transducer, *Sensors and Actuators,* A21 (1990) 137-141.

[1.12]   Petersen K. E., Silicon as a mechanical material, *Proc. IEEE*, Vol. 70 No. 5 (1982) 420-457.

[1.13]   Ko W. H., Solid-state capacitive pressure transduces, *Sensors and Actuators,* 10 (1986) 303-320.

[1.14]   Guckel H., Surface micromachined pressure transducers, *Sensors and Actuators*, A28 (1991) 122-

         146.

[1.15]   Lee Y. S., A silicon capacitive pressure transducer: performance and limitations, *PhD Thesis*,

         University of Michigan, (1981).

[1.16]   Kudoh T., Shoji S. and Esashi M., An integrated miniature capacitive pressure sensor, *Sensors and

         Actuators*, A29 (1991) 185-193.

[1.17]   Ko W. H., Bao M.-H. and Hong, Y.-D., A high sensitivity integrated circuit capacitive pressure

         transducer, *IEEE Trans.* Vol. ED-29 No. 1 (1982) 48-56.

[1.18]   Nathanson H. C., Newell W. E., Wickstrom R. A. and Davis J. R., Jr., The resonant gate transistor,

         IEEE Trans. Vol. ED-14 No. 3 (1967) 117-133.

[1.19]   Newell W. E., Miniaturization of tuning forks, *Science* (1968) 1320-1326.

[1.20]   Langdon R. M., Resonators sensors - a review, *J. Phys. E: Sci. Instrum.,* Vol. 18 (1985) 103-115.

[1.21]   Pointon A. J., Piezoelectric devices, *IEE Proc.,* Vol. 129 Pt. A No. 5 (1982).

[1.22]   Brignell J. and White N., *Intelligent sensor systems*, IOP Publishing, (1994).

[1.23]   Eernisse E. P., Ward R. W. and Wiggins R. B., Survey of quartz bulk resonator sensor technologies, *IEEE Trans. Ultrasonics and Frequency Control*, Vol. 35 No. 3 (1988) 323-330.

[1.24]   Clayton L. D., Eernisse E. P., Ward R. W. and Wiggins R. B., Miniature crystalline quartz electromechanical structures, *Sensors and Actuators,* 20 (1989) 171-177.

[1.25]   Stemme G., Resonant silicon sensors, *J. Micromech Microeng*. Vol. 1 (1991) 113-125.

[1.26]   Prak A., Silicon resonant sensors: operation and response, *PhD Thesis*, University of Twente, Enschede, The Netherlands, (1993).

[1.27]   Gast T., Sensors with oscillating elements, *J. Phys E: Sci. Instrum.*, Vol. 18 (1985) 783-788.

[1.28]   Karrer H., and Leach J., A quartz resonator pressure transducer, *IEEE Trans.* Vol. IECI-16 No. 1 (1969) 44-50.

[1.29]   Hauptmann P., Resonant sensors and their applications, *Sensors and Actuators,* A25-27 (1991) 371-377.

[1.30]   Tilmans H. A. C., Elwenspoek M. and Fluitman J. H. J., Micro resonant force gauges, *Sensors and Actuators*, A30 (1992) 35-53.

[1.31]   Tang W. C-K., Electrostatic comb drive for resonant sensor and actuator applications, *PhD Thesis,* University of California, Berkeley, (1990).

[1.32]   Tang W. C., Nguyen T.-C. H., Judy M. W. and Howe R. T., Electrostatic comb drive of lateral polysilicon resonators, *Sensors and Actuators*, A21-23 (1990) 328-331.

[1.33]   Cho Y.-H., Kwak B. M., Pisano A. P. and Howe R. T., Slide film damping in laterally driven microstructures, *Sensors and Actuators,* A40 (1994) 31-39.

[1.34]   Howe R. T., Surface micromachining for microsensors and microactuators, *J. Vac. Sci. Technol.* B6 (1988) 1809-1813.

[1.35]   Fan L.-S., Tai Y.-C. and Muller R. S., Integrated moveable micromechanical structures for sensors and actuators, *IEEE Trans.*, Vol. ED-35 No. 6 (1988) 725-730.

[1.36] Guckel H., Sniegowski J. J., Christenson T. R., Moheny S. and Kelly T. F., Fabrication of micromechanical devices from polysilicon films with smooth surfaces, *Sensors and Actuators*, A20 (1989) 117-122.

[1.37] Putty M. W., Chang S.-C., Howe R. T, Robinson A. L. and Wise K. D., Process integration for active polysilicon microstructures, *Sensors and Actuators*, A20 (1989) 143-151.

[1.38] Tilmans H.A.C., Micro-mechanical sensors using encapsulated built-in resonant strain gauges, *PhD Thesis*, University of Twente, Enschede, The Netherlands, (1993).

[1.39] Love J. S. and Juanarena D. B., Design and application of vibrating cylinder based pressure standards, *Proc. Instrumentation in the Aerospace Industry*, No. 1988. (1988) 337-345.

[1.40] Paros J. M., Digital pressure transducers, *Measurements and data*, March-April 1976, 74-79.

[1.41] Ueda F., Kohsaka F. and Ogita E., Precision force transducers using mechanical resonators, *Measurement,* Vol. 3 No. 2 (1985) 89-94.

[1.42] Miller J. R., Operating equation, pressure, temperature coefficients and other charactersistics of a quartz resonator pressure transducer, *Proc. Instrumentation in the Aerospace Industry*, A (1988) 317-324.

[1.43] Smits J. G., Tilmans H. A. C., Hoen K., Mulder H., van Vuuren J. and Boom G., Resonant diaphragm pressure measurement system with ZnO excitation, *Sensors and Actuators,* 4 (1983) 565-571.

[1.44] Greenwood J. C., Etched silicon vibrating sensor, *J. Phys. E: Sci. Instrum.* Vol. 17 (1984) 650-652.

Greenwood J. C. and Satchell D.W., Miniature silicon resonant pressure sensor, *IEE Proc.*, Vol. 135 Pt. D No. 5 (1988) 369-372.

Greenwood J. C. Silicon in mechanical sensors, *J. Phys. E: Sci. Instrum.,* Vol. 21 (1988) 1114-1128.

[1.45] Schmidt M. A., Silicon wafer bonding for micromechanical devices, *IEEE Solid-State Sensor and Actuator Workshop*, Hilton Head, South Carolina (1994) 127-131.

[1.46] Chung G. S., Kawahito S., Ishida M. and Nakamura T., High resolution pressure sensors fabricated by silicon wafer direct bonding, *Electronics Letters*, Vol. 27 No. 12 (1989) 1098-1100.

[1.47]   Ikeda K., Kuwayama H., Kobayashi T., Watanabe T., Nishikawa T., Yoshida T., and Harada K., Three dimensional micromachining of silicon presssure sensor intergrating resonant strain gauge on diaphragm, S*ensors and Actuators*, A21-23 (1990) 1007-1010.

[1.48]   Stemme E. and Stemme G., A balanced dual-diaphragm resonant pressure sensor in silicon, *IEEE Trans.,* Vol. ED-17 No.1 (1990) 649-653.

Stemme E. and Stemme G., A balanced resonant pressure sensor, *Sensors and Actuators*, A21 (1990) 336-341.

[1.49]   Dufour M., Delaye M.T., Michel F., Danel J.S., Diem B. and Delapierre G., A comparison between micromachined pressure sensors using quartz or silicon vibrating beams, *6th Int. Conf. Solid State Sensors and Actuators (Transducers '91),* (1991) 668-671.

[1.50]   Buser R. A. and De Rooij N. F., Silicon pressure sensor based on a resonating element, *Sensors and Actuators,* A25-27 (1991) 717-722.

[1.51]   Kvisteroy T., Guslan O., Stark B., Nakstad H., Eriksrud M., and Bjornstad B., Optically excited silicon sensor for permanently installed downhole pressure monitoring applications, *Sensors and Actuators,* A31 (1992) 164-167.

[1.52]   Zook J. D., Burns D. W., Guckel H., Sniegowski J. J., Engeistad R. L. and Feng Z., Resonant microbeam strain transducers, 6th *Int. Conf Solid-State Sensors and Actuators* (*Transducers '91),* (1991) 529-532.

Guckel H., Rypstata C. and Nesnidal M., Polysilicon resonant microbeam technology for high performance sensor applications, *IEEE Solid-State Sensor and Actuator Workshop,* Hilton Head, South Carolina, (1992) 203-207.

Burns D. W., Zook J. D., Horning R. D., Herb W. R. and Guckel H., A digital pressure sensor based on resonant microbeams, *IEEE Solid-State Sensor and Actuator Workshop,* Hilton Head, South Carolina, (1994) 221-224.

Burns D.W., Zook J.D., Horning R. D., Herb W. R. and Guckel H., Sealed-cavity resonant microbeam pressure sensor, *Sensors and Actuators,* A48 No.3 (1995) 179-186.

Zook J. D., Burns D.W., Guckel H., Sniegowski J. J. Engelstad R. L., and Feng Z., Characteristics of polysilicon resonant microbeams, *Sensors and Actuators*, A35 No.1 (1992) 51-59.

[1.53]   Tilmans H. A. C. and Bouwstra S., A novel design of a highly sensitive low differential-pressure

         sensor using built-in resonant strain gauges, *J. Micromech. Microeng*. 3 (1993) 198-202.

[1.54] Mandle, J. Lefort O. and Migeon A., A new micromachined silicon high-accuracy pressure sensor,

         Sensors and Actuators, A46-47 (1995) 129-132.

Contents

2. Design and predicted performance of the pressure sensor

Chapter 2

Design and predicted performance of the pressure sensor

The objectives of this chapter are to describe the design and performance of a novel type of resonant pressure sensor which is based on a lateral resonant strain gauge. First, the structural design and mode of operation of the lateral resonant pressure sensor are presented. Secondly, the issues that affect the performance of a resonant pressure sensor, including a description of damping mechanisms, are discussed. Thirdly, expressions for the fundamental frequency and gauge factor of the resonant strain gauge are derived and the non-linear spring rate of the flexure highlighted. Lastly, the operation of the pressure sensor is modelled using linear analysis and an estimation is made of the pressure sensitivity and resolution.

2.1 Pressure sensor design

A resonant pressure sensor is, in general, based upon a vibrating mechanical element connected in some way to a pressure sensitive elastic structure, such as a diaphragm. Under an applied pressure the elastic structure deforms, so inducing a shift in the natural frequency of the resonant element. In this instance the resonator is referred to as a *resonant strain gauge* (or *force transducer*) and is commonly used to measure mechanical quantities such as pressure or force [2.1-2.4].

With reference to the review of resonant pressure sensors given in the previous chapter (see Table 1.1), a convenient way to characterise a resonant pressure sensor is by the structure of the resonant element and the nature of the diaphragm/resonator interface. Perhaps the simplest structure of resonant element is the clamped-clamped beam; other more complex shapes include suspended plate structures [2.5,2.6], 'H'-shaped beam

structures [2.7,2.8] and the well known double-ended tuning fork configurations shown in Figure 2.1.
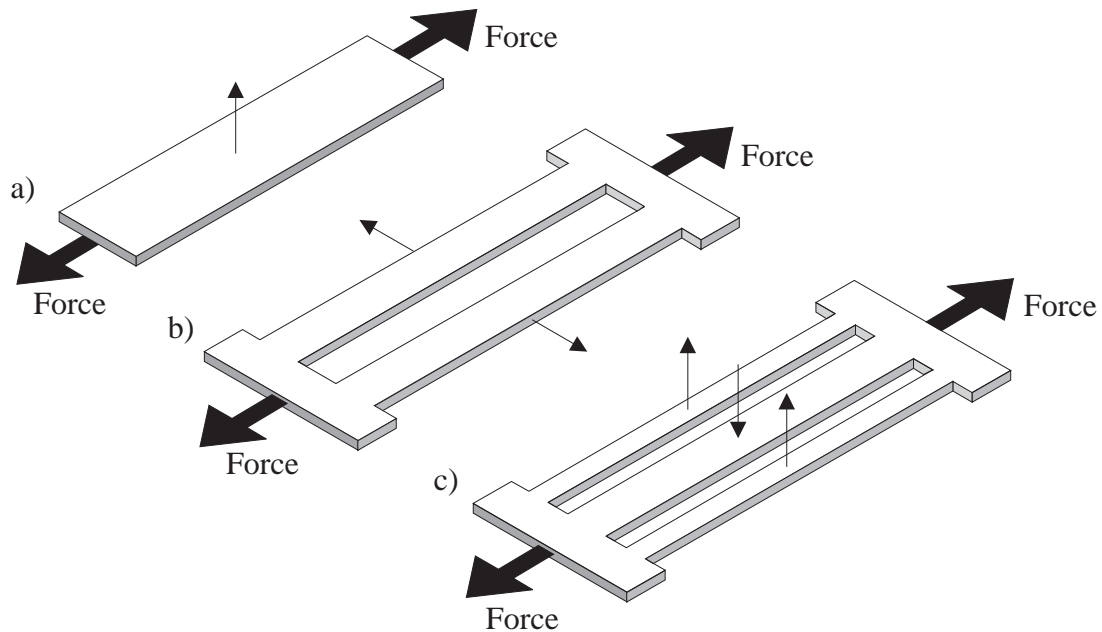

Figure 2.1 Resonant strain gauges (or force transducers) based on a) simple clamped-clamped beam, b) double-ended double bridge structure vibrating in lateral mode, and c) triple beam structure vibrating out of plane. The direction of the fundamental mode is indicated in each case.

Unlike previous devices, the resonant pressure sensor described in this thesis is based on a mechanical resonator whose fundamental mode of oscillation is parallel to the plane of the substrate. The resonator is fabricated from polysilicon using surface micromachining and is located centrally upon a $\approx 20\,\mu\text{m}$ thick bulk-etched single crystal silicon (SCS) diaphragm. A schematic of the resonator and planar silicon diaphragm is shown in Figure 2.2. The square sensor device has a 5 mm side length. Under an applied pressure the diaphragm deforms, so straining the resonator and inducing a frequency shift. The operation of the resonator is analogous to the piezoresistive elements used in conventional pressure sensors, in that it converts the pressure induced strain in the diaphragm into a measurable output, and for this reason is termed a resonant strain gauge. To preserve the selectivity of resonant strain gauge to an applied load, i.e. the pressure induced diaphragm deflection, it is important to minimise any fluctuations in the kinetic energy, such as those caused by mass loading. For this reason the resonator is hermetically sealed within an evacuated chamber. This also serves to increase the

Q-factor of the resonator by removing air/gas damping effects, as is discussed further in section 2.3.2.
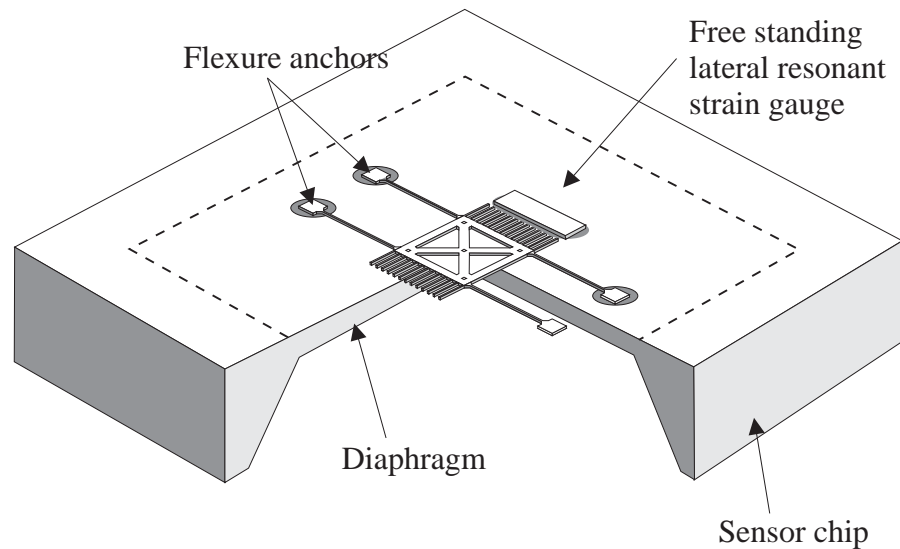
Figure 2.2 3-D schematic of the resonant pressure sensor showing lateral resonant strain gauge mounted upon single crystal diaphragm (not to scale). The encapsulation chip has been omitted for the sake of clarity.

2.2 Resonant strain gauge design

In Figure 2.3 the design of the resonant strain gauge is shown in more detail. The gauge is 2 µm thick and approximately 450 µm long by 150 µm wide and consists of an inertial mass suspended 2 µm above the diaphragm by four trusses, or beams. Each truss is 150 µm in length, and together the four form a *hammock* type flexure. The flexure provides an elastic force for motional parallel to the plane of the substrate, hence the term lateral resonator or lateral resonant strain gauge. Each flexure truss is anchored at one end to the diaphragm. As the diaphragm deforms it both rotates and translates the anchor points, so straining the resonator and inducing the frequency-shift.
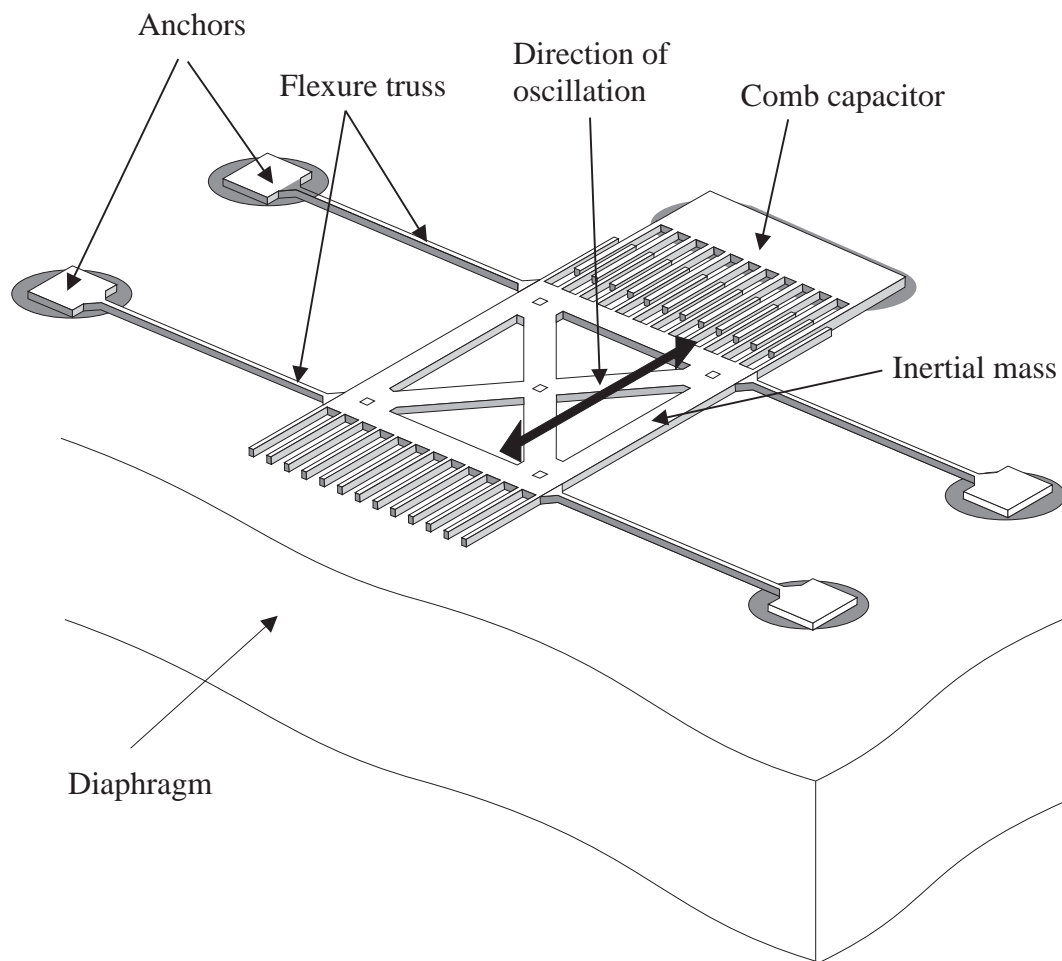
Figure 2.3 Schematic of a 2 μm thick lateral resonant strain gauge consisting of an inertial mass suspended by four trusses, each 150 μm long by 3 μm wide, that together form a hammock flexure. Comb capacitors (only one of which is shown in full above) are used to excite the resonator and/or sense the resultant motion. Some devices also possess an integrated piezoresistive pick-up (not shown).

As is mentioned in chapter 1, all resonant sensors require an excitation and detection mechanism to allow the resonant frequency of the resonant element to be determined. The lateral resonator shown in Figure 2.3 is designed to be excited electrostatically and the motion sensed capacitively via two interdigitised comb capacitors. Some devices also possess an integrated piezoresistive pick-up. These excitation and detection mechanisms are discussed in more detail in the following chapter. At this point it is sufficient to note that the advantage of these mechanisms is that they are easily integrated into the fabrication process.

2.3 Resonant pressure sensors: performance issues

2.3.1 Mode coupling

In all micro-mechanical resonant sensors the vibrating mechanical elements possess several fundamental (and harmonic) modes of oscillation where each mode exhibits its own displacement shape, resonant frequency, Q-factor and strain sensitivity. The existence of these modes can be problematic if they possess a frequency close to that of the desired mode. This is because during closed-loop operation (when the resonator is integrated into an electronic oscillator) they can limit the range of the sensor. The problem is easily understood if one considers that typical full-scale frequency shifts seen in resonant sensors of this type are at least $\pm$ 10 % [2.9]. This means that if any spurious frequency exists in this range then it is possible for the electronic oscillator to lock on to the wrong frequency [2.2,2.10].

The problem of mode coupling, sometimes referred to as an activity dip, is best avoided by employing structures that possess modes of oscillation that are widely spaced in the frequency domain and/or by using an excitation/detection mechanism that does not excite, or cannot detect the unwanted modes [2.12]. However, this can be difficult to achieve where the fabrication process restricts the design of the resonator. The advantage of employing surface micromachining to fabricate the resonator is that it enables a greater flexibility of design. This allows a resonator design to be realised where the relative amplitudes of the spurious modes, compared to the fundamental mode, are minimised. Moreover, by controlling the structure of the resonator, the frequency of the spurious modes can be shifted away from the fundamental mode frequency.

In the lateral resonator design the relative amplitudes and frequency of these spurious modes are controlled by adjusting the dimensions of flexure and inertial mass. For example, the flexure can be designed to have a high compliance in the direction of the fundamental mode, while having a low compliance in all other directions, so reducing the relative amplitudes of the spurious modes.

Mode coupling can also occur between a resonator and its supporting structure, leading to the excitation of spurious modes in the supporting structure. This also limits the range of the sensor and makes interpretation of the frequency response difficult [2.9]. In a resonant pressure sensor the problem is more likely to occur when the resonant

element vibrates in a mode perpendicular to the plane of a diaphragm [2.13]. However, the potential for mode coupling of this type is reduced with the lateral resonator design because its fundamental mode of oscillation is perpendicular to the fundamental mode of the diaphragm. Coupling between a resonator and its surroundings is also undesirable as it leads to a reduction in the Q-factor of the resonator when it is operated in high vacuum (< 1 Pa), as is described below.

2.3.2 The Q-factor

The Q-factor of a resonator is a measure of the energy lost from the vibrating structure and is defined in terms of the ratio of energy stored per period to energy dissipated per period [2.12] hence,

$$Q \triangleq \frac{2\pi. \text{Maximum energy stored per period}}{\text{Energy dissipated per period}}$$

Low energy losses generate a high Q-factor, which is advantageous. Firstly, it enables the resonant frequency to be measured to a high resolution. Secondly, when a resonator is integrated into an electronic oscillator it minimises the effect of the electronics circuitry used to sustain the oscillation on the measured resonant frequency, see section **2.7**. Thirdly, a high Q-factor means that the resonator has excellent material properties and a low level of coupling to the support, both of which may influence the long term stability of the resonator. Finally, a high Q-factor means that the energy required to sustain oscillation is low, so reducing both heat generation and power consumption. To attain a high Q-factor a microresonator must be operated in high vacuum (< 1 Pa) to remove dominant air damping effects. Operation in a vacuum also protects a resonator from the environment, e.g. dust, condensation and chemical attack, that can otherwise cause unwanted frequency shifts or lead to the failure of the device.

In a microresonator, mechanical energy losses occur through three mechanisms namely; air/gas damping, intrinsic material losses and support losses [2.14,2.15]. The overall mechanical Q-factor, Q_m, of a microresonator is related to relative energy loss from each damping mechanism by the expression,

$$\frac{1}{Q_m} = \sum_i \frac{1}{Q_i} \qquad (2.1)$$

where the Q-factor associated with each mechanism, *i*, is denoted by Q_i. As is clear from equation (2.1), the Q-factor of the resonator is dominated by the lowest Q-factor and hence the largest energy loss mechanism.

Air/ gas damping

The damping factor of a resonator that operates in air is related to its geometry and the pressure of the surrounding medium. Three pressure regions can be distinguished.

In the first region near atmospheric pressure, the air surrounding the resonator effectively acts as a fluid and energy losses occur via acoustic radiation and viscous drag. Acoustic radiation occurs due the perpendicular movement of the gas molecules surrounding the resonator, whereas viscous drag occurs due to their lateral transport. Acoustic damping comes into effect where the acoustic wavelength is equal or less than the dimensions of the resonator. This type of damping is only significant in vibrating plate or diaphragm resonators, the latter of which effectively acts as a loudspeaker. The acoustic radiation losses in vibrating plate resonators can be significantly reduced if the air transport occurs internally between two different areas of the resonator vibrating in anti-phase, e.g. the balanced resonator of Stemme and Stemme [2.5].

A microresonator is usually located close to (< 10 µm) another surface to provide a means of support and/or to increase the efficiency of the excitation/detection mechanism. Resonators that oscillate in a mode perpendicular to this surface usually have a high viscous drag coefficient due to the enhanced pressure in the restricted space. This phenomenon is known as squeeze film damping [2.1]. One advantage of a lateral mode of oscillation (although not relevant here as the resonator is designed to be operated in vacuum) is that squeeze film damping is obviated due to the motion of the resonator parallel to the stationary surface.

As the pressure is reduced, the mean free path of the gas molecules increases so that the air no longer acts as a viscous fluid. In this second region, known as the molecular or Knudsen region, energy losses are now caused by the individual collisions of the gas molecules with the resonator. In this region the quality factor, Q_m, is inversely proportional the gas pressure [2.15].

In the third region, the intrinsic region, the gas pressure is so low (usually below ≈ 1 Pa [2.14]) that the level of gas damping is negligible compared to the energy radiated

at the supports or the intrinsic damping of the resonator itself.

A related topic is that the resonant frequency is a function of the pressure of the surrounding gas, so that a reduction in the pressure of this gas leads to a negative frequency-shift. Note that it is not the damping itself that causes the frequency shift, but the additional mass of the gas molecules to be accelerated. For micromachined resonators the sensitivity of the resonant frequency to the pressure of the surrounding gas is limited to a range of 1×10^2 to 1×10^5 Pa [2.16].

Intrinsic damping

A vibrating resonator will also dissipate energy via intrinsic material losses. The mechanisms include thermoplastic internal friction (due to heat conduction resulting from the flexural vibration), magnetic effects, and atomic restructuring, e.g., the movement of dislocations and stress relaxation at grain boundaries [2.1]. Theoretically, internal losses are lower in single crystal material than in a polycrystalline or amorphous material. This means that a resonator made from a single crystal material has the potential to possess a higher intrinsic Q-factor than if it were made from a polycrystalline or amorphous material.

Support losses

Energy is dissipated from a vibrating resonator though its supports, or mounting points. This energy loss arises because of the action of moments and shear forces, created by the motion of the resonator, on the mounting points. One method of reducing the energy lost through this mechanism is to use a balanced resonator configuration where there is no shift in the centre of gravity, such as the well known double-ended tuning fork, shown in Figure 2.1. In this resonator configuration two beams vibrate 180° out of phase, so that the sum of the forces and moments acting on the resonator supports is zero. When a resonator exhibits a strong coupling to its supports the energy loss can be minimised by de-coupling the resonator with a low pass mechanical filter. The filter consists of a large mass-spring system which forms a vibrating support, or mounting frame. The frame isolates the moments and shear forces of the resonator from the mounting point. The mass of the frame has to be large enough to allow an efficient clamping edge for the resonant structure. To minimise the energy loss the resonant frequency of mass-spring system should be much lower ($< 10 \%$) than that of the resonator itself [2.9,2.16]. Buser and de

Rooij [2.13] implemented such a filter to overcome strong resonator to diaphragm coupling and measured Q-factors in high vacuum of up to 150 000. Low energy loss at the resonator support also provides good long term stability because the resonator is mechanically isolated from its surroundings.

2.3.3 Long term stability

The long term stability of a resonant pressure sensor is, in part, determined by the ageing properties of the materials from which the resonator is made. Thus, in this respect single crystal materials, such as silicon and quartz, are preferable to polycrystalline or amorphous materials, because they are almost entirely free from creep [2.17]. A further source of drift is the effect of spurious strain induced by the mounting and/or encapsulation of the sensor. This source of error is normally reduced by careful design of the sensor mounting and/or by the use of an integrated stress relief zone encircling the resonant element [2.18]. One potential advantage of a lateral resonator is the small surface area in the plane of motion. This means that the Q-factor of the resonator is potentially less sensitive to residual gas levels in the evacuated cavity that may rise over the lifetime of the pressure sensor, so leading to an improved long term stability.

2.3.4 Temperature dependence

Aside from mode coupling, a primary source of error in resonant pressure sensors is through temperature variation. Both Young's modulus and the physical dimensions of the resonator are temperature dependent, so a temperature change will cause a shift in resonant frequency. The performance of a resonator may also be degraded by a thermally induced strain. This may result from the thermal expansion of the resonator itself or from a differential thermal expansion between the sensor chip and mount. In practice it is difficult to avoid significant temperature errors and so precision resonant pressure sensors are calibrated, usually with a polynomial curve fitting technique and 3-D look up tables. One way to improve the calibration is to employ a reference (or inactive) resonator that is insensitive to the measurand, e.g. pressure, but subject to the same temperature variation. Here, the effect of temperature variation can be reduced by taking the ratio of the two frequencies, and so the calibration improved [2.19]. A variation on this technique, often referred to as a push-pull mode of operation employs two (or more) resonators. Here, the sensor is designed so that the frequency of one resonator changes by $+\Delta f$, whilst that of

the other changes by $-\Delta f$. Taking the difference of the two frequencies leads to an effective sensitivity of $2\Delta f$. This method can also be used reduce cross-sensitivity to temperature, provided both resonators possess equal temperature sensitivities [2.20].

2.4 Predicted performance

As was indicated in the previous chapter, resonant pressure sensors are attractive because they offer a superior sensitivity, resolution and stability over more conventional piezoresistive and capacitive pressure sensors.

In theory, the smallest change in pressure, δP_{min}, that a resonant pressure sensor can measure is described by its relative pressure sensitivity, G_p, and the minimum resolution of frequency measurement system, $(\delta\omega/\omega)_{min}$ [2.1] so that,

$$\delta P_{min} = \left(\frac{1}{G_p}\right)\left(\frac{\delta\omega}{\omega}\right)_{min} \tag{2.2}$$

The relative pressure sensitivity of the sensor is the normalised change in the unloaded resonant frequency, ω_1, with applied pressure P,

$$G_P = \left(\frac{1}{\omega_1}\right)\left(\frac{d\omega_1}{dP}\right)_{P=P_0} \tag{2.3}$$

and is a function of the mechanical design of the resonant strain gauge and its integration with the pressure sensitive structure. In this thesis, G_p is defined as the product of the gauge factor of the strain gauge, denoted G_N, and a transduction factor denoted G_D;

$$G_p = \left(\frac{1}{\omega_1}\frac{d\omega_1}{dP}\right)_{P=P_0} = \underbrace{\left(\frac{1}{\omega_1}\frac{d\omega_1}{dN}\right)_{N=N_0}}_{G_N}\underbrace{\left(\frac{dN}{dP}\right)_{P=P_0}}_{G_D} \tag{2.4}$$

The gauge factor is a measure of sensitivity of the resonant strain gauge to an axial load N, while the transduction factor describes the rate of change of axial load applied to the resonant strain gauge with applied pressure.

Following these principles the remainder of this chapter is divided into three sections. In section 2.5 expressions are derived for the resonant frequency and gauge

factor of the lateral resonant strain gauge. In section 2.6 expressions are derived for the relative pressure sensitivity and transduction factor. Finally, in section 2.7 the factors that determine the minimum frequency resolution of the pressure sensor when it is integrated into an electronic oscillator are highlighted, and estimates are made of the pressure resolution.

2.5 Resonant frequency and gauge factor

A useful indicator of the performance of a resonant strain gauge is the relationship between the axial load and the fundamental frequency, or *gauge factor*. Using the notation Andres [2.10] and Tilmans [2.1], the gauge factor of a resonant strain gauge vibrating at $\omega = \omega_1$, under applied axial load $N = N_0$, is defined as,

$$G_N = \left(\frac{1}{\omega_1} \frac{d\omega_1}{dN} \right)_{N=N_0=E_f A_f \varepsilon / l_f} \tag{2.5}$$

where ω_1 is the fundamental unloaded frequency of the resonator, E_f Young's modulus, ε the residual strain and A_f the cross-sectional area of the supporting flexure.

2.5.1 Rayleigh's energy method

A convenient way to calculate the resonant frequency and gauge factor of the resonant strain gauge is to employ Rayleigh's energy method. Raleigh's energy method may be applied to any lumped element or continuous system, and enables the frequency of any simple harmonic motion to be calculated if the amplitude of vibration of every part of the system is known [2.11]. Rayleigh's energy method is derived from the principle that for any conservative system exhibiting simple harmonic motion the mean values of the kinetic and potential energies over one cycle are equal, i.e.,

$$\overline{T} = \overline{V} \tag{2.6}$$

where T denotes the kinetic energy of the system and V the potential energy of the system. In practice, it is usually simpler to equate the maximum kinetic energy and maximum potential energy because the need to integrate over one cycle is avoided, i.e.,

$$T_{max} = V_{max} \tag{2.7}$$

Since the resonator design is symmetrical, it is conceptually simpler to analyse the element consisting of a flexure truss AB of length l_f attached to the inertial mass $M_i/4$, as shown in Figure 2.4. Under a static deflection force $f_x/4$, the inertial mass exhibits a maximum displacement x_0. The load N is the axial load applied to the resonator by the diaphragm deflection. If the flexure is rigidly anchored to the diaphragm, then the truss AB also experiences a horizontal reaction force of magnitude H. This reaction force arises as a result of the axial elongation of the truss under a transverse deflection, and results in a non-linear spring rate. This type of non-linearity is commonly known as the hard spring effect and leads to a characteristic bending of the frequency (and phase) response [2.21]. It also means the that the amplitude of vibration is dependant on the applied axial force.

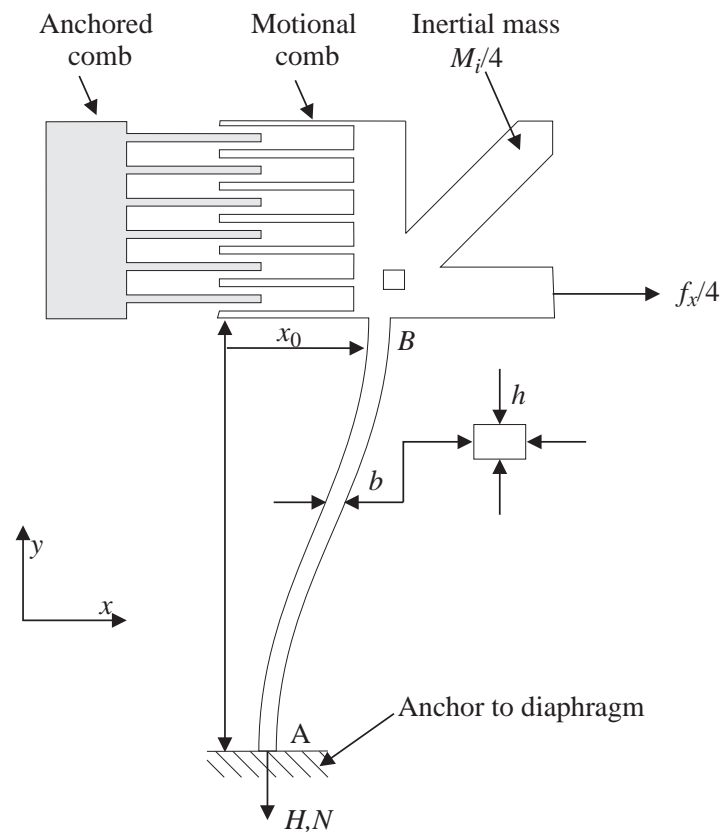*Figure 2.4 Transverse deflection profile of lateral strain gauge under static load.*

For small amplitudes of vibration the effect of deflection induced axial strain can be ignored. With this assumption the mode shape of the flexure truss shown in Figure 2.4 is found by solving the differential equation that describes the static deflection of the flexure truss under an applied load $f_x/4$, given by Roark [2.22] to be,

$$x(y) = \frac{f_x}{4(12E_f I)}\left(3l_f y^2 - 2y^3\right) \tag{2.8}$$

where E_f is Young's modulus of the truss and I the area moment of inertia about the centroid of the truss cross-section, given by

$$I = hb^3/12 \tag{2.9}$$

where b is the width of the truss and h the thickness of the truss. It follows from equation (2.8) that at the point of maximum displacement, i.e. $x(l_f)=x_0$,

$$\left(\frac{f_x}{48E_f I}\right) = \frac{x_0}{l_f^3} \tag{2.10}$$

which leads directly to an expression for the linear spring rate, k_{xl}, of the flexure,

$$k_{xl} = \frac{48E_f I}{l_f^3} \tag{2.11}$$

Kinetic energy

The total kinetic energy of the resonator is the sum of the kinetic energy of the truss and the kinetic energy of the inertial mass. As a starting point, the inertial mass and flexure truss shown in Figure 2.4 are assumed to oscillate sinusoidally about the equilibrium position with a displacement,

$$x = x_0 \sin \omega_1 t \tag{2.12}$$

where x_0 and ω_1 are the maximum amplitude and angular frequency of oscillation, respectively. If the truss AB possesses a mass per unit length of M_t/l_f, then the kinetic energy of a small element dy moving in the plane of oscillation is,

$$\delta T = \frac{M_t}{l_f}\left[\frac{dx(y)}{dt}\right]^2 dy \tag{2.13}$$

so that the kinetic energy of the truss and inertial mass, $M_i/4$, is given by,

$$T = \frac{M_t}{l_f} \int_0^{l_f} \left[\frac{dx(y)}{dt} \right]^2 dy + \underbrace{\frac{1}{2} \left(\frac{M_i}{4} \right) \left[\frac{dx}{dt} \right]^2}_{\text{Inertial mass}} \tag{2.14}$$

$$\underbrace{\phantom{\frac{M_t}{l_f} \int_0^{l_f} \left[\frac{dx(y)}{dt} \right]^2 dy}}_{\text{Truss}}$$

Substitution of equation (2.10) into equation (2.8), to eliminate the f_x/EI term, yields an expression for the deflection curve of the flexure of the form,

$$x(y) = \frac{x_0}{l_f^3} \left(3l_f y^2 - 2y^3 \right) \tag{2.15}$$

Now, it follows that the kinetic energy of the truss is at a maximum when it passes through the equilibrium position at which point the velocity profile of the truss is,

$$\frac{dx(y)}{dt} = \omega_1 \left[\frac{x_0}{l_f^3} \left(3l_f y^2 - 2y^3 \right) \right] \tag{2.16}$$

It also follows that the velocity, dx/dt, of the inertial mass is a maximum at the equilibrium position and equal to,

$$\frac{dx}{dt} = \omega_1 x_o \tag{2.17}$$

Substituting equations (2.16) and (2.17) and into equation (2.14) leads to an expression for maximum kinetic energy of the resonator,

$$T_{max} = \frac{M_t \omega_1^2 x_0^2}{2 l_f^7} \int_0^{l_f} \left(3l_f y^2 - 2y^3 \right)^2 dy + \frac{M_i}{8} \omega_1^2 x_0^2 \tag{2.18}$$

which upon integration of the first term yields,

$$T_{max} = \frac{\omega_1^2 x_0^2}{2} \left(\frac{13M_t}{35} + \frac{M_i}{4} \right) \tag{2.19}$$

Potential energy

The potential energy stored by the deformed flexure truss is the sum of the strain energy of bending of the truss and the work done in stretching the flexure truss. The strain energy of bending of the flexure truss is given by Gere to be [2.23],

$$V_t = \frac{1}{2} \int_0^{l_f} E_f I \left[\frac{d^2 x(y)}{dy^2} \right]^2 dy \tag{2.20}$$

There are two mechanisms that lead to a stretching of the flexure truss, and so an increase in potential energy. Firstly, there is the work done by the load N, applied to the truss by the deformation of the diaphragm. Secondly, there is the work done in stretching the truss as it undergoes a transverse displacement, leading to a reaction force H on the supports of the truss, see Figure 2.5a. In the following analysis the potential energy stored by virtue of the work done by the load N, is denoted V_N. Similarly, the energy stored by virtue of the work done against the reaction force H is denoted V_H.

A first approximation of the work done in stretching the flexure truss is made by assuming a linear force-deflection relation and calculating the axial elongation. Suppose the truss AB shown in Figure 2.5a is subjected to a load N and a horizontal reaction force H. If end B of the beam is allowed to displace longitudinally, then it will move through a small distance λ to B', as shown in Figure 2.5b. The relationship between the axial elongation λ, also known as the curvature shortening, and the mode shape is given by Gere [2.23] to be,

$$\lambda = \frac{1}{2} \int_0^{l_f} \left(\frac{dx(y)}{dy} \right)^2 dy \tag{2.21}$$

Now, the total potential energy stored by the axial elongation of the truss is the sum of the work done in stretching the flexure truss against the horizontal reaction force and the applied load, i.e.,

$$V_N + V_H = \frac{E_f A_f}{l_f} \int_o^{\lambda} (\lambda_N + \lambda_H) d\lambda \tag{2.22}$$

where λ_N represents the axial elongation induced by the applied load N and λ_H the axial elongation induced by the reaction force H. Integrating equation (2.22) yields,

$$V_N + V_H = \frac{E_f A \lambda_N^2}{2l_f} + \frac{E_f A \lambda_H^2}{2l_f} \tag{2.23}$$

and since $N = E_f A \lambda_N / l_f$ this equation reduces to,

$$V_N + V_H = \frac{N\lambda_N}{2} + \frac{E_f A_f \lambda_H^2}{2l_f} \tag{2.24}$$

Finally, the substitution of equation (2.21) into equation (2.24) yields an expression for the energy stored due to axial elongation,

$$V_N + V_H = \frac{N}{4} \int_0^{l_f} \left(\frac{dx(y)}{dy} \right)^2 dy + \frac{E_f A_f}{8l_f} \left[\int_0^{l_f} \left(\frac{dx(y)}{dy} \right)^2 dy \right]^2 \tag{2.25}$$
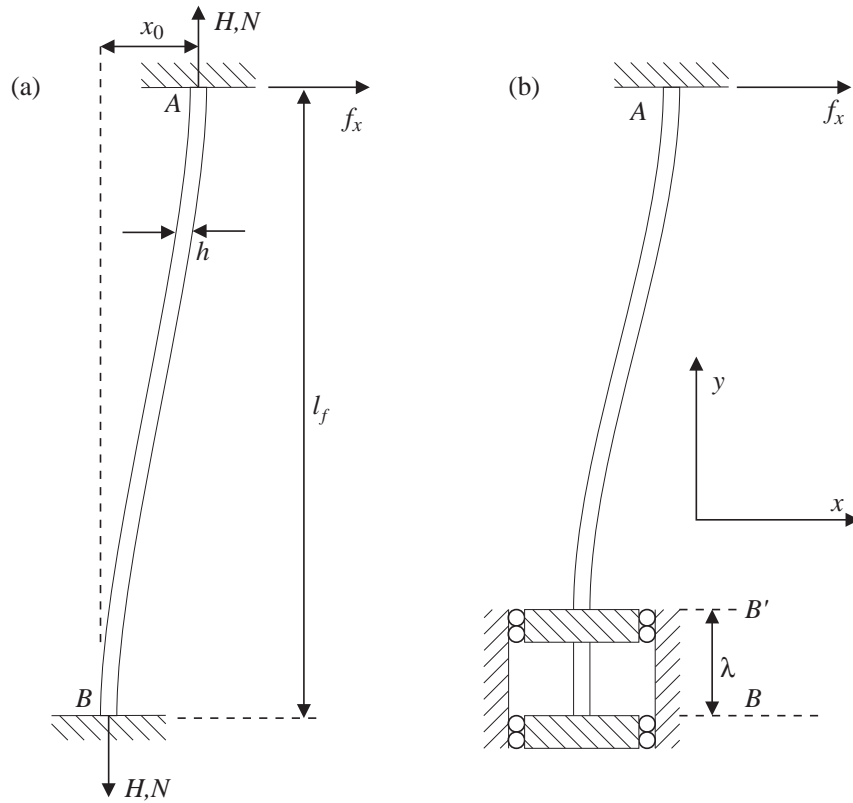

Figure 2.5 Elongation of flexure truss under a transverse deflection.

Proceeding with the calculation, the total potential energy of the deformed truss is the sum of equations (2.20) and (2.25),

$$V = \frac{1}{2} \int_0^{l_f} E_f I \left[\frac{d^2 x(y)}{dy^2} \right]^2 dy + \frac{N}{4} \int_0^{l_f} \left(\frac{dx(y)}{dy} \right)^2 dy + \frac{E_f A_f}{8l_f} \left[\int_0^{l_f} \left(\frac{dx(y)}{dy} \right)^2 dy \right]^2 \tag{2.26}$$

Substitution of the expression for the mode shape of the deformed truss given by equation (2.8) yields,

$$V = \frac{E_f I}{2} \int_0^{l_f} \left(\frac{f_x}{48EI}\right)^2 \left(36 l_f^2 - 144 l_f y + 144 y^2\right) dy$$
$$+ \frac{E_f IN}{4} \int_0^{l_f} \left(\frac{f_x}{48EI}\right)^2 \left(36 l_f^2 - 72 l y^3 + 36 y^4\right) dy \qquad (2.27)$$
$$+ \frac{E_f A_f}{8 l_f} \left[\int_0^{l_f} \left(\frac{f_x}{48EI}\right)^2 \left(36 l_f^2 - 72 l_f y^3 + 36 y^4\right) dy\right]^2$$

which upon integration leads to a general expression for the potential energy of the deformed truss,

$$V = \frac{1}{2}\left(\frac{f_x}{48EI}\right)^2 \left[12 E_f I l_f^3 + \frac{6 T l_f^5}{5} + \frac{9 E_f A_f}{50}\left(\frac{f_x}{48EI}\right)^2\right] \qquad (2.28)$$

It follows that the potential energy is at a maximum at the point of maximum displacement, so that the substitution of equation (2.10) into equation (2.28) to remove the $f_x/48 E_f I$ term yields,

$$V_{max} = \frac{x_0^2}{2}\left[\frac{12 E_f I}{l_f^3} + \frac{6N}{5 l_f} + \frac{9 E_f A_f x_0^2}{50}\right] \qquad (2.29)$$

Resonant frequency

According to Rayleigh's energy method, an expression for the fundamental resonant frequency is found by equating the maximum potential energy and kinetic energy, given by equations (2.19) and (2.29), respectively,

$$\omega = \sqrt{\frac{6}{25 l_f^3}\left[\frac{200 E_f I + 20 N l_f^2 + 3 E_f A_f x_0^2}{M_i + \frac{52 M_t}{35}}\right]} \qquad (2.30)$$

For small transverse deflections the effect of the reaction force due to the axial elongation is small compared to that of the load, so that equation (2.30) reduces to,

$$\omega = \sqrt{\frac{24}{5l_f^3}\left[\frac{10E_f I + Nl_f^5}{M_i + \frac{52M_t}{35}}\right]} \qquad (2.31)$$

Furthermore, if the applied axial load N is set to zero then this equation simplifies to the familiar expression for the natural circular frequency of a system with one degree of freedom,

$$\omega_1 = \sqrt{\frac{48E_f I}{l_f^3(M_i + \frac{52M_t}{35})}} \qquad (2.32)$$

Usually $M_t \ll M_i$ so that,

$$\omega_1 \approx \sqrt{\frac{48E_f I}{l_f^3 M_i}} \quad ; \quad f_1 \approx \frac{1}{2\pi}\sqrt{\frac{4E_f hb^3}{l_f^3 M_i}} \quad ; \quad f_1 \approx \frac{1}{2\pi}\sqrt{\frac{k_{xl}}{M_i}} \quad (2.33\text{a,b,c}).$$

where f_1 is the unloaded fundamental frequency of the lateral resonator and the other parameters are given previously.

Equation (2.33) can be used to design the lateral resonator, so that it possesses the desired resonant frequency. In this research a resonant frequency of ≈ 50 kHz is chosen to integrate with the electronics used to operate the resonant pressure sensor shown in Figure 1.8 of Chapter 1.

In practice, a low flexure spring rate is desirable because it reduces the magnitude of drive voltage required to drive the resonator to a given amplitude. As is clear from equation (2.33), the spring rate is best minimised by forming the hammock flexure from long, thin, trusses. The minimum width of the flexure truss is determined by the resolution of the photolithographic process used to fabricate the resonator, which in this research is 3 μm, see chapter 4. The maximum truss length is determined by the ability of the resonator to support itself. This is gauged from a parameter known as the maximum free-standing length. As the term implies, a microstructure whose length exceeds its

maximum free-standing length will be not be self supporting, i.e., it will collapse onto the substrate during processing. As the maximum free-standing length of a microstructure is process dependent, it must be estimated in the design phase. Here, a truss length of 150 µm is used. This value is based upon the work of Howe [2.24], who has investigated the maximum free-standing length of 2 µm thick polysilicon clamped-clamped beams.

Young's modulus of the polysilicon flexure truss is also process dependent, and so must be estimated in the design phase. Young's modulus of polysilicon varies according to deposition, doping and annealing conditions, and has been measured to be between 100-175 GPa [2.24,2.25]. Here, a value of 140 GPa is used, again based upon the measurements of Howe [2.24] for a polysilicon film doped by diffusion at 1050 $^{\circ}$C.

Having selected the process dependent parameters the inertial mass is adjusted by setting its shape/dimensions to achieve the desired resonant frequency. For example, for the lateral resonator design shown in Figure 2.3 the following parameters are relevant: b=3 µm, h=2 µm, l_f= 150 µm, M_i= 73 ng, M_t=8 ng and E_f=140 GPa (estimated). Inserting the values into equation (2.33b) leads to a predicted resonant frequency of ~ 55 kHz.

Gauge factor

An expression for the gauge factor of the lateral resonator is found by assuming a small deflection so that the effect of deflection induced strain is negligible. The substitution of equation (2.32) into equation (2.5), together with the differential of equation (2.31) with respect to the applied load N, where $N = N_0 = E_f A_f \varepsilon / l_f$, yields the expression,

$$G_N = \frac{3}{E_f A_f \left[5 \left(\frac{l_f}{b} \right)^2 + 6\varepsilon \right]} \qquad (2.34)$$

It is evident from this equation that a high gauge factor is obtained when the hammock flexure possesses long thin trusses with a low residual strain. The variation of G_N with residual strain and the normalised flexure dimension $\left(l_f/b\right)$ is plotted graphically in Figure 2.6, from which it can be seen that the optimal residual strain is below about 10^{-4} ε, where a gauge factor is attained of between 10^3 and 10^4 N^{-1}. The other parameters in equation (2.34) are given in the caption of Figure 2.6.
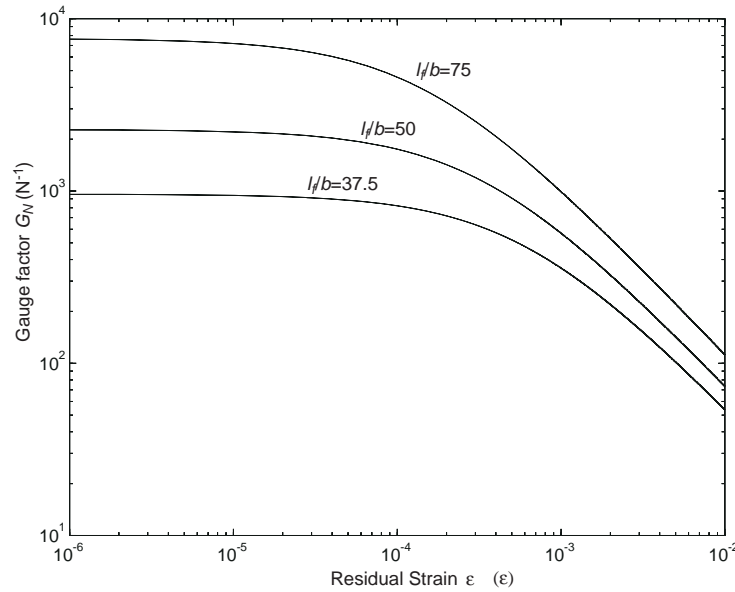

Figure 2.6 Variation in Gauge factor G_N of the hammock flexure resonator with flexure length to width ratio and residual strain ε. The other parameters in equation (2.34) are, $A_f=6\times10^{-12}m^2$ and $E_f=140$ GPa.

2.5.2 Non-linear spring rate

It is clear from equation (2.30) that the resonant frequency of the strain gauge is dependant on the load applied by the diaphragm and the amplitude of vibration, x_o. In order to operate the resonator the amplitude of vibration needs to be high enough so that its motion can be measured. However, if the resonator is over-modulated the effect of the non-linear spring rate becomes significant and a frequency shift is seen. Clearly, there is a trade-off between increasing the amplitude of vibration whilst avoiding a deflection induced frequency shift. The increase in fundamental frequency with vibration amplitude also leads to a skewed frequency (and phase) response and an apparent decrease in Q-factor, see section 3.2.5 of chapter 3. In practice, the amplitude of vibration is generally determined by the geometry of the resonator, the power of the drive signal, the efficiency

of the excitation/detection mechanism and the Q-factor of the resonant mode. A stable amplitude is usually achieved by controlling the power of the drive signal, using an automatic gain control (AGC) amplifier.

The magnitude of the non-linearity in the transverse spring rate can be determined by considering the total potential energy stored in a flexure truss, given by equation (2.27) and repeated below for convenience,

$$V_{max} = \frac{x_0^2}{2} \left[\frac{12E_f I}{l_f^3} + \frac{6N}{5l_f} + \frac{9E_f A_f x_0^2}{50} \right] \tag{2.35}$$

Noting that the hammock flexure comprises four trusses, the differentiation of equation (2.35) with respect to the maximum transverse displacement, x_0, yields an expression for the transverse force-deflection relationship of the hammock flexure,

$$f_x = \frac{dV_{max}}{dx_0} = 4 \left[\frac{12E_f I x_0}{l_f^3} + \frac{6N x_0}{5l_f} + \frac{9E_f A_f x_0^3}{25} \right] \tag{2.36}$$

From equation (2.36), shown graphically in Figure 2.7, it is clear that the restoring force of the flexure has a cubic dependence on the transverse displacement. As was mentioned earlier, this type of cubic non-linearity is commonly known as the hard spring effect and leads to a characteristic bending of the frequency (and phase) response [2.21]. Equation (2.36) also shows that, for a given drive force, the amplitude of vibration of the resonator is dependant on the load applied to the resonator.
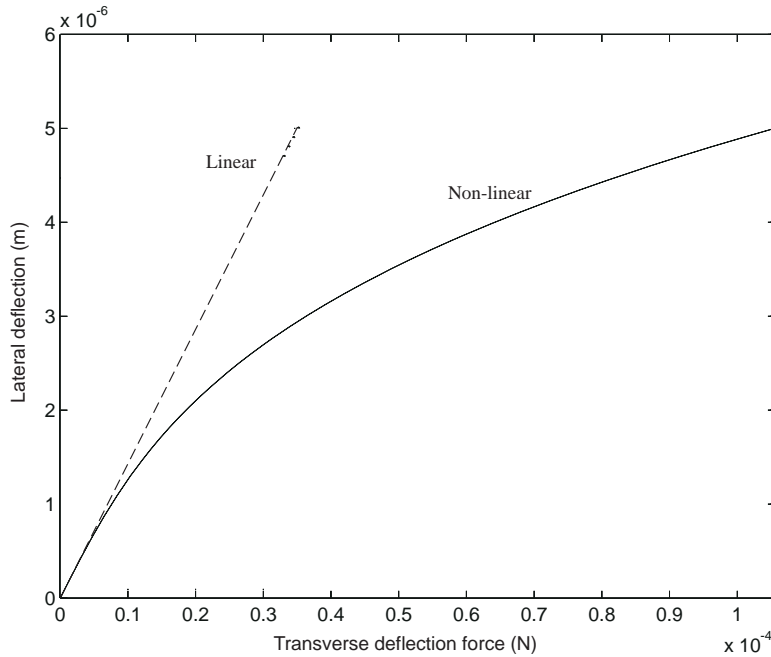
Figure 2.7 Linear (dashed line) and non-linear force (solid line) force-deflection relation for the unloaded (N=0) hammock flexure as predicted by equation (2.36) with the following parameters: $A_f=6\times10^{-12}$ m^2, $l_f=150$ µm, $E_f=140$ GPa and $I=4.5\times10^{-18}$ m^4.

Lateral resonators can generally be categorised according to the mode of oscillation and method of support. Two other types of translational lateral resonator are the folded flexure resonator and crab-leg resonator. Other rotary mode designs employing serpentine or spiral type flexures have also been realised [2.27]. Unlike the hammock flexure, these configurations possess a linear spring rate, i.e. one that is insensitive to an applied load, and so have no application in resonant strain gauges. However, their linearity makes them useful for the construction of test resonators which, in combination with other structures, may be used to determine the material properties of a resonator.

2.5.3 A folded flexure resonator

Figure 2.8 presents the design of a lateral resonator employing two folded flexures and two interdigitised comb capacitors, for electrostatic excitation/capacitive detection. Each folded flexure is formed from four (100 µm long by 3 µm) wide trusses and allows for the relief of residual strain within the material and the axial strain induced by large amplitudes of vibration. As the flexure exhibits a linear behaviour it is useful for measuring Young's modulus of the structural polysilicon used to fabricate the resonator.
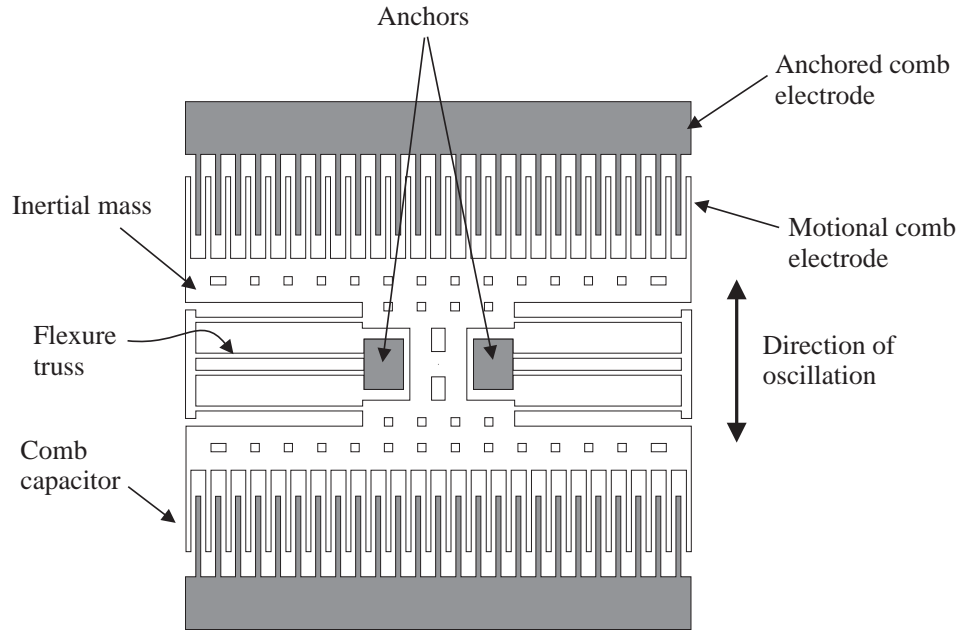
Figure 2.8 Diagram of lateral resonator employing a folded type flexure formed from four 100 μm long trusses. Two 51 plate interdigitised comb capacitors are employed for electrostatic excitation and capacitive detection.

The fundamental frequency of the folded flexure resonator can also be found by the application of Rayleigh's energy method, and is given by Tang [2.27] to be,

$$f_1 \approx \frac{1}{2\pi} \sqrt{\frac{24E_f I}{M_i l_f^3}} \qquad (2.37)$$

where M_i is the inertial mass, E_f Young's modulus, l_f the length and I the cross sectional moment of inertia of a flexure truss. The resonant frequency of this folded flexure resonator is predicted to be ~ 49 kHz. This is based upon a Young's modulus of 140 GPa (estimated), inertial mass of 120 ng, truss length of 100 µm, truss width of 3 µm and resonator thickness of 2 µm.

2.6 Relative pressure sensitivity

The relative pressure sensitivity of the resonant pressure is a measure of the shift in fundamental frequency of the resonant strain gauge with applied pressure and, as stated earlier, is defined by the expression,

$$G_p = \underbrace{\left(\frac{1}{\omega_1} \frac{d\omega_1}{dN} \right)_{N=N_0}}_{G_N} \underbrace{\left(\frac{dN}{dP} \right)_{P=P_0}}_{G_D} \tag{2.38}$$

An expression for the gauge factor, G_N, is derived in the previous section by considering the relationship between an axial load and the change in fundamental frequency. To determine the transduction factor, G_D, it is necessary to examine the pressure/deflection relationship of the diaphragm and the positioning of the resonator, or, more precisely, the location of the flexure anchors, on the diaphragm.

2.6.1 Transduction factor

Consider the cross-section of the diaphragm and resonator shown in Figure 2.9. The resonator is located centrally upon the diaphragm. Under an applied pressure the diaphragm deforms, so rotating and translating the flexure anchor points in the directions shown. For small deflections of the diaphragm, the flexure anchor acting at point *A* will rotate through an angle θ_1, so elongating the flexure truss a small distance δx, see Figure 2.9. The strain, ε_r, induced in a single flexure truss by the rotation of the diaphragm is therefore,

$$\varepsilon_r = \frac{z_0}{l_f} \sin \theta_1 \tag{2.39}$$

where z_0 is the distance between the mid-plane of the diaphragm and the mid-plane of the resonator (at the anchor point) and l_f the length of a flexure truss. Taking account of the fact that each pair of anchors rotate in opposition, the general expression for the load applied to the hammock flexure by the action of the diaphragm deflection is of the form,

$$N = A_f E_f \left[\varepsilon_n + \frac{z_0}{2l_f} \sin(\theta_1 - \theta_2) \right] \tag{2.40}$$

where ε_n is the normal strain due to in plane loads acting on the flexure anchor, A_f is the cross-sectional area of the flexure truss and E_f Young's modulus of the flexure truss. Also θ_1 and θ_2 are the rotation angles of the anchor points, as shown in Figure 2.9. In calculating the transduction factor the following assumptions are made:

- The deflection of the diaphragm is small, so that the affect of normal strains due to in plane loads can be ignored.

- The diaphragm deforms so as to increase the strain in the lateral resonator.

- The diaphragm is free from residual strain.

- The resonator is located symmetrically about the centre of the diaphragm.

- The flexure anchors act at single point on the diaphragm.

- The width of the resonator is small compared to the side length of the diaphragm, so that the twisting action of the anchor points is negligible.

- The influence of the resonator on the deflection of the diaphragm is negligible.

With these assumptions the equation (2.40) reduces to,

$$N \approx A_f E_f \left[\frac{z_0}{2l_f} \sin 2\theta \right] \tag{2.41}$$

where $\theta_1 \approx -\theta_2$. For small angles of rotation $\sin 2\theta \approx \tan 2\theta$, equation (2.41) is re-written as,

$$N \approx A_f E_f \left[\frac{z_0}{l_f} \frac{dZ}{dx_0} \right] \tag{2.42}$$

where dZ/dx_0 is the gradient of the mid-plane of the diaphragm at the anchor point, see Figure 2.9. An expression for the transduction factor is found from equations (2.38) and (2.42), yielding,

$$G_D \approx \frac{d}{dP} \left(A_f E_f \frac{z_0}{l_f} \frac{dZ}{dx_0} \right) \tag{2.43}$$

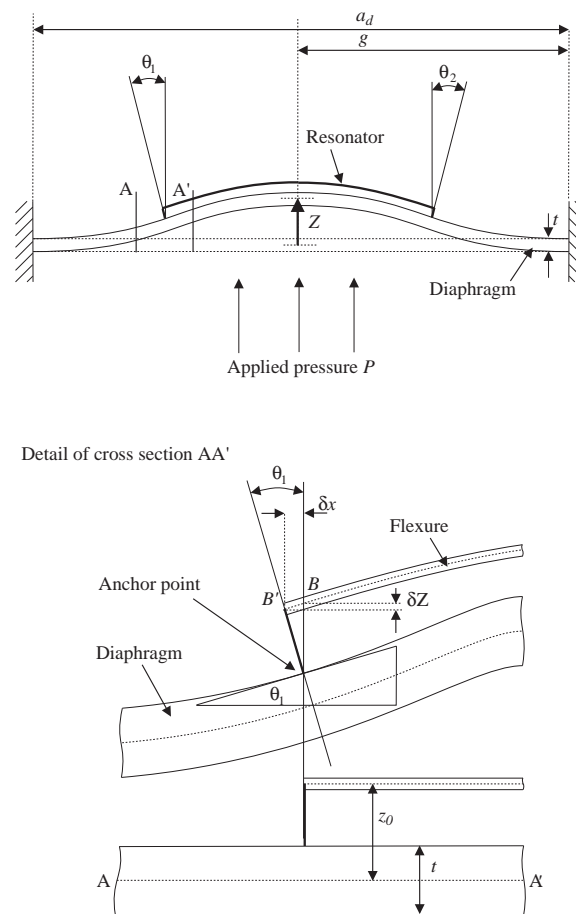where the constants have the same meaning as those given previously.

Figure 2.9 Schematic cross-section of diaphragm showing rotation of flexure anchor due to diaphragm deflection.

The next step is to determine the change in slope of the diaphragm with the applied pressure, i.e. $d/dP(dZ/dx_0)$ in equation (2.43). The pressure sensor described in this thesis employs a square diaphragm because it is easily fabricated from silicon using anisotropic etching. Assuming the diaphragm is perfectly clamped along all edges and loaded by a lateral pressure, it tends to bend into the quasi-spherical shape shown in Figure 2.9. Unfortunately, an exact analysis of the pressure deflection curve for a rectangular diaphragm with all edges clamped is somewhat mathematically intractable, (e.g. see Clark and Wise [2.28]) and so to simplify the analysis an assumed deflection curve is used.

Consider the square diaphragm of side length $a_d = 2g$ shown in Figure 2.9. Under a uniform pressure P, the deflection at the centre of the diaphragm is,

$$Z = \frac{16\alpha P g^4}{E_D t^2}(1 - \upsilon^2)$$ (2.44)

where α is a non-dimensional deflection coefficient which depends on the ratio of diaphragm to side length to diaphragm thickness, E_D is the Young's modulus, t the thickness, and υ Poisson's ratio of diaphragm, respectively [2.29]. On inspection it is reasonable to assume that the deflection curve is of the same form to that of the clamped-clamped beam shown in Figure 2.4. With this assumption the deflection curve of a thin axial element of length g is given by the combination of equations (2.8) and (2.44),

$$Z(x) \approx \frac{16\alpha P g}{E_D t^2}(1 - \upsilon^2)(3gx^2 - 2x^3)$$ (2.45)

and the gradient is,

$$\frac{dZ(x)}{dx} \approx \frac{16\alpha P g}{E_D t^2}(1 - \upsilon^2)(6gx - 6x^2)$$ (2.46)

which is at a maximum at $x = 0.5g$.

Having determined an expression for dZ/dx_0, an expression for the transduction factor is found by simply substituting equation (2.46) into (2.43),

$$G_D \approx \frac{d}{dP}\left(A_f E_f \frac{z_0}{l_f}\right)\left(\frac{16\alpha P g}{E_D t^2}(1 - \upsilon^2)(6gx - 6x^2)\right)$$ (2.47)

which upon differentiation yields,

$$G_D \approx \frac{z_0 A_f E_f 16\alpha g}{l_f E_D t^2}(1 - \upsilon^2)(6gx - 6x^2)$$ (2.48)

The maximum pressure sensitivity is attained when the flexure anchors are located on the point of maximum rotation, i.e. at $x = 0.5g$, and hence the substitution of $x = 0.5g$ into equation (2.48) yields,

$$G_D \approx \frac{3\alpha z_0 A_f E_f (1 - \upsilon^2)}{l_f E_D}\left(\frac{a_d}{t}\right)^3$$ (2.49)

Finally, having calculated an expression for the transduction factor, the relative pressure sensitivity is obtained directly from equations (2.34), (2.38) and (2.49),

$$G_P = \frac{9z_0\alpha(1-\upsilon^2)}{E_D l_f (5b^2 / l_f^2 + 6\varepsilon)}\left(\frac{a_d}{t}\right)^3 \qquad (2.50)$$

where the parameters have the same meaning as those given previously. It is clear from equation (2.50) that a high pressure sensitivity is attained when a diaphragm with a high side length to thickness ratio is employed, which is a natural and reasonable result. The diaphragm side length to thickness ratio also determines strength of the diaphragm and hence the burst pressure. In practice, a pressure sensor is generally required to withstand an over-pressure of three times the specified pressure range. This means that the minimum diaphragm to side length thickness ratio is set by the operating range of the sensor. Equation (2.50) also shows that the pressure sensitivity is increased by forming the hammock flexure from long thin trusses that possess a low residual strain. An increase in z_0, the distance between the mid-plane of the resonator and diaphragm is also advantageous, but is difficult to achieve with the fabrication process used to produce the pressure sensor.

At this point it is instructive to estimate the relative pressure sensitivity for the lateral resonator design presented earlier in Figure 2.2. The variation between the relative pressure sensitivity and the diaphragm side length to thickness ratio, as defined by equation (2.50), is shown graphically in Figure 2.10. The resonator is 450 µm long, so that for the resonator anchors to be located on the point of maximum rotation, i.e. at $0.5g$, the required diaphragm side length is 900 µm. The proposed fabrication process allows a minimum diaphragm thickness of approximately 20 µm, leading to a side length to thickness ratio of 45. Using these parameters together with the parameters listed in the caption of Figure 2.10 a relative pressure sensitivity of ≈ 2.43 ppm/Pa is predicted.
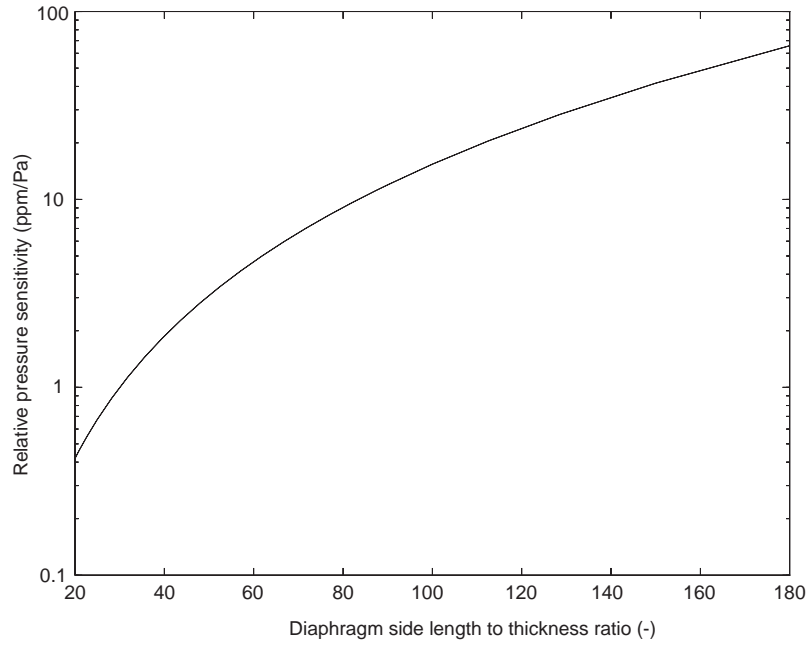
Figure 2.10 Predicted relative pressure sensitivity of the lateral resonant pressure sensor as a function of diaphragm side length to thickness ratio. The design parameters are as follows: $v=0.3$ $z_0=0.5t+3$ μm, a=900 μm, $\alpha=0.0151$, $E_D=195$ GPa, $l_f=150$ μm and $\varepsilon=1\times10^{-5}$ ε.

2.6.2 Linearity

In the foregoing analysis it is assumed that the deflection of the diaphragm is small. In practice, for large deflections (i.e. greater than 10% of the diaphragm thickness) the stretching of the mid plane of the diaphragm introduces a non-linearity in the pressure deflection relationship. The magnitude of the non-linearity may be estimated by treating the resistance of the diaphragm to an external load as the as the sum of the resistance to bending and the resistance to in-plane tension. Using the method of superposition the approximate relation between the pressure applied and the centre deflection is given by Giovanni [2.29] to be,

$$P = \frac{66.225}{\left(1-\upsilon^2\right)}\frac{E_d a_d^3}{t^4}Z + 31.1\frac{E_D a_d}{t^4}Z \qquad (2.51)$$

where the parameters have the same meaning as those given previously.

A further source of non-linearity is the square-root relationship between the fundamental frequency of the resonant strain gauge and the axial load, as shown by

equation (2.30). In practice these two non-linearities tend to act in opposition so that the overall linearity of the pressure sensor is increased. This leads to the interesting possibility, in theory at least, of producing a resonant pressure sensor that possesses a linear pressure-frequency relationship.

If, for the purpose of example, a linear relationship between applied pressure and frequency-shift is assumed, the linear sensitivity of the pressure sensor is computed directly from equation (2.38), such that

$$\frac{\delta\omega}{\delta p} = \omega_1 G_p \tag{2.52}$$

For small diaphragm deflections of 2 µm or less the linear sensitivity of the pressure sensor design presented in Figure 2.2 is computed to be ≈ 0.13 Hz/Pa. It is interesting to note that, in theory, a reduction in the thickness of the diaphragm to 5 µm increases the linear sensitivity by a factor of 27 to ≈ 3.62 Hz/Pa.

2.7 Pressure resolution

As is mentioned earlier, the minimum pressure resolution of the pressure sensor is a function of relative pressure sensitivity, G_P, and the minimum resolution of the frequency measurement system, $(\delta\omega/\omega)_{min}$,

$$\delta P_{min} = \left(\frac{1}{G_p}\right)\left(\frac{\delta\omega}{\omega}\right)_{min} \tag{2.53}$$

An analytical expression of the short term pressure resolution, valid for small linear deflections, is found by the direct substitution equation (2.50) into (2.53),

$$\delta P_{min} = \left[\frac{E_D l_f (5b^2 / l_f^2 + 6\varepsilon_o)}{9 z_0 \alpha (1 - \upsilon^2)}\left(\frac{t}{a_d}\right)^3\right]\left(\frac{\delta\omega}{\omega}\right)_{min} \tag{2.54}$$

so that all that is necessary to estimate δP_{min} is a value for $(\delta\omega/\omega)_{min}$.

As is outlined earlier, for continuous operation a resonant sensor is usually integrated with electronic drive and sense circuitry, so that it forms the frequency determining element of an electronic oscillator. This mode of operation is indicated

schematically in Figure 2.11. Here, an oscillator is formed by connecting a feedback network *B* to an amplifier *A*. The system starts to oscillate when the when the phase shift around the feedback loop is 180° and the is gain greater than 1, i.e.,

$$A(j\omega).B(j\omega) = -1 \quad \Rightarrow \quad Arg(A(j\omega).B(j\omega)) = 180$$
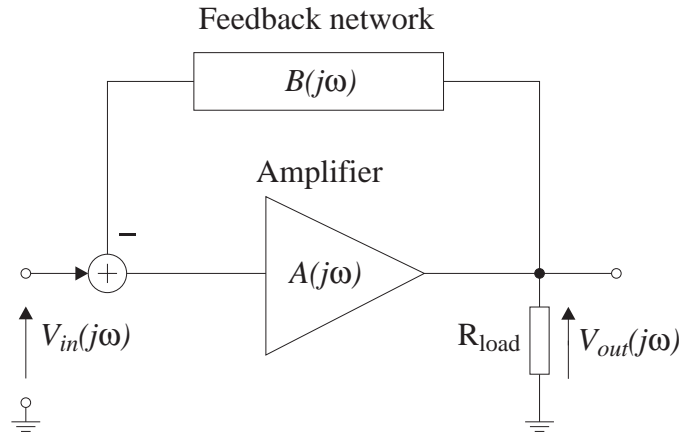$$|A(jw)B(j\omega)| = 1$$

(2.55)

Figure 2.11 Block diagram of an oscillator consisting of an amplifier and feedback loop.

Usually the resonant element of a sensor is incorporated into the feedback network of the oscillator. In chapter 3 it is shown that the response of the two-port resonator is described by a second-order bandpass filter with a -90° phase shift at resonance. To satisfy the phase condition for oscillation given in equation (2.55) the supporting electronics must supply a further -90° phase shift. However, in practice noise the supporting electronics also introduces a phase shift inaccuracy, $\delta\varphi$. This leads to a frequency uncertainty, $\delta\omega$, in the measured resonant frequency of the mechanical resonator. For a second-order response, the relationship between the short term phase inaccuracy and frequency uncertainty is given by the expression [2.16],

$$\delta\omega = \frac{\omega}{2Q}\delta\varphi$$

(2.56)

so that the minimum resolution of the electronic oscillator is simply,

$$\left(\frac{\delta\omega}{\omega}\right)_{min} = \frac{\delta\varphi_{min}}{2Q}$$

(2.57)

where Q is the mechanical Q-factor of the resonator and $\delta\varphi_{min}$ the minimum short term phase error of the oscillator. Thus, a high Q-factor leads to a high frequency resolution and consequently a high pressure resolution, see equation (2.54). A further point is that the oscillation frequency of the electronic circuit is influenced by the electrical parameters of the drive circuit. However this dependency is minimised by ensuring the Q-factor of the resonator is as large as possible, preferably greater than 1000 [2.16].

In this type of resonant sensor, the resonant frequency is usually measured by counting the number of pulses generated by a high frequency ($\approx$ 10 MHz) reference oscillator (usually quartz) during fixed time period defined by the resonator. This is achieved by using the output frequency of the resonator is to define the start and stop signals of the counting period. For the purpose of this analysis, the frequency resolution of the electronic oscillator shown in Figure 2.11 is assumed to be 2 ppm. This value is the typical frequency resolution of the resonant pressure sensor shown in Figure 1.9 of chapter 1 [2.6], and is obtained from measurements of the Allan variance of the sensor [2.30]. (The Allan variance is the standard method of describing the short term stability of an oscillator.) Based on this frequency resolution, a prediction of the minimum short term pressure resolution of the lateral resonant pressure sensor, calculated from equation (2.54), is presented in Figure 2.6. For continuity, the side length to thickness ratio of the diaphragm is the assigned parameter. Reference is made to the caption of Figure 2.10 for the value of the other parameters contained in equation (2.52).
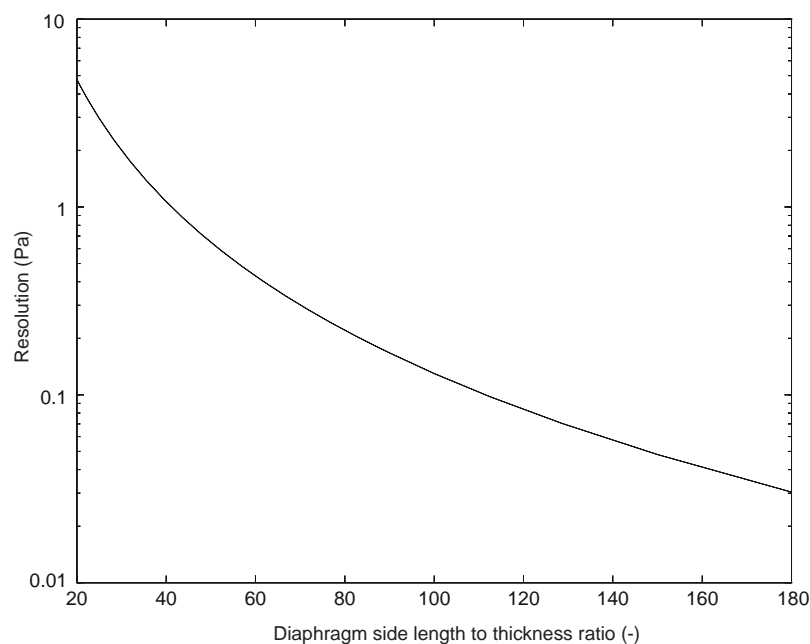
Figure 2.12 Predicted variation in resolution with diaphragm side length to thickness ratio, with an assumed frequency resolution of 2 ppm.

With a diaphragm side length to thickness ratio of 45 the predicted short term pressure resolution is ≈ 0.82 Pa. It is interesting to note by reducing the diaphragm thickness to 5 µm (i.e. a diaphragm side length to thickness ratio of 180) leads to a theoretical resolution of ≈ 0.03 Pa. However, such a high resolution is likely to be obscured by the effects of temperature variation, the level of noise in the sensor and the ability to calibrate the sensor output against a traceable standard.

2.8 Conclusions

In this chapter a novel pressure sensor design based on a surface micromachined lateral resonant strain gauge and planar SCS diaphragm has been presented.

Expressions for the fundamental resonant frequency and gauge factor of the lateral resonator have been derived using Rayleigh's method. The resonant frequency of lateral resonator is predicted to be 55 kHz, based upon an assumed Young's modulus of 140 GPa. The gauge factor is predicted to be $\approx 10^3 \, \text{N}^{-1}$, provided the residual strain is less than $\approx 1 \times 10^{-4}$. High levels of residual strain should be avoided as this degrades performance of the pressure sensor by reducing the gauge factor of the lateral resonator. Over-modulation of the resonator leads to frequency shift and so should also be avoided.

Expressions for the relative pressure sensitivity and resolution of the resonant pressure sensor have been derived using linear elastic analysis. Using these expressions, the relative pressure sensitivity and pressure resolution of the pressure sensor are predicted to be ≈ 2.43 ppm/Pa and ≈ 0.82 Pa, respectively, when a 20 µm thick diaphragm of side length 900 µm is employed. Theoretically, reducing the thickness of the diaphragm to 5 µm improves the sensitivity and resolution by a factor of 27. However, the fabrication of a thinner diaphragm may prove problematic and will also reduce the range of the pressure sensor.

As well as possessing a high sensitivity, this pressure sensor design offers the advantages of an enhanced fundamental mode whose direction is perpendicular to that of the diaphragm. This should leading to a wide dynamic range and a Q-factor that is less sensitive to small increases in cavity gas-levels at low pressure (< 1 Pa).

References

[2.1] Tilmans H. A. C., Elwenspoek M., Fluitman J. H. J., Micro resonant force gauges, *Sensors and Actuators*, A30 (1992) 35-53.

[2.2] Stemme G., Resonant silicon sensors, *J. Micromech Microeng.*, Vol. 1 (1991) 113-125.

[2.3] Langdon R. M., Resonators sensors - a review, *J. Phys. E: Sci. Instrum.*, Vol. 18 (1985) 103-115.

[2.4] Gast T., Sensors with oscillating elements, *J. Phys E: Sci. Instrum.*, Vol. 18 (1985) 783-788.

[2.5] Stemme E. and Stemme G., A balanced resonant pressure sensor, *Sensors and Actuators*, A21 (1990) 336-341.

[2.6] Greenwood J. C. and Satchell D.W., Miniature silicon resonant pressure sensor, *IEE Proc.*, Vol. 135 Pt. D No. 5 (1988) 369-372.

[2.7] Ikeda K., Kuwayama H., Kobayashi T., Watanabe T., Nishikawa T., Yoshida T. and Harada K., Three dimensional micromachining of silicon presssure sensor integrating resonsnant strain gauge on diaphragm, S*ensors and Actuators*, A21-23 (1990) 1007-1010.

[2.8] Guckel H., Rypstata C. and Nesnidal M., Polysilicon resonant microbeam technology for high performance sensor applications, *IEEE Solid-State Sensor and Actuator Workshop,* Hilton Head, South Carolina, (1992) 203-207.

[2.9] Ernisse E. P., Ward R. W. and Wiggins R. B., Survey of quartz bulk resonator sensor technologies, *IEEE Trans. Ultrasonics and Frequency Control*, Vol. 35 No. 3 (1988) 323-330.

[2.10] Andres M. V. Sensitivity and mode spectrum of a frequency-output silicon pressure sensor, *Sensors and Actuators*, 15 (1988) 417-426.

[2.11] Temple G. and Bickley T. M., *Rayleigh's principle and its application to engineering*, Dover Publications, (1956).

[2.12] Prak A., Silicon resonant sensors: operation and response, *PhD Thesis*, University of Twente, Enschede, The Netherlands, (1993).

[2.13] Buser R. A. and De Rooij N. F., Silicon pressure sensor based on a resonating element, *Sensors and Actuators*, A25-27 (1991) 717-722.

[2.14] Blom F. R., Bouwstra S., Elwenospoek M. and Fluitman J. H. J., Dependence of the quality factor of micromachined silicon beam resonators on pressure and geometry, *J. Vac. Sci. Technol.,* Vol. B10 No. 1 (1992) 19-26.

[2.15] Christen M., Air and gas damping of quartz tuning torks, *Sensors and Actuators*, 4 (1983) 555-564.

[2.16] Gopel W., Hesse J. and Zemel J. N. (eds.), *Sensors a comprehensive survey,* Mechanical sensors, Vol. 7, Weinham, NewYork, (1994) 513-556.

[2.17] Dufour M., Delaye M.T., Michel F., Danel J.S., Diem B. and Delapierre G., A comparison between micromachined pressure sensors using quartz or silicon vibrating beams, *6th Int. Conf. on Solid State Sensors and Actuators, (Transducers '91)* (1991) 668-671.

[2.18] Spiering V. L., Bouwstra S. and Elwenspoek M., On chip decoupling zone for package stress reduction, *6th Int. Conf. on Solid State Sensors and Actuators, (Transducers '91)* (1991) 982-985.

[2.19] Brignell J. and White N., *Intelligent sensor systems*, IOP Publishing, (1994).

[2.20] Tilmans H. A. C., Bouwstra S., Intema D., Elwenspoek M. and Klein C. F., Differential resonator design using a bossed structure for applications in mechanical sensors, *Sensors and Actuators*, A26 (1991) 385-393.

[2.21] Stoker J. J., *Non-linear vibrations in mechanical and electrical systems*, Interscience, Inc. New York, (1963).

[2.22] Roark R. J. and Young W. C. (eds.), *Formulas for Stress and Strain*, fifth edition, McGraw-Hill, New York, (1975).

[2.23] Gere J. M. and Timoshenko S. P., *Mechanics of materials*, third edition. PWS-Kent, Boston, (1991).

[2.24] Howe R. T. and Muller R. S., Polycrystalline and amorphous silicon micromechanical beams: annealing and mechanical properties, *Sensors and Actuators*, 4 (1983) 447-454.

[2.25] Kamins1 T. I., Design properties of polycrystalline silicon, *Sensors and Acuators*, Vol. A21-A23 (1990) 817-825.

[2.26] Howe R. T., Microsensor and Microactuator Application of Thin Films, *Thin Solid Films*, Vol. 181 (1989) p 235-243.

[2.27] Tang W. C., Nguyen T.-C. H., and Howe R. T., Laterally driven polysilicon resonant microstructures, *Sensors and Actuators*, A20 (1989) 25-32.

[2.28] Clark S. C. and Wise K.W., Pressure sensitivity in anisotropically etched thin-diaphragm pressure sensors, *IEEE Trans.*, Vol. ED-26 No. 12 (1979) 1887-1896.

[2.29] Giovanni, M. D., *Flat and corrugated diaphragm design handbook*, Marcel Dekker, New York, (1982).

[2.30] Kirman R., Druck Ltd., personal communication.

Contents

3. The operation and response of the lateral resonator

Chapter 3

The operation and response of the lateral resonator

The objectives of this chapter are to investigate the operation and response of the lateral resonator described in this thesis. By way of an introduction, microresonator excitation and detection mechanisms are reviewed. The remainder of the chapter is split into three parts. First, the operation of the lateral resonator is outlined and both the linear and non-linear responses are described. In the second part, the one-port mode of operation is investigated and the response of the lateral resonant strain gauge modelled using an energy method. The model is used to derive expressions for the input impedance and input admittance of the resonator. These responses are then explained with the aid of an electrical equivalent circuit. The equivalent circuit also illustrates the effect of external electrical components on the resonant frequency of the strain gauge. In the third part, the model is extended to include the two-port mode of operation and an expression for the transconductance of the resonator determined. Finally, the motional sense current of the lateral resonator is predicted and the importance of minimising the electrical cross-talk stressed.

3.1 Excitation and detection mechanisms

In general, a micromechanical resonator consists of a mechanical structure and a vibration excitation and detection mechanism. The purpose of the excitation and detection mechanisms are to enable the fundamental resonant frequency[1], or if needed, the

---

[1] Unless otherwise stated, the resonant frequency is defined as the fundamental mode of oscillation.

harmonics of the mechanical structure to be determined. The excitation mechanism drives the mechanical structure, whilst the detection mechanism measures its movement. The resonant frequency is found by comparing the magnitude and/or phase of the excitation and detection signals.

Excitation and detection elements usually take the form of electromechanical transducers and are classified according to the 'transduction principle' employed. There are two types of excitation elements, those based on energy dissipation (irreversible mechanisms), and those based on reversible power flow and energy storage (reversible mechanisms). There are four recognised reversible type excitation mechanisms, *viz.*; magnetic, piezoelectric, dielectric and electrostatic/capacitive, and two irreversible type excitation mechanisms, *viz.*; optothermal and electrothermal [3.1,3.2]. Since reversible mechanisms are based on energy exchange they can also be used to form detection elements. Another type of detection mechanism is based on the modulation of an energy flow that is supplied by an external source. The piezoresistor is a well known example of a modulator type detection mechanism. The operation of each of these mechanisms is described below.

A resonator is usually operated in either a 'one-port' or 'two-port' mode. In the one-port mode a single element (which must be of the reversible type) is used for both vibration excitation and motion detection, whereas in a two-port mode two elements are used, one for excitation and one for detection. The response of the lateral resonator when operated in the one-port mode or two-port mode is described further in sections 3.4 and 3.5, respectively.

3.1.1 Magnetic excitation and detection

Magnetic excitation is based upon the principle that a current carrying conductor positioned perpendicular to a magnetic field experiences a Lorenz force. The resonator forms part of the current loop and the magnetic field is provided by a permanent magnet, see Figure 3.1a. A permanent magnet is preferred because resistive heating within an electromagnet can lead to a temperature induced frequency shift. The reverse operation - vibration detection - is also feasible because the motion of the resonator in the magnetic field causes a flux change in the current loop, so inducing a voltage in the external circuit. The resonant pressure sensor of Ikeda *et al.* [3.3] uses a magnetic excitation and detection mechanism, see Figure 1.10 of Chapter 1.

3.1.2 Piezoelectric excitation and detection

Piezoelectric excitation and detection are based on the direct and indirect piezoelectric effect, respectively. The resonator is excited by a mechanical strain, produced by applying an electric field to a piezoelectric material. The reverse operation allows the motion of the resonator to be measured, because the motion of the resonator will deform the piezoelectric, so inducing a charge that can be converted into an electric signal, see Figure 3.1b [3.4]. Quartz is a well known piezoelectric material which is widely used to fabricate quartz crystal resonators [3.5,3.6]. Single crystal silicon, however, does not exhibit piezoelectric properties because its crystal structure is centrosymmetric. To excite/detect a silicon resonator piezoelectrically it is necessary to pattern the resonator with a thin layer of piezoelectric material, e.g. zinc oxide (ZnO) [3.7]. Unfortunately ZnO is not IC compatible. This means that additional passivation layers, e.g. silicon nitride, are needed to prevent contamination of the process line and to protect the ZnO from chemical attack during processing. Together with the ZnO, these additional layers lead to in an increase in temperature sensitivity and are likely to degrade the mechanical Q-factor of the resonator [3.8,3.9].

3.1.3 Dielectric excitation and detection

A dielectric excitation/detection element consists of a thin dielectric material sandwiched between two electrodes. The three layers form a capacitor. The application of a potential across the capacitor leads to an electrostatic force between the electrodes that deforms the dielectric material, so inducing a bending moment which drives the resonator, see Figure 3.1c. The process is reversible because an applied strain also induces a change in capacitance, which is measured with an external circuit [3.10]. As with the piezoelectric excitation/detection mechanism the performance of the resonator is likely to be degraded by the additional layers integrated onto the surface of the resonator.

3.1.4 Electrostatic excitation and capacitive detection

Electrostatic excitation is based on the principle that a coulomb force is developed between two charged electrodes. Capacitive detection is based on the principle that an electrical signal is generated if the geometric coefficients of the charged capacitor change, see Figure 3.1d. Usually one of the electrodes is an integral part of the resonator whilst the other is located in close proximity to maximise the efficiency of the

drive/pickup. Generally, capacitance changes occur as a result of a change in the separation of the electrodes (as in a parallel plate capacitor) or a change in their effective area (as seen in an interdigitised comb capacitor). The advantages of the electrostatic excitation and capacitive detection mechanism are that it is readily integrated into the fabrication process and requires no additional material layers. The disadvantage of this mechanism is that the static force generated by the bias voltage (usually) displaces the resonator from the equilibrium position, so inducing a mechanical strain which results in a frequency shift.

3.1.5 Optothermal and electrothermal excitation

Both optothermal excitation and electrothermal excitation are achieved by applying a thermal impulse to a localised area of the resonator. The resulting temperature change induces an expansion bending moment which is used to drive the resonator. With electrothermal excitation the thermal impulse is generated by resistive heating, achieved by modulating the current flow through an integrated resistor. With optothermal excitation a light source, usually a laser, is directed at the resonator and the thermal impulse is generated by the absorption of the incident radiation. The disadvantage of thermal excitation mechanisms is the frequency-shift associated with the static heating of the resonator.

Thermal excitation mechanisms are based on energy dissipation, rather than energy storage. This means that a different transduction mechanism must be used to measure the response of the resonator. Optical detection is often used in conjunction with optothermal excitation [3.11], whilst piezoresistive detection is used in combination with electrothermal excitation, and can be integrated into a single element [3.12].

Optical detection and piezoresistive detection are both modulator type detection mechanisms. Optical detection can be achieved in a number of ways, one of which, the optical chopper is illustrated in Figure 3.2b. Piezoresistive detection differs little from that used in conventional diffused strain-gauge pressure sensors. The resistivity of the piezoresistor (and hence the voltage/current across it) is modulated by a mechanical strain that is induced by the motion of the resonator [3.13].

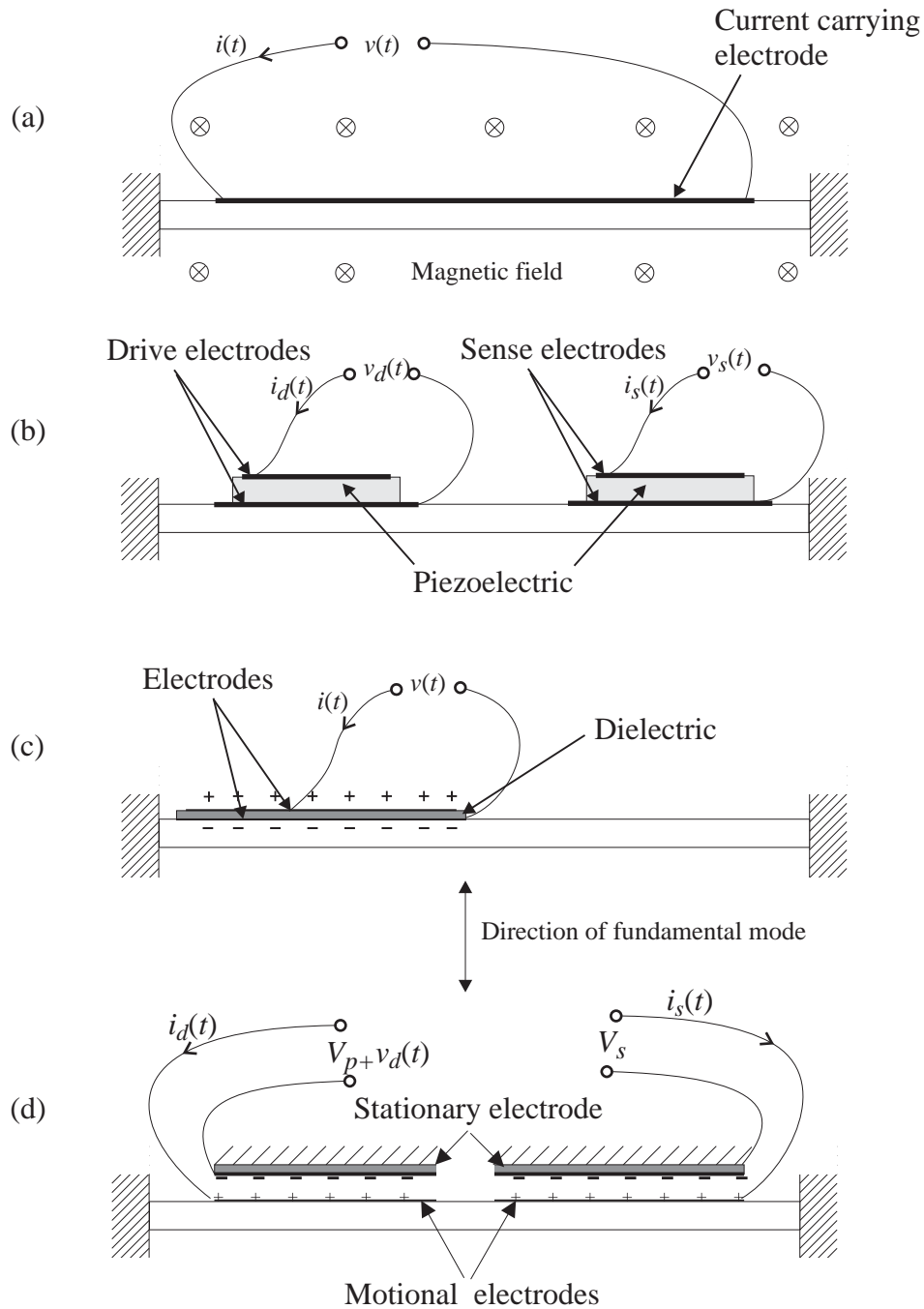*Figure 3.1 Reversible excitation/detection mechanisms. The clamped-clamped beam is used as an example; (a) Magnetic excitation and detection in a one-port mode, (b) piezoelectric excitation/detection in a two-port mode, (c) one-port dielectric excitation/detection and (d) two-port electrostatic excitation/capacitive detection. The one-port and two-port modes of operation are explained in section 3.3.*
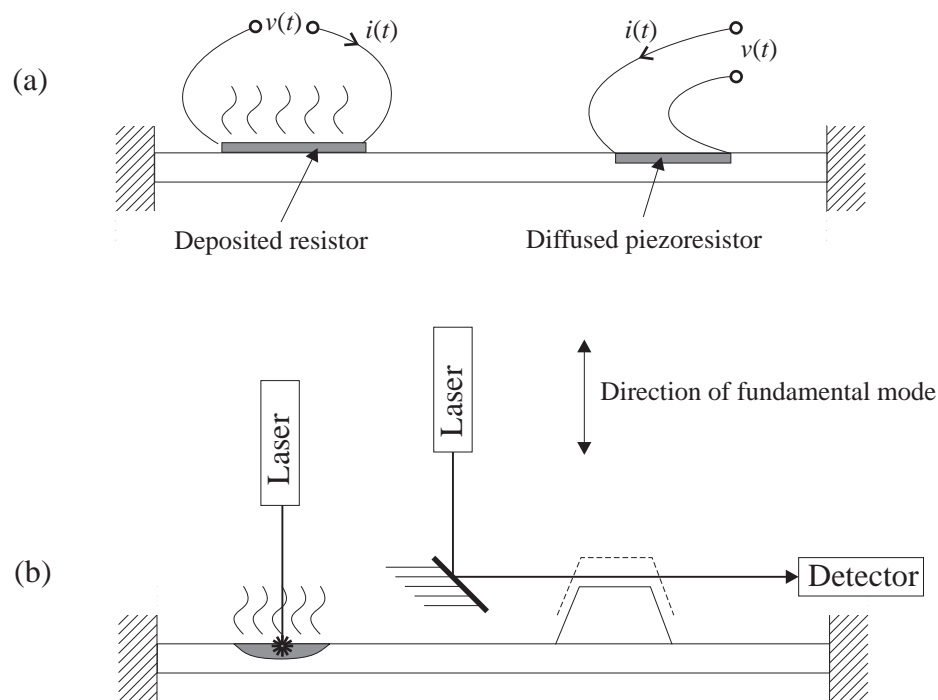
Figure 3.2 Irreversible excitation and detection mechanisms. The clamped-clamped beam is used as an example. (a) Electrothermal excitation and piezoresistive detection. Here, the thermal impulse is produced by a resistor on the surface of the resonator. The motion is sensed by monitoring the resistance of a diffused or deposited piezoresistor; (b) Optothermal excitation and optical detection using a laser radiation source.

The usual criteria for choice of excitation/detection mechanism are the ease of integration into the fabrication process and the operating conditions of the sensor. Electrostatic excitation is often used in conjunction with capacitive or piezoresistive detection, see Table 1.1 of chapter 1, as these methods integrate well with the fabrication process. Optothermal excitation and optical detection are attractive where the resonator is to be operated in a harsh or hazardous environment. This is because they are able to operate at high temperature (≈ 200 $^{\circ}$C), present no electrical hazard and are immune to electromagnetic radiation [3.11]. However, they are rather bulky when compared to other techniques and are generally used for device characterisation. In summary each mechanism has its own advantages and disadvantages; it is the task of the designer is to select the mechanism that is most suited to the application.

3.2 Excitation and detection of the lateral resonator

The lateral resonator described in this thesis is designed to be driven using electrostatic excitation and the resultant motion measured using either capacitive or piezoresistive detection.

3.2.1 Electrostatic excitation and capacitive detection

In this mode of operation, two multi-plate interdigitised comb capacitors, henceforth referred to as combs or comb capacitors, are used to excite the resonator and measure its response. One electrode of each comb capacitor forms part of the resonator inertial mass, whilst the other electrode is anchored to the substrate. When operated in a one-port mode, a single comb capacitor is used for both excitation and motional detection. The resonant frequency is determined by monitoring the motional impedance or motional admittance of the comb capacitor. In a two-port mode both comb capacitors are used, one for excitation and one for detection. One set of possible electrical connections for the two-port mode of operation is shown in Figure 3.3. Here, the resonant frequency is determined by monitoring the motional transconductance of the resonator. The motional electrodes of the comb capacitors are connected to the ground plane via the flexure anchors. The stationary electrodes (shaded) are insulated from the ground plane and connected to external circuitry via conductive tracks and contact pads. The drive comb, C_d, is biased with a polarisation voltage V_p and the resonator excited with a sinusoidal drive signal. The motion of the resonator is determined by applying a d.c. bias V_s to the sense comb, C_s, and measuring the current generated by the motional capacitance.

3.2.2 Electrostatic excitation and piezoresistive detection

In this mode of operation the resonator is driven electrostatically via an interdigitised comb capacitor. The motion of the resonator is determined by monitoring the resistance of a piezoresistive bar attached to the flexure, see Figure 3.3. The resistance of the bar is modulated by the action of the mechanical strain induced by the motion of the resonator. Piezoresitive detection is a modulator type mechanism and so can only operate in a two port mode. As well as integrating well with the fabrication process, piezoresistive detection offers the advantage of higher motional sense signal than capacitive detection. This is because it is a modulator type detection mechanism, where

the energy of the sense signal is provided by an external source, rather than being generated directly by the motion resonator itself, as occurs in a reversible detection mechanism.
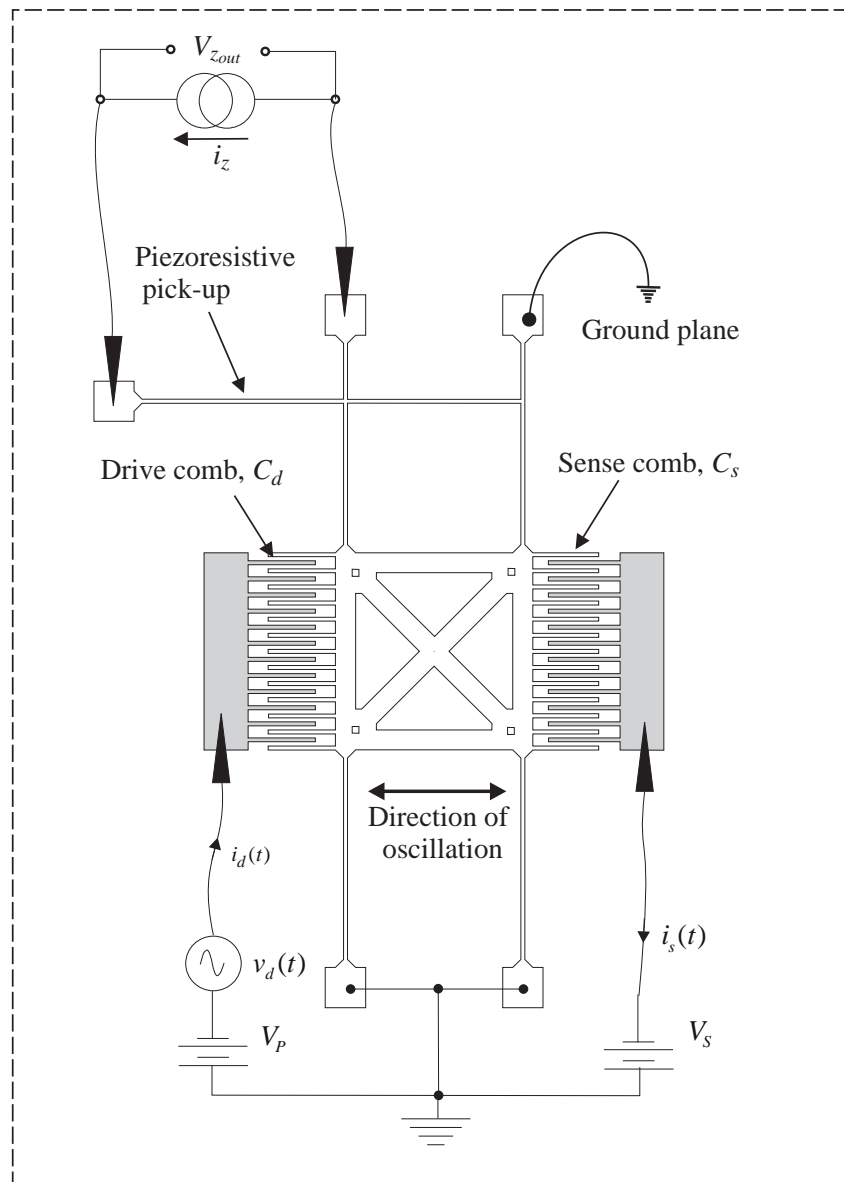
Figure 3.3 Schematic showing the electrical connections to the lateral resonator when operated in a two-port transconductance mode. The electrical connections to an integrated piezoresitive pick are also shown.

The output of the piezo-bar is characterised by its gauge factor G_z, which for a piezoresistor, is defined as the relative change in resistance per unit strain. For homogenous materials with isotropic elastic properties, the gauge factor is given by [3.8,3.14],

$$G_z = 1 + 2v + \frac{\Delta\rho_z}{\varepsilon_z \rho_z} \tag{3.1}$$

where v is Poisson's ratio, ε_z the strain, ρ_z the resistivity and $\Delta\rho_z$ the change in resistivity.

The first two terms in equation (3.1) are due to the dimensional change of the piezoresistor, while the later is due to the change in resistivity. Silicon is an excellent piezoresitive material and generally exhibits a gauge factor from 10 to 100 [3.2,3.15]. For large gauge factors the change in resistivity is the dominant mechanism, so that the effect of a dimensional change can be neglected. The resistance of the piezo-bar is determined by measuring its current/voltage characteristics, i.e., $V_{z_{out}}/i_z$ in Figure 3.3.

In theory, the mechanical elements of the resonator, i.e., the flexure and inertial mass, possess a number of resonant (harmonic) modes. In practice, however, only those modes which exhibit measurable response to the system excitation are of interest. At low frequencies it is reasonable to assume that the mechanical elements of the lateral resonator do not vibrate themselves and can therefore be modelled as ideal lumped system elements. The amplitude (and phase) response of these elements is linear for small displacements, where the stretching of the flexure is small, but becomes increasingly non-linear as the amplitude of vibration increases.

3.2.3 Linear response

For small displacements the deflection induced axial stiffening of the flexure is small and the motion of the resonator in the vicinity of the fundamental lateral mode described by the second-order linear differential equation[2],

$$M_i \ddot{x} + c\dot{x} + k_{xl}x = f_d - f_s \tag{3.2}$$

where f_d is the excitation force, f_s the force due to the bias across the sense comb[3], and x the displacement of the resonator from the equilibrium position. M_i, c, and k_{xl} denote the inertial mass, damping coefficient, and linear spring-rate of the flexure, respectively. If the resonator drive comb is biased with a polarisation voltage V_p and driven with a signal,

---

[2] A dot indicates a time differential.

[3] Note when the piezoresistive pick-up is employed the sense bias is zero.

of the form[4,5] $\bar{v}_d e^{j\omega t}$ and the sense comb biased with a voltage V_s, (as indicated in Figure 3.3) then the total force acting on the resonator is given by the expression,

$$f_d - f_s = \frac{1}{2}\frac{dC}{dx}\left[(V_p + \bar{v}_d e^{j\omega t})^2 - V_s^2\right]$$ (3.3)

which expands to,

$$f_d - f_s = \frac{1}{2}\frac{dC}{dx}\left(V_p^2 + 2V_p\bar{v}_d e^{j\omega t} + \bar{v}_d^2 e^{j2\omega t} - V_s^2\right)$$ (3.4)

where dC/dx is the capacitance gradient of the comb capacitors[6]. In this analysis an ideal capacitance gradient, dC/dx, is assumed and obtained from the expression for the capacitance of an *n*-plate comb capacitor,

$$C = \frac{\varepsilon_0 h(a + x)(n - 1)}{d}$$ (3.5)

where x is the displacement from the equilibrium position, ε_0 is the permittivity of free space[7], a is the comb overlap, h the comb thickness and d the comb-finger gap. It is clear from equation (3.4) that there are three forces acting on the resonator,

    (1) A static force whose magnitude is proportional to the square of both the polarisation voltage V_p and the sense bias V_s. The static drive force displaces the resonator from the equilibrium position, so stretching the flexure and inducing a frequency shift. As an example, the resonator shown in Figure 1.9 of Chapter 1, (which is also operated using electrostatic excitation and capacitive detection) has a bias dependence of ≈ 20 HzV^{-1}, at a polarisation voltage of 10 V [3.16].

    (2) An excitation force of frequency ω.

    (3) A harmonic excitation force of frequency 2ω.

---

[4] Note that it is equally possible to drive the resonator from a current source.

[5] The overstrike is used to represent complex amplitude.

[6] Assuming the capacitance gradient of the drive comb and sense comb are equal.

[7] the resonator is assumed to operate in high vacuum (< 1 Pa).

The harmonic excitation force is a well known characteristic of the electrostatic excitation mechanism and is often referred to as frequency doubling. Frequency doubling is the generation of an excitation force whose frequency is twice that of the drive signal, and occurs because the excitation force is proportional to the square of the drive signal. This phenomenon can be used to excite the resonator by supplying an *anharmonic* drive signal, i.e. one that is half the fundamental frequency of the resonator. In this configuration maximum drive efficiency is attained when the polarisation voltage is set to zero, see equation (3.4). The advantage of an anharmonic drive is that electrical cross-talk is reduced because the drive and sense signals are separated in the frequency domain. Electrical cross-talk is the electrical coupling of the drive signal to the sense signal, and is described further in section 3.5.2. The disadvantages of the anharmonic drive are that a higher drive signal amplitude is needed and, when implemented in a closed-loop mode, frequency division of the sense signal is necessary, which increases the complexity of the sensor electronics.

In this thesis it is assumed that $\bar{v}_d << V_p$ so that the magnitude of the harmonic excitation force is negligible. With this assumption, the steady state lateral motion of the resonator for small displacements from the equilibrium position is,

$$x(t) = M(j\omega)\bar{f}_d e^{j\omega t} \tag{3.6}$$

The mechanical transfer function of the resonator, $M(j\omega)$, is obtained from equations (3.2) and (3.4),

$$M(j\omega) = \frac{1/k_{xl}}{1 - \frac{\omega^2}{\omega_1^2} + \frac{j\omega}{Q\omega_1}} \tag{3.7}$$

where ω is the excitation frequency, ω_1 the (unloaded) resonant frequency and k_{xl} the linear spring rate. The quality factor is defined by $Q \approx \omega_1 M_i / c$, where c is a damping coefficient and M_i the inertial mass [3.17]. One further mode of interest is the vertical mode of oscillation. It is possible to excite this spurious mode because of a unique characteristic of the electrostatic comb drive known as the vertical levitation effect.

3.2.4 Levitation of lateral comb drive resonators

The levitation effect seen in lateral comb drive resonators arises because of charge imaging on the passivating layer that covers the ground plane. This leads to an asymmetric electrostatic field distribution around the plates of the comb capacitor, resulting in a net vertical force. The phenomenon is illustrated in Figure 3.4. Here, a positive bias on the anchored comb induces a negative charge on both the moveable comb finger and the passivating layer that covers the ground plane. These like charges repel, yielding a vertical force that tends to levitate the resonator. If the biases are reversed the levitation force acts in the opposite direction, pushing the resonator towards the substrate [3.18]. It follows that an alternating voltage will result in an alternating force, which may excite a vertical mode, depending on the vertical spring-rate of the flexure and the Q-factor of the vertical mode.
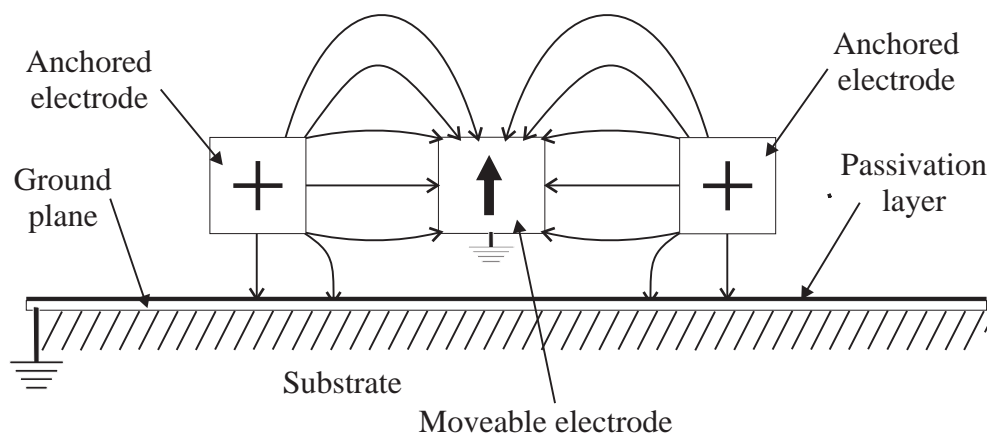

Figure 3.4 Schematic showing the origin of the vertical levitation force acting on the resonator.

There are several ways to control the effects of charge imaging. First, the cross-section of the supporting flexure should be rectangular, so that the lateral and vertical mode frequencies are widely spaced. Second, a differential drive may be employed. Here, the bias on alternate (anchored) comb fingers is reversed. This alters the electric field distribution around the fingers so reducing the levitation force by an order of magnitude [3.18]. Thirdly, the distance between resonator and the ground plane is increased, so increasing the charge separation, and thus reducing the magnitude of the vertical

levitation force. In my work the first method is used, because the other two techniques increase the complexity of the fabrication process.

3.2.5 Non-linear response

The non-linear frequency (and phase) response of the resonator is a direct result of the axial force induced in the flexure by a transverse deflection and is characterised by an increase in fundamental frequency with vibration amplitude.

The effect of the non-linearity is understood by examining the large amplitude *forced* response of a clamped-clamped beam shown in Figure 3.5. At a low amplitude of vibration the non-linearity is small and the dynamic response of the resonator is described by equations (3.6) and (3.7). As the amplitude of vibration increases the effect of the non-linearity is to bend the frequency response to the right, away from the linear curve. This is known as the hard spring effect [3.19]. Note that if the flexure anchors are not perfectly clamped the magnitude of the hard-spring rate is reduced, and can even revert to a soft-spring (in which case the frequency response curve would bend to the left). By increasing the magnitude of the drive force past a critical value, denoted by f_{crit} in Figure 3.5, the amplitude response becomes multi-valued, within a range of frequencies that define the hysteresis interval of the resonator. The multi-valued response curve has a significance from the physical point of view because it leads to a *jump phenomenon.*

Jump phenomenon

To explain the *jump phenomenon* consider the frequency response curve shown in Figure 3.5. If the excitation frequency is increased from a low value ($\omega \ll \omega_1$) then, under a constant drive force, the vibration amplitude follows the left hand response curve to a point *A*. Here, an extraneous disturbance causes the amplitude to drop suddenly from *A* to *A'*. A subsequent increase in the impressed frequency then causes the response to follow the ever diminishing portion on the right hand branch of the response spectrum. Conversely, if the forcing frequency is slowly decreased from a high value ($\omega \gg \omega_1$) the amplitude will slowly increase until point *B*, where it will suddenly jump to point *B'*. Further decreasing the frequency leads to a reduction in amplitude.
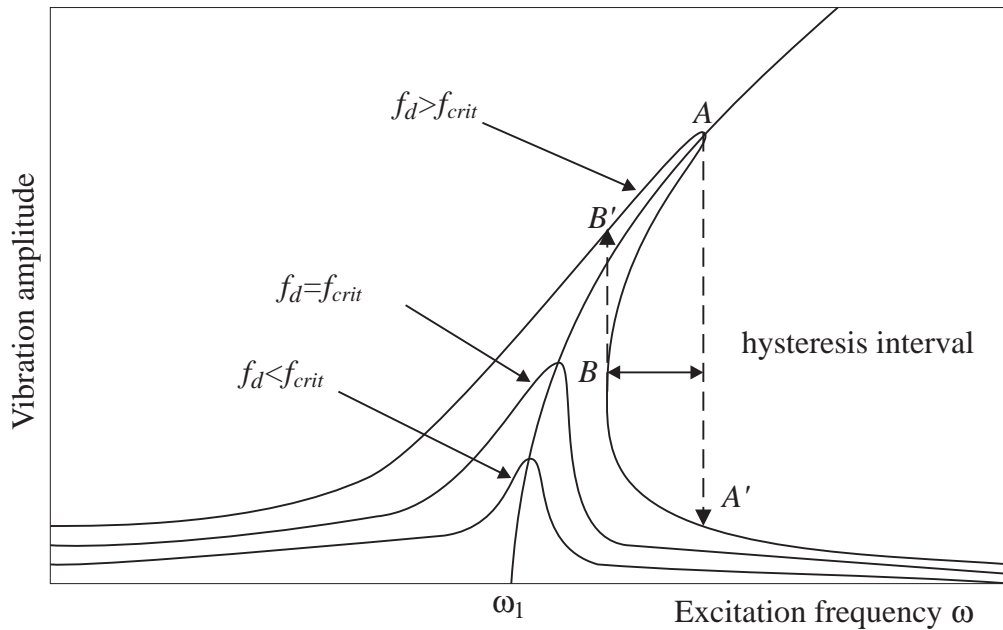
Figure 3.5 Schematic non-linear frequency response of resonant strain gauge or force transducer. If the magnitude of the drive force exceeds a critical value $f_d > f_{crit}$ the amplitude response becomes multi-valued and a hysteresis interval is observed.

In section 2.5.2 of chapter 2, it is shown that the spring rate of the flexure exhibits a cubic dependence on the deflection force. The inclusion of this term in equation (3.2) leads to a non-linear differential equation describing the motion of the resonator,

$$M_i \ddot{x} + c\dot{x} + k_{xl}x + k_{xnl}x^3 = f_d - f_s \qquad (3.8)$$

where k_{xnl} is the non-linear spring rate and the other parameters are defined previously. In general exact analytical solutions to non-linear differential equations do not exist and so it is necessary to employ either numerical techniques or an analytical approximation to determine the periodic solutions. Although not investigated here, one possible approach is the iterative method developed by Duffing, who first obtained significant results concerning the harmonic solutions to second order differential equation with cubic non-linearities. Other analytical techniques include Ritz's averaging method and the method of Rauscher [3.19,3.20].

3.3 Modelling the lateral resonator response

In general all physical systems are composed of a number of interconnected subsystems or elements. It is well known that the elements of a system can be categorised according to how they process energy [3.17,3.21]. A resonator, for example, can be modelled as a number of interconnected mechanical elements, i.e. springs, masses and dampers, and a vibration excitation/detection mechanism. The springs and masses store energy whilst the dampers dissipate energy. The excitation mechanism acts as an energy source, exciting the resonant modes of mechanical elements by injecting energy, whereas the detection mechanism acts as an energy sink[8], extracting energy so that the resonant frequency may be measured.

An elegant way to model the dynamics of the resonator is to therefore to adopt a systems approach based upon the storage and flow of energy. Systems modelling is based on the concept that each element of a system can be modelled as an energy source, energy store or energy dissipater. A further premise of the systems approach is that the exchange of energy between these elements occurs through a *powerport*, and is characterised by a pair of generalised system *power* variables called *effort, e_i,* and *flow, f_i.* The power flowing into or out of a powerport is expressed as the product of an effort and flow variable, and thus in general notation is given by $P_i = e_i . f_i$. To complete a description of the system a further pair of generalised variables are required. These are defined as the energy variables, momentum, p_i, and displacement q_i. [3.21,3.22].

As has already been mentioned, there are two methods of determining the natural modes of a resonator. The first approach is to employ a single excitation/detection mechanism. Here, the energy flow associated with the excitation/detection mechanism is described by a single electrical energy port, as indicated in Figure 3.6a. The resonant frequency is determined by measuring the constitutive relationship[9] between the generalised system variables e_i and f_i. In the electrical domain this means measuring the admittance f_i/e_i, or conversely the impedance e_i/f_i, at the energy port. The second approach is to use two electrical energy ports, one for vibration excitation and one for

---

[8] Assuming a reversible type detection mechanism.

[9] A constitutive relation is any experimental curve or law which specifies the physical charactersitic of a system element. For example the constitutive relationship between the absolute velocity, *u,* and momentum, *p*, of an purely translational Newtonian mass, *m*, is *p=mu* [3.25].

vibration detection, as shown in Figure 3.6b. In this configuration the motion of the resonator is determined by measuring the constitutive relation between variables at each port. For example, the voltage transfer function is the ratio of the effort variables e_{i_1} and e_{i_2}. In all four possible measurement combinations exist for the two-port resonator, *viz.*; e_{i_2}/e_{i_1}, e_{i_2}/f_{i_1}, f_{i_2}/f_{i_1}, f_{i_2}/e_{i_1}.
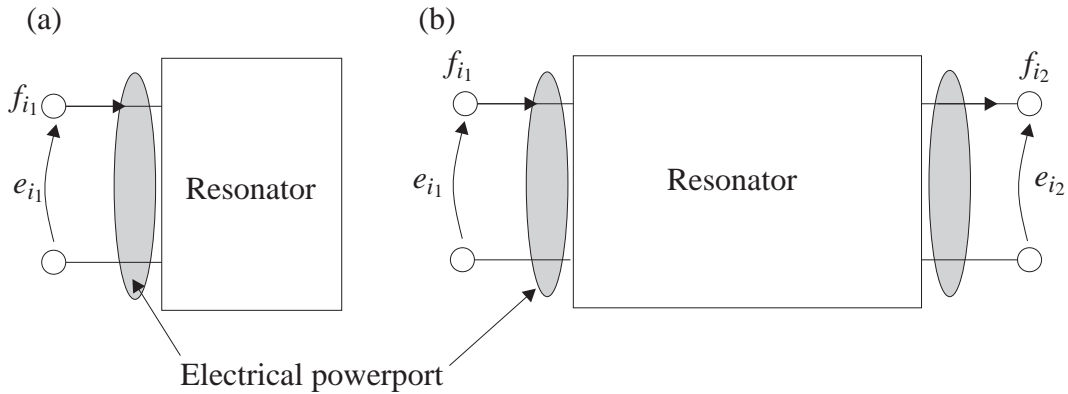

Figure 3.6 'Black box' representation of; (a) one-port and, (b) two-port resonator showing the generalised system variables and powerports.

In the remainder of this chapter the dynamic response of the resonator when operated using the electrostatic excitation and capacitive detection is investigated. First, the one-port mode of operation is modelled using the energy approach of Prak [3.2] and theoretical expressions are derived for the input impedance and input admittance of the resonator. The characteristic frequency response of the one-port mode of operation is then explained with the aid of an electrical equivalent circuit. Second, the model of the one-port resonator is extended to include the two-port mode of operation and an expression derived for the motional transconductance.

3.4 One-port excitation and detection

When a resonator is operated in a one-port configuration the resonant frequency is determined by monitoring the phase and/or magnitude of the effort and flow variables at the electrical port of the resonator, i.e. the admittance $Y(j\omega) = \bar{i}/\bar{v}$, or conversely, the impedance, $Z(j\omega) = \bar{v}/\bar{i}$ where $\bar{i}$ and $\bar{v}$ denote the complex amplitudes of the harmonic voltage and current, respectively. Generally, if the admittance is measured the resonator is driven from a voltage source and the current flowing through the circuit monitored. Resonance is observed as a peak in the current, or a maximum in the input admittance.

On the other hand, if the impedance is measured then the resonator is driven from a current source and the voltage monitored. Here, resonance is observed as a peak in the voltage or maximum in the input impedance [3.23,3.24].

3.4.1 Systems model

The first stage in analysing the dynamic behaviour of the one-port resonator is to construct a conservative systems model. Each element of the resonator, e.g. the flexure, is classified as an electrical energy store, mechanical energy store or energy dissipater. The energy coupled to each electrical energy store is represented by a single pair of electrical effort and flow variables and a conjugate pair of electrical energy variables. Similarly, the energy stored by the mechanical elements of the resonator are described by pair of mechanical effort and flow variables and a conjugate pair of mechanical energy variables [3.21].

A schematic systems model of the one-port resonator is shown in Figure 3.7. One electrode of the n plate comb capacitor is anchored to the substrate, and other electrode forms part of the vibrating inertial mass. The charge on the electrodes is denoted by q, and the voltage across the electrodes denoted by v. The electric field between the plates of the comb capacitor is composed of normal fields $\mathcal{E}_N$, associated with a capacitance C_n, and fringe fields $\mathcal{E}_F$, associated with a capacitance C_f. The electrostatic forces created by the normal electric fields balance, whereas the imbalance in the fringing fields results in a net force that is used to drive the resonator. Note that in this analysis it is assumed the electrical energy stored by the normal fields is much higher than the energy stored in the fringing fields. The electrostatic force generated by the excitation/detection mechanism and the opposing mechanical force of the flexure are defined as internal forces. Conversely, the viscous drag force[10] and inertial friction forces are regarded as external (mechanical) forces. When the internal and external forces balance the system is in equilibrium. The flow of energy between the internal and external elements of the network is modelled by the application of Newton's 2nd law and Kirchoff's current/voltage laws. Also, any purely mechanical or electrical coupling is included in the external network [3.21].

---

[10] By definition the force due to viscous drag must act externally because it is purely dissipative.
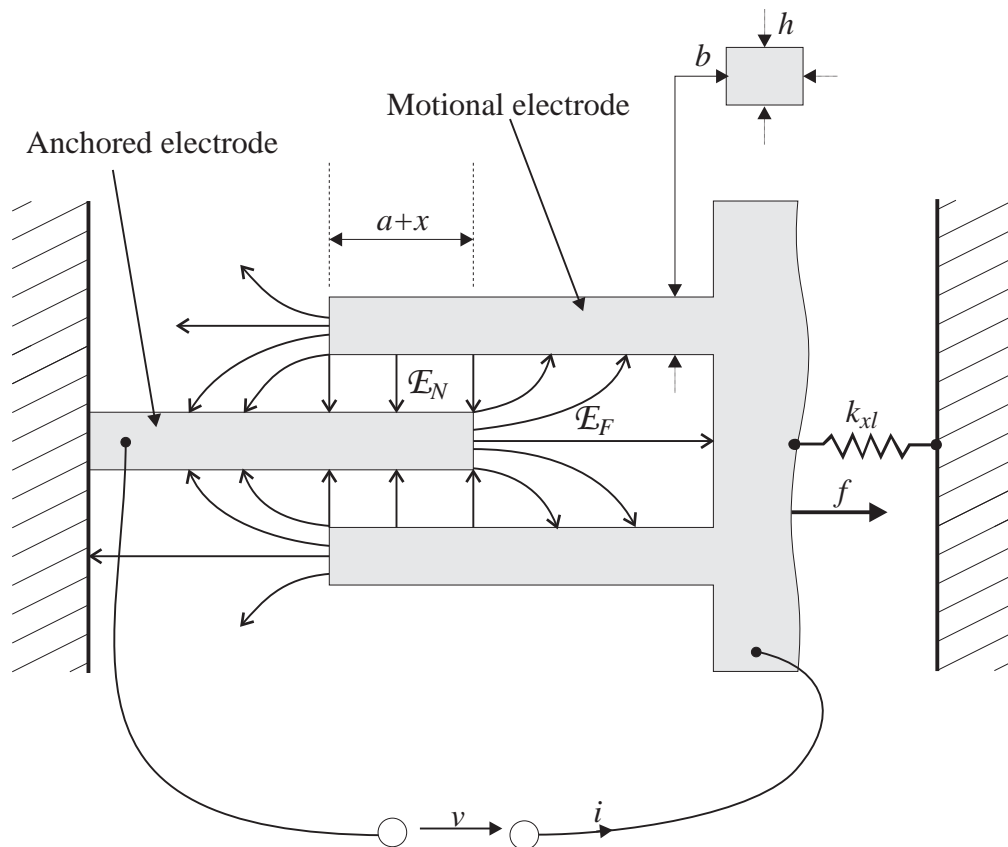
Figure 3.7 Schematic energy storing systems model the of the one-port lateral resonator.

Before proceeding, it is necessary to establish which variables of both the electrical and mechanical components of the resonator can be chosen as the generalised power and energy variables. In this analysis the generalised system variables are defined according to the classical (or direct) analogy, in which potential is analogous to force and current analogous to velocity, see Table 3.1. Note that this method of assignment is completely arbitrary. The mobility analogy, also shown in Table 3.1, is an equally valid way to assigning the generalised mechanical effort and flow variables [3.21,3.22].

Table 3.1 Power and energy variables for mechanical translation systems and electrical ports as defined by Karnopp [3.22].

Generalised Variables	Mechanical		Electrical
	Classical	Mobility	
Effort, e_i	Force, f (N)	Velocity, u (msec^{-1})	Voltage, v (V)
Flow, f_i	Velocity, u (ms^{-1})	Force, f (N)	Current, i (A)
Momentum, p_i.	Momentum, p_i (Ns^{-1})	Displacement, x (m)	Flux linkage, λ (Vs^{-1})
Displacement, q_i	Displacement, x, (m)	Momentum, p (Ns^{-1})	Charge, q (C)

If it is assumed that both the voltage and force in the energy storing system shown in Figure 3.7 depend on the charge and displacement, i.e.,

$$v = v(q,x) \tag{3.9}$$

$$f = f(q,x) \tag{3.10}$$

then the total energy stored is the sum of the electrical energy and mechanical energy and given by Karnopp [3.22] to be,

$$U_t(t) = U_0 + \underbrace{\int_0^t vi\,dt}_{\substack{\text{electrical}\\\text{energy}}} + \underbrace{\int_o^t fu\,dt}_{\substack{\text{mechanical}\\\text{energy}}} = U_0 + \int_{0,0}^{q,x} v(q,x)\,dq + \int_{0,0}^{q,x} f(q,x)\,dx = U_t(q,x) \tag{3.11}$$

where u is the velocity of the motional electrode and U_0 represents the initial energy of the system and is assumed to be zero. Note that the subscript 't' is used to indicate the total energy of the internal network, i.e. the sum of the electrical and mechanical energy.

If the constitutive laws of the capacitor and the flexure are assumed to be linear, i.e. $v = q/C(x)$ and $x = f / k_{xl}$, then the total energy stored by the system is obtained by setting $q=0$ and integrating x to a chosen value, and then charging the capacitor while holding the displacement constant, as indicated by equation (3.11), yielding,

$$U_t(q,x) = \underbrace{\frac{q^2}{2C(x)}}_{\substack{\text{energy stored}\\\text{by capacitor}}} + \underbrace{\frac{k_{xl}x^2}{2}}_{\substack{\text{energy stored}\\\text{by flexure}}} \tag{3.12}$$

where *C(x)* is given by (3.5) so that,

$$U_t(q,x) = \frac{q^2 d}{2\varepsilon_0 h(n-1)(a+x)} + \frac{k_{xl}x^2}{2} \tag{3.13}$$

where k_{xl} is the linear spring-rate of the flexure and the other parameters have been given previously. Note that the condition of constant charge implies that the resonator is driven from a *current* source and the voltage across the capacitor is the independent variable.

The constitutive laws of equations (3.9) and (3.10) can be recovered directly from equation (3.11), from which it follows that,

$$f = \left.\frac{\partial U_t}{\partial x}\right|_q \quad , \quad v = \left.\frac{\partial U_t}{\partial q}\right|_x \tag{3.14a,b}$$

where *f* is defined as the external force required to balance the sum of the internal electrostatic and spring force, and the *v* is the voltage induced across the electrical port [3.22]. Applying the differentials of equation (3.14) to the total energy equation (3.13) yields,

$$f = \frac{-q_0^2 d}{2\varepsilon_0 h(n-1)(a+x_0)^2} + k_{xl}x_0 \tag{3.15}$$

and

$$v = \frac{q_0 d}{\varepsilon_0 h(n-1)(a+x_0)} \tag{3.16}$$

These two equations describe the constitutive relationship between the energy variables *q* and *x*, and the effort variables *v* and *f*. Note that the subscript '0' is introduced to indicate that these equations are valid in the static case as no assumption has yet been made about the dynamic behaviour of the resonator.

Dynamic response

To determine the dynamic response of the resonator the total differentials of equations (3.15) and (3.16) are first evaluated, yielding,

$$df = \left(\frac{-q_0 d}{\varepsilon_0 h(n-1)(a+x_0)^2}\right)dq + \left(\frac{q_0^2 d}{\varepsilon_0 h(n-1)(a+x_0)^3} + k_{xl}\right)dx \tag{3.17}$$

and

$$dv = \left(\frac{d}{\varepsilon_0 h(n-1)(a+x_0)} \right) dq + \left(\frac{-q_0 d}{\varepsilon_0 h(n-1)(a+x_0)^2} \right) dx \qquad (3.18)$$

In the limit δt→0, it follows that,

$$\dot{f} = \left(\frac{-q_0 d}{\varepsilon_0 h(n-1)(a+x_0)^2} \right) \dot{q} + \left(\frac{q_0^2 d}{\varepsilon_0 h(n-1)(a+x_0)^3} + k_{xl} \right) \dot{x} \qquad (3.19)$$

$$\dot{v} = \left(\frac{d}{\varepsilon_0 h(n-1)(a+x_0)} \right) \dot{q} + \left(\frac{-q_0 d}{\varepsilon_0 h(n-1)(a+x_0)^2} \right) \dot{x} \qquad (3.20)$$

For small variations about the bias point it is assumed that the voltage v, charge q, displacement x, and force f, are of the form $v(t) = \bar{v}e^{j\omega t}$, $q(t) = \bar{q}e^{j\omega t}$, $x(t) = \bar{x}e^{j\omega t}$ and $f(t) = \bar{f}e^{j\omega t}$, respectively [3.22]. Substitution of these values into equation (3.19) and (3.20) yields,

$$j\omega\bar{f}e^{j\omega t} = \left(\frac{-q_0 d}{\varepsilon_0 h(n-1)(a+x_0)^2} \right) j\omega\bar{q}e^{j\omega t} + \left(\frac{q_0^2 d}{\varepsilon_0 h(n-1)(a+x_0)^3} + k_{xl} \right) j\omega\bar{x}e^{j\omega t} \quad (3.21)$$

$$j\omega\bar{v}e^{j\omega t} = \left(\frac{d}{\varepsilon_0 h(n-1)(a+x_0)} \right) j\omega\bar{q}e^{j\omega t} + \left(\frac{-q_0 d}{\varepsilon_0 h(n-1)(a+x_0)^2} \right) j\omega\bar{x}e^{j\omega t} \quad (3.22)$$

which, after elimination of the exponential terms[11,12] yields, is in matrix form,

$$\left| \begin{array}{c} \bar{v} \\ \bar{f} \end{array} \right| = \frac{1}{j\omega} \left| \begin{array}{cc} \dfrac{d}{\varepsilon_0 h(n-1)(a+x_0)} & \dfrac{-q_0 d}{\varepsilon_0 h(n-1)(a+x_0)^2} \\ \dfrac{-q_0 d}{\varepsilon_0 h(n-1)(a+x_0)^2} & \dfrac{q_0^2 d}{\varepsilon_0 h(n-1)(a+x_0)^3} + k_{xl} \end{array} \right| \left| \begin{array}{c} \bar{\dot{q}} \\ \bar{\dot{x}} \end{array} \right| \qquad (3.23)$$

or in the notation of Prak [3.2],

---

[11] A non-trivial solution is assumed.

[12] Note that $\bar{\dot{f}} = j\omega\bar{f}$, $\bar{\dot{q}} = j\omega\bar{q}$ $\bar{\dot{x}} = j\omega\bar{x}$ and $\bar{\dot{v}} = j\omega\bar{v}$.

$$\begin{vmatrix} \bar{v} \\ \bar{f} \end{vmatrix} = \frac{1}{j\omega} \begin{vmatrix} E & C \\ C & M \end{vmatrix} \begin{vmatrix} \bar{\dot{q}} \\ \bar{\dot{x}} \end{vmatrix} \tag{3.24}$$

where the E, M and C are determined from the partial differentials,

$$E = \left(\frac{\partial U_t^2(q,x)}{\partial q^2} \right)_0 \quad , \quad C = \left(\frac{\partial U_t^2(q,x)}{\partial x \partial q} \right)_0 \quad , \quad M = \left(\frac{\partial U_t^2(q,x)}{\partial x^2} \right)_0 \tag{3.25a,b,c}$$

and the subscript '0' indicates that the partial derivatives of the energy function $U_t(q,x)$ are evaluated about the bias point with all other variables held constant.

Equation (3.23) consists of three matrices. The left hand column represents amplitudes of the generalised effort variables[13], i.e. the voltage and force at the electrical and mechanical ports, respectively. For free vibrations the magnitude of the external force, $\bar{f}$, acting on the mechanical port is equal to the sum of the external mechanical load, i.e., the inertial force and viscous friction force,

$$\bar{f} = -j\omega M_i \bar{x} - c\bar{x} \tag{3.26}$$

where M_i is the inertial mass and c a viscous-drag damping coefficient. The right hand column of equation (3.21) represents the amplitudes of the generalised flow variables, i.e. the current and velocity at the electrical and mechanical ports, respectively. The relationship between the system variables is described by the central matrix, formed by the parameters E, M and C. The parameter E represents the coupling at the electrical port, M the coupling at the mechanical port and C coupling between the electrical and mechanical ports. The level of energy coupling between the electrical and mechanical ports of the resonator is an indicator of the efficiency of the excitation/detection mechanism, and its magnitude is described by quantity known as the electromechanical coupling factor [3.2].

3.4.2 Electromechanical coupling factor

The coupling factor of an electromechanical transducer is a measure of the energy transfer between two prescribed ports of the system in one cycle and is analogous to the degree of coupling of magnetic flux between two inductive circuits [3.25]. In this model

---

[13] Assuming the classical analogy.

of the electrostatic comb drive it is a measure of the energy transfer between the electrical and mechanical ports of the resonator. A coupling factor of 1 means that all the electrical energy presented at the electrical energy port is converted into mechanical energy. Conversely, a coupling factor of zero implies no energy transfer, and consequently no coupling. The coupling factor of a single terminal resonator is defined by Prak [3.2], in terms of the matrix elements of equation (3.24) as,

$$\kappa = \sqrt{\frac{C^2}{EM}} \qquad (3.27)$$

and for the lateral resonator design presented in Figure 3.3 is calculated from equations (3.23) and (3.24) to be,

$$\kappa \approx \sqrt{\frac{1}{1 + \left(k_{xl} a d \big/ \varepsilon_0 h (n-1) V_p^2 \right)}} \qquad (3.28)$$

where $x_0 \ll a$, and the parameters are the same as those given previously. A high coupling factor is advantageous since it implies that a low energy input is needed to excite the resonator to a given amplitude. Moreover the amplitude of the motional sense signal generated by the resonator increases with the coupling factor, leading to an increased signal to noise ratio. Equation (3.28) shows that the coupling factor of the lateral resonator can be increased by altering the geometric coefficients of the comb capacitor, decreasing the flexure spring rate or increasing the polarisation voltage. Typically, for the lateral resonator design shown in Figure 3.3, equation (3.26) predicts a coupling factor of 0.015 under a polarisation voltage of 20 V (where h=2 µm, d=3 µm, a=40 µm, E=140 GPa, k_{xl}=7.0 Nm^{-1} and ε_0=8.86 $\times 10^{-12}$ Fm^{-1}).

3.4.3 One-port input impedance/admittance

Impedance

The input impedance of the resonator is equal to the ratio of the complex voltage and current amplitudes at the electrical power port,

$$Z(j\omega) = \frac{\bar{v}}{\dot{\bar{q}}} \tag{3.29}$$

A general expression for the input impedance is obtained from equations (3.24), (3.26) and (3.29),

$$Z(j\omega) = \frac{\bar{v}}{\dot{\bar{q}}} = E + \frac{C^2}{-j\omega M_i - c - M} \tag{3.30}$$

Inserting the values for E, C, and M given by equation (3.23) yields,

$$Z(j\omega) = \frac{1}{j\omega C_0} - \frac{1}{j\omega} V_p^2 \left(\frac{dC_0}{dx}\right)^2 \frac{1/k_{xl}}{\left(1 + \frac{\kappa^2}{1-\kappa^2}\right) - \frac{\omega^2}{\omega_1^2} + \frac{j\omega}{\omega_1 Q}} \tag{3.31}$$

where $C_0 = q_0/V_p$, dC_0/dx is the capacitance gradient, V_p is the polarisation voltage, k_{xl} the linear spring rate, ω the excitation frequency, ω_1 the unloaded resonant frequency and κ the electromechanical coupling factor.

Admittance

The input admittance of the one-port resonator is the ratio of the current and voltage amplitudes at the electrical port, i.e.,

$$Y(j\omega) = \frac{j\omega \bar{q}}{\bar{v}} = \frac{\dot{\bar{q}}}{\bar{v}} \tag{3.32}$$

and is best evaluated by re-arranging equation (3.24) so that the charge, q, is the independent variable, yielding,

$$\begin{vmatrix} \bar{q} \\ \bar{f} \end{vmatrix} = \frac{1}{j\omega} \begin{vmatrix} \dfrac{1}{E} & \dfrac{-C}{E} \\ \dfrac{C}{E} & \left(M - \dfrac{C^2}{E^2}\right) \end{vmatrix} \begin{vmatrix} \dot{\bar{v}} \\ \dot{\bar{x}} \end{vmatrix} \tag{3.33}$$

where the parameters have the same meaning as those given previously. A general expression for the input admittance is found from equations (3.26), (3.32) and (3.33);

$$Y(j\omega) = \frac{j\omega\overline{q}}{\overline{v}} = \frac{j\omega}{E} + \frac{j\omega C^2}{E^2\left(j\omega M_i + c + \left(M - \frac{C^2}{E}\right)\right)} \qquad (3.34)$$

Substituting the values for E, C, and M given in equation (3.23) yields an expression for the input admittance,

$$Y(j\omega) = \frac{j\omega\overline{q}}{\overline{v}} = j\omega C_0 + j\omega V_p^2 \left(\frac{dC_0}{dx}\right)^2 \frac{1/k_{xl}}{1 - \frac{\omega^2}{\omega_1^2} + \frac{j\omega}{\omega_1 Q}} \qquad (3.35)$$

There are two interesting points to note from the expression for the input impedance, described by equation (3.31), and the input admittance, described by equation (3.35). First, the initial term in both expressions is simply the input impedance/admittance of the comb capacitor, whilst the second term describes the *motional* impedance/admittance loop of the resonator near the fundamental frequency, where $\omega \approx \omega_1$.

The second point is that frequency of maximal motional impedance is different from the frequency of maximal motional admittance. According to equation (3.31), when the resonator is driven from a current source the frequency of maximum motional impedance occurs where,

$$\frac{\omega^2}{\omega_1^2} = 1 + \frac{\kappa^2}{1 - \kappa^2} \qquad (3.36)$$

This frequency is termed as the *parallel* resonant frequency, ω_p, [3.2,3.24] such that,

$$\omega_p^2 = \omega_1^2 \left(1 + \frac{\kappa^2}{1 - \kappa^2}\right) \qquad (3.37)$$

where κ is the coupling factor, described in section 3.4.2, and ω_1 is the mechanical resonant frequency, defined here as the resonant frequency of the resonator under zero bias. Conversely, according to equation (3.35), when the resonator is driven from a

voltage source the frequency of maximum motional admittance, defined as the *series* resonant frequency [3.2,3.24], is simply equal to the mechanical resonant frequency,

$$\omega_s = \omega_1 \tag{3.38}$$

It is important to note that parallel resonant frequency is not a true mechanical resonant frequency but is observed as a consequence of the electromechanical coupling between the mechanical elements of the resonator and the electrical energy stored by the excitation/detection mechanism, in this instance the energy stored by the drive/sense comb capacitor. The existence of a parallel frequency is a well known phenomenon in one-port quartz crystal resonators and arises when a series resonant circuit is loaded with a parallel reactance. In point of fact, the measured resonant frequency is also sensitive to other electrical energy storing elements, such as those formed by parasitic capacitance, parasitic inductance and the load of the current or voltage source used to drive the resonator [3.24]. These points are illustrated in the next section where the effect of (parasitic) electrical loads on the resonator is shown by constructing an electromechanical equivalent circuit of the resonator.

3.4.4 Electrical equivalent circuit

A lumped electrical equivalent circuit of the resonator is constructed by replacing the mechanical elements, i.e. the inertial mass, flexure and viscous damper with their electrical equivalents [3.17]. In this model the relationship between the mechanical elements of the resonator and the electrical equivalents is determined using the classical analogy, see Table 3.1. This means that the mechanical force acting on the resonator is represented by a voltage in the electrical equivalent circuit, while the displacement of the resonator is represented by a charge. Note that the classical analogy implies a change in system variable from flow (force) to effort (voltage). Consequently, the mechanical flow store, i.e. the compliance of the flexure is represented by an electrical effort store, i.e. the capacitor. Similarly, the inertial mass is represented by an inductor. Further, the dissipative drag-force acting on the resonator is represented by a resistor (a change in system variable here is irrelevant). In a limited frequency range ($\approx$ kHz) around the fundamental mode the resonator can be modelled by linking these elements to form a single terminal branch as shown in Figure 3.8a. Note that the static capacitance, C_0, of the comb capacitor is truly electrical in nature and that the resonator is also loaded with a

parallel parasitic capacitance C_p. Parasitic capacitance is formed by the contact pads, conductive tracks and wire bonds used to connect the resonator to the external circuit, that will itself load the resonator.
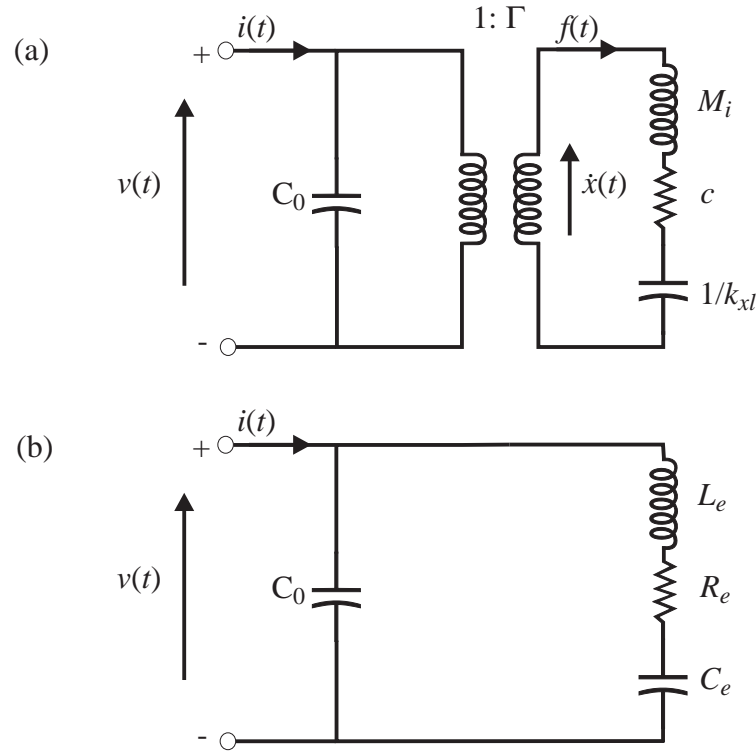

Figure 3.8 (a) Lumped equivalent circuit for a one-port resonator loaded with a capacitor C_p near the fundamental mode and (b) after elimination of transformer.

The purpose of the electrical transformers shown in Figure 3.8a is to model the electromechanical coupling between the electrical and mechanical ports of the resonator. The transformer turns ratio, denoted by Γ, is determined by the level of energy coupling between the electrical and mechanical domains [3.26]. In practice the transformer serves no useful purpose in the electrical equivalent circuit and is eliminated by transforming the mechanical elements, M_i, c, and $1/k_{xl}$ across to the electrical side of the model, leading to the unloaded electrical equivalent circuit as shown in Figure 3.8b. The relationships between the components values M_i and L_e, $1/k_{xl}$ and C_e, R_e and c, are determined by ensuring that the power flow through each pair is equal, such that,

$$R_e = \frac{c}{\Gamma^2} \quad , \quad L_e = \frac{M_i}{\Gamma^2} \quad , \quad C_e = \frac{\Gamma^2}{k_{xl}} \qquad (3.39a,b,c)$$

The electromechanical interaction between the mechanical resonant element and the electrical components in the system becomes clear by examining the equivalent circuit in Figure 3.8b. If the resonator is driven from a voltage source, series resonance occurs when the admittance of the series combination of L_e and C_e tends to a maximum. On the other hand, if the resonator is driven from a current source, parallel resonance occurs when the overall impedance of L_e and C_e in parallel with the electrical capacitances C_0 and C_p tends to a maximum. The series resonant frequency of the electrical circuit is given by the equation [3.27],

$$\omega_s = \sqrt{\frac{1}{L_e C_e}} \tag{3.40}$$

whereas the parallel frequency is dependant on the static capacitance of the comb capacitor C_0 and parasitic capacitance C_p,

$$\omega_p = \sqrt{\frac{1}{L_e \left(C_e \, // \, C_0 \, // \, C_p \right)}} \tag{3.41}$$

where L_e is the equivalent electrical inductance and C_e the equivalent electrical capacitance as defined by equation (3.39b,c), respectively.

The locations of the serial and parallel resonant frequencies are shown on the vector admittance curve of Figure 3.9, which is of the same form as the parallel plate electrostatic microresonator described by Tilmans [3.24] and also the one-port piezoelectric quartz crystal [3.28]. The curve describes a vertical line that loops about the mechanical resonant frequency. Away from mechanical resonance the real part of the admittance is zero and the susceptance of the resonator determined solely by the capacitances C_0 and C_p. In addition to the series and parallel resonant frequencies two additional characteristic frequency pairs can be identified [3.28]. The frequencies of maximal and minimal *absolute* admittance are denoted by ω_{max} and ω_{min}, respectively. The frequency range over which the motional admittance of the resonator is inductive is defined by ω_R and ω_A, the *resonant* and *anti-resonant* frequencies that are located on the axis of zero susceptance. Series resonance occurs at the frequency of maximal motional admittance, between ω_R and ω_{max}. The parallel resonant frequency lies between ω_{min} and ω_A. Note that the Q-factor of the resonator is obtained from the -3 dB frequencies, i.e. the

frequencies where the motional admittance of the series resonant frequencies are reduced to $1/\sqrt{2}$ of their original value, denoted by ω^+ and ω^- in Figure 3.9.
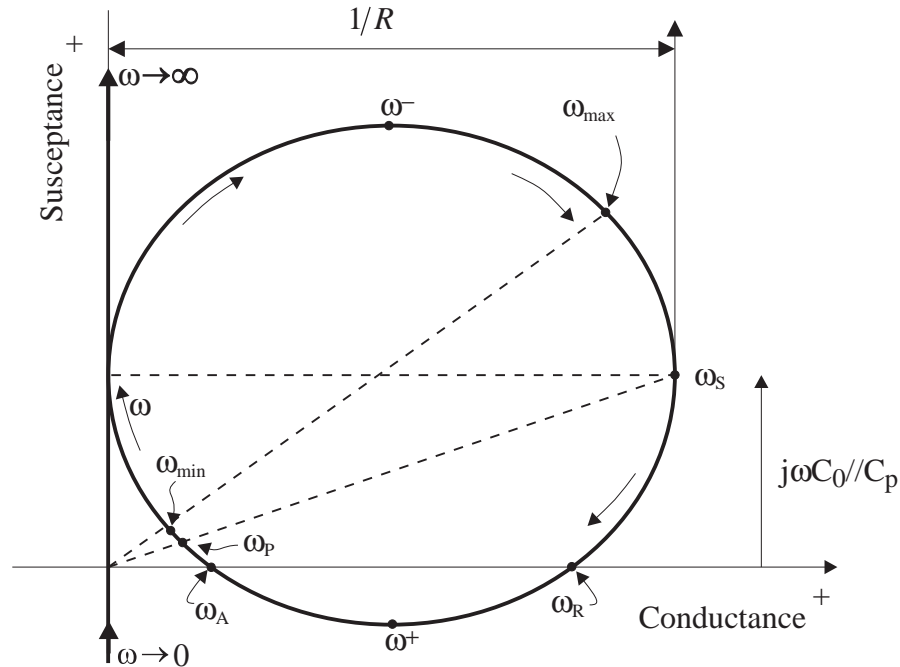

Figure 3.9 Typical polar admittance plot for a one-port resonator loaded with a capacitance C_p , [3.24,3.28].

As is clear from equation (3.41), the parallel resonant frequency is dependant on the static capacitance C_0, and the (parasitic) capacitive load C_p. In practice, therefore, it is preferable to measure the series resonant frequency (i.e. the input admittance) of the electrostatic resonator, because any instability in the value of the capacitive load will be reflected in a shift of the parallel resonant frequency [3.8]. Note that the series frequency is also sensitive to parasitic capacitance in series with the resonator, but that these are usually easier to minimise than parallel parasitic capacitance.

The predicted one-port input admittance plot for the unloaded lateral resonator (i.e. C_p=0), calculated using equations (3.5) and (3.35) is shown in Figure 3.10. The plot is relevant where the resonator is operated in vacuum where the Q-factor is assumed to be 20 000. Note that the other parameters are given in the Figure caption.
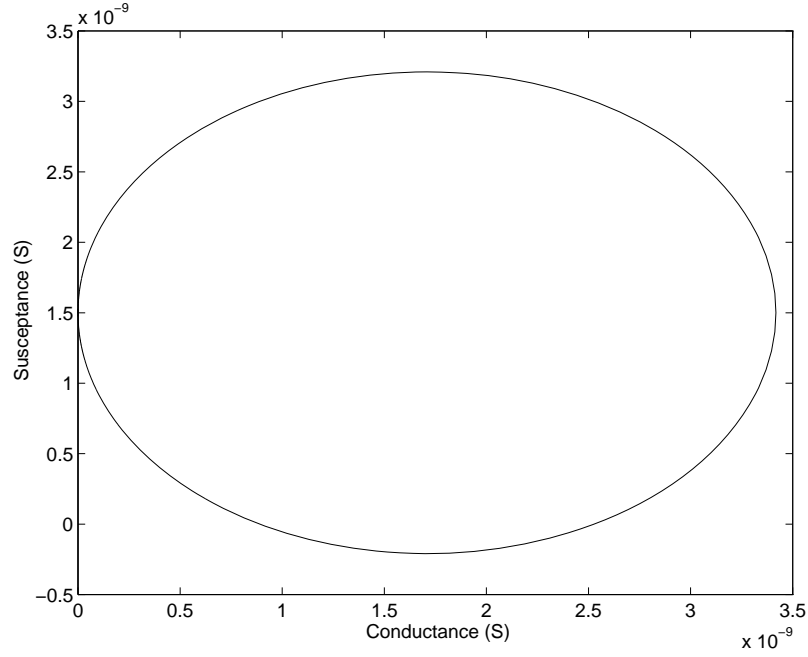
Figure 3.10 Predicted one-port admittance plot for the unloaded (C_p=0) lateral resonator with an assumed Q-factor of 20 000. The relevant variables in equations (3.5) and (3.35) are: ε_0=8.86×10^{-12} Fm^{-1} n=25, h=2 μm, d=3 μm a=40 μm, V_p=15 V, ω_l=301 rads/s, and k_{xl}=7.0 Nm^{-1}.

3.4.5 Figure of merit

As is outlined earlier, the total input admittance of the one-port resonator consists of a static part, $Y_{stat}(j\omega_s)$, and a motional part, $Y_{mot}(j\omega_s)$, represented by $C_0 // C_p$ and the *RLC*-branch in Figure 3.8b, respectively. The figure of merit, *M*, of a one-port resonator is a measure of the relative magnitude of $Y_{stat}(j\omega_s)$ and $Y_{mot}(j\omega_s)$ at resonance i.e.,

$$M = \frac{\left|Y_{mot}(\omega_s)\right|}{\left|Y_{stat}(\omega_s)\right|} = \frac{1/R}{\omega_s C_0 // C_p} \tag{3.42}$$

where $1/R$ is the motional input admittance and $j\omega_s C_0 // C_p$ the static input admittance, see Figure 3.9 [3.24]. An expression for the figure of merit for the lateral resonator is obtained directly from equation (3.35) such that,

$$M = \frac{V_p^2 (dC_0 / dx)^2 Q(1/k_{xl})}{C_0 // C_p} \tag{3.43}$$

In practice a high figure of merit is desirable, as it makes the motional admittance loop more pronounced and so easier to detect. However, as is clear from Figure 3.8, the effect of parasitic capacitance is to increase the magnitude of the static input admittance, so reducing the figure of merit and making resonance more difficult to observe. The lateral resonator is especially sensitive to parasitic capacitance because the motional admittance at resonance is very small ≈ 3.5 nS, (see Figure 3.10). For example, the figure of merit for the unloaded (i.e. C_p=0) lateral resonator is predicted to be 2.3, using equations (3.5) and (3.43) togther with the parameters given in the caption of Figure 3.10. A parasitic capacitance of only 1 pF (typically 20 times smaller than that formed between a 300 µm square contact pad and the resonator ground plane) in parallel with C_0 reduces the figure of merit to 0.013. Hence, the operation of the lateral resonator in a one-port mode is likely to be problematic due to the presence of parasitic capacitance formed by the contact pads, tracks, sensor packaging and the electronics used to operate the resonator.

3.5 Two-port excitation and detection

In the two-port mode, two separate transduction elements are used to excite the resonator and measure its response. This method is a more flexible approach than the one-port mode because irreversible type detection elements, e.g. piezoresistors, can be employed. Also, using two transduction elements separates the energy of the excitation and detection signals and this implies that the motion of the resonator will be easier to resolve than in the one-port mode.

In the two-port mode the resonant frequency is determined by monitoring the magnitude or phase of the voltage gain, $\bar{v}_s/\bar{v}_d$; current gain, $\bar{i}_s/\bar{i}_d$; transconductance, $\bar{i}_s/\bar{v}_d$; or transimpedance, $\bar{v}_s/\bar{i}_d$. However, in the previous section it is shown that to avoid coupling the resonant frequency to parasitic capacitance a motional sense current, rather than a motional sense voltage, should be generated and therefore a current gain or transconductance measurement should be employed. In this section an expression for the transconductance of the resonator is derived, because this is the intended mode of operation.

In the transconductance formulation the resonator is driven from a voltage source and the motional sense current monitored. Resonance is observed as a peak in the

motional sense current, or a maximum in the motional transconductance. The electrical connections to the resonator are shown earlier in Figure 3.3. A polarisation voltage, V_p, and a sinusoidal drive signal, $\bar{v}_d$, are applied to the drive comb. The motion of the resonator is determined by applying a d.c. bias, V_s, to the sense comb and measuring the current generated by the time varying sense capacitor C_s.

3.5.1 Systems model

An expression for the transconductance is derived using the energy method described earlier in section 3.4.1. The first step is to construct a systems model of the two-port resonator by classifying each lumped element of the resonator as a mechanical energy store, electrical energy store, or energy dissipater. The energy flow associated with each energy storage element is described by a pair of power variables and a conjugate pair of energy variables. In the two-port mode two electrical ports are required, one to represent the electrical energy associated with the drive comb and one to represent the electrical energy associated with the sense comb. As in the one-port analysis, only the fundamental mode of oscillation is considered and, consequently, only a single mechanical energy powerport is required in the model.

The total energy stored in the two-port network is the sum of the electrical energy and mechanical energy and (assuming zero initial energy) equal to,

$$U_t(t) = \underbrace{\int_0^t v_d i_d dt + \int_0^t v_s i_s dt}_{\text{electrical energy}} + \underbrace{\int_o^t f u dt}_{\substack{\text{mechanical} \\ \text{energy}}} \tag{3.44}$$

where v and i are the voltage and current associated with the electrical drive and sense ports, as denoted by the subscript 'd' or 's', and f and u are the force and velocity associated with the mechanical port, respectively. The condition that resonator is driven from a voltage source and the motional sense current monitored implies that both the current and force in the energy storing system depend on the charge and displacement, i.e.,

$$q_d = q_d(v_d, v_s, x) \; , \; q_s = q_s(v_s, v_d, x) \; , \; f = f(v_s, v_d, x) \tag{3.45a,b,c}$$

With this condition it is appropriate that energy stored by the comb capacitor should be expressed in terms of a voltage, and the charge set as the independent variable.

This is achieved by expressing the total stored energy as the sum of the complementary energy function (co-energy function) of the comb capacitor and the energy stored by the flexure,

$$U_t(v_d, v_s, x) = \int_{0,0,0}^{v_d, v_s, x} q_d(v_d, v_s, x)dv_d + \int_{0,0,0}^{v_d, v_s, x} q_s(v_d, v_s, x)dv_s$$
$$+ \int_{0,0,0}^{v_d, v_s, x} f(v_d, v_s, x)dx$$

(3.46)

Note that the relationship between the energy, U, and co-energy, U^*, of a linear capacitor is simply [3.25],

$$U^* = \int_0^q v\,dq = U = \int_0^v q\,dv$$

(3.47)

so that the total energy stored by the system can be written as,

$$U_t(v_d, v_s, x) = \frac{1}{2}C_d(x)v_d^2 + \frac{1}{2}C_s(x)v_s^2 + \frac{1}{2}k_{xl}x^2$$

(3.48)

where v_d is the voltage across the drive comb, v_s the voltage across the sense comb, k_{xl} the linear spring rate of the hammock flexure and x the displacement of the flexure from the equilibrium position. The drive capacitance $C_d(x)$, and sense capacitance $C_s(x)$, are given by the expressions[14],

$$C_d(x) = \frac{\varepsilon_0 h(a+x)(n-1)}{d} \quad , \quad C_s(x) = \frac{\varepsilon_0 h(a-x)(n-1)}{d}$$

(3.49a,b)

where the parameters have the same meaning as those given previously. The constitutive relationships of the two-port resonator are obtained directly from equation (3.44) by taking the partial differentials [3.25],

$$f = -\frac{\partial U_t(v_d, v_s, x)}{\partial x}\bigg|_{v_s, v_d} \quad , \quad q_d = \frac{\partial U_t(v_d, v_s, x)}{\partial v_d}\bigg|_{x, v_s} \quad , \quad q_s = \frac{\partial U_t(v_d, v_s, x)}{\partial s}\bigg|_{x, v_d}$$

(3.50a,b,c)

where q_d is the charge induced on the drive comb, q_s the charge induced on the sense comb, x the displacement of the resonator from the equilibrium position and f is the

---

[14] An ideal parallel plate capacitor is assumed

external force required to balance the sum of the internal electrostatic force and spring force[15].

By strictly following the same procedure outlined in 3.4.1 the constitutive equation describing the dynamic response of the two-port resonator can be derived;

$$
\begin{vmatrix} \bar{q}_d \\ \bar{q}_s \\ \bar{f} \end{vmatrix} = \frac{1}{j\omega} \begin{vmatrix} E_{dd} & E_{ds} & C_{dd} \\ E_{sd} & E_{ss} & C_{ss} \\ C_{dd} & C_{dd} & M \end{vmatrix} \begin{vmatrix} \bar{v}_d \\ \bar{v}_s \\ \bar{x} \end{vmatrix}
\tag{3.51}
$$

The central matrix of equation (3.51) is composed of four sub-matrices: the matrix E couples the electrical domains, and is given by[16],

$$
E_{dd} = \left(\frac{\partial^2 U_t}{\partial v_d^2} \right)_0 , E_{sd} = E_{ds} = \left(\frac{\partial^2 U_t}{\partial v_d \partial q_s} \right)_0 , E_{ss} = \left(\frac{\partial^2 U_t}{\partial v_d^2} \right)_0
\tag{3.52a,b,c}
$$

The matrix C the couples the electrical and mechanical domains and the matrix M couples the mechanical domains (and is a single valued function because only one mode of oscillation is considered in this model), whereby,

$$
C_{dd} = \left(\frac{\partial^2 U_t}{\partial x \partial v_d} \right)_0 , \quad C_{ss} = \left(\frac{\partial^2 U_t}{\partial x \partial v_s} \right)_0 , \quad M = \left(\frac{\partial^2 U_t}{\partial x^2} \right)_0
\tag{3.53a,b,c}
$$

The magnitude of the mechanical force acting on the resonator through the mechanical port is equal to the sum of the inertial force and viscous damping force and is given by,

$$
\bar{f} = j\omega M_i \bar{x} + c\bar{x}
\tag{3.54}
$$

where M_i is the inertial mass, and c a damping factor.

At this point it is helpful to explain the components of the two-port constitutive equation by expanding the first row, giving an expression for the current flowing though the electrical drive port,

---

[15] Note that the sign of the force is opposite to that in the one-port mode analysis. This a necessary consequence of expressing using the electrical co-energy function of the comb capacitors.

[16] In obtaining these expressions the '0' indicates that the partial derivatives of the energy function $U_t(v_d, v_s, x)$ are evaluated about the bias point with all other variables held constant.

$$\bar{i}_d = j\omega\bar{q}_d = E_{dd}\bar{v}_d + E_{ds}\bar{v}_s + C_{dd}\bar{x} \tag{3.55}$$

that is composed of three components;

(1) $E_{dd}\bar{v}_d$ is the current flowing through the drive comb C_d, due to the drive voltage $\bar{v}_d$.

(2) $E_{ds}\bar{v}_s$ is the current flowing through the drive comb C_d, due to the electrical cross-talk induced by the sense voltage $\bar{v}_s$. In this model of the resonator the cross-talk is ignored and hence $E_{ds}=E_{sd}=0$.

(3) $C_{dd}\bar{x}$ is the motional current generated at the drive comb by the motion of the resonator. Note that comparing the magnitude and/or phase of this current with the drive voltage is equivalent to a one-port measurement.

Transconductance

An expression for sense current flowing through the sense port is found in the same way, using equations (3.51) and (3.54),

$$\bar{i}_s = j\omega\bar{q}_s = j\omega\bar{v}_d\left(\frac{C_{dd}C_{ss}}{\omega^2 M_i - j\omega c - M}\right) + j\omega\bar{v}_s\left(\frac{E_{ss}}{\omega^2 M_i - j\omega c - M} + C_{ss}\right) \tag{3.56}$$

which leads directly to a general expression for the transconductance because, according to the d.c. bias conditions on the sense comb $j\omega\bar{v}_s = 0$, so that,

$$\frac{\bar{i}_s}{\bar{v}_d} = \frac{j\omega C_{dd}C_{ss}}{\omega^2 M_i - j\omega c - M} \tag{3.57}$$

Inserting the values for C_{dd}, C_{ss} and M, calculated using equations (3.48), (3.49) and (3.53) yields,

$$\frac{\bar{i}_s}{\bar{v}_d} = \frac{(j\omega/k_{xl})(dC_{d0}/dx)(dC_{s0}/dx)V_pV_s}{1-\left(\dfrac{\omega}{\omega_1}\right) + \dfrac{j\omega}{Q\omega_1}} \tag{3.58}$$

where k_{xl} is the linear spring rate of the flexure, dC_{s_0}/dx and dC_{d_0}/dx the capacitance gradient of the drive comb and sense comb, respectively, V_p the polarisation voltage, V_s the sense-comb bias and Q the mechanical quality factor of the resonator. The comb

capacitors of the lateral resonator have an identical geometry and so (theoretically) are of equal capacitance, thus $dC_{s_0}/dx = dC_{d_0}/dx$ and equation (3.58) simplifies to,

$$\frac{\bar{i}_s}{\bar{v}_d} = \frac{(j\omega/k_{xl})(dC_0/dx)^2 V_p V_s}{1 - \left(\dfrac{\omega}{\omega_1}\right) + \dfrac{j\omega}{Q\omega_1}} \tag{3.59}$$

where $C_0 = C_s = C_d$. Equation (3.59) describes the characteristic response of the lateral resonator when operated in a two-port transconductance mode. The amplitude and phase responses are obtained directly from equation (3.59),

$$|G(j\omega)| = \left|\frac{i_s}{v_d}\right| = \frac{(j\omega/k_{xl})(dC_0/dx)^2 V_p V_s}{\sqrt{\left[1 - \left(\dfrac{\omega}{\omega_1}\right)^2\right] + \left(\dfrac{\omega}{Q\omega_1}\right)^2}}$$

$$\angle G(j\omega) = \arctan\left[\frac{-\omega/\omega_1}{Q(1 - (\omega/\omega_1)^2)}\right] \tag{3.60a,b}$$

Note that equation (3.60) describes the typical response of a second-order (bandpass) electromechanical filter where the sense current lags the drive voltage by 90° at resonance (i.e $\omega = \omega_1$).

3.5.2 Cross-talk

Electrical cross-talk (otherwise known as electrical feed-through) occurs as a consequence of the parasitic capacitive and/or resistive coupling between the electrical ports of a resonator. On chip parasitic capacitance is formed between the conductive track/contact pads and the ground plane, both of which have finite resistance. Electrical cross-talk in the two-port mode is illustrated in the (unloaded) lumped electromechanical equivalent circuit shown in Figure 3.11a. Here, the overall transfer function of the resonator is the sum of the contribution from the mechanical response, $M(j\omega)$, and the electrical response $E(j\omega)$. The two transformers couple energy from the electrical domain to the mechanical domain and vice versa. The purely electrical coupling between the drive and sense ports is modelled with a simple resistor/capacitor network (inductance values are assumed to be negligible and are therefore omitted). The electrodes of the parasitic capacitances C_{p1}, C_{p2} and C_{p3} are formed between the tracks/contact pads, the

substrate ground plane and sensor packaging, respectively. The resistors R_{s1} and R_{s2} model the resistance of the ground plane of the resonator. Note that the resistance of the connective tracks and contact pads is assumed to be negligible. For the meaning of the other elements reference is made to section 3.4.4.

In practice the effect of electrical cross talk on the second order mechanical transfer function is to make the resonance less pronounced or, in the worst case, totally obscure it, see Figure 3.11b, from [3.29]. In the first place cross-talk is reduced by minimising parasitic capacitance (C_{p1}, C_{p2} and C_{p3} in Figure 3.11), increasing the electrical impedance between the drive and sense ports (R_{s2} in Figure 3.11) and reducing series resistance to ground (R_{s1} in Figure 3.11). The effects of electrical cross-talk can also be minimised by using a compensation scheme, whereby a difference amplifier is employed to subract the electrical signal generated by a compensation (or inactive) resonator from that generated by an active resonator. To avoid repetition, a detailed description of these techniques is not given here. Instead, the reader is referred to the following references Tilmans [3.24] (one-port mode) and van Mullem [3.29] (two-port mode) for further information on this subject.

The importance of minimising electrical cross-talk (and electrical noise) is demonstrated by predicting the magnitude of the motional sense current of the lateral resonator at resonance. In the two-port mode of operation the motional sense current at resonance is obtained directly from equation (3.58), such that,

$$\left|\bar{i}_s\right| = \left|\frac{\left(dC_0/dx\right)^2 \bar{v}_d V_p V_s Q \omega_1}{k_{xl}}\right| \tag{3.61}$$

where the parameters have the same meaning as those given previously. It is assumed the resonator is biased with a polarisation voltage of 15 V and sense bias of 10 V, close to the maximum value permitted in standard integrated microelectronics. The magnitude of the drive voltage needed to excite the resonator in vacuum is assumed to be ≈ 50 mV, close to that reported by Tang [3.18], who has operated similar lateral comb-drive resonators. Inserting these values and the other parameters given in the caption of Figure 3.10 into equation (3.61) yields an estimate for the motional sense current at resonance of ≈ 0.2 nA. It is clear that to be able to measure such an extremely small motional current, electrical cross-talk and all sources of noise must be minimised. This subject is discussed

further in chapter 5 where the sense current of the lateral resonator is measured using a high gain ($\times 10^{8\Omega}$) amplifier.
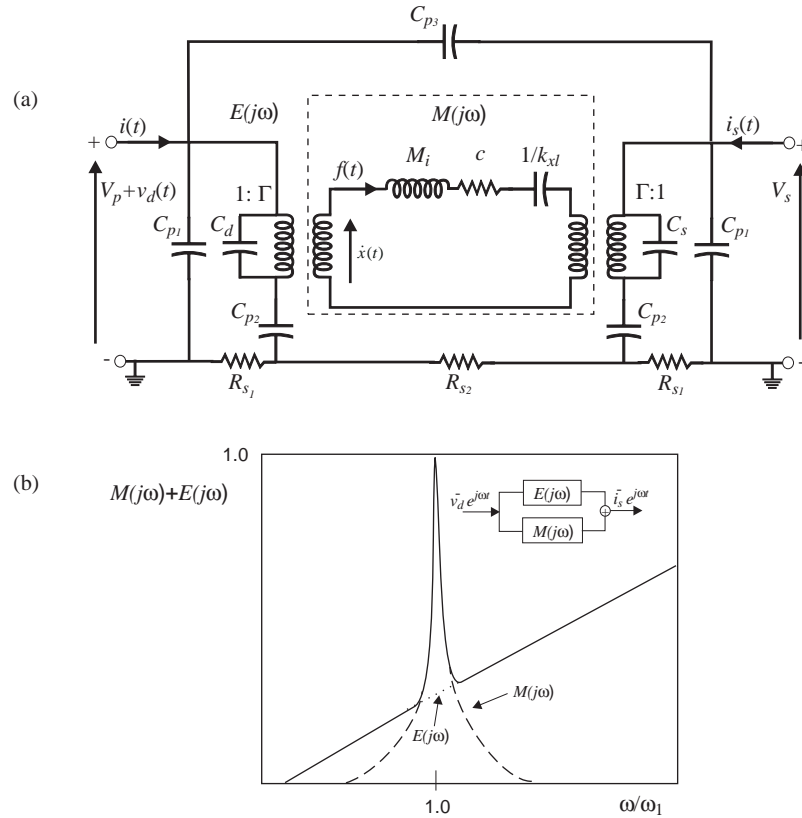

Figure 3.11 (a) Electrical equivalent circuit for the two-port resonator. The purely mechanical response of the resonator, M(jω), is modelled by an inductor, resistor and capacitor. The purely electrical response, E(jω), is modelled with a resistor and capacitor network. (b) Schematic showing the how the mechanical response of the two-port resonator is obscured by the electrical response, from [3.29].

The primary reason for the extremely small motional sense current generated by the lateral resonator is the small capacitance gradient, dC_0/dx, predicted to be ≈ 0.15 pFm^{-1}, using equation (3.5) and the parameters given in the caption of Figure 3.10. In turn, the reason for the small capacitance gradient is the fabrication process, which restricts the thickness of the resonator to a few microns. Apart from increasing the thickness of the resonator, the magnitude of the sense current can also be increased by reducing the flexure spring rate, k_{xl}, or by increasing the polarisation voltage, V_p. However, the spring rate is also fixed by the fabrication process, see section 2.5.1 of chapter 2, and the polarisation voltage is limited by the need to use standard IC devices. The Q-factor is maximised by operating the resonator in vacuum.

3.6 Conclusions

Micromechanical resonant sensors are operated using a variety of excitation and detection mechanisms. Each mechanism has its advantages and disadvantages and the designer must select the mechanism that is most appropriate to the resonator design, fabrication process and application.

Lateral resonators are usually driven electrostatically via interdigitised comb capacitors. This scheme integrates well with the fabrication process. It is also a reversible mechanism, which enables the resonant frequency to be determined by monitoring the motional impedance or admittance of a single comb capacitor. When the resonator is operated in a two-port mode, two comb capacitors are employed; one to excite the resonator and one to measure the response. In this mode the resonant frequency is determined by measuring the motional transconductance of the resonator. Alternatively, the resonator is driven electrostatically and the resonant frequency determined by monitoring the resistance of an integrated piezoresistive pick-up.

For small vibrations near the fundamental mode of oscillation, the response of the resonator is described by a second-order linear differential equation. One characteristic of resonant strain gauges and force transducers is that this response becomes non-linear when the resonator is over-modulated. The non-linear response arises because of the non-linear spring rate of the flexure - which is itself necessary for strain or force sensitivity. The non-linearity is characterised by a distortion of the amplitude (and phase) responses. Beyond a critical drive force, the non-linear response becomes multi-valued leading to hysteresis.

The linear response of the lateral resonator when operated using electrostatic excitation/capacitive detection has been modelled using a systems approach that is based upon the storage and flow of energy. The model is valid for small deflections about the equilibrium position, where the non-linearity is assumed to be negligible. The model has been used derive expressions for the input impedance and input admittance of the one-port resonator. The expressions show that the series resonant frequency is equal to the mechanical resonant frequency of the resonator, and is measured when the input admittance of the resonator is monitored. On the other hand, the parallel resonant frequency is measured when the input impedance of the resonator is monitored. The

parallel frequency arises because of the electromechanical coupling between the resonator and the excitation/detection mechanism.

An alternative approach to modelling a resonator is to construct an electrical equivalent circuit. This straightforward approach has the benefit of allowing the effect of external electrical components, e.g. parasitic capacitance, on the frequency response to be determined. Parasitic capacitance is formed by the contact pads, conductive tracks and sensor packing and can effect the performance of the resonator in several ways. First, the parallel resonant frequency of the resonator is shifted by a parallel (parasitic) capacitance, whose value may shift with time so leading to a poor frequency stability. This problem can be avoided by monitoring a motional sense current, i.e., the input admittance of the resonator. Second, parallel (parasitic) capacitance increases the static input admittance of the resonator, so reducing the figure of merit. This is likely to make detection of the resonant frequency in a one-port mode difficult because the motional admittance is predicted to be very small (≈ 3.9 nS).

In the later part of the chapter the one-port model is extended and an expression for the transconductance of the two-port resonator derived. The advantage of the two-port mode is that the energy of the drive and sense signals are separated. This implies that detection signal should be easier to monitor than in the one port mode, although the response can still be degraded by electrical coupling, or cross-talk. An electrical equivalent circuit of the resonator has been constructed to show the nature of the cross-talk. At resonance the motional sense current of the two-port resonator is predicted to be ≈ 0.2 nA. It is clear that to be able to measure such an extremely small sense current a precision high gain amplifier is required, and moreover, the levels of electrical cross-talk and electrical noise must be kept to an absolute minimum.

References

[3.1]   Stemme G., Resonant silicon sensors, *J. Micromech Microeng*. Vol. 1 (1991) 113-125.

[3.2]   Prak A., Silicon resonant sensors: operation and response, *PhD Thesis*, University of Twente, Enschede, The Netherlands, (1993).

[3.3]   Ikeda K., Kuwayama H., Kobayashi T., Watanabe T., Nishikawa T., Yoshida T., and Harada K., Three dimensional micromachining of silicon presssure sensor intergrating resonant strain-gauge on diaphragm, S*ensors and Actuators*, A21-23 (1990) 1007-1010.

[3.4]   Pointon A. J., Piezoelectric devices, *IEE Proc.,* Vol. 129 Pt. A No. 5 (1982).

[3.5]   Ernisse E. P., Ward R. W. and Wiggins R. B., Survey of quartz bulk resonator sensor technologies, *IEEE Trans. Ultrasonics and Frequency Contr*ol, Vol. 35 No. 3 (1988) 323-330.

[3.6]   Dufour M., Delaye M.T., Michel F., Danel J.S., Diem B. and Delapierre G., A comparison between micromachined pressure sensors using quartz or silicon vibrating beams, 6th *Int. Conf. Solid State Sensor and Actuators, (Transducers '91)* (1991) 668-671.

[3.7]   van Mullem C. J., Blom F. R., Fluitman J. H. J. and Elwenspoek M., Piezoelectrically driven silicon force beam sensor, *Sensors and Actuators,* A25-27 (1991) 279-383.

[3.8]   Gopel W., Hesse J. and Zemel J. N. (eds.), *Sensors a compreshensive survey*, Vol. 7 Mechanical Sensors, Weinham, (1994).

[3.9]   Tilmans H. A. C., Elwenspoek M. and Fluitman J. H. J., Micro resonant force gauges, *Sensors and Actuators*, A30 (1992) 35-53.

[3.10] Bouwstra S., Blom F. R., Lammerink T. S. J., Yntema H., Scharp P., Fluitman J. H. J. and Elwenspoek M., Excitation and dectection of micromechanical strucutures using a dielectric thin film, *Sensors and Actuators*, 17 (1989) 219-223.

[3.11] Kvisteroy T., Guslan O., Stark B., Nakstad H., Eriksrud M., and Bjornstad B., Optically excited silicon sensor for permanently installed downhole pressure monitoring applications, *Sensors and Actuators*, A31 (1992) 164-167.

[3.12] Othman M. B. and Brunnschweiler A., Electrothermally excited silicon beam mechanical resonators, *Electronics Letters*, Vol. 23 No. 14 (1987) 728-730.

[3.13] Zook J. D., Burns D. W., Guckel H., Sniegowski J. J., Engeistad R. L. and Feng Z., Resonant microbeam strain transducers, *6th Int. Conf. Solid-State Sensors and Actuators*, *(Transducers '91),* (1991) 529-533.

[3.14] Kanda, Piezoresistance effect in silicon, *Sensors and Actuators*, A28 (1991) 83-91.

[3.15] Guckel H., Rypstata C. and Nesnidal M., Polysilicon Resonant microbeam technology for high performance sensor applications, *IEEE Solid-State Sensor and Actuator Workshop,* Hilton Head, South Carolina, (1992) 203-207.

[3.16] Smith R., Druck Ltd., Personal communication.

[3.17] Shearer J. L., Murphy A. T. and Richardson H. H., *Introduction to system dynamics*, Addison Wesley, second edition, (1971).

[3.18] Tang W. C.-K., Electrostatic comb drive for resonant sensor and actuator applications, *PhD Thesis*, University of California, Berkeley, (1990).

[3.19] Stoker J. J., *Nonlinear vibrations in mechanical and electrical systems*, Interscience Inc. New York, (1963).

[3.20] Timoshenko S., Young D. H., and Weaver Jr. W., *Vibration problems in engineering*, 4th edition, J. Wiley and Sons, New York, (1974).

[3.21] White D. C. and Woodsen H. H., *Electromechanical energy conversion*, J. Wiley, New York, (1959).

[3.22] Karnopp D. C., Margolis D. L. and Rosenburg R. C., *Systems dynamics: a unified approach*, second edition, J. Wiley & Sons New York, (1990).

[3.23] Kuh E. S. and Rohrer R. A., *Theory of linear active networks*, Holden-Day, (1967).

[3.24] Tilmans H.A.C., Micro-mechanical sensors using encapsulated built-in resonant strain gauges, *PhD Thesis*, University of Twente, Enschede, The Netherlands, (1993).

[3.25] Wellstead P. E., *Introduction to physical system modelling*, Academic Press, New York, (1979).

[3.26] Mason W. P., *Electromechanical transducers and wave filters*, second edition, Van Nostrand, New York, (1948).

[3.27] Savant Jr., C. J., Roden M. S. and Carpenter C., *Electronic design circuits and systems*, second edition, Benjamin Cummings Inc, (1987).

[3.28] Berlincourt D. A., Curran D. R. and Jaffe H., *Piezoelectric and Piezomagnetic materials and their function in transducers,* in *Physical acoustics*, Mason W. P. (ed), Vol. 1. Pt. A, Academic press, New York, 1964.

[3.29] van Mullem C. J., Tilmans H. A. C., Mouthaan A. J. and Fluitman J. H. J., Electrical cross-talk in two-port resonators - the resonant silicon force beam sensor, *Sensors and Actuators*, A31 (1992) 168-173.

Contents

4. Fabrication details

Chapter 4

Fabrication details

The objectives of this chapter are to introduce the technique of micromachining and to show how this technology can be used produce the lateral resonant pressure sensor described in this thesis. At the beginning of this chapter. the importance of material strain, stiction, and dry etching in the production of surface micromachined structures is discussed. The structure, mounting and encapsulation of the lateral resonant pressure sensor are then presented. A detailed description of the fabrication of the pressure sensor is then given, and a number of processed resonators and microstructures are shown. Finally, an estimation is made of the Young's modulus and residual strain of the polysilicon lateral resonator.

4.1 Micromachining

It was in the mid to late 1970's that the idea to use microelectronic fabrication techniques to produce functional 3-D microstructures from single crystal silicon (SCS) and other materials was first promulgated. Perhaps the first device to be produced using this new technology was a piezoresistive diaphragm pressure sensor [4.1], although other interesting devices, such as silicon accelerometers, were also being developed at the same time [4.2]. The technology of micromachining developed from the microelectronics industry where the essentially 2-D fabrication techniques and processes, e.g., thin film deposition, micro-lithography and wet/dry etching, were adopted to make a range of silicon micromechanical components, e.g., diaphragms, simple bridges and cantilevers.

One of the strengths of micromachining is that it retains all the benefits of the physical and chemical processes of microelectronics, namely, precise control of material composition and structure, precise dimensional control and batch production techniques,

the latter of which can lead to low cost devices [4.3-4.9]. In point of fact, SCS is a material ideally suited for use in micromechanical devices; it is a high precision, high strength, highly reliable material available at a relatively low cost. A further benefit of silicon technology is the ability to produce an integrated smart sensor. Such as sensor may be realised by integrating the micromechanical transducer and signal conditioning electronics and microprocessor on the same chip, providing the fabrication process of the mechanical and electrical elements are mutually compatible. Aside from other single crystal materials such as quartz [4.10], gallium arsenide and diamond, a variety of thin films are used in micromachining. A complete list would be exhaustive, but some primary materials include Si, SiO_2, Si_3N_4, ZnO, Al and Cr.

Today there are many different fabrication techniques used in micromachining. The term *bulk micromachining* is used to describe a set of processes that are based on the etching and bonding of SCS. Examples of these processes include: wet anisotropic etching, boron/electrochemical etch-stops, complex corner compensation [4.8,4.9], silicon fusion bonding, deep reactive ion-etching [4.11] and laser ablation. *Surface micromachining* on the other hand, utilises the deposition and selective etching of thin films to form a free-standing microstructure, such as a diaphragm, cantilever or clamped-clamped beam on the surface of a (SCS) wafer. The term sacrificial layer is used as this layer is etched away, or sacrificed, to leave a free-standing structure. According to Benecke [4.3], this technique was first demonstrated in the 1960's by H. C. Natheson using thin metal films. In the early 1980's the technique was further developed by Howe [4.12], who fabricated free-standing cantilevers by the removal of a silicon dioxide layer from beneath a structural polysilicon layer.

The advantage of surface micromachining is that it is not restricted by crystal orientation and the microstructures are assembled by virtue of the fabrication process. Hence, by depositing and etching multiple structural and sacrificial layers it is possible to fabricate complex microstructures, such as sealed cavities, gears, pinions and electrostatic motors. [4.13-4.15]. The disadvantage of surface micromachining is that it is only practical to produce structures that are few microns in thickness, and therefore not truly 3-dimensional. With the exception of diaphragms and similar inherently flat structures, this can limit the performance of devices. In particular the operation of electrostatic micromotors, x-y stages, microgrippers, and other actuators is limited as they are unable to produce large, and therefore useful, forces or displacements at low voltages (< 20 V).

4.2 Materials and processing

Currently, most surface micromachined structures are produced using a structural polysilicon layer, a sacrificial oxide layer and a silicon nitride passivation/insulation layer. These materials are used because they are both IC compatible and their material characteristics are well understood [4.13-4.19].

A central question for the design of surface micromachined structures is the mechanical properties, such as surface texture and residual strain, of the thin films laid down, especially polysilicon. Residual strain is particularly important as a constrained microstructure will buckle under excessive compressive strain or crack under high tension. Also, a strain gradient through the microstructure will also cause a deflection towards or away from the substrate, depending on the direction of the strain gradient. Generally, the optimum is a low tensile strain because this allows large flat microstructures to be realised. A further well known problem in the production of surface micromachined devices is that of stiction, the collapse and bonding of the microstructure to the substrate during, or after, processing. Of equal importance is the selection of the dry etch process to give the ability to control the side-wall profile of the microstructure and also to obtain a uniform feature width across the process wafer.

4.2.1 Polysilicon

Thin ($\leq 5\mu m$) LPCVD silicon films are usually grown by the pyrolysis (thermal decomposition) of silane (SiH_4) at a temperature between $570\,^o$C and $650\,^o$C and a pressure of between 200 mTorr to 500 mTorr [4.20,4.21]. Silicon films deposited in the amorphous or polycrystalline phase always exhibit a residual strain, typically between zero and -6 $\times 10^{-3}$ ε [4.22,4.23]. Low strain, fine grained, polysilicon is attained by depositing amorphous, or partly amorphous and partly polycrystalline silicon, and annealing the film at a high temperature to facilitate crystal growth. The magnitude and sign (i.e. compressive or tensile) of the residual strain in the crystallised silicon film is dependent on the morphology of the as-deposited layer, doping, and the annealing process. As-deposited amorphous silicon typically possesses a residual strain of $+2 \times 10^{-4}$ ε (tensile) after annealing at a temperature above $800\,^o$C [4.24], although prolonged treatment at $600\,^o$C is also feasible [4.23]. Residual strain in partly amorphous and partly polycrystalline silicon is of the same magnitude but may be either compressive

or tensile, depending on the ratio of the two phases after initial deposition [4.20]. The mechanism governing the magnitude and sign of the residual strain after the anneal is a result of crystal growth and re-ordering of defective regions and the reader is referred to the literature above and the following references for further detailed explanation [4.25,4.26].

4.2.2 Silicon oxide and silicon nitride

Silicon oxide is often used as a sacrificial layer as it is etched rapidly in hydrofluoric acid (HF), while (poly)silicon remains essentially untouched. Phosphorous silicate glass (PSG), or borosilicate glass (BSG) are also used to obtain increased etch rates or for profile control of the polysilicon [4.27,4.28]. Silicon nitride is extensively used in (surface) micromachining because it provides a good passivation and electrical/thermal insulation layer and also etches very slowly in HF (≈ 6 nm/minute).

A further point is that in the lateral resonant pressure sensor design, a high residual strain in the oxide or nitride layers will cause the diaphragm to deform during processing. Stoichimetric Si_3N_4 has a strong tensile stress which becomes compressive for silicon rich films and thus the residual strain of LPCVD Si_3N_4 is easily controlled by adjusting the silicon content. Low strain silicon nitride typically exhibits a strain of $\approx 1 \times 10^{-3}$ ε. The residual strain of silicon oxide varies according to the deposition method. Thermal oxide typically has a high residual stress of $\approx 3 \times 10^8$ N/m^2, whereas plasma enhanced chemical vapour deposition (PECVD) oxide has a lower residual stress and both a reasonable uniformity and deposition rate [4.29]. Thus PECVD oxide is preferrable to thermal oxide for the fabrication of the resonant pressure sensor.

4.2.3 Stiction

A well known necessity of surface micromachining is the need to use a specialised process to prevent the adhesion, or stiction, of the microstructure and substrate after the sacrificial layer is removed. Without such a process capillary forces created between the microstructure and substrate during evaporative drying can cause the microstructure to collapse [4.30]. If the elastic restoring force of the deformed microstructure (which is a function of the device dimensions) cannot overcome the adhesion energy of the interface then the microstructure remains permanently bonded to the substrate. The bonding mechanism is thought to be due to either etch residues, electrostatic forces or van der

Waals forces [4.31]. Release related stiction is commonly avoided by freeze drying [4.32], critical point drying [4.33], the use of temporary polymer/mechanical supports or by vapour HF etching [4.34]. Alternatively, by reducing the contact area with *stand off dimples* [4.16] or by surface roughening techniques the adhesion energy of the interface may be reduced and permanent bonding avoided [4.35]. Even after release stiction can still occur if the microstructure and substrate contact, e.g., as a result of high acceleration (shock), static charge or levitation effects. After initial contact condensation on the hydrophilic native oxide is thought to precipitate capillary action that pulls the microstructure down. Post-release stiction can be discouraged by attaining a hydrophobic surface, e.g., by chemical treatment [4.36] or by the deposition of a passivating layer, e.g. fluorocarbon [4.37].

4.2.4 Anisotropic dry etching of (poly)silicon

Dry etching plays an important role in the manufacture of micromechanical devices and modern integrated circuits. The advantages of dry etching are that some variants offer fine line definition, good selectivity[1], are highly directional (i.e. they exhibit an anisotropic etching characteristic) and not limited by crystal orientation, as with anisotropic wet enchants. Mask adhesion problems and the chemical hazards and waste treatment often inherent with wet chemical etching are also avoided or reduced. [4.37-4.42].

Dry etching can proceed by four basic mechanisms, *viz.*, physical etching (sputtering), chemical reaction, ion-assisted chemical mechanisms and photo-chemical mechanisms. The advantages of ion assisted chemical etching, commonly referred to as reactive ion etching (RIE) are that it offers excellent profile control, high etch rates and high selectivity. RIE is a synergistic process combining the physical process of ion beam etching (IBE) with reactive chemical (plasma) etching, (PE). RIE can occur by one of three mechanisms, *viz.*, chemically enhanced physical sputtering (i.e. chemically weakened bonds facilitate physical sputtering), ion-enhanced chemical reaction (ion induced surface damage precipitates the reaction between the material and reactive species) or chemical sputtering (ion bombardment provides energy to drive chemical reactions). An RIE process exhibits high selectivity due to the chemical nature of the

---

[1] Selectivity is defined as the ratio of etch rates between two materials.

etching and anisotropic feature profiles due to the directional ion bombardment [4.43,4.44].

The last mechanism usually involves the use of a passivation layer, and is referred to as inhibitor controlled RIE. During etching, vertical side-walls are protected from the active species with a passivation, or inhibitor layer. Directional ion bombardment removes the inhibitor from exposed horizontal surfaces, allowing active species to chemically attack, and etch, the exposed material. By varying the plasma chemistry, and thus the rate of passivation, vertical, positively tapered and even negatively tapered anisotropic etch profiles are possible. The passivation layer is usually introduced into the plasma via a polymer precursor or oxidising agent. Passivation may also be achieved by cryogenically freezing the volatile silicon reaction products and radicals onto the exposed material [4.45].

Recently there has been an increasing interest in inhibitor controlled RIE of silicon microstructures using a silicon hexafluoride/oxygen (SF_6/O_2) plasma. This is because it provides high etch rates (up to 5 µm/min), controllable etch profiles and good selectivity. It is also favoured over other halogen gasses, e.g. chlorine and bromine, as the latter are particularly hazardous and special operating precautions are needed. [4.46,4.47]. The mechanics of this dry etching process is somewhat complex and further explanation is warranted, not least because the same etch chemistry may be used for the deep reactive ion etching of SCS (see chapter 6).

Gas chemistry and etch mechanism in an SF_6/O_2 plasma

In an SF_6/O_2 gas plasma, exposed silicon is chemically etched (isotropically) by F* radicals forming volatile reaction products, which are removed by the vacuum pumping system. The introduction of oxygen into the plasma provides a source of O* radicals which passivate the silicon surface with a siliconoxyflouride (SiO_xF_y) inhibitor layer. Anisotropic (vertical) profiles are attained when there is a balance between passivation, chemical etching and ion bombardment. In practice the optimum etch chemistry is best determined using the *Black Silicon Method* developed by H. Jansen [4.46]. The preferred pressure, power and SF_6 flow rate is set and the oxygen content gradually increased until the silicon sample appears black or grey. The apparent change in colour of the surface is due to the formation of silicon microspikes (or grass) that have a length which exceeds the wavelength of visible radiation and so absorb, or

partially reflect, the incoming light. From this point the gas chemistry is tuned i.e. by altering gas flow rates, pressure and power, so that the etch proceeds with a slightly negative undercut, preventing the formation of micro-spikes, and giving near vertical side-walls. For a detailed discussion on the mechanics of the etching process the reader is referred to the following references: Jansen [4.46], Pinto [4.47], Parrens [4.48], Syau [4.49], Light [4.50], and Meith [4.51].

Selectivity and loading

When reactive ion etching (poly)silicon on (sacrifical) silicon oxide it is important to consider the material selectivity, mask selectivity and loading of the etch chamber. Photoresist masks are well established and their application is straightforward but they usually suffer from poor selectivity when compared to other masking materials, e.g., silicon oxide and chromium. For example, the selectivity of a photoresist mask in an optimised SF_6/O_2 plasma is approximately 10, whereas a chromium mask would have an almost infinite selectivity. Photoresist is etched by the oxygen and fluorine radicals present in a SF_6/O_2 plasma at a rate that increases strongly with temperature. Wafer heating can be significant (up to 200 ^{o}C) when etching silicon in an SF_6/O_2 plasma because the etching process is exothermic. Hence, to attain a high mask selectivity it is necessary to minimise wafer heating. Temperature control may be achieved by introducing a cooling gas (e.g. helium) into the gas mixture or, more simply, by cooling the cathode and ensuring good thermal contact between the wafer and anode (by physical clamping and/or the use of a thermally conductive layer, such as vacuum grease). Photoresist is still removed, however, by ion impact, which may be reduced by re-tuning the plasma to lower the d.c. bias (and thus ion energy) [4.52].

When trying to attain fine line widths in (poly)silicon on oxide films it is important to achieve a uniform etch rate across the wafer. The uniformity of the etch rate is dependent on a number of variables the most important being the gas flow, which is usually optimised for a particular reactor geometry. A further variable to consider is the relative reactivity of the wafer with respect to the electrode material. When the electrode is inert there is a higher concentration of active species at the wafer edge than in the centre, where the active species are consumed by the reaction process, see Figure 4.1. Under these conditions the etch rate will be higher at the wafer edge than in the centre and this results in a 'bulls eye effect'. The variation in etch rate across the wafer is

especially important when etching thin (< 5 µm) (poly)silicon film on oxide in an SF_6/O_2 plasma because the selectivity between the two materials is high. As the etch front reaches the oxide layer the micro-loading, that is to say the area of exposed silicon, drops significantly and the fluorine radicals etch (isotropically) the remaining silicon at an increased rate. Since the etch rate increases in direct proportion to the area reduction the remaining features defined by the mask are rapidly undercut.

To alleviate this problem, the non-uniformity in the etch rate over the wafer is usually reduced by using a cathode that absorbs fluorine radicals (such as a 6" silicon wafer). This has the effect of reducing the variation in active species concentration at the wafer edge, so that a more uniform etch rate is obtained across the wafer. The increased loading also reduces the silicon etch rate (in direct proportion to the increased area of silicon) as less fluorine radicals are available per unit area to etch the silicon. Although a reduction in etch rate is not usually a problem, it is difficult to obtain a perfectly uniform etch rate so that the problems associated with micro-loading still exist. The exact etch time is therefore quite critical and can usually be determined by visual observation.
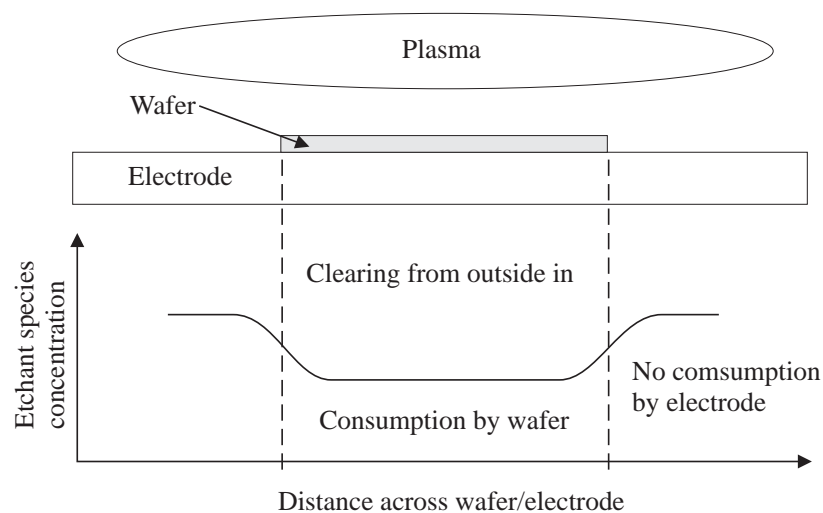
Figure 4.1. Variation in active species concentration in etch chamber with inert electrode.

4.3 Resonant pressure sensor design

As Figure 4.2 shows, the resonant pressure sensor is designed to be assembled

from 3 components, the transduction element[2], an encapsulation chip and a mounting header. The complete assembly is supported by a glass tube which is itself attached to the header chip. Encapsulation of the resonator is necessary primarily to allow operation in vacuum, and so an increased Q-factor, but also serves to protect the resonator from the environment, e.g. condensation, dust, and corrosive elements.

Vacuum encapsulation of resonant (pressure) sensors is traditionally achieved by bonding a cover chip over the resonator and diaphragm and evacuating the chamber created [4.53]. In a more recent technique, the resonator is encapsulated during the fabrication process, using an integrated polysilicon cap and a technique known as reactive sealing [4.54,4.55]. The pressure sensor described in this thesis is designed to be encapsulated using a separate cover chip, which is bonded onto the tranduction element with a glass frit. A separate cover chip is employed because the use of an integrated polysilicon cap and reactive sealing technique greatly increases the processing effort. There are, however, two advantages of this latter method that deserve a mention. The first is that it enables the sensor to measure a differential pressure because the evacuated cavity only covers the resonator itself, and not the complete diaphragm. The second is that the level of spurious strain induced by the cap is minimised as there is no mechanical bonding process involved, and so the stability of the sensor is improved. Furthermore, temperature induced strain in a totally silicon device is likely to be lower than in other devices where dissimilar materials, possessing different thermal coefficients of expansion are employed.

---

[2] To avoid confusion the *transduction element* is defined as the diaphragm and resonator, whereas the pressure sensor refers to all three components shown in Figure 4.2.
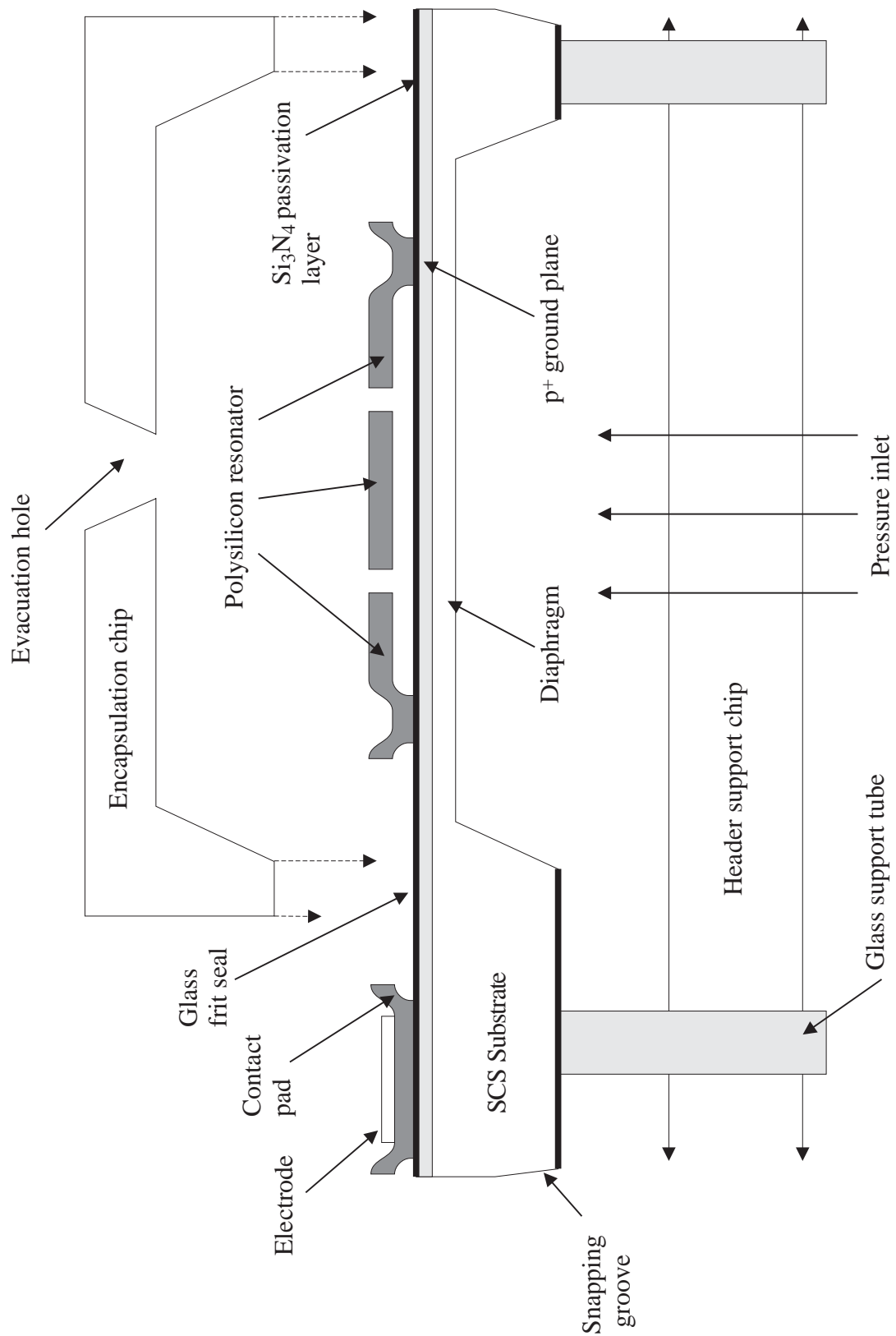
Figure 4.2 Cross section of the lateral resonant pressure sensor showing resonator, diaphragm, encapsulation chip and mounting header (not to scale).

Electrical connection to the resonator is achieved via wire bonding pads and conducting tracks. The bonding pads are located at the edge of the chip (outside the cavity) to reduce the effect of spurious strain induced at the wire-bond/silicon interface on the resonator, see Figure 4.2. The glass frit seal used to bond the encapsulation chip is designed to allow the electrical tracks to be fed-through to the contact pads without reducing the integrity of the vacuum inside the cavity. To operate the resonator in the intrinsic damping region, (see Chapter 2), the cavity pressure must be held below about 1 Pa for the lifetime of the resonator [4.56]. The cavity is evacuated through the glass tube, which is then sealed. If a reliable seal is obtained between the encapsulation chip and substrate then the only source of gaseous products is via de-gassing of the silicon cavity and glass frit seal.

4.4 Pressure sensor fabrication

The process used to fabricate the transduction element with the layer structure shown in Figure 4.2 required five photolithographic masks. These masks were designed using L-EDIT™ (Tanner Tools Ltd.) and produced by Compugraphics International Ltd. The encapsulation chip (supplied by Druck Ltd.) shown in Figure 4.2 was fabricated using a simple double sided KOH etch process.

4.4.1 Mask geometry

A number of resonator designs, test structures and resonator geometries were integrated onto a 3" silicon wafer. The masks were designed to allow some flexibilty in the fabrication process. For example, by using only three of the five masks it was possible to reduce the process effort and attain a planar layer structure, so avoiding potential thin film step coverage problems.

The standard chip configuration consisted of a single resonator and diaphragm element, see Figure 4.3. Other geometries included reference resonators (for calibration) and dual diaphragm configurations to allow differential pressure measurement. The lateral resonators all employed interdigitised comb capacitors to enable electrostatic excitation/capacitive detection. Some resonators also possessed integrated piezoresistive pickups, as described in section 3.2 of Chapter 3. Each resonator design was characterised by the capacitance of the interdigitised comb capacitor employed and the minimum feature width. High specification devices had a minimum feature width of 3 µm and

possessed an estimated static comb capacitance of $\approx$ 10 fF, while low specification devices had a minimum 6 µm feature size and an estimated static comb capacitance of $\approx$ 2.4 fF. All the resonators were supported by hammock type flexures of 150 µm in length, apart from the linear resonator design that employed two folded-flexures consisting of 100 µm long trusses. To minimise the sacrificial etch time small (≈ 5 µm^2) etch windows were integrated into the inertial mass of each resonator to expose the underlying oxide to the sacrificial etchant.
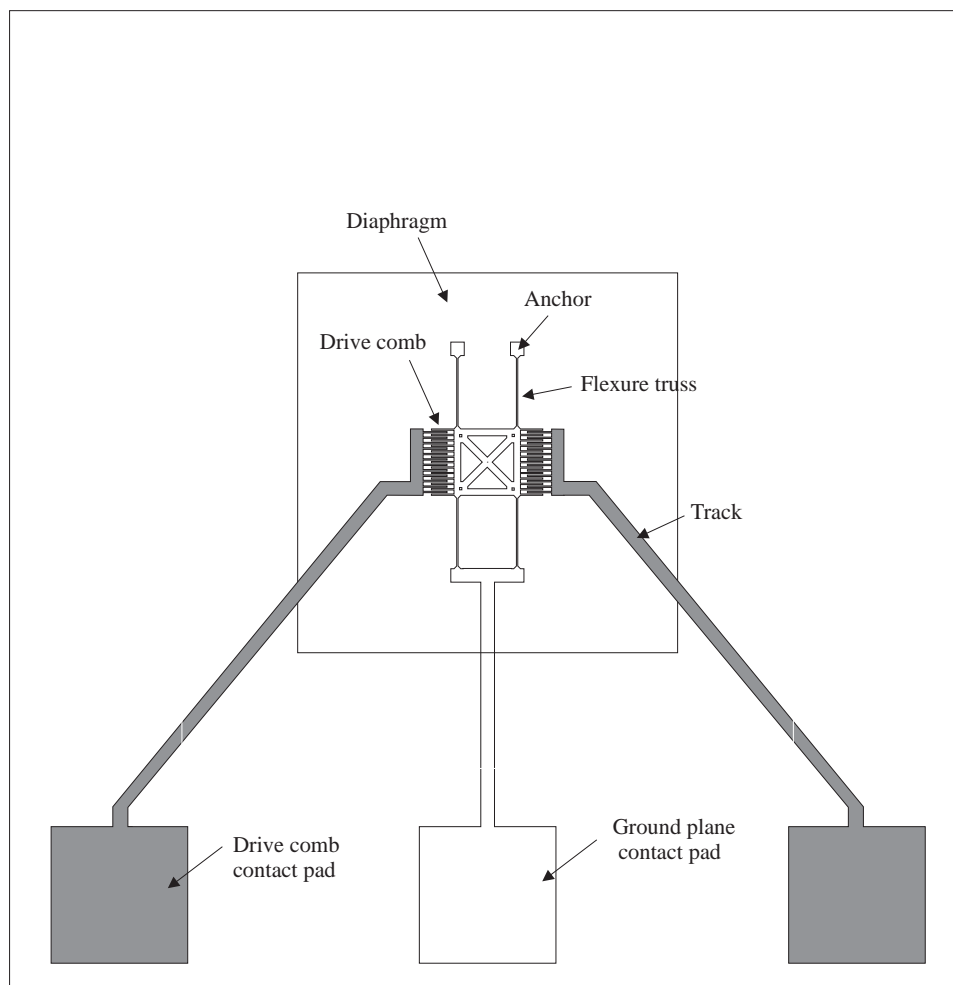
Figure 4.3 Scale plan-view of 5 mm^2 pressure sensor chip, showing diaphragm, lateral resonator, conductive connecting track and contact pads.

Several *drop in* test chips were also included in the mask design to characterise the process and material properties. These chips consisted of folded-flexure type resonators, cantilevers and clamped-clamped bridges, passive micro-strain gauges and

sacrificial lift off structures. The wafer was designed to break into individual chips of size 5 mm^2 with the aid of snapping grooves etched into the back-side.

4.4.2 Process sequence

The pressure sensors were fabricated by the author at The University of Twente, The Netherlands, using 3" 380 µm thick, double-sided-polished *p*-type $\langle 100 \rangle$ substrates. In total approximately fifteen 3" silicon wafers were processed, from which ten usable wafers were procured. The other wafers broke during fabrication or were discarded due to poor processing.

Before processing, the wafers were marked and the curvature and the thickness variation measured. The process began with an ultrasonic clean, to remove solid particulate matter from the wafers, followed by a standard cleaning process to remove organic contaminants.

After cleaning, the native oxide was removed from the wafers with an HF dip (60 s) and a ground plane formed by a standard front-side solid source boron diffusion at 1150 ^{o}C. Next, a 250 nm layer of LPCVD low stress (silicon rich) nitride was grown as an insulation layer (front-side) and anisotropic etch mask (back-side), see Figure 4.4a. Prior to deposition an HF dip was necessary to remove native oxide. The back-side nitride was patterned with a photoresist mask (mask DI) to define the diaphragms and snapping grooves, and dry etched in a CHF_3/O_2 plasma. Before the dry etch additional photoresist was manually applied to the wafer edge. This prevented handling marks being transferred into the nitride mask and then subsequently being etched into micro cracks (that weakened the wafer) by the anisotropic etchant. After plasma ashing the photoresist mask (removing the photoresist in an oxygen plasma at high temperature) the diaphragms and snapping grooves were etched in a solution of KOH (500 g) and de-ionised water (1500 *l*) at 72 ^{O}C. A pre-etch HF dip was required to remove native oxide that would have otherwise impeded the etch process. A timed etch stop was used to achieve a diaphragm thickness of about 20 µm, see Figure 4.4b. As the timed etch-stop technique was relatively inaccurate (due to variations in wafer thickness and etch rate) it was necessary to measure the exact etch rate and adjust the etch time for each wafer (by as little as 2 minutes over a period of 6 hours).

Following the timed anisotropic KOH etch, the residual potassium ions were removed with a 5:1:1 solution of H_2O: H_2SO_4: H_2O_2 to prevent contamination of the

processing line. Next, the front-side was patterned with a photoresist (mask ON) and then electrical contact windows etched through the nitride with a CHF_3/O_2 plasma. The mask was aligned with the backside alignment marks using double-sided wafer alignment. Plasma ashing was used to remove the photoresist mask. A 2 µm sacrificial oxide layer was then grown by PECVD from a mixture of 2% SiH_4 (in N_2) and N_2O. The oxide layer was densified for 30 minutes in N_2 at 800 °C to de-gas hydrogen and improve the thermal stability. Flexure and contact pad anchor windows were then defined in a photoresist mask (mask SA) etched in the oxide using BHF, see Figure 4.4c.

After further cleaning, a 2 µm layer of amorphous silicon was grown by pyrolising silane at a temperature of 590 °C and a pressure of 250 mTorr. To ensure good mechanical and electrical contact of the silicon layer the wafers were given a pre-deposition HF dip (60 s) to remove the native oxide. To create a dopant source, a borosilicate glass (BSG) oxide sandwich was grown by atmospheric pressure chemical vapour deposition (APCVD) onto the silicon. The BSG/oxide sandwich was densified at 650 °C for 30 minutes and the wafer annealed at 1000 °C for 1 hour in a nitrogen ambient. During the anneal low stress polysilicon was formed via crystal growth in the amorphous silicon (see section 4.2.1) and, at the same time, the layer was doped as boron atoms diffused from the BSG, see Figure 4.4d. Following the anneal the BSG/oxide dopant layer was removed with HF.

Before etching the polysilicon the wafer was given an HF dip and a chromium (10 nm) gold (150 nm) sandwich was deposited onto a lift off mask (mask AL) by resistive evaporation. The lift-off mask was removed with acetone (by gentle rinsing) leaving a metal electrode on the contact pads[3]. The polysilicon resonator, tracks and contact pads were then defined with photoresist (mask PO) and dry etched in an SF_6/O_2 plasma, see Figure 4.4e. For the plasma chemistry detailed in Appendix 1 the optimum etch time was about 9 minutes. Typically an over etch time of 30 s or more led to a feature undercut of $\approx$ 0.5 µm.

The final step in the fabrication the process was to free the microstructures by etching the sacrificial oxide layer with 25 % HF for 29 minutes. The etch front was monitored with an optical microscope focused through the polysilicon. To help determine the sacrificial etch time test structures were also used that detached from the wafer when

---

[3] Note that if contact electrodes are not required then this stage can be omitted

fully undercut, see Figure 4.13. Normal evaporative drying of the microstructures at this stages would have resulted in the collapse and bonding of microstructure to the substrate, as described in section 4.2.3. To prevent stiction of the resonator to the substrate, the wafers were freeze dried with cyclohexane. First, the HF/DIW solution was diluted until its pH was neutral. The excess water was then removed and isopropanol alcohol (IPA) added to the solution. This allowed the wafer to be safely removed from the etch container and repeatedly rinsed in IPA and then cyclohexane. The wafer was then freeze dried at -10 ^{o}C in a nitrogen ambient for at least 30 minutes, or until all the solid cyclohexane had sublimed, see Figure 4.4f.

After doping, the resistivity of the polysilicon was measured to be 180 Ω/ during a test run, but the final devices exhibited a value of 260 kΩ/ , leading to a high 13 MΩ track resistance. Several explanations for the high resistance are possible, such as a poor gas supply or incomplete removal of the native oxide before deposition of the BSG/oxide sandwich. To overcome the problem a thin (40 nm) layer of aluminium was deposited onto the wafer. Aluminium was chosen as it possesses a low residual strain, compared to other possible metallic conductors, e.g. chromium. Generally, achieving electrical conduction by this method is undesirable as it is known to result in a reduced Q-factor (see Chapter 5) and increases the temperature sensitivity of the resonator.

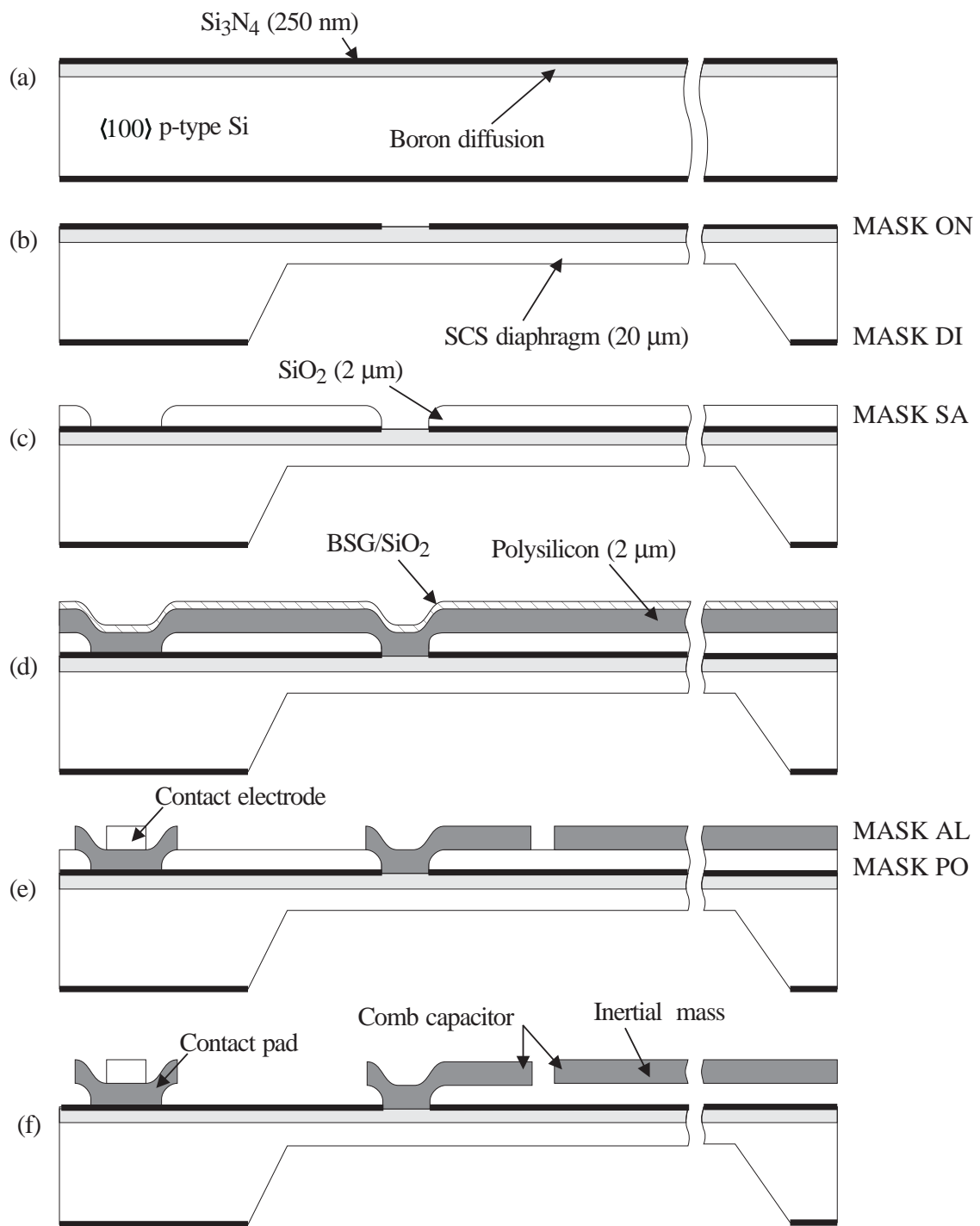The reader is also referred to Appendix 1 for a detailed listing of the process flow and equipment used.

(a) Si$_3$N$_4$ (250 nm)

⟨100⟩ p-type Si

Boron diffusion

(b) MASK ON

SCS diaphragm (20 μm)

MASK DI

SiO$_2$ (2 μm)

(c) MASK SA

BSG/SiO$_2$ Polysilicon (2 μm)

(d)

Contact electrode

(e) MASK AL

MASK PO

Comb capacitor   Inertial mass

Contact pad

(f)

Figure 4.4 Fabrication sequence for lateral resonant pressure sensor: a) boron diffusion and LPCVD Si$_3$N$_4$, b) etch SCS diaphragm, c) PECVD SiO$_2$ and photo-engrave, d), LPCVD silicon, APCVD BSG/SiO$_2$ and anneal, e) strip BSG/SiO$_2$, define contact electrodes using lift-off technique and photo-engrave polysilicon, and f) sacrificial etch and freeze dry to leave free-standing resonator.

As has been noted, one of the strengths of micromachining is that the production process provides some degree of flexibility. Consequently, it was possible to fabricate the resonator and diaphragm using only three of the five photolithographic masks. Here, the front-side nitride and oxide were not photo-engraved. This led to a reduced process effort and to a more planar layer structure where the resonator anchors, contact pads and tracks were supported by oxide pedestals, see Figure 4.5. (In fact the number of masks could be further reduced to two, if contact pad electrodes are not required.)
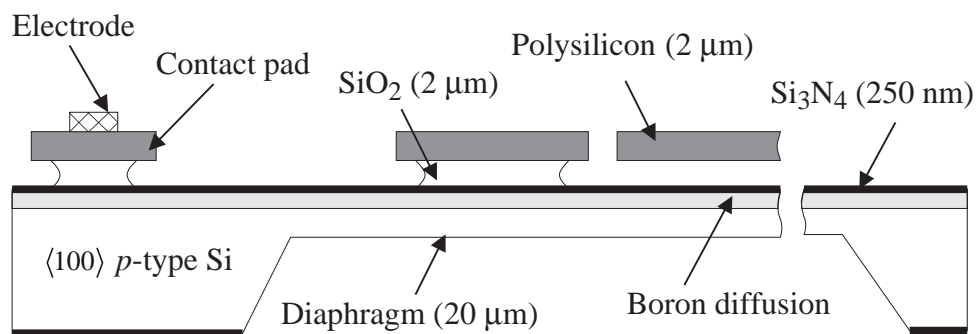
Figure 4.5 Layer structure obtained with a three mask process.

The size of the pedestals was determined by the sacrificial etch time and geometry of the mask used to define the resonator, tracks and contact pads (mask PO). The mask was designed so that the resonator was fully undercut before the contact pads, tracks and resonator anchors. As there are no step-up limitations with layer structure the thickness of sacrificial layer may, theoretically, be increased, which offers several advantages. Firstly, an increased pedestal height leads to a higher sensitivity as the strain applied to the resonator by the rotational deformation of the diaphragm increases. Secondly, the induced levitation force on the structures as a result of charge imaging on the ground plane is reduced and, thirdly, the air damping coefficient is reduced, although this is less relevant as the resonator is designed to operate in a vacuum. One drawback of this layer structure is that the electrical design is limited because the resonator is insulated from the substrate. Furthermore, the area of the resonator anchors must be increased to prevent their premature detachment. PECVD oxide layers are also limited in thickness to about 4 μm, not only because of the extended deposition time required, but also because the increased residual strain in the oxide film causes cracks to appear [4.29].

4.5 Fabrication results

The scanning electron micrographs shown in Figure 4.6 through to Figure 4.10 show four different resonator designs, based upon 3 μm feature widths. Figure 4.11 shows an infrared photograph of a lateral resonator, conductive tracks and diaphragm. An array of free standing 3 μm wide clamped-clamped beams used to characterise the fabrication process is shown in Figure 4.12. Figure 4.13 shows the lift-off structures used as an aid in determining the sacrificial etch time. These structures were freed from the substrate when fully undercut and, as can be seen from Figure 4.13 were washed away from their anchor points by the etch solution.

After processing, only 5 - 10 % of the lateral resonators fabricated using all five photolithographic masks were found to be stuck down. This suggests that the processing envelope can be expanded to give a longer flexure, hence a lower flexure spring rate and an increased sensitivity, see section 2.5 of chapter 2. However, many of the resonators and conductive tracks processed using the three mask process detached from the substrate. This was because the mask design did not allow sufficient margin for variation in sacrificial etch rate, either locally across a single wafer or between several wafers in a batch. Hence, whilst some flexure anchors remained attached to the substrate others were fully undercut. Further processing, using a comprehensive array of test structures, would enable the full scope of the fabrication envelope to be determined and so allow the design of the lateral resonator to be optimised.
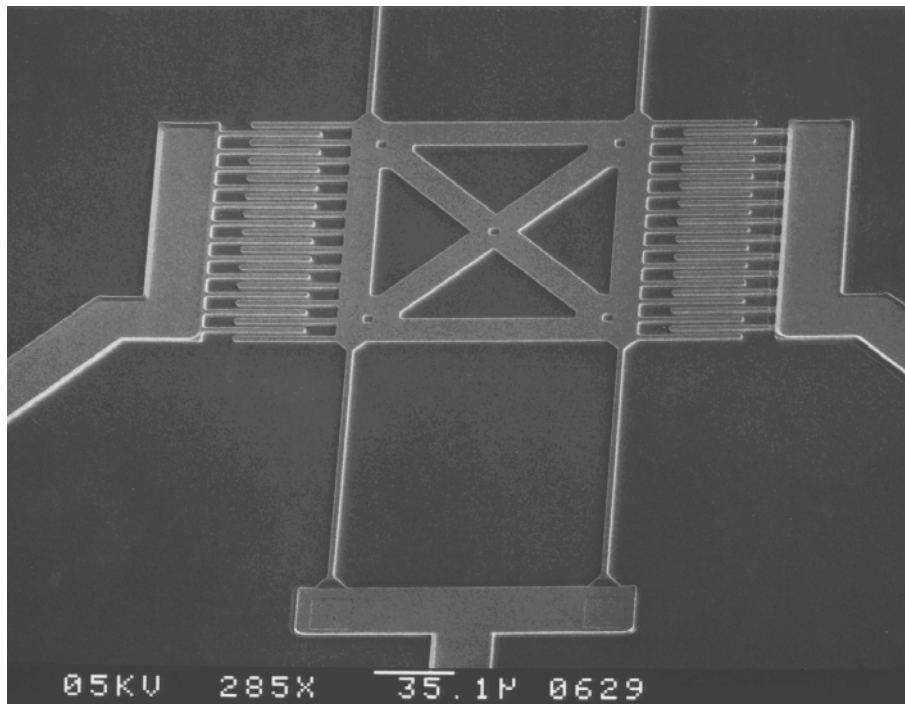
Figure 4.6 SEM of the lateral resonator showing the shuttle mass, hammock flexure and 25 plate comb capacitors.
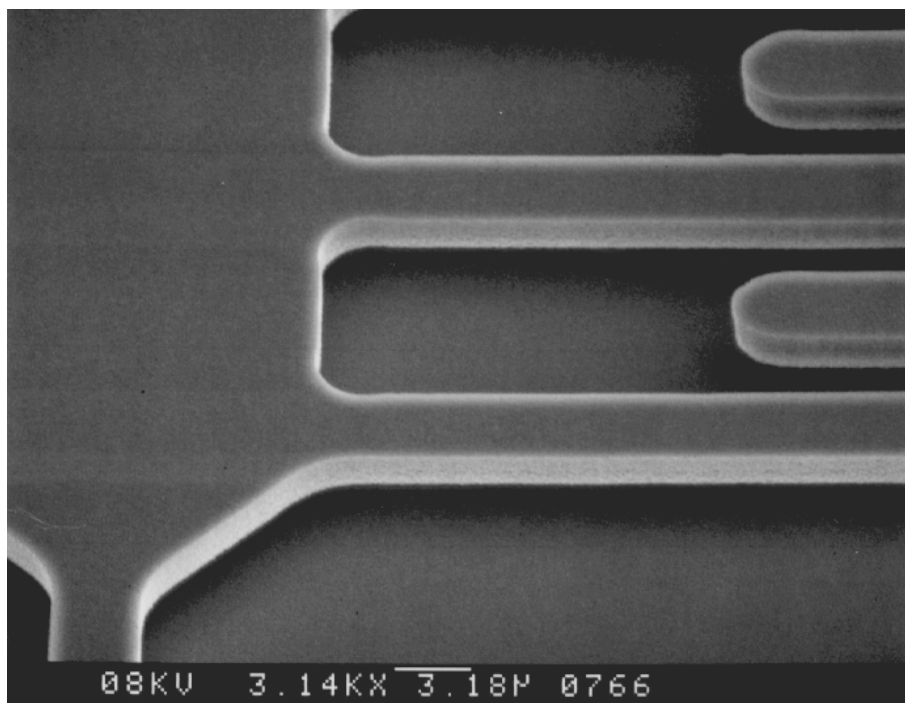

Figure 4.7 SEM showing a close up of the shuttle mass. suspended above the substrate by the flexure, and comb capacitor fingers.
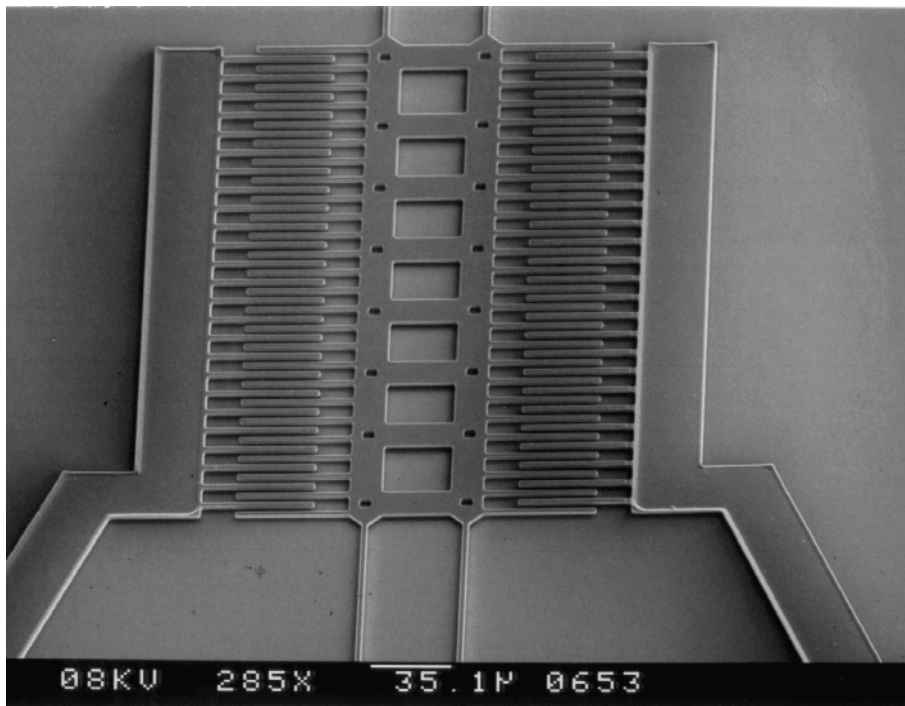
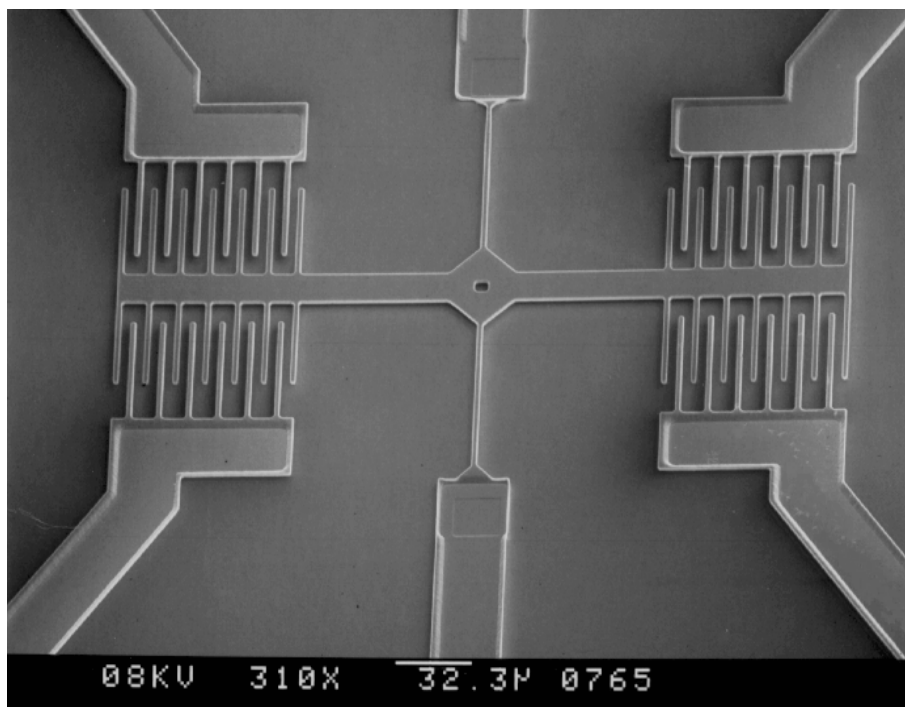*Figure 4.8 SEM of a lateral resonator employing 51 plate comb capacitors.*

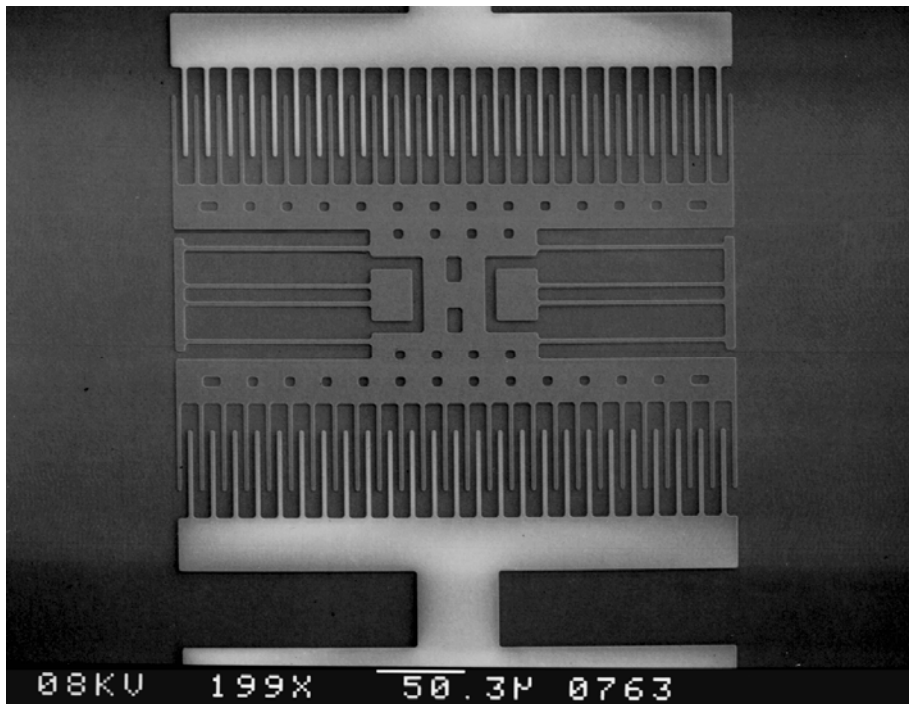*Figure 4.9 SEM showing a rotary type resonator employing 4 comb capacitors and a simple beam supporting flexure.*

Figure 4.10 SEM showing lateral a resonator formed from two folded flexures and two 51 plate comb capacitors. Note that this resonator is 'stuck down' to the substrate.
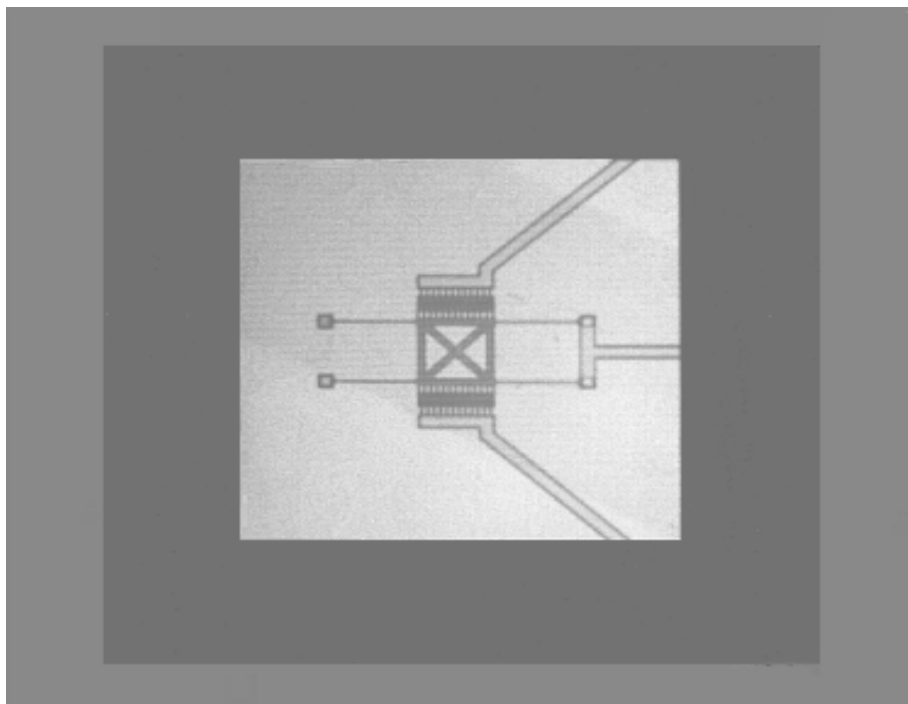
Figure 4.11 Infrared transmission photograph of lateral resonant strain gauge mounted centrally upon a SCS diaphragm.
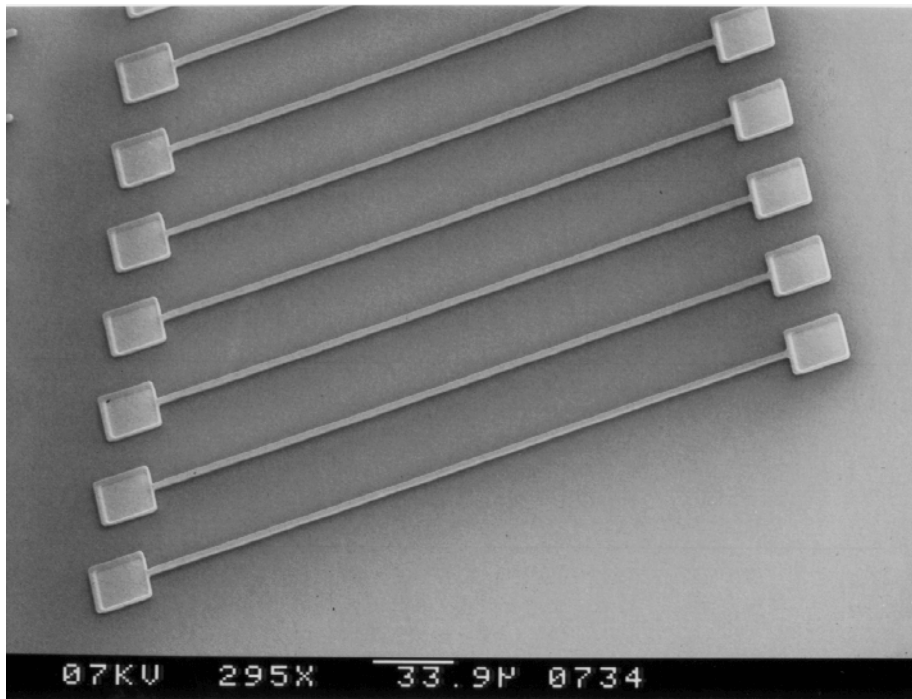
Figure 4.12 SEM showing array of free standing 3 µm wide clamped-clamped beams, the longest of which is 300 µm in length.
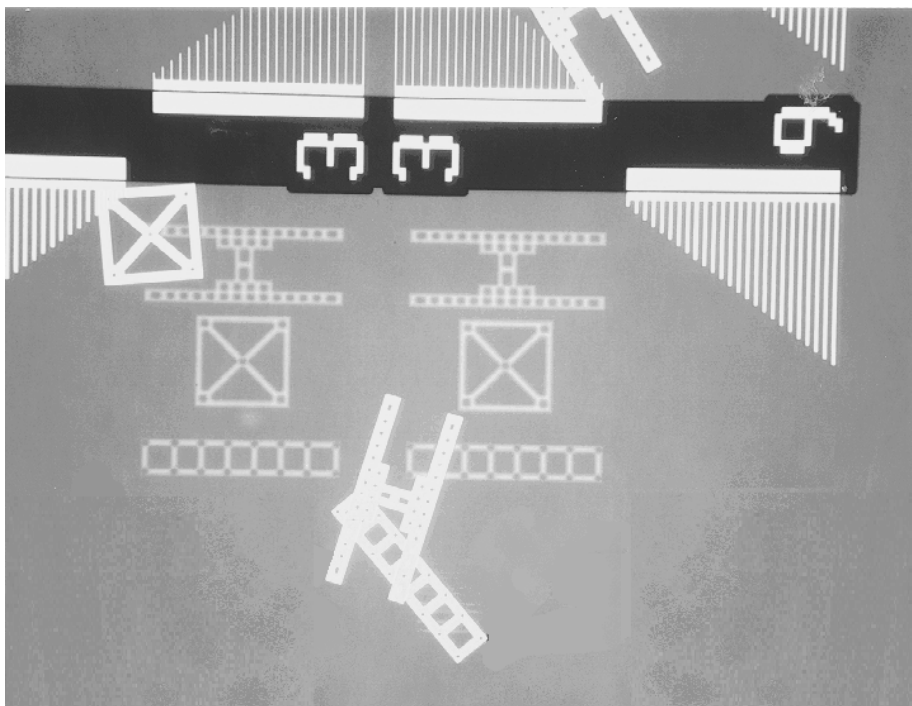

Figure 4.13 Photograph showing lift-off microstructures and cantilevers. The lift-off structures are released from the substrate when the sacrificial oxide has been etched.

4.6 **Material characterisation**

When designing a microstructure, e.g. a lateral resonator, two material properties that are of interest to the designer are the residual strain and Young's modulus of the polysilicon from which the microstructure is fabricated. For example, the resonant frequency of the lateral resonant strain gauge is determined by both the Young's modulus and the residual strain of the polysilicon. As with most thin films used in the semiconductor industry, the material properties and morphology of structural polysilicon are determined by the deposition and annealing conditions, i.e., the deposition pressure, temperature and gas flow rates. The material properties of polysilicon are also dependent on the type of equipment used, the purity of the process gases and the substrate preparation before deposition.

4.6.1 **Young's modulus**

The Young's modulus of the structural polysilicon layer was estimated by measuring the fundamental frequency of the folded flexure resonator design shown in Figure 4.10. According the equation (2.35) of chapter 2, the relationship between the resonant frequency, f_l, of the folded flexure resonator and Young's modulus, E_f, of the structural polysilicon is,

$$E_f \approx \frac{2\pi^2 f_1^2 l_f^3 M_i}{hb^3} \qquad (4.1)$$

where l_f , h and b are the length (100 µm), thickness (2 µm) and width (3 µm) of a flexure truss, respectively, and M_i the inertial mass (120 ng). Note that a folded-flexure type resonator was employed because it possesses a fundamental frequency that is independent of residual strain.

The fundamental frequency of the folded-flexure resonator was determined experimentally via visual observation of the vibrating resonator (a technique discussed in more detail in the next Chapter) and measured to be ≈ 44 kHz, yielding an estimated Young's modulus of ≈ 94 GPa. This value is lower than the expected value of 130 - 175 GPa [4.23,4.57]. The variation between the measured value and the expected value is probably due to a variation in feature width of the flexure truss, caused by the dry etching process. Small changes in the feature width induce large changes in the resonant frequency due to their cubic relationship, see equation (4.1). For example, a reduction in

feature width of only 300 nm increases the modulus to 129 GPa, closer to the expected value of 140 GPa.

4.6.2 Measurement of residual strain

Wafer curvature method

The conventional way to measure thin film strain is to measure the change in curvature of a wafer caused by the strain in the deposited thin film. The average residual strain in one or more thin films is related to the deflection, δ, of the centre of the wafer by the equation [4.58];

$$\varepsilon = \frac{4}{3}\left(\frac{E_{scs}}{1-\upsilon}\right)\frac{t_s^2\delta}{t_f DE_f} = 96.3\frac{t_s^2\delta}{t_f E_f D} \qquad (4.2)$$

where E_{scs} and ν are Young's modulus and Poisson's ratio for SCS, respectively, D the wafer diameter and t_s the substrate thickness. Also, E_f is the Young's modulus and t_f ($t_f \ll t_s$) the thickness of the thin film, respectively.

Although this method can be applied to measure the strain in any film, it relies on an accurate measurement of wafer deflection, which is not always possible, and is rather cumbersome as the wafer curvature must be measured before film deposition. Moreover, the equation assumes that the curvature of the wafer is constant, which may not always be the case.

Passive strain gauges

A more convenient method of measuring the residual strain in the polysilicon is to use a passive micro-strain gauge integrated directly onto the wafer. When such a structure is released from the supporting sacrificial layer there is a change in the dimensions of the structure that is proportional to the residual strain. Normally, for a simple structure, such as a clamped-clamped beam, this change is very small and so that a mechanism is necessary to convert the small change in dimensions to a measurable reading. Of course, it is only possible to measure the strain in the structural layer but in the case of micromachining this is primarily the one of interest.

Mechanisms to measure tensile strain include 'T' and 'H' type structures. Compressive strain can be determined from the maximum buckling length of a clamped-clamped beam, which will buckle if the residual compressive strain, ε, exceeds a critical

value, ε_{crit}, given by;

$$\varepsilon_{crit} = \frac{\pi^2 h^2}{3l^2} \qquad (4.3)$$

where the beam is of length l and thickness h [4.59]. The buckling effect can also be utilised to measure tensile strain by using an additional structure, such as a ring, to convert a tensile strain into a compressive force. The disadvantage of these buckling methods is that an array of structures of increasing sensitivity is needed to cover the possible range of residual strain expected. Furthermore, uncertainties in the boundary conditions of the beams makes accurate determination of the residual strain difficult.

The rotary micro-strain gauge proposed by van Drieenhuizen [4.59] shown in Figure 4.14 overcomes the limitations of the buckling methods and the small displacements of 'T' and 'H' structures. The gauge works by converting a strain into a rotation. The angle of rotation is measured from the deflection of a pointer. The pointer is supported by two cantilevers whose centre lines are offset by a length O. When released from the supporting sacrificial layer the length of cantilevers increases or decreases depending on the sign of the residual strain. As the centre lines of the cantilevers are offset the pointer rotates. For small deflections the residual strain, ε, in the cantilevers is related to the displacement of the pointer tip by the equation [4.59],

$$\varepsilon = \frac{2\,Y\,O}{(l_a + l_b)(l_c + O)} \qquad (4.4)$$

where l_c is the length of the pointer, l_a and l_b are the lengths of the supporting beams, O is the offset of the beam centre lines and Y is the deflection of the pointer tip.
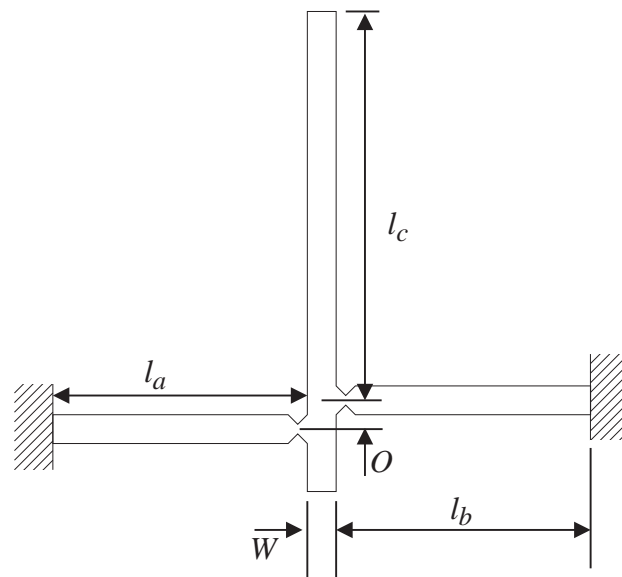
Figure 4.14 Passive rotary type micro-strain gauge

Equation (4.4) assumes that the pointer is free to rotate about the points *A* and *B*. However, in practice this is not the case. The error in the analytical solution, due to this assumption, was determined by constructing a finite element model of the structure and comparing the result of a numerical analysis with the analytical result of equation (4.3). Here, the finite element analysis shows that difference between the analytical solution and finite element is small enough to be ignored, see Figure 4.15.
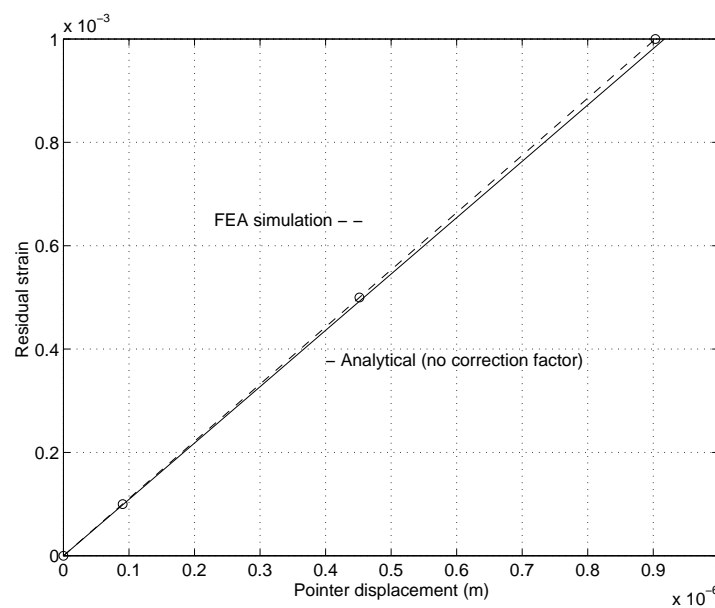
Figure 4.15 Predicted variation in pointer displacement with residual strain. The parameters in equation (4.4) are: $l_c = 65$ μm, $l_a = l_b = 70$ μm and O=5 μm..

To measure the deflection of the pointer it is necessary to have some point of reference, such as bar or similar marking. A neat way to increase the sensitivity is to employ two rotary gauges, back to back, whose pointers deflect in opposite directions, as shown in Figure 4.16. The residual strain is now proportional to the misalignment of the two pointers.
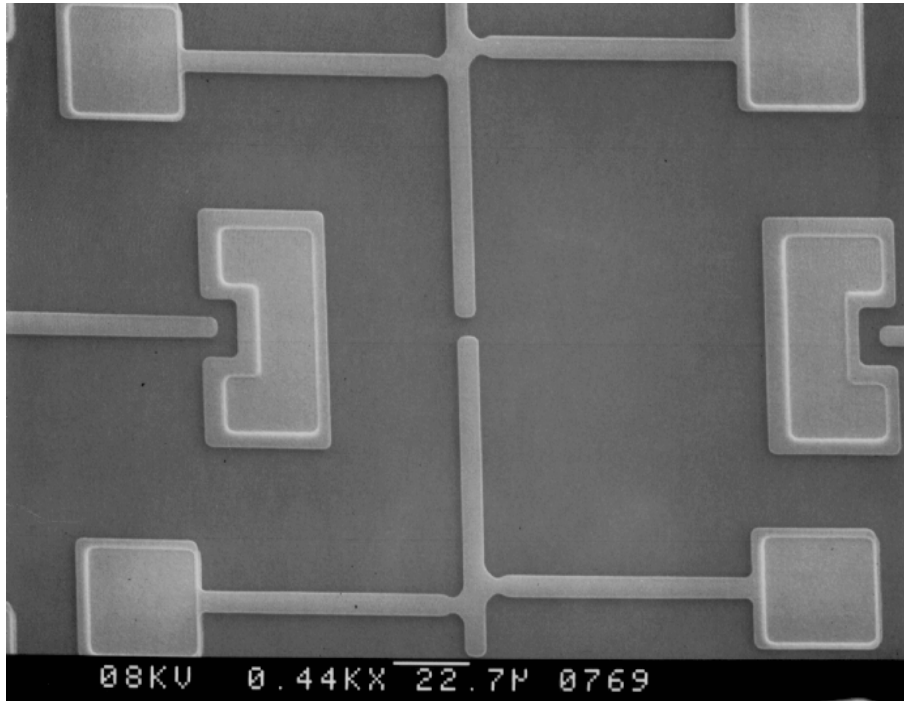

Figure 4.16 SEM of two passive rotary micro-strain gauges aligned back-to-back

Results

To measure the residual strain of the structural polysilicon the centre deflection, δ, of a bare 380 µm thick, 3" diameter, silicon wafer was measured using a DETAK surface profiler. A 2 µm thick layer of polysilicon was then deposited, removed from one side of the wafer, and the centre deflection again measured to give a value for δ of 6 µm. Using an assumed[4] Young's modulus for the polysilicon of 140 GPa, the residual strain was determined using equation (4.2) and was found to have a value of $+37 \times 10^{-5} \varepsilon$ (tensile).

The residual strain was also measured using the microstrain gauges shown in Figure 4.16. Here, the deflection of each pointer tip was measured using a scanning electronic microscope and found to be 0.3 µm. Using equation (4.4) (shown graphically

---

[4] As noted in section 4.6.1, the measured value is close to this but thought to be inaccurate due to an uncertainty in the flexure feature width.

in Figure 4.14) the residual strain was found to be $+32 \times 10^{-5}$ ε (tensile).

The experimental values of residual strain are in good agreement, having an average value of $\approx +35 \times 10^{-5}$ ε. This level of residual strain is within the range expected and is considered optimal for surface micromachined polysilicon microstuctures [4.25,4.26].

4.7 Conclusions

At the beginning of this chapter the layer structure and geometry of a novel type of resonant pressure sensor based on a lateral resonant strain gauge is presented. By combining the flexibility of surface micromachining with conventional bulk anisotropic etching, an increase in design flexibility has been realised and a new type of resonant pressure sensor produced. The flexibility of the fabrication method is demonstrated by the successful fabrication of several pressure sensor configurations, such as dual diaphragms (for differential pressure measurement) and reference resonators (for calibration), which would have been problematic using conventional bulk etching techniques.

The important issues in the production of surface micromachined structures are profile control, uniformity, residual strain and stiction. For the fabrication process described in this chapter good profile control and uniformity was attained by optimising the dry etch process. The residual strain in the structural polysilicon was controlled by using an optimised LPCVD process and post-deposition anneal, and measured to be $+35 \times 10^{-5}$ ε. Stiction was avoided by using a freeze drying process and in this case only about 5 to 10 % of the resonators were found to have collapsed. This suggests that the longer flexures may be employed, which would lower the flexure spring rate. It may also be feasible to use a thicker structural layer (≈ 5 μm), by extending the deposition time (to 15 hours). This should allow a further increase in flexure length and will also lead to a higher capacitance gradient. Further processing, using a comprehensive array of tests structures, is therefore required to determine the limitations of the fabrication process, so that the optimum resonator design can be realised.

References

[4.1] Peterson K. E., Silicon as a mechanical material, *Proc. IEEE*, Vol. 70 No. 5 (1982) 420-457.

[4.2] Frobenius W. D., Zeitman S. A., White M. H., O'Sullivan D. P. and Hamel R. G., Microminiature ganged threshold accelerometers compatible with IC technology, *IEEE Trans.* Vol. ED-39 (1972) 37-39.

[4.3] Benecke W, Silicon micromachining for microsensors and microactuators, *Microelectonics Engineering,* Vol. 11 (1990) 73-82.

[4.4] Delapierre G., Micromachining: a survey of the most commonly used processess, *Sensors and Actuators*, Vol. 17 (1989) 123-138.

[4.5] Howe R. T., Surface micromachining for microsensors and microactuators, *J. Vac. Sci. Technol.* B6 (1988) 1809-1813.

[4.6] Muller R. S., Integrating sensors and electronics - new challenges for silicon, *Technical Digest, International Electron Devices Meeting,* (1984) 206-209.

[4.7] Muller R. S., From IC's to microstructures: materials and technologies, *Acta Polytechnica Scandinavias-Electrical Eng. Series,* No. 63 (1988) 143-146.

[4.8] Kaminsky G, Micromachining of silicon mechanical structures, *J. Vac. Sci. Technology*, B3 (1985) 1015-1024.

[4.9] Angell J. B., Terry S. C. and Barth P. W., Silicon micromechanical devices, *Scientific American*, Vol. 248 No. 4 (1983) 44-55

[4.10] Clayton L. D., Errnisse E. P., Ward R. W. and Wiggins R. B., Miniature crystalline quartz electromechanical structures, *Sensors and Actuators*, 20 (1989) 171-177.

[4.11] Klassen E. H., Peterson K., Nowonlski M., Logn J., Maluf N., Brown J., Storrment C., McCulley W. and Kovacs G. T. A., Silicon fusion bonding and deep reactive ion etching, a new technology for microstructures, *Proc. 8th Int. Conf. Solid State Sensors and Actuators, (Transducers '95)*, Stockholm, Vol. 2 (1995) 139-C3.

[4.12] Howe R. T. and R. S. Muller, Polycrystalline silicon micromechanical beams, *Spring Meeting Electrochem. Soc.*, (1982) 184-185.

[4.13] Fan L.-S., Tai Y.-C. and Muller R. S., Integrated moveable micromechanical structures for sensors and actuators, *IEEE Trans.*, Vol. ED-35 No. 6 (1988) 725-730.

[4.14] Guckel H., Sniegowski J. J., Christenson T. R., Moheny S. and Kelly T. F., Fabrication of micromechanical devices from polysilicon films with smooth surfaces, *Sensors and Actuators*, A20 (1989) 117-122.

[4.15] Putty M. W., Chang S.-C., Howe R. T, Robinson A. L. and Wise K. D., Process integration for active polysilicon microstructures, *Sensors and Actuators*, A20 (1989) 143-151.

[4.16] Tang W. C., Nguyen T.-C. H., and Howe R. T., Laterally driven polysilicon resonant microstructures, *Sensors and Actuators*, A20 (1989) 25-32.

[4.17] Tang W. C., Nguyen T.-C. H., Judy. M. W. and Howe R. T., Electrostatic comb drive of lateral polysilicon resonators, *Sensors and Actuators*, A21-23 (1990) 328-331.

[4.18] Judy M. W. and Howe R. T., Polysilicon hollow beam lateral resonators, *IEEE Micro Elec. Mech. Sys.*, (1993) 265-270.

[4.19] Pisano A. P. and Cho Y.-H., Mechanical design issues in laterally-driven microstructures, *Sensors and Actuators*, A21-23 (1990) 1060-1064.

[4.20] Benitez A., Bausells J., Cabruja E., Esteve J. and Samitier J., Stress in low pressure chemical vapour deposition polycrystalline silicon thin films deposited below 0.1 Torr, *Sensors and Actuators*, A37-38 (1993) 723-726.

[4.21] Koleshko V. M., Belitsky V. F. and Kiryushin I. V., Mechanical stresses in low pressure chemically vapour deposited silicon films, *Thin Solid Films*, 165 (1988) 181-191.

[4.22] Guckel H., Burns D. W., Rutigliano C. R., Showers D. K. and Uglow J., Fine grained polysilicon and its application to planar pressure transducers, *Proc. 4th Int. Conf. Solid State Sensors and Actuators*, *(Transducers '87)* (1987) 227-281.

[4.23] Kamins T. I., Design properties of polycrystalline silicon, *Sensors and Acuators*, A21-23 (1990) 817-825.

[4.24] Guckel H., Sniegowski J. J., Christenson T. R. and Raissi F., The application of fine-grained, tensile polysilicon to mechanically resonant transducers, *Sensors and Actuators*, Vol. A23 (1990) 346-351.

[4.25] Guckel H., Burns D. W., Visser C. C. G., Tilmans H. A. C. and Deroo D., Fine-grained polysilicon films with built in tensile strain, *IEEE Trans.*, Vol. ED-35 No. 6 (1988) 801-803.

[4.26] Howe R. T. and Muller R. S., Stress in polycrystalline and amorphous silicon thin films, *J. Appl. Phys.*, Vol. 54 No. 8 (1983) 4674-4675.

[4.27] Poenar D., French P. J., Mallee., Sarro P. M. and Wolffenbuttel R. F., PSG layers for surface micromachining, *Sensors and Acuators*, A41, No. 3 (1994) 304-309.

[4.28] French P. J. and Wolffenbuttel R. F., Reflow of BPSG for sensor applications, *J. of Micro. and Microeng.* Vol. 3 No. 3 (1993) 135-137.

[4.29] Sze S. M. (ed.), *VLSI technology*, second edition, McGraw-Hill, (1988).

[4.30] Mastrangelo C. H. and Hsu C. H., Mechanial stability and adhesion of microstrutures under capillary forces-part 1: basic theory, *J. Microelectro. Sys.* Vol. 2 No. 1 (1992) 33-44.

[4 31] Alley R. L., Cuan G. J., Howe R. T. and Komvopoulos J., The effect of release-etch processing on surface microstructure stiction, *IEEE Solid-State Sensor and Actuator Workshop*, Hilton Head, South Carolina, (1992) 203-207.

[4 32] Legtenburg R. Tilmans H. Elders J. and Elwenspoek M., Stiction of surface micomachined structures after rinsing and drying: model and investigation of adhesion mechanisms, *Sensors and Actuators*, A43 (1994) 230-238.

[4.33] Mulhern G. T., D. S. Soane and Howe R. T., Supercritical carbon dioxide drying of microstrcutures, *Proc. 7th Int. Conf. Solid-State Sensors and Actuators (Transducer '93) Yokohama, Japan,* (1993) 296-299.

[4.34] Wang M., Moslehi M., and Reed D. W, Characterization of wafer cleaning and oxide etching using vapour-phase hydrogen fluoride., *J. Electrochem. Soc.*, Vol. 138 No. 6 (1991) 1799-1801.

[4. 35] Yee Y., Chun K. and Lee J. D., Polysilicon surface modification technique to reduce sticking of microstructures, *Proc. 8th Int. Conf. Solid State Sens Actuators*, *(Transducers '95),* Stockholm, (1995) Vol. 1. 206-209.

[4. 36] Houston M. R., Maboudian R. and Howe R. T., Ammonium fluoride anti-stiction treatments for polysilicon microstructures, *Proc. 8th Int. Conf. Solid State Sensors and Actuators*, *(Transducers '95)*, Stockholm, (1995) 45-A5.

[4.37] Jansen H. V., Gardiniers J. G. E., Elders J., Timans H. A. C. and Elwenspoek M., Applications of flourocarbon polymers in micromechanics and micromachining, *Sensors and Actuators,* A41-42 (1994) 135-140.

[4.38] Rangelow I. W., Skocki S., Dumania P., Plasma etching for micromechanical sensor applications, *Microelectronic Engineering,* 23 (1944) 365-368.

[4.39] Li Y. X., Wolffenbuttel M. R., French P. J., Laros M., Sarro P. M. and Wolffenbuttel R. F., Reactive ion etching (RIE) techniques for micromachining applications, *Sensors and Actuators,* A41-42 (1994) 317-323.

[4.40]] Sawin H. H., A review of plasma processing fundamentals, *Solid State Technology*, April 1985.

[4 41] Honike Y., Dry etching: an overview, *Japan Annual Reviews in Electronics Computers and Telecommunications*, Vol. 8 (1983) 55-72.

[4 42] Broydo S., Important considerations in selecting anisotropic plasma etching equipment, *Solid State Technology*, April 1983.

[4.43] Fonash S. J., Advances in dry etching processes - a review, *Solid State Technology*, January 1985.

[4.44] Coburn J. W., Pattern transfer, *Solid State Technology*, April 1986.

[4.45] Bollinger D., Lida S. and Matsumoto O., Reactive ion etching: its basis and future, Part I, *Solid State Technology*, May 1984.

[4.46] Jansen H. J., de Boer, M., Legtenburg R. and Elwenspoek M., The black silicon method, a universal method for determining the parameter setting of a fluorine-based reactive ion etcher in deep silicon trench etching with profile control, *J. of Micromech. Microeng.* Vol. 5 No. 2 (1995) 115-120.

[4.47] Pinto R., Ramanthan K. V. and Babu R. S., Reactive ion etching in SF_6 gas mixtures, J. *Electrochem. Soc.: Solid-State Science and Technology*, (1987) 165-175.

[4.48] Parrens P., Anisotropic and selective reactive ion etching of polysilicon using SF_6, *J. Vac. Sci. Technol.* Vol. 19 No. 4 (1981) 1403-1981.

[4.49] Syau T., Baliga J. and Hamaker R. W., Reactive ion etching of silicon trenches using SF_6 gas mixtures., *J. Electrochem. Soc.* Vol. 138 No. 10, (1991) 3076-3081.

[4.50] Light R. W. and Bell H. B., Profile control of polysilicon lines with an SF_6/O_2 plasma etch process, *J. Electrochem. Soc.: Solid-State Sci. Tech.*, (1983) 1567-1571.

[4.51] Meith M. and Barker A., Anisotropic plasma etching of polysilicon using SF_6 and $CFCl_3$, *J. Vac. Sci. Technol.*, Vol. 1 No. 2 (1983) 629-635.

[4.52] Jansen H, De Boer M., Burger J., Legtenburg R. and Elwenspoek M., The black silicon method 2. The effect of mask materal and loading on the reactive ion etching of deep silicon trenches, *Microelectronic Engineering,* Vol.27, No.1-4 (1995) 475-480.

[4.53] Greenwood J. C. and Satchell D.W., Miniature silicon resonant pressure sensor, *IEE Proc.*, Vol. 135 Pt. D No. 5 (1988) 369-372.

[4.54] Ikeda K., Kuwayama H., Kobayashi T., Watanabe T., Nishikawa T., Yoshida T., and Harada K., Three dimensional micromachining of silicon presssure sensor integrating resonsnant strain gauge on diaphragm, S*ensors and Actuators*, A21-23 (1990) 1007-1010.

[4.55] Tilmans H. A. C., Untema D. J. and Fluitman J. H. J., Single element exicitation and detection of (micro-)mechanical resonators, *Proc. 6th Int. Conf. Solid State Sens. Actuators, (Transducers '91)* (1991) 533-537.

[4.56] Blom F. R., Bouwstra S., Elwenospoek M. and Fluitman J. H. J., Dependence of the quality factor of micromachined silicon beam resonators on pressure and geometry, *J. Vac. Sci. Technol.* Vol. B10 No. 1 (1992) 19-26.

[4.57] Howe R. T. and Muller R. S., Polycrystalline and amorphous silicon micromechanical beams: annealing and mechanical properties, *Sensors and Actuators*, 4 (1983) 447-454.

[4.58] Maissel L. I. and Glang R., *Handbook of thin film technology*, McGraw-Hill, New York, (1990).

[4.59] van Drieenhuizen B. P., D., Goosen J. F L., French R. J. and Wolffenbuttel R. F., Comparison of techniques for measuring compressive and tensile stress in thin films, *Sensors and Acuators*, A37-38 (1993) 756-765.

Contents

5. Testing and results

Chapter 5

Testing and results

The objectives of this chapter are to describe the techniques employed to characterise the performance of the pressure sensor and report preliminary results. Optical measurements of a number of vibrating lateral resonators show that this pressure sensor design possesses a relative pressure sensitivity as high as 3.4 ppm/Pa, range of up to 4×10^5 Pa and temperature sensitivity of -240 ppm/^{o}C. A novel optical interrogation technique is described, and used to measure the Q-factor variation of the lateral resonator with cavity pressure. The results show that the lateral resonator possesses a Q-factor of 51 in air an atmospheric pressure, rising to 26 000 in high vacuum[1]. As part of these measurements, the linear and non-linear frequency response of the lateral resonator are presented. Finally, the integration of the lateral resonator into an electronic oscillator is discussed. The first stage of this process is implemented using comb capacitor detection and a high gain amplifier, in conjunction with an indirect piezoelectric drive scheme to avoid problems encountered with electrical cross-talk.

5.1   Performance characterisation

Predominately, the performance of a resonant pressure sensor is defined by its pressure resolution over a pre-defined pressure range and its stability with time and external disturbances (e.g. temperature). Broadly speaking, the resolution is determined by the mechanical pressure sensitivity of the pressure sensor and the resolution of the frequency measurement system. Resonant sensors are usually designed to be operated in a closed loop mode, whereby the mechanical resonator is integrated with the drive and

---

[1] In this chapter high vacuum is defined as a pressure less than 1 Pa.

sense electronics, so that it forms the frequency determining element of an electronic oscillator. When the mechanical resonator is integrated with the sensor electronics the bias-sensitivity, onset of non-linearity and the presence of spurious modes become important factors that influence the measured resonant frequency. Consequently, the repeatability and temperature sensitivity of a resonant pressure sensor is related to both the stability of the mechanical elements, i.e. the resonator, diaphragm and packaging materials, and the supporting electronics that enable closed loop operation.

To completely characterise the performance of the lateral resonant pressure sensor it would be necessary to attain a closed loop mode of operation and then calibrate the measured resonant frequency against a pressure standard over a suitable temperature range. The long term stability of the pressure sensor could then be determined by monitoring the accuracy of the pressure reading over a period of at least six months. The aim of research described in this chapter is to cover the first stages of this characterisation process. The objectives are to demonstrate the operation of the pressure sensor and assess its performance by observing four device parameters;

(1)   The relative pressure sensitivity (at constant temperature). This is determined by the gauge-factor of the resonant strain gauge, the pressure deflection relationship of the diaphragm, and the nature of the diaphragm/resonant strain gauge interface.

(3)   The pressure range. This is determined by the ability of the electronics to track the fundamental mode of the resonator as the applied pressure and operating temperature change, and is ultimately limited by the strength of the diaphragm.

(3)   The temperature dependence of the resonant frequency. This is a function of the absolute and differential temperature sensitivities of the materials used to fabricate and package the pressure sensor.

(4)   The Q-factor of the lateral resonator and its variation with cavity pressure. The Q-factor is a measure of the energy loss from the resonator. A high Q-factor increases the resolution of the pressure sensor and also implies a good long term stability.

In the next section, the testing techniques employed to measure the pressure sensitivity, pressure range and temperature dependence are described. A novel optical method of measuring the Q-factor of the resonator is described in section 5.5.

5.2 Testing techniques

5.2.1 Visual observation in air

In chapter 3 it is shown that for small amplitudes of vibration, the response of the resonator is described by a linear second order damped system, where the maximum amplitude of vibration occurs at the resonant frequency. Visual observation is a convenient and simple method of finding the maximum amplitude of vibration, and hence the resonant frequency. This is achieved by slowly sweeping the frequency of the excitation signal in the vicinity of the predicted lateral resonant frequency, whilst observing the image of the resonator in the eyepiece of a high power microscope. When the frequency of the excitation signal is close to the fundamental lateral resonant frequency (i.e. within the bandwidth of the fundamental frequency of the resonator) the image of the resonator blurs in the direction oscillation. From this point, the excitation signal is tuned to the resonant frequency by maximising the envelope of the blur, where the amplitude of vibration is highest.

The general apparatus used to drive the resonator and observe its response is shown in Figure 5.1a. The resonator was placed under the objective lens of a microscope, which had a magnification of at least ×600. Electrical connections to the resonator and contact pads were made via precision probe-tip manipulators (Karl Suss PH100). The resonator was biased with a stabilised voltage source (Farnell TOPS2) and driven with a sinusoidal signal from a precision function generator (Advance Instruments High Power L. F. Oscillator SG 70). The electrical connections made to the resonator are indicated schematically in Figure 5.1b.
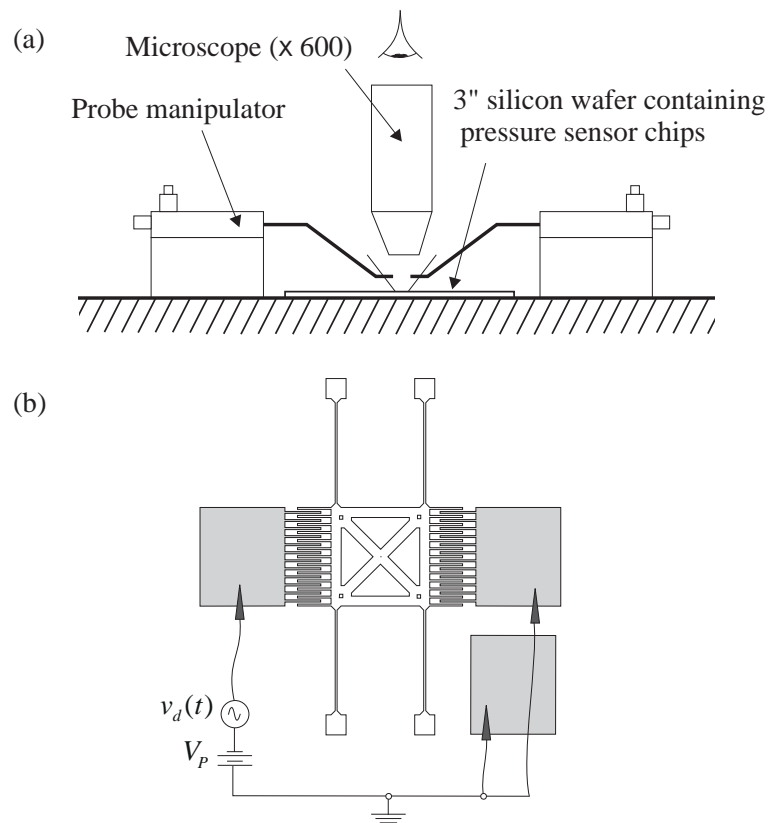
Figure 5.1. (a) General apparatus and, (b) electrical connections to the resonator for measuring the resonant frequency with an optical microscope.
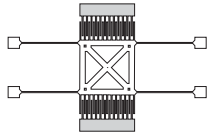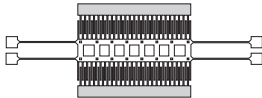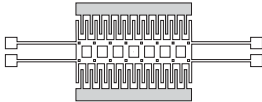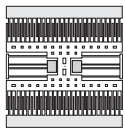
5.2.2 Visual observation in vacuum

To reflect the true operating conditions of the resonant pressure sensor, the visual observation technique was extended by exciting the lateral resonator in high vacuum. In high vacuum the bandwidth of the second order frequency response was reduced to < 3 Hz (see section 5.5), which enabled the resonant frequency to be measured to a higher accuracy than in air.

To operate the lateral resonator in vacuum both the sensor chip and optical microscope were housed inside a vacuum chamber. The resonator was viewed via a CCD camera (COHU solid state camera, mounted on the microscope) and video monitor (Sony PVM 1444OQM). Electrical connections to the resonator and CCD-camera were made via suitable electrical feed-throughs into the vacuum chamber. The resonator was biased with a stabilised d.c. voltage source (Farnell TOPS2) and the drive signal supplied by a precision systems analyser (HP-83536A Control Systems Analyser).

Without further comment Table 5.1, lists the spread of fundamental frequencies, measured using visual observation in air of four design variations of lateral resonator, denoted types 'A, B, C and D'.

Table 5.1 Comparison of the predicted and experimental resonant frequencies of 4 lateral resonator designs. The resonant frequency of each resonator was measured via visual observation (in air at atmospheric pressure). The predicted resonant frequency assumes a Young's modulus[2] of 140 GPa.

Resonator design	Type	Predicted resonant frequency (kHz)	Measured resonant frequency (kHz)	
			Minimum	Maximum
	A	55.78	47.68 ± 0.35	70.10 ± 0.35
	B	50.03	55.52 ± 0.35	70.95 ± 0.35
	C	142.45	129.96 ± 0.35	149.31 ± 0.35
	D	57.65	39.27 ± 0.35	44.82 ± 0.35

19B

Discussion

The first point to note from Table 5.1 is the spread of frequencies measured for each design. There are two reasons for this spread. First, it is probable that there is a variation in resonator geometry, due to variations in the RIE process used to define the resonators. A small variation in the width of the flexure results in high (unloaded) frequency-shift, because the linear spring rate of the hammock flexure is proportional to cube of the flexure width, see equation (2.31) of Chapter 2. Second, the resonant frequency is sensitive to variations in both the Young's modulus and the residual strain of

---

[2] The actual measured value is close to this but, thought to be inaccurate due to an uncertainty in the feature widths of the folded-flexure resonator used to measure Young's modulus experimentally, see section 4.7.2 of chapter 4.

the polysilicon structural layer. The fact that the folded-flexure resonator, which is insensitive to residual strain showed a smaller variation in resonant frequency suggests that the residual strain plays a significant part. These differences in material properties and resonator geometry occur both between wafers and at difference locations on a wafer. However, on a *local* scale the variation in residual strain and resonator geometry was small and consequently the variation in resonant frequency was also small. For example, the maximum variation in resonant frequency between four identical resonators, each located on the corner of a 2 mm square was found to be typically less than 1 kHz.

Excitation voltages

In air at atmospheric pressure it was found that a d.c. polarisation voltage of the order of 50 V and drive voltage amplitude of at least 25 V_{pk-pk} were needed to drive the lateral resonator (types 'A and B') to a reasonable vibration amplitude of ≈ 1 µm. These relatively high bias and drive voltages meant that a high electric field of ≈ 200 $V\mu m^{-1}$ was developed between the electrical contact pad and the ground plane, which often led to the electrical breakdown of the silicon nitride electrical insulation layer. This problem was particularly acute when electrical connections to the contact pads were made via wire bonds, although the reason for this is unclear.

When the same resonators were operated in a high vacuum the magnitude of excitation voltages were lowered in line with the increased Q-factor, see equations (3.6) and (3.7) of chapter 3. Here, it was found that a d.c. polarisation voltage of the order of 20 V and drive voltage amplitude of at least 1 V_{pk-pk} were needed to attain a vibration amplitude of ≈ 5 µm. Unfortunately, it was found that even with these drive voltages the level of cross-talk was high enough to saturate the high gain amplifier employed to amplify the motional sense current. This effectively prevented the normal operation, i.e. electrostatic excitation and capacitive detection, of the lateral resonator.

The level of electrical cross-talk between the drive and sense comb of the resonator is governed by the electrical characteristics of the substrate and sensor packaging, as described in section 3.5.2 of chapter 3. An attractive method of reducing the level of cross-talk to an acceptable level is to integrate an electrostatic shield between the ground plane of the resonator and the electrical contact pads. Pratt *et al.* [5.1] have demonstrated that this provides sufficient attenuation of the drive signal to allow the

normal operation of the lateral resonator, even in air, when both a high polarisation and drive voltage are required to overcome the viscous drag force acting on the resonator.

An alternative method of reducing the level of cross-talk that avoids the necessity of a redesign and fabrication run, is to employ an indirect piezoelectric drive scheme. This is achieved by attaching the resonator onto a piezoelectric disc, via a silicon cantilever, see Figure 5.2. The piezoelectric disc is driven at the resonant frequency of the lateral resonator, which is then excited by the vibrations generated by the piezoelectric disc. This technique has two advantages. First, the resonator sense comb and piezoelectric drive are separated by a large distance of several cm (compared to the 100 µm separation of the drive comb and sense comb). This allows an electrostatic shield to be introduced, so reducing cross-talk to a level where it is practically eliminated. The effectiveness of this technique in minimising electrical cross-talk is described further in section 5.6.1. The problem of dielectric breakdown associated with the high drive voltages in air is also avoided.
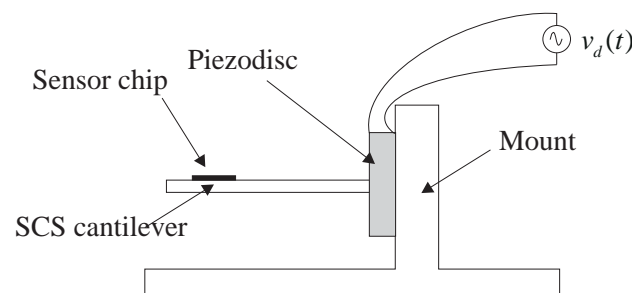

Figure 5.2 Schematic showing the piezoelectric excitation of the lateral resonator. The resonator is mounted onto a single crystal silicon cantilever that is attached to a piezoelectric disc. The resonator is driven by the vibration of the piezoelectric disc.

5.2.3 Visual observation with a scanning electron microscope

Another interesting method of observing the vibrating resonator is to use a scanning electron microscope. This is a useful technique because it allows the oscillation of the strain gauge to be observed over a wide range of angles at a high magnification, and is therefore an ideal way to detect any spurious modes of vibration.

To view the resonator using a scanning electron microscope the sensor chip was mounted onto a suitable header and the complete assembly placed on a X-Y-Z table (mounted inside the SEM). Electrical connections to the resonator were made via vacuum feed-throughs and the resonator driven using a precision control systems analyser (HP-

83536A Control Systems Analyser). The acceleration potential of the scanning electron microscope was limited to 5 kV to minimise the build up of electrical charge on the resonator. Above 5 kV the electrostatic force acting between the resonator and substrate was sufficient to pull the resonator down onto the substrate.

The scanning electron micrograph (SEM) in Figure 5.3 shows a lateral strain gauge (type 'C') vibrating in a high vacuum. The resonator was excited using the indirect piezoelectric drive scheme, which was driven with a 10 mV$_{pk-pk}$ amplitude sinusoid. The blur of the vibration envelope is clearly visible. In this instance the resonant frequency of the strain gauge[3] was 129 ± 2 kHz, and the vibration amplitude was ≈ 6 µm. Note that the resonator is clearly defined in the Y and Z plane, indicating the absence of any vibration in either of these directions. Figure 5.4 shows an SEM of the folded-flexure resonator (type 'D') vibrating in high vacuum. This resonator was also excited using the indirect piezoelectric drive scheme. The lateral resonant frequency of the folded-flexure resonator (type 'D') was measured to be 48291.55 Hz ± 50 mHz.

The advantage of the visual observation technique is that it is a simple method of determining the resonant frequency, and thus provides a straightforward method measuring the pressure sensitivity and temperature dependence, as is described below. Visual observation techniques may also be used to estimate the amplitude response of the resonator, specifically to measure the Q-factor and observe the onset of non-linearity. However, they are some what limited in this respect because they rely on an visual estimation of the vibration amplitude, which is prone to error. This topic is discussed further in section 5.5.

---

[3] Note that at a vibration amplitude of 6 µm the response of the resonator is highly non-linear, which makes an accurate estimate of the resonant frequency difficult.
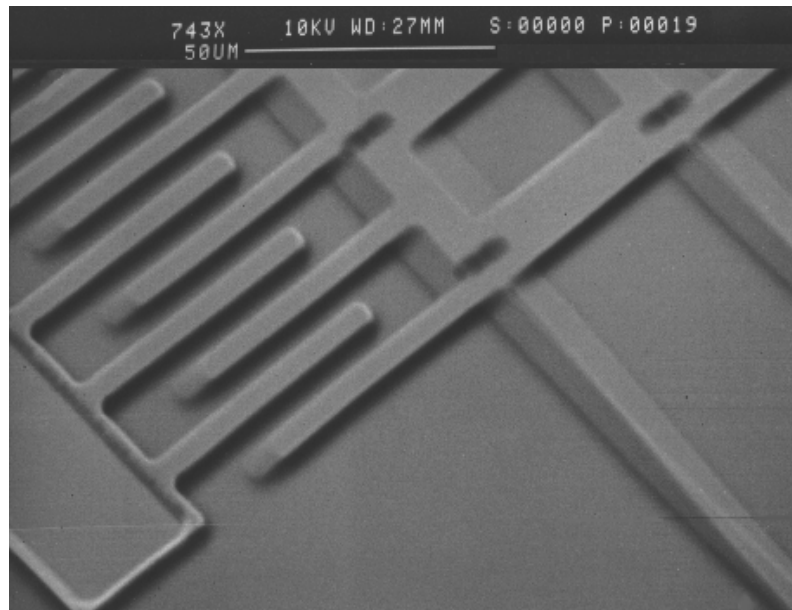
Figure 5.3 SEM showing a lateral resonator (type 'C') operated in a high vacuum. This device had a measured resonant frequency[4] of 129 ± 2 kHz. The amplitude of vibration was estimated from the magnitude of the blur of the vibration envelope to be ≈ 6 μm.
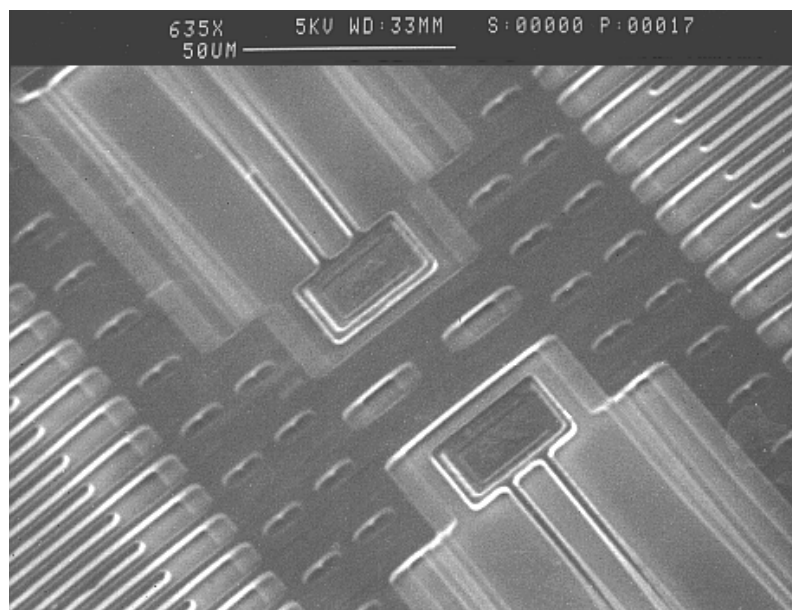

Figure 5.4 SEM showing a folded-flexure resonator (type 'D') vibrating in high vacuum. The amplitude of vibration was estimated from the magnitude of the blur of the vibration envelope to be ≈ 9 μm. The measured resonant frequency was 42291.55 Hz ± 50 mHz and the measured Q-factor ≈ 18000 ± 2000, see section 5.5.

---

[4] see footnote 3.

5.3 Relative pressure sensitivity

To measure the pressure sensitivity a sensor chip was mounted onto a glass tube which was in turn mounted inside a vacuum chamber, so that the cavity pressure could be controlled. The glass tube was connected to a portable pressure calibration instrument (Druck DPI 602). The resonator was driven using the indirect piezoelectric drive scheme and the resonant frequency was measured at equal static pressure intervals over a pressure range using the visual observation technique outlined earlier. The pressure sensitivities of three different pressure sensors are presented below.

5.3.1 Results

Figure 5.5 presents the variation of resonant frequency F_R with gauge pressure P, for a pressure sensor based upon the 'C type' lateral resonator design shown in Table 5.1 Gauge pressure is defined as the pressure referenced to ambient pressure [5.2]. This measurement is relevant when the resonant strain gauge is operated in air at atmospheric pressure. A second order polynomial of the form,

$$F_R = K_2 P^2 + K_1 P + K_0 \qquad (5.1)$$

was fitted to the data set and shows an excellent fit with a correlation coefficient of 0.9999. The values of the polynomial coefficients K_0, K_1, and K_2 fitted to the data are shown in Figure 5.5. The linear pressure sensitivity, defined by coefficient K_1 in equation (5.1), was found to be 0.072 Hz/Pa. The relative pressure sensitivity is given by the ratio of the linear pressure sensitivity K_1 and the unloaded fundamental frequency K_0,

$$G_{p_m} \overset{\Delta}{=} \frac{K_1}{K_0} \qquad (5.2)$$

The unloaded fundamental frequency was measured to be 133.94 ± 0.35 kHz, to give a relative frequency sensitivity of 0.54 ppm/Pa. The pressure range of this sensor was found to be 3×10^5 Pa. Note that the pressure sensitivity of a second resonator was also recorded. The purpose of this resonator was to provide a temperature dependent reference frequency and its use is described further in section 5.4.
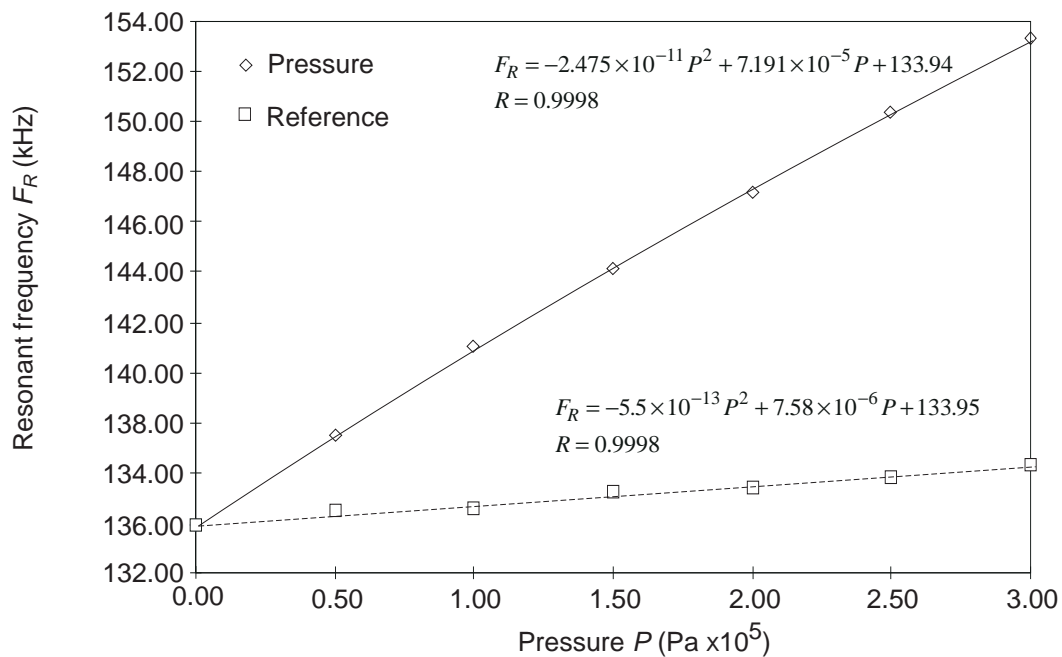
The chart shows resonant frequency F_R (kHz) versus Pressure P (Pa x10^5). Legend: ◇ Pressure, □ Reference.

$$F_R = -2.475 \times 10^{-11} P^2 + 7.191 \times 10^{-5} P + 133.94$$
$$R = 0.9998$$

$$F_R = -5.5 \times 10^{-13} P^2 + 7.58 \times 10^{-6} P + 133.95$$
$$R = 0.9998$$

Figure 5.5 Measured pressure-frequency relationship of a pressure sensor based upon the lateral resonator design type 'C'. This particular device had an unloaded resonant frequency 133.94 ± 0.35 kHz and relative pressure sensitivity of 0.54 ppm/Pa. The dashed curve is the pressure-frequency relationship of a resonant temperature sensor integrated on the diaphragm edge. Error bars are omitted for the sake of clarity but are typically $\pm 1.5\%$.

Figure 5.6 shows the variation of resonant frequency with absolute pressure for the lateral strain gauge design 'type B' shown in Table 5.1. Note that an absolute pressure measurement is referenced to zero pressure [5.2]. This is the normal mode of operation for this pressure sensor when the resonant strain gauge is operated in a high vacuum. A second-order polynomial was again fitted to the measured data and has an excellent fit with a correlation coefficient of 0.9998. This pressure sensor had an unloaded resonant frequency of 59.32 ± 0.35 kHz and a pressure sensitivity of 0.12 Hz/Pa, resulting in a relative pressure sensitivity of 2.02 ppm/Pa. The range of this particular device was 4×10^5 Pa.

One further pressure measurement of interest is the ability of the sensor to measure a differential pressure. One way of achieving a differential mode of operation is to enclose the resonator with a silicon cap that is itself an integral part of the diaphragm, so that both sides of the diaphragm are exposed to the pressure medium. The pressure sensor described in this thesis is not designed to take advantage of such a sophisticated
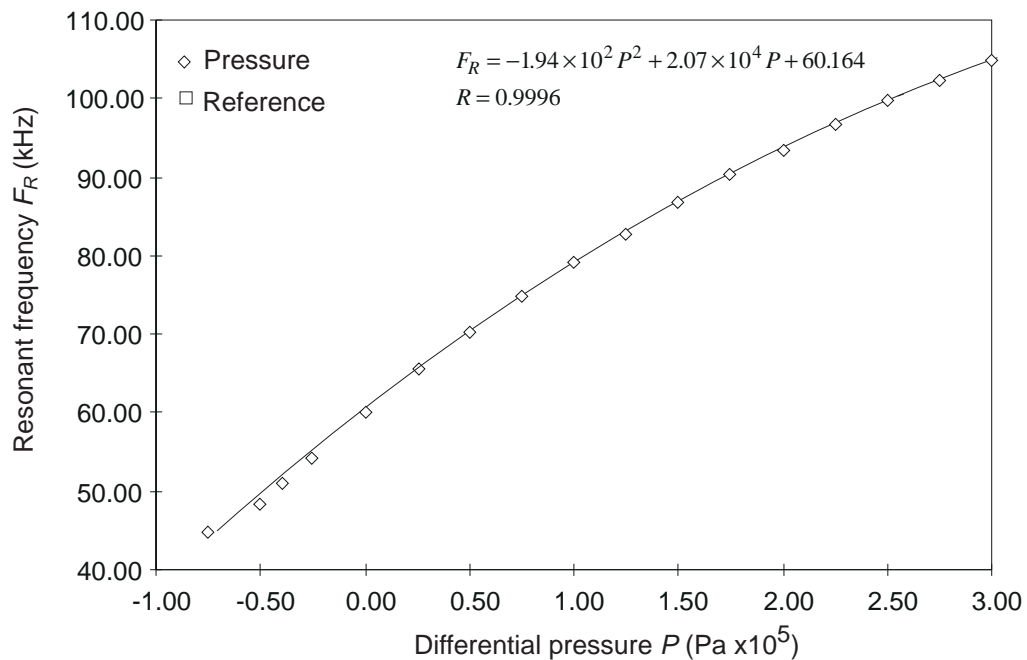
Figure 5.6 Measured pressure-frequency relationship of a pressure sensor based upon the lateral resonator design type 'B', operated in air at atmospheric pressure. This particular device had an unloaded resonant frequency 59.32 ± 0.35 kHz and relative pressure sensitivity of 2.02 ppm/Pa. Error bars are omitted for the sake of clarity but typically $\pm 1.5\%$.

encapsulation scheme. However, a measure of differential pressure sensitivity was made by referencing one side of the diaphragm to atmospheric pressure and varying the pressure on the other side of the diaphragm accordingly.

Figure 5.7 shows the variation in resonant frequency with differential pressure for the design type 'A' in Table 5.2. Note that in this instance the positive differential pressure was effectively a gauge pressure measurement. This pressure sensor exhibited an unloaded resonant frequency of 60.16 ± 0.35 kHz and an impressive linear pressure sensitivity of 0.21 Hz/Pa. The relative pressure sensitivity of this pressure sensor was calculated to be 3.49 ppm/Pa, over a pressure range of -0.75 to 3.0×10^5 Pa. It is expected that the negative pressure range was actually less than -0.75×10^5 Pa, which was the limit of the calibrated pressure line used in the experimental work.
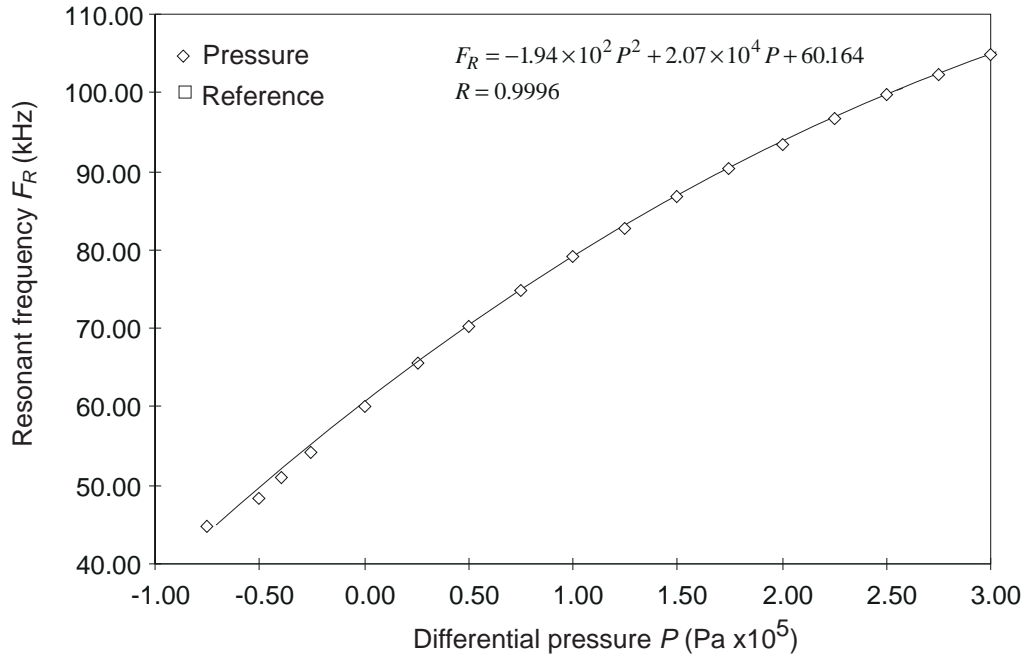
Figure 5.7 Measured pressure-frequency relationship of a pressure sensor based upon the lateral resonator design type 'A'. This particular device had an unloaded resonant frequency 60.16 ±0.35 kHz and relative pressure sensitivity of 3.49 ppm/Pa. Note that the minimum absolute pressure of -0.75 ×10⁵ Pa was a limitation of the calibration line rather than the pressure sensor. Error bars are omitted for the sake of clarity but typically ±1.5%.

Discussion

At this point it is interesting to compare the experimental relative pressure sensitivities with those predicted by the theory presented in Chapter 2. The experimental values were calculated from the second order polynomials fitted to each data set, according to equation (5.1), whilst the theoretical values were calculated using equation (2.48) of Chapter 2, which is repeated here for convenience,

$$G_p = \frac{9z_0\alpha(1-\upsilon)}{E_D l_f (5b^2/l_f^2 + 6\varepsilon)}\left(\frac{a_d}{t}\right)^3 \qquad (5.3)$$

where α is a constant, ν Poisson's ratio of single crystal silicon (SCS), E_D Young's modulus of SCS and the other parameters are process dependent. Across a single 3" processed wafer the diaphragm thickness, t, has a nominal value of 20 ± 10 μm. The

relatively large error stems from the inaccuracy of the technique used to control diaphragm thickness, see section 4.4.2 of Chapter 4. For this comparison, the thickness of the diaphragm was ascertained experimentally by measuring the thickness of an adjacent diaphragm using a linear variable displacement transducer (LVDT) (Slyvac 100). The residual strain, ε, of the flexure truss is taken as 34.5×10^{-5} ε, which is the average of the experimental values given in Chapter 4. The other process dependent parameters; z_0, the distance between the centre lines of the resonator and diaphragm; a_d, the side length of the diaphragm; l_f, the length, and b the width of the flexure truss are taken as the design values. This is because the effect of a difference between the designed value and actual value for these parameters on the overall error in the predicted relative sensitivity is small compared to the uncertainty in the diaphragm thickness.

Table 5.2 lists the experimental and theoretical relative pressure sensitivities. The theoretical values, predicated by equation (5.3) (for positive diaphragm deflections), and the experimental values are in good agreement. It is likely that the small difference between the predicted and measured values was a consequence of assumptions made in the theoretical model and, more significantly, the error in measuring the thickness of the diaphragm.

Table 5.2 Comparison between measured and theoretical relative pressure sensitivities for the lateral resonant pressure sensor. The measured sensitivities are calculated from the second order polynomials given in Figures 5.5,, 5.6 and 5.7. The theoretical sensitivities are predicted using equation (5.3).

Figure No.	Type	Measured range (Pa $\times 10^5$)	Typical F_R (± 0.35 kHz)	Diaphragm		Relative pressure sensitivity (ppm/Pa)	
				Thickness (μm)	Burst pressure (Pa $\times 10^5$)	Experimental	Theory
5.5	C	0 - 3.0	133.94	26 ± 2	≈ 16	0.54 ± 0.03	0.65 ± 0.15
5.6	B	0 - 4.0	59.32	27 ± 2	≈ 16	2.02 ± 0.1	2.30 ± 0.5
5.7	A	-0.75 - 3.0	60.16	16 ± 2	≈ 9	3.49 ± 0.2	3.38 ± 0.12

The results presented in Table 5.2 demonstrate that the lateral resonant pressure sensor offers an impressive relative pressure sensitivity, exceeding that of most of the pressure sensors reviewed in Table 1.1 of chapter 1. Moreover, this level of sensitivity is sustained over a pressure range of up to 4×10^5 Pa. Note that the range of this pressure sensor is limited by the ability to track the resonant frequency, rather than the strength of

the diaphragm. The most likely reason for the loss of resonance is the grounding of bottom surface of the resonator on the surface of the diaphragm. Interestingly, this mechanism could provide a useful way of determining over-pressure. It is worth pointing out that, for reasons of safety, the pressure sensor must be able to withstand an over pressure of at least 3 times the maximum working pressure. This criterion is satisfied for the pressure sensors tested here, because the burst pressure of the $26\,\mu\text{m}$ thick diaphragms was found to be $\approx 16 \times 10^5$ Pa whilst the $16\,\mu\text{m}$ thick diaphragm failed at $\approx 9 \times 10^5$ Pa, see Table 5.2.

A related point is the behaviour of the lateral strain gauge and diaphragm when a negative differential pressure was applied. Visual observation of the sensor under these conditions showed that the vertical separation between the resonator and the diaphragm increases. This behaviour was to be expected and occurs because (for this sensor design) the negative deflection of the diaphragm rotates the anchor points towards each other. This reduces the level of the residual strain in the resonator, leading to a negative frequency-shift. A reduction in residual strain implies that the curvature of the resonator is at minimum, and determined by the magnitude of the residual strain and the rotation of the anchor points. Thus, as the diaphragm deforms the difference in curvature between the resonator and diaphragm leads to an increased separation, see Figure 5.8. This effect must be considered if the resonator is to be encapsulated using an integrated silicon cap.
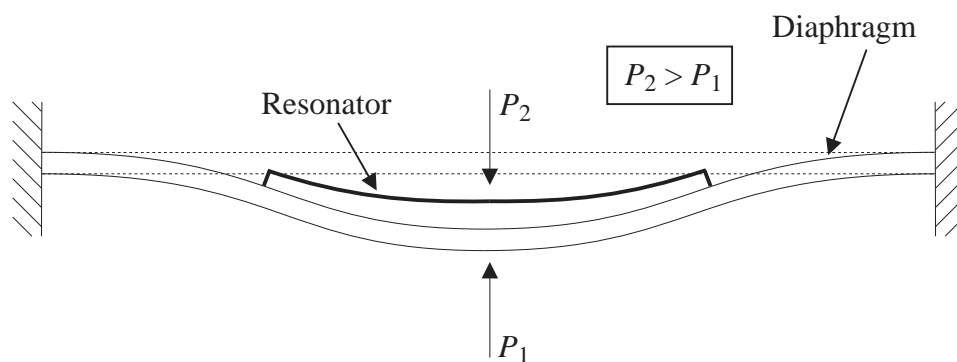

Figure 5.8 Schematic showing the separation of diaphragm and resonator under a negative differential pressure. The deflection of the diaphragm rotates the flexure anchors so reducing the residual strain in the resonator. The difference in curvature between the resonator and diaphragm is seen as an increased separation.

5.4 Temperature dependence

The dependence of the resonant frequency on temperature was determined using the visual observation technique, in conjunction with the piezo-electric drive scheme. The microscope and pressure chip were placed in an oven and the resonant frequency was measured at several temperature intervals between room temperature (25 ^{o}C) and 92 ^{o}C.

Figure 5.9 shows the variation of the resonant frequency with temperature for two identical lateral resonant strain-gauges. One resonator is located in the centre of a diaphragm and so is designed to be sensitive to pressure. The other resonator is located just off the edge diaphragm, see Figure 5.10. The aim is to provide a temperature dependent reference frequency, and so allow the cross-sensitivity of the pressure sensor to temperature to be reduced. This is achieved by comparing the frequency-shift of each resonator during calibration, a method often referred to as structural compensation [5.3]. Note that in this case, the reference resonator exhibited a small pressure sensitivity, see Figure 5.5, probably because it was located too close to the diaphragm edge.

The temperature dependence of each strain gauge was determined by fitting a second order polynomial to the data. The coefficients, see Figure 5.9, indicate a linear temperature dependence over the measured temperature range. The reference resonator showed a temperature dependence of -114 ppm/^{o}C, whilst the pressure sensitive resonator had a higher dependence of -240 ppm/^{o}C. Both sensitivities are much greater then the intrinsic dependence (the variation of Young's modulus) of polysilicon that is reported by Biebl [5.4] to be between -42 and -70 ppm/^{o}C. The most likely reason for this discrepancy is the structural elongation of the resonator caused by thermal expansion. This reduces the residual tension in the resonator, which results in a negative frequency-shift. The difference between the two values is likely to be due to differential expansion effects between the pressure sensitive resonator and the diaphragm.
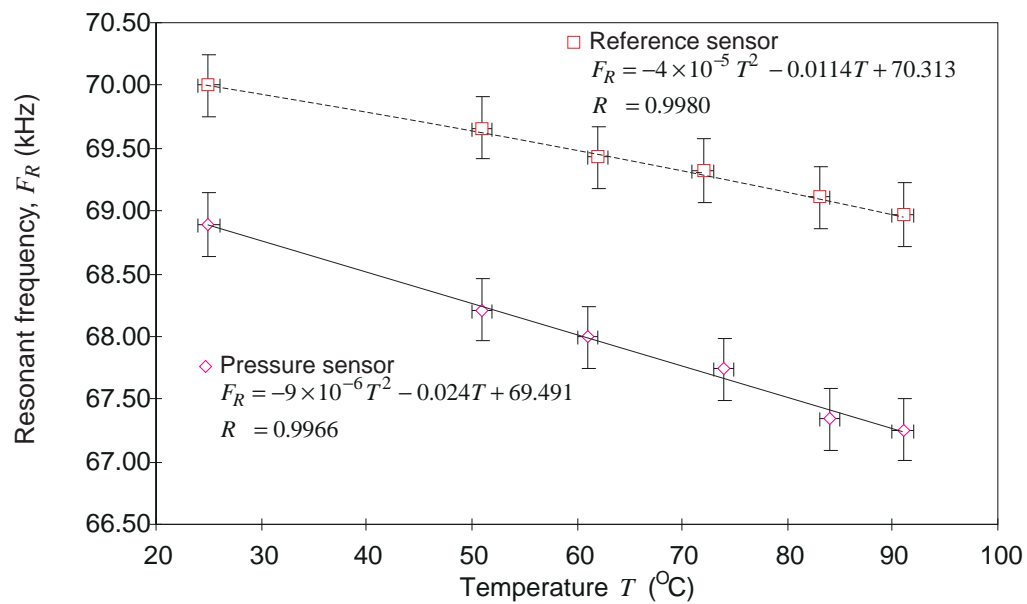
Figure 5.9 Measured variation of resonant frequency with operating temperature for a type 'C' resonator. Two data sets are shown and a second order polynomial curve fitted to each. The solid line represents the temperature dependence of a pressure sensitive strain gauge whilst the dashed line is that of a reference resonator.
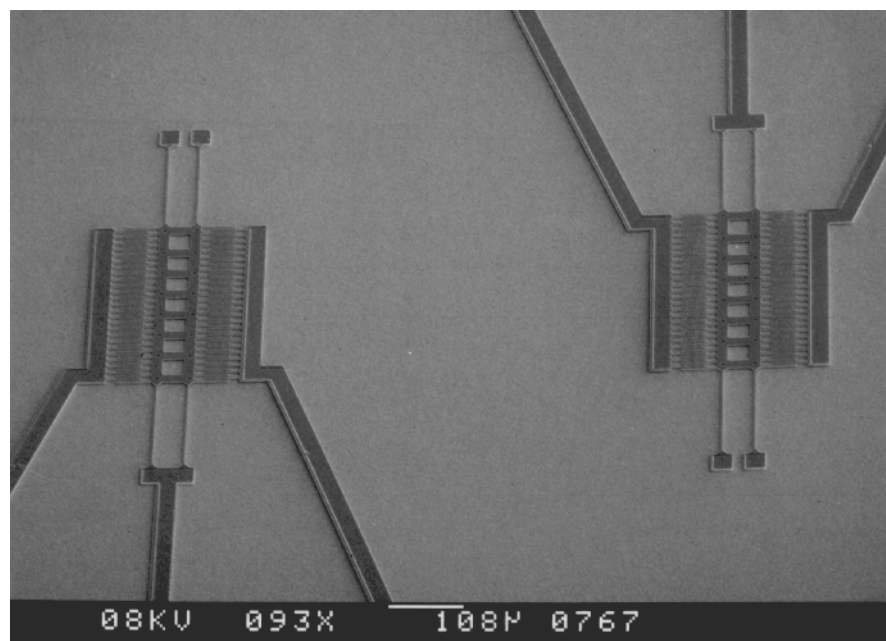

Figure 5.10 SEM showing a dual resonator arrangement that has potential application in reducing the cross-sensitivity of the pressure sensor to temperature. One resonator is located centrally on the diaphragm whilst the reference is located at the diaphragm edge.

5.5 Q-factor

If a resonator exhibits a high Q-factor (in high vacuum) it is likely that it is well isolated from its surroundings and so likely to possess a good long term stability, provided the material properties of the sensor are stable over time [5.2]. A high Q-factor also increases the accuracy of the frequency measurement system and consequently the resolution of the pressure sensor. As is mentioned previously in chapter 3, it is known that the intrinsic Q-factor of a microresonator is reduced by additional layers deposited onto the resonator. Previous research has shown that aluminium, in particular, can significantly degrade the intrinsic Q-factor [5.2]. Hence, the measurements presented in this section were obtained from a resonator that did not possess an additional layer of aluminium.

The Q-factor of a resonator can be measured in either the frequency domain or the time domain. In the frequency domain the Q-factor is defined by,

$$Q = \frac{f_1}{f^+ - f^-} \tag{5.4}$$

where f^+ and f^- define -3 dB points and f_1 is the unloaded resonant frequency. In the time domain the Q-factor is computed from the time decay of the resonator,

$$Q \approx 1.43 f_1 (t_2 - t_1) \tag{5.5}$$

where t_2-t_1 is the time for the oscillation amplitude to drop from 90% to 10% of its full amplitude after the drive signal is removed [5.5].

One method of measuring the Q-factor is to observe the envelope of the vibrating resonator and estimate the -3 dB points. The excitation frequency is tuned to the point where the amplitude of the vibration envelope falls to 70% of its maximum, i.e. the -3 dB points. The disadvantage of this method it that it is inaccurate, because of the error associated with the visual estimation of the -3 dB points. Testing in vacuum using a CCD camera and video monitor to observe the resonator is also problematic because of the loss in visual resolution. In point of fact, measuring the Q-factor of our lateral strain-gauge resonator by any visual method is problematic. The reason is that to estimate the -3 dB points it is necessary to have reasonable vibration amplitude, $\approx 5\,\mu\text{m}$ at $\times 600$ magnification. However, the response of the strain gauge becomes non-linear at an

amplitude of $\approx 2\,\mu m$ (see section 0), and above this amplitude the -3 dB points are no longer valid. The exception to this is the folded-flexure resonator, because it possesses a linear frequency response. The Q-factor of this resonator, shown in Figure 5.4, was measured using a scanning electron microscope and was found to be 18000 ± 2000 at a pressure of ≈ 1 Pa.

5.5.1 Optical detection

In order overcome the inaccuracy of the visual methods I have developed a novel optical technique for detecting the motion of the lateral resonator.

The general apparatus is shown in Figure 5.11. The resonator is illuminated using a laser and mono-mode optical fibre. The optical fibre is held in a micro manipulator (Karl Suss PH 100) so that its position can be accuracy controlled. When the end of the fibre is correctly positioned, an image of the resonator is formed by the light reflected from the surface of the resonator. Exciting the resonator (either electrostatically or with the piezo-drive scheme) causes this image to vibrate. The vibration is detected by measuring the intensity of the image at a fixed point with a photodiode.
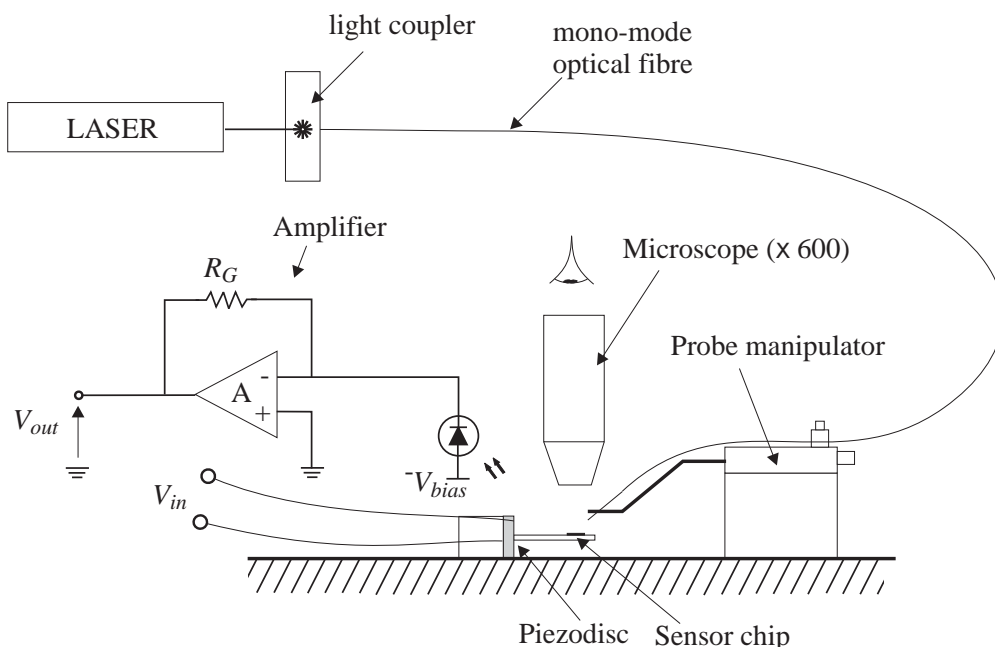

Figure 5.11 Schematic showing the apparatus used to for the novel optical pickup. An image of the resonator is formed by illuminating the resonator with via an optic fibre and laser. Here, the resonator is driven using an indirect piezo-dive and the motion detected by monitoring the intensity of the image at a fixed point with a photodiode.

The formation of the resonator image is shown in more detail in Figure 5.12. Along the paths ABC and ADE the light from the laser is reflected from the surface of the resonator to form an image on the plane Z. Consider the beam ABC, which is incident with an angle θ_i and is reflected with an angle θ_r. If the resonator is displaced a small distance Δx, then θ_i changes such that,

$$\delta\theta_i \approx \frac{\Delta x}{l_1}\cos\theta_i \qquad (5.6)$$

where l_1 is the path length AB. Similarly, if the resonator is displaced a small vertical distance Δy (which would be the case if a vertical mode were excited) then θ_i changes such that,

$$\delta\theta_i \approx \frac{\Delta y}{l_1}\sin\theta_i \qquad (5.7)$$

It follows that a change in position of the resonator causes a change in position of its image on the plane Z. Thus, by measuring the variation in radiation intensity at a fixed point on image with a photodiode the motion of the resonator can be determined. The change in position of the image at point C shown in Figure 5.12 is,

$$\Delta z \approx l_2\delta\theta_r \qquad (5.8)$$

where l_2 is the path length BC and θ_r the angle of reflection. The substitution of equations (5.6) and (5.7) into equation (5.8) yields a relationship between the displacement of the resonator and the shift in position of its image,

$$\Delta z \approx \frac{l_2}{l_1}\left[\Delta x\cos\theta_i + \Delta y\sin\theta_i\right] \qquad (5.9)$$

where $\theta_i = \theta_r$. It is clear from equation (5.9) that the position of the image is determined by the angle of incidence of the laser light, the displacement of the resonator and the ratio of the paths lengths l_1 and l_2. Thus, for a high sensitivity l_1 should be small ($\approx$ mm) and l_2 large ($\approx$ cm) and the photodiode positioned at the point on the image where the change in intensity is highest. Note that as the ratio of the paths lengths is increased, the light intensity incident of the photodiode decreases, resulting in a lower photocurrent and hence a lower signal to noise ratio.
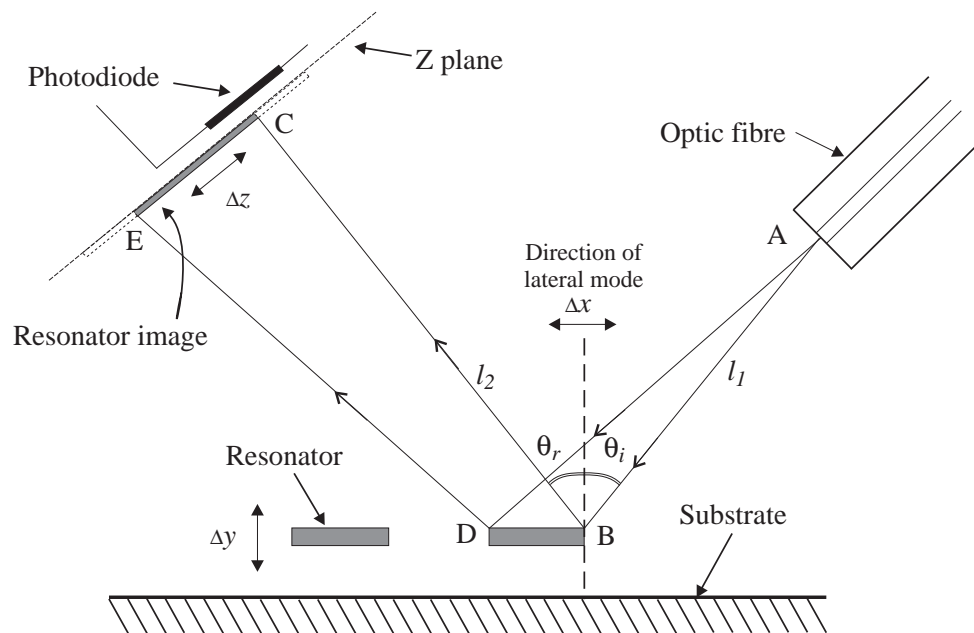
Figure 5.12 Schematic showing the formation and movement of the resonator image as the resonator moves. The reader is referred to the text for further explanation.

5.5.2 Experiments in air

Linear response

Figure 5.13 shows the linear (i.e. small deflection) amplitude and phase response of a type 'A' lateral strain gauge in air. The resonator was excited using the remote piezoelectric drive scheme and the amplitude and phase response were measured using the optical pickup technique described above. The direction of the frequency sweep in each case is indicated by the line type. Here, a positive sweep indicates a sweep from a low to a high frequency, while a negative sweep indicates the opposite. Note that both the positive and negative amplitude (and phase) response match, indicating a linear response. The Q-factor was determined from the frequency response to be 51.0 ± 1. The amplitude of oscillation at resonance was estimated from visual observation though an optical microscope to be 1 ± 0.25 μm. The amplitude of the piezoelectric drive signal was 7.75 $V_{pk\text{-}pk}$.

The sensitivity of the optical method is demonstrated by the amplitude response plot shown in Figure 5.14. Here, the amplitude of the piezoelectric drive voltage was reduced from 7.5 $V_{pk\text{-}pk}$ to 3.0 $V_{pk\text{-}pk}$, 1.5 $V_{pk\text{-}pk}$ and to finally to 0.75 $V_{pk\text{-}pk}$.
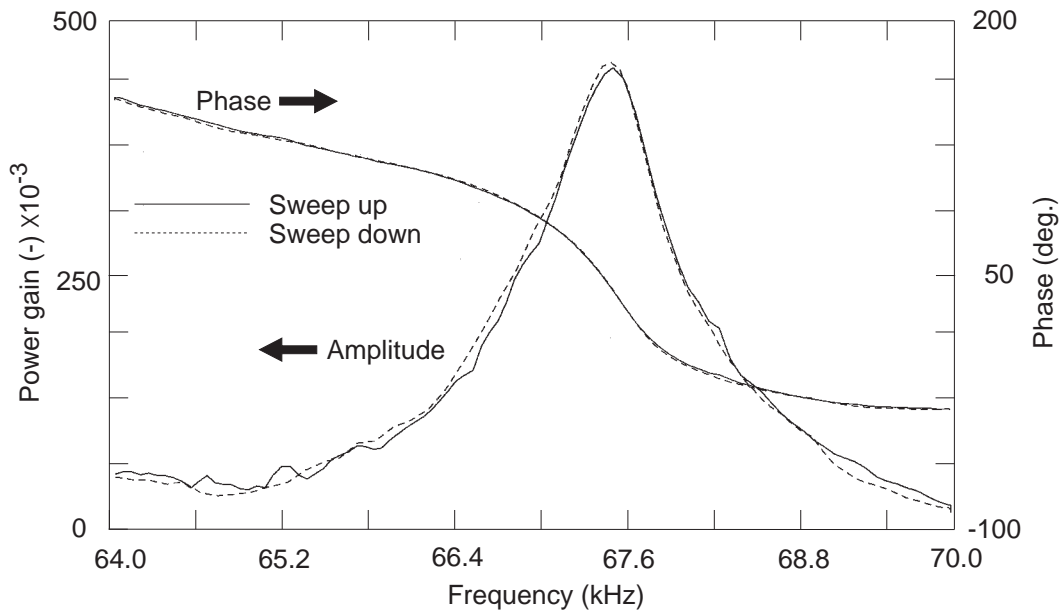
Figure 5.13. Linear amplitude and phase response of a lateral strain gauge (type 'A') operated in air. A linear response is indicated by the absence of any hysteresis between the positive frequency sweep (solid line) and the negative sweep (dotted line).
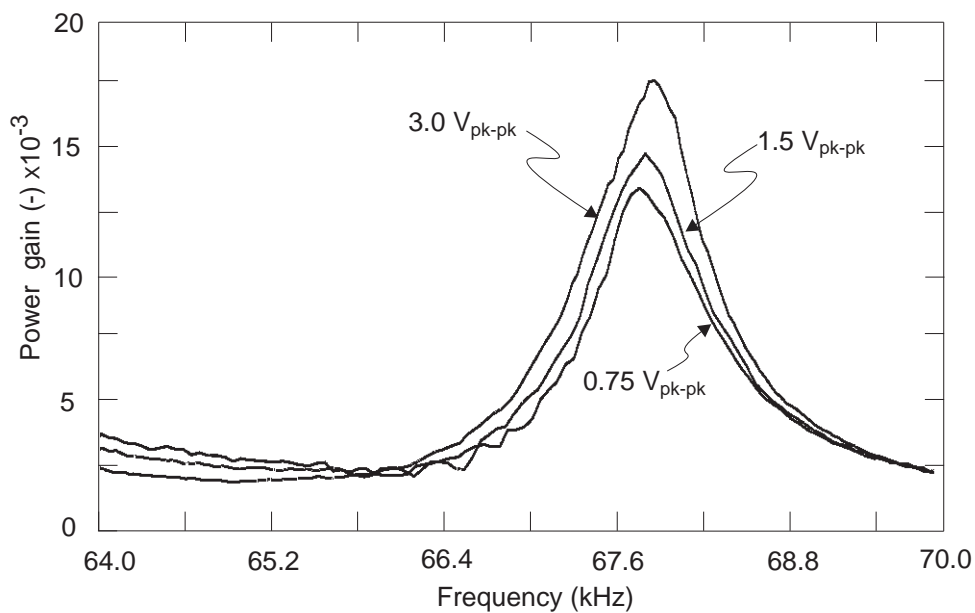

Figure 5.14 Linear amplitude response of lateral strain gauge (type 'A') for three different piezo-drive voltages. The negative frequency sweep response is omitted for clarity.

If it is assumed that as piezo-drive voltage is reduced by a factor of ten (i.e. 7.5 to 0.75 V_{pk-pk}) the amplitude of vibration also drops by a factor of ten, then it is reasonable to suggest that this optical detection method is sensitive to vibrations of at least a few tens

of nanometres, or less, given the noise-free response curve. Note this assumption has been made on the basis un-calibrated measurements, i.e. the relationships between the piezo-drive voltage, amplitude of vibration and the magnitude of the current generated by the photodiode (and thus the V_{out} in Figure 5.11) have not been determined.

Non-linear response

The non-linear amplitude and phase response of the lateral resonator (type 'A') is shown in Figure 5.15. Here, the amplitude of the piezoelectric drive signal was increased to 25 V_{pk-pk} to over-modulate the resonator. The effect of the non-linear spring rate was to bend the frequency response to the right, as is described in section 3.22 of Chapter 3. In this instance the level of the drive force was greater than the critical drive force, so that the frequency and phase response of the resonator became multi-valued. This is clear in Figure 5.15 where, with a positive frequency sweep (indicated by the solid line), the amplitude gradually increases until 68.26 kHz at which frequency it jumps to a lower value. On the other hand, with a negative frequency sweep (indicated by the dotted line) the amplitude gradually increases until at a frequency of 68.26 kHz it jumps up to a higher level. The hysteresis interval between the positive and negative frequency sweep is ≈ 660 Hz.
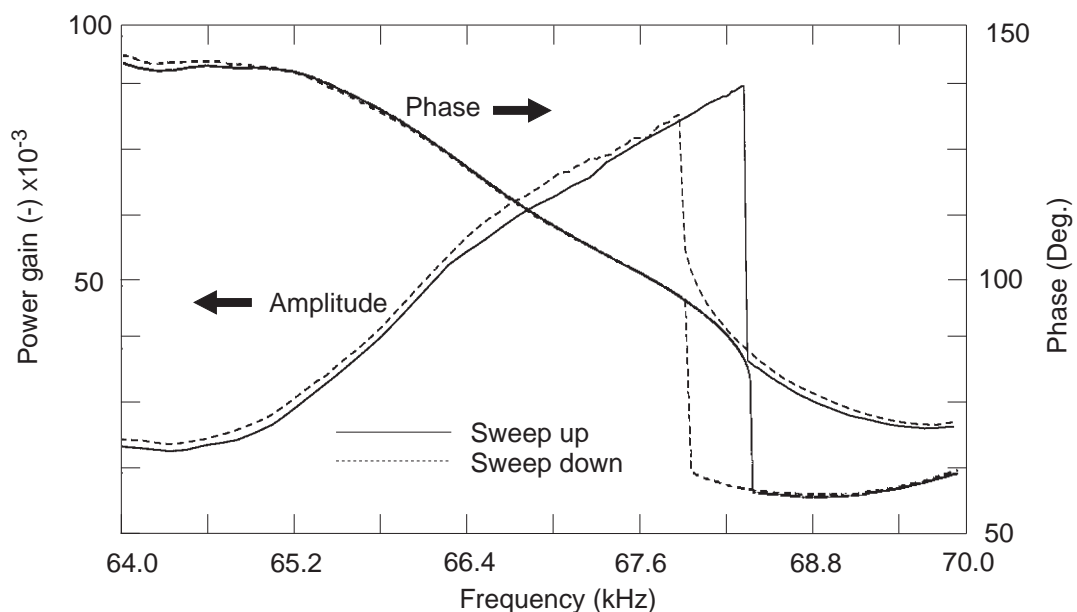
Figure 5.15 Non-linear amplitude and phase response of the lateral strain gauge design (type 'A') when operated in air. The region of instability, or hysteresis interval, is defined by bandwidth between the jumps in the response curve and is approximately 660 Hz.

The transition from a linear to a non-linear response for a 'type A' resonator is shown in Figure 5.16, where only a positive amplitude sweep is shown for the sake of clarity. At a low drive voltage (5 V_{pk-pk}) the response of the resonator is linear. The effect of an increase in the drive voltage (to 7.75 V_{pk-pk}) is to bend the response to the right, making it asymmetric. Increasing the drive voltage further (to 14 V_{pk-pk}) causes the response curve to become multi-valued and enter the region of instability. Visual observation of this lateral resonator showed that the non-linearity in the frequency response is significant when the amplitude of vibration is greater than $\approx$ 2 µm. This means that for linear operation the vibration amplitude must < 2 µm, which is a practical limitation because it restricts the magnitude of the motional sense current (see equation (3.45) of chapter 3). Note that the peak amplitudes of the response curves recorded in Figure 5.16 are constant, and do not follow that of a typical second order system with a cubic non-linearity, as is described in section 3.2.3 of chapter 3. The reason for this behaviour is unclear, and warrants further investigation. This behaviour could also mean that this optical pick-up technique ill-suited for application in a closed loop mode of operation.
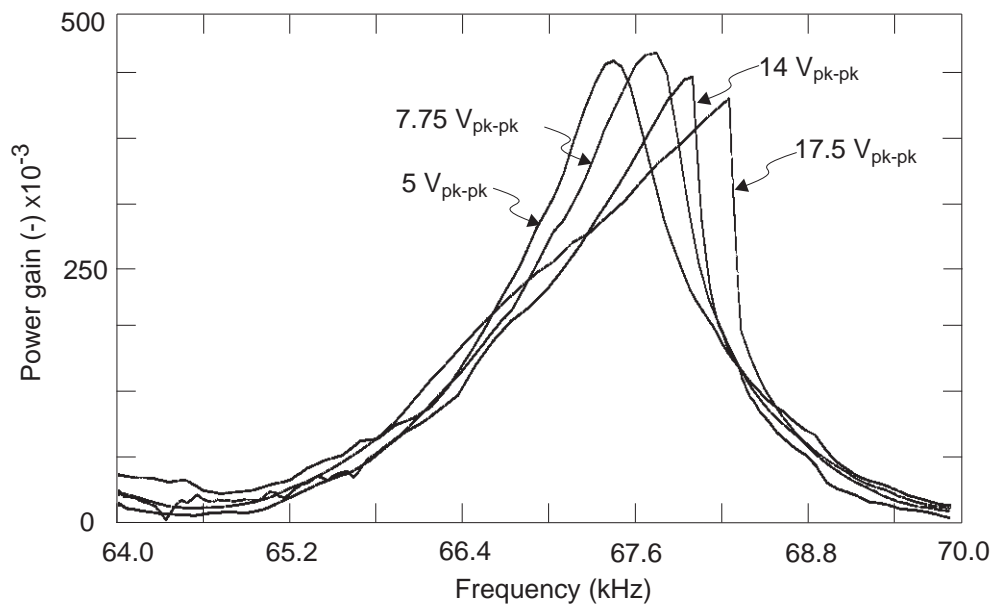
Figure 5.16 The transition from a linear to a non-linear response for a positive frequency sweep for a type 'A' resonator operated in air at atmospheric pressure. At 5 V_{pk-pk} the lateral resonator exhibits a linear response. Increasing the piezo-drive voltage to 7.75 V_{pk-pk} results in a asymmetric amplitude response. Increasing the drive voltage further past a critical value, 14 V_{pk-pk} leads to a multi-valued response curve that is characterised by a sudden jump in amplitude.

5.5.3 Q-factor variation with cavity pressure

To measure the variation in Q-factor with cavity pressure the resonator was housed in a vacuum chamber (bell jar) which was connected to an Edwards two stage high vacuum pump. The optical fibre and drive signal were routed via feed-throughs. Note that the use of a transparent housing (e.g. bell-jar) enabled an image of the resonator to be monitored on the *outside* of the vacuum system.

When measuring a high Q-factor, i.e. one greater than 1000, it is preferable to measure the time decay of the resonator rather than the frequencies of the -3 dB points. There are several reasons for this. First, the measurement period is short, typically less than 1 s. A disadvantage associated with optically based excitation and detection mechanisms is a thermally induced frequency-shift caused by the static heating of the resonator by the radiation source. Small variations in the incident power are reflected in the frequency stability of the resonator. Over a time period of 1 s these frequency shifts

are negligible. However over several minutes, the time needed to perform a frequency response measurement (using an HP-3536A Control Systems Analyser), significant thermally induced frequency shifts (up to 1 kHz) were observed. The importance of avoiding a (thermally induced) frequency shift is easily understood if one considers that the bandwidth of a resonator with a Q-factor of 18 000 and resonant frequency of 48 kHz, is ≈ 2.6 Hz. Thus, a change in resonant frequency of only 1 Hz during the measurement period leads to an error of approximately 50% in the measured Q-factor. The second reason is it is possible to excite the resonator using a fast-frequency sweep, or periodic chirp, whose power bandwidth is centred on the resonant frequency. This means that it is not necessary to accurately determine the resonant frequency, but only to know its approximate location.

Figure 5.17 shows a time domain response of the lateral resonator operating in a vacuum at a pressure of 10 Pa. The resonator was excited by a periodic chirp with a bandwidth of 1 kHz centred on the resonant frequency. The periodic chirp ceased after a time period of 100 ms, as indicated by the dotted line in Figure 5.17, and the response of the resonator (i.e. V_{out} in Figure 5.11) was recorded using the optical pick-up technique whose operation is outlined above. The Q-factor of the resonator was determined from the decay time, according to equation (5.5), and for this measurement was calculated to be $20\,800 \pm 400$. It is noted that the frequency of the recorded signal was not equal to the actual resonant frequency of the lateral resonator because, for this measurement the frequency resolution of the analyser was only set to ≈ 6 kHz.

To determine the variation of the Q-factor with cavity pressure a range of decay times were measured over a pressure range of 1×10^5 - 1×10^{-3} Pa and the Q-factor computed according to equation (5.5). The variation in decay time over a range of cavity pressures from 26 Pa to 13.2×10^2 Pa is illustrated graphically in Figure 5.18, where only the peak of the decay amplitudes are recorded. Here, the longest decay time is 74.5 ms corresponding to a Q-factor of ≈ 7000, whilst the shortest decay time of 13 ms corresponds to a Q-factor of ≈ 1200.
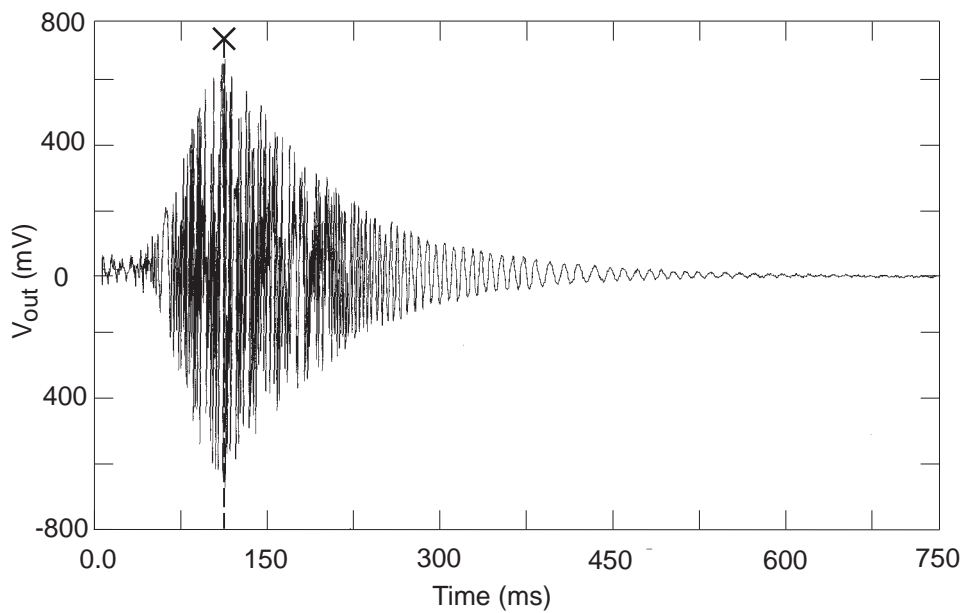
Figure 5.17 Typical decay time of lateral resonator measured using piezo-drive and optical pickup.
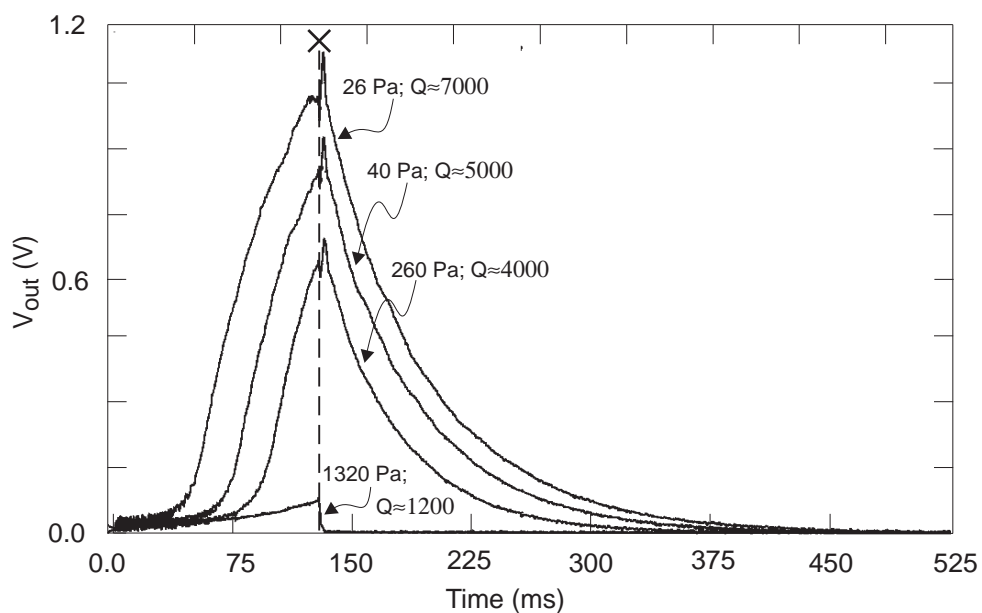

Figure 5.18 Variation of experimental decay time with cavity pressure for the lateral resonant strain gauge over a range of pressures from 26 Pa to 13.2 $\times10^2$ Pa.

Discussion

The variation of the Q-factor of the lateral strain gauge with cavity pressure is shown in Figure 5.18. Three main pressure regions are distinguished, namely, the viscous damping region, the molecular or Knudsen region and the intrinsic region, see section 2.32 of chapter 2. In the viscous region, between $\approx$ 50 Pa and atmospheric pressure, the

Q-factor of the resonator is dominated by the viscous drag force acting on the resonator. In the molecular or Knudsen region, between $\approx$ 50 Pa and $\approx$ 5 Pa, damping is caused by the collision of air molecules with the resonator and the Q-factor, and is inversely proportional to the pressure [5.6]. In the third (intrinsic) region below $\approx$ 5 Pa, the air pressure is so low that molecular damping is negligible compared to the intrinsic damping of the vibrating resonator. In this region the mechanical Q-factor of the resonator is at a maximum and was found to be 26 000 at 10^{-3} Pa.

Ideally, the intrinsic Q-factor of a resonant pressure sensor should be as high as possible (within the limits of operation of the electronic oscillator used for closed loop control). This is because increasing the Q-factor leads to a higher pressure resolution (or, alternatively, reduces the need for an oscillator with a low phase uncertainty) and lowers the amplitude of the drive/polarisation voltages needed to sustain a given amplitude of vibration. A higher Q-factor should also translate into an improved long term stability. Hence, for high performance pressure sensors a high Q-factor is important. As a comparison, most of the resonant pressure sensors reviewed in Table 1.1 of chapter 1 have a higher Q-factor than that measured for lateral resonator (26 000). To increase the Q-factor of the lateral resonator it would be necessary to reduce the intrinsic energy losses and/or the energy loss through the resonator supports. Intrinsic losses may be difficult to reduce because they are inherently related to the crystal structure of the structural polysilicon layer. One way of reducing the support losses would be to use a balanced resonator configuration, such as the double-ended tuning fork.
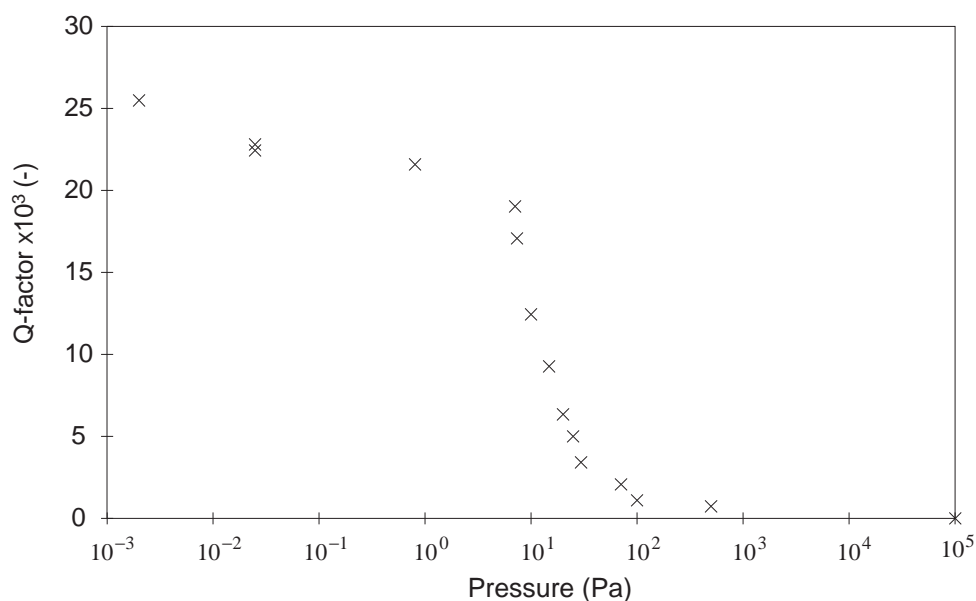
Figure 5.19 Variation of the Q-factor with cavity pressure. Errors are omitted for clarity but typically 10%, apart from the measurement at atmospheric pressure.

5.6 Pressure sensor electronics

The primary task of the pressure sensor electronics is to sustain the oscillation of the resonator over a pre-defined pressure and temperature range. This is usually achieved by placing the mechanical resonator in the feedback network of an electronic oscillator, so that it forms the frequency determining element. This is illustrated in Figure 5.20a where an oscillator is formed from a resonator and an amplifier, which controls the phase shift and gain to meet the oscillation conditions [5.8]. Another method of forming an electronic oscillator is to use the phase locked loop concept shown in Figure 5.20b. Here, a phase detector is used to compare the phase difference between the drive signal and sense signal. The drive signal is generated by a voltage controlled oscillator (VCO), whose frequency is set by the output of the phase detector. If the phase of drive signal and sense signal changes, due to a change in the frequency of the sense signal, the output from the phase detector automatically adjusts of the frequency VCO to bring it back to a fixed phase relation with the pickup. If the fixed phase relationship is set to the phase shift of the mechanical resonator at resonance, then the system will oscillate at the resonant frequency of the mechanical resonator [5.9].

Within the electronic oscillators described above several stages are distinguished, including, amplification, impedance matching, signal conditioning (buffering and filtering) and automatic gain control. When integrating a mechanical microresonator into a closed loop mode of operation the first, and often the most problematic stage is the measurement and subsequent amplification of the sense signal. This is because the magnitude of the sense signal is usually very small and may be obscured by electrical cross-talk and/or electrical noise.
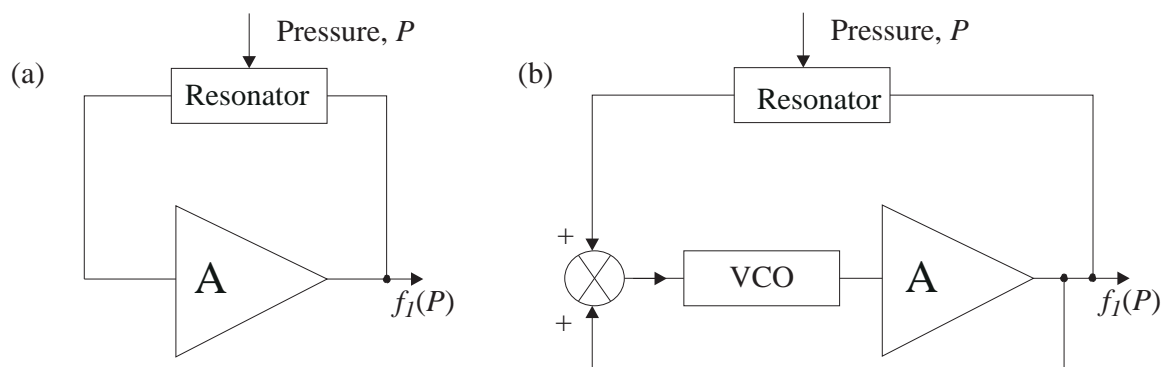
Figure 5.20 Two-port mode resonant sensor oscillator electronics,(a) feedback amplifier and (b) using a phase locked loop.

As is mentioned earlier, normal operation of the lateral resonator proved problematic precisely for these reasons. It was found that the high level of cross-talk between the drive and sense combs of the resonator was sufficient to saturate the amplifier used to measure the motional sense current (predicted to be less than 0.2 nA, see section 3.5.2 of chapter 3). However, as is described in the next section, this problem was bypassed using the indirect piezoelectric drive scheme, which enabled effective shielding of the drive signal and so a reduction in the level of electrical cross-talk.

5.6.1 Indirect piezoelectric excitation and capacitive detection.

To operate the lateral resonator using the indirect piezoelectric drive and capacitive detection scheme a pressure chip was first mounted on an electrically conductive header. Electrical connections were made to the ground plane and either one of the comb capacitors (both of which were effectively sense combs). An electrical shield was placed around the piezo-drive and connected to electrical ground. The header chip was also grounded. The flying leads to the piezoelectric disc were also shielded as was the cantilever that supported the header chip.

The motional sense current was measured using a high gain ($1 \times 10^{6\Omega}$) transimpedance amplifier (i.e. a current to voltage amplifier). One electrode of the sense comb was biased by connecting it to the inverting input of the transimpedance amplifier, and connecting the non-inverting input of the amplifier to a bias voltage V_s. The other electrode was biased with a voltage $-V_s$, so that the total voltage acting across the sense comb was $2V_s$, in this case equal to 30 V. The output of the transimpedance amplifier was further amplified using a precision op-amp to give an overall current to voltage gain of $1 \times 10^{8\Omega}$, see Figure 5.21. To minimise parasitic capacitance the electronics and header chip were integrated onto a printed circuit board and the header chip was located close to the input of the transimpedance amplifier. The complete assembly was then mounted inside a vacuum chamber, which was evacuated to maximise the Q-factor of the resonator.
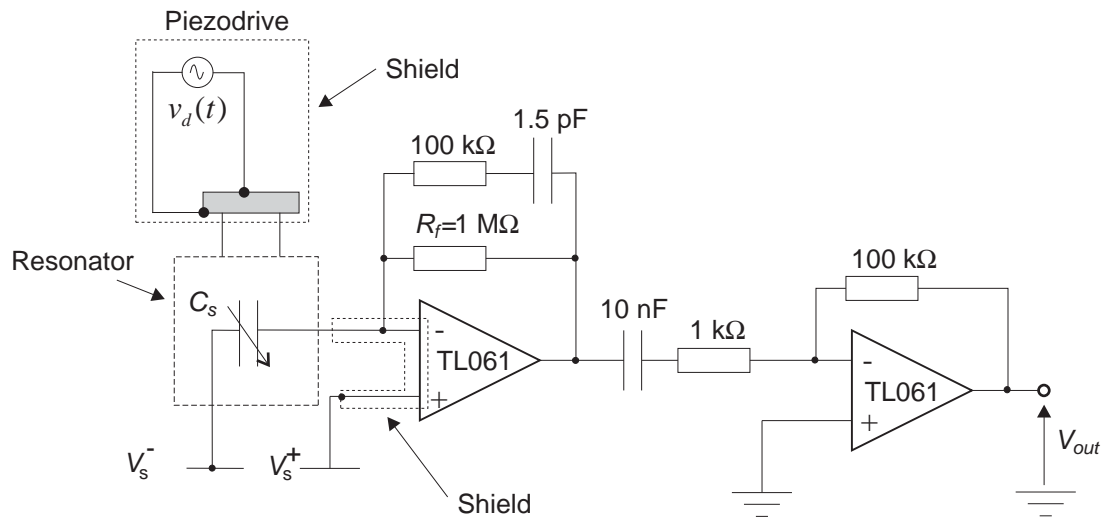
Figure 5.21 Circuit diagram shown in primary amplification stage used to measure the motional sense current of the lateral resonator. The gain of a transimpedance amplifier is equal to the feedback impedance.

5.6.2 Transfer function

Figure 5.23 shows a measured non-linear frequency response of a lateral resonator (type 'B') operated using the indirect piezoelectric drive and capacitive detection scheme. The transfer function was measured using a HP-3536A Control Systems Analyser. The piezoelectric disc was driven directly from the Analyser with a 250 mV$_{pk-pk}$ sinusoid and the motional sense current measured via the amplification stage shown in Figure 5.21. The non-linearity in the frequency and phase responses is clear, and for this measurement the hysteresis is 3.26 kHz. The effectiveness of the electrostatic shield is demonstrated by the noise free response curve.
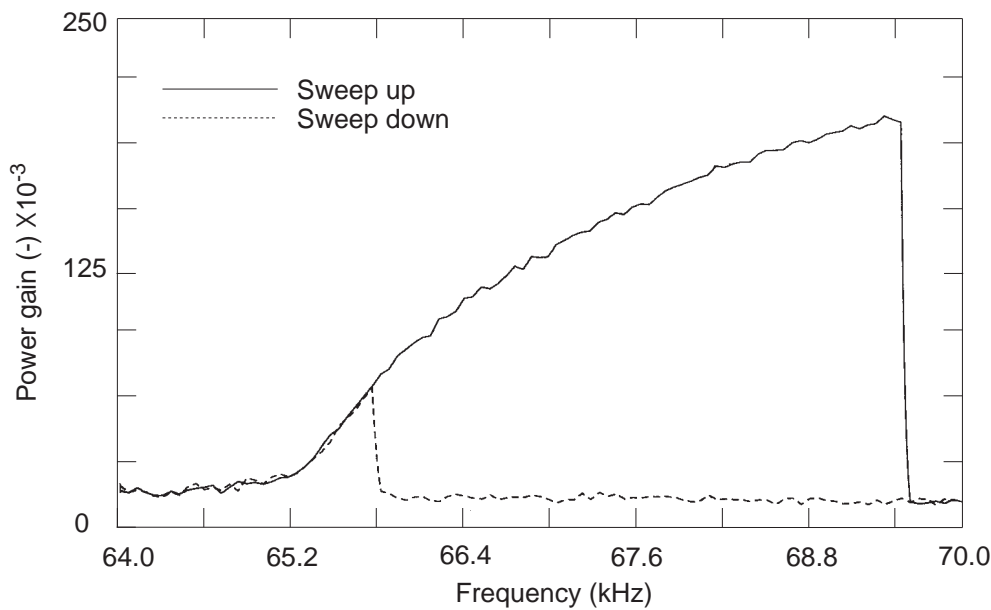
Figure 5.22 Non-linear amplitude response of the lateral resonator (type 'B'). The resonator was driven using the indirect piezoelectric drive scheme and its motion measured using capacitive detection.

Figure 5.23 shows the amplitude response of the same lateral resonator as the peak to peak drive voltage applied to the piezoelectric disk was reduced from 200 mV$_{pk-pk}$ to 50 mV$_{pk-pk}$, in 50 mV$_{pk-pk}$ steps. As the drive voltage was lowered, the amplitude of vibration decreased and the magnitude of the non-linearity was reduced. A linear transfer function was obtained by further reducing the amplitude of the drive signal to 10 mV$_{pk-pk}$ (the lowest amplitude sinusoid provided by the HP-3536A Control Systems Analyser). Note that a linear response implies a small amplitude of vibration ($< 2\,\mu$m) and consequently a small motional sense current. This is reflected by the noisy response function.
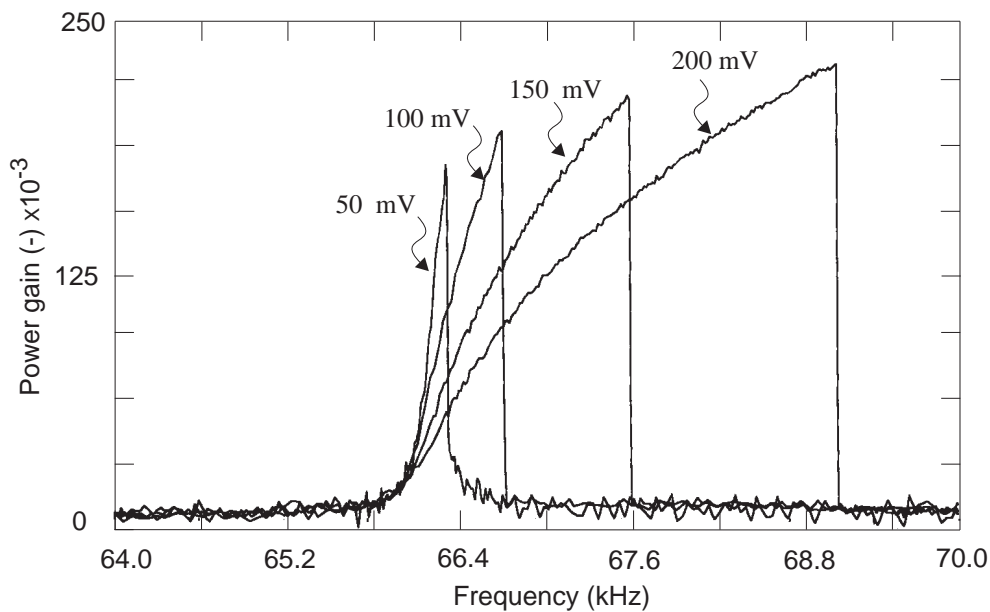
Figure 5.23 Non-linear transfer functions of the lateral resonator (type 'B'), measured using piezoelectric drive and capacitive pickup. The drive voltage is shown for each curve.

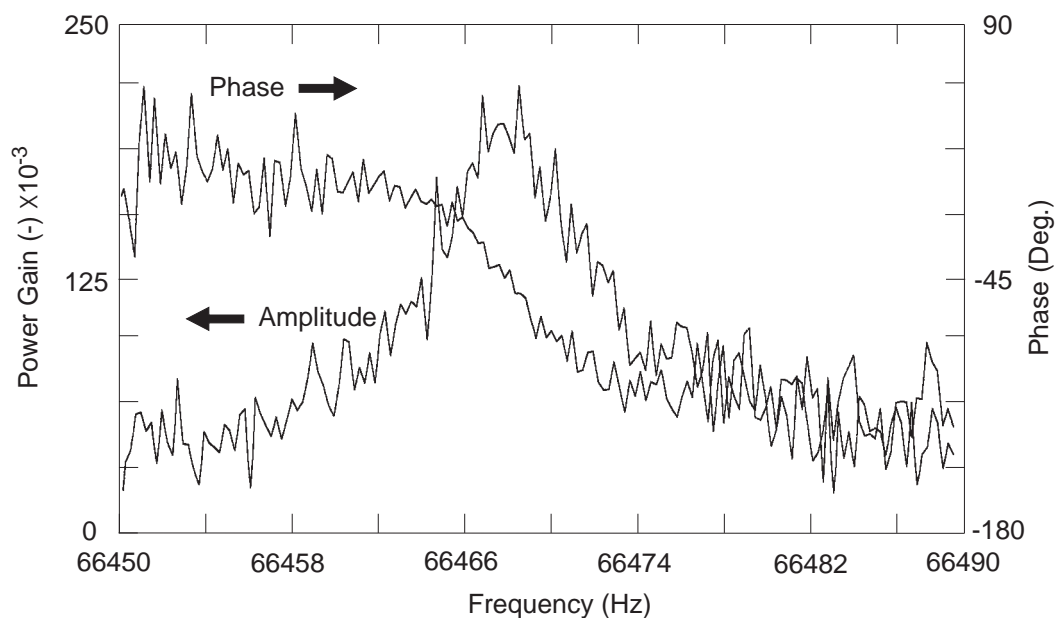*Figure 5.24 Linear amplitude response of the lateral resonator (type 'B'), measured using the shielded indirect piezo-drive and capacitive pickup.*

These measurements demonstrate that it is feasible to detect the motion of the lateral resonator using the capacitive pick-up, and moreover obtain a *linear* response, provided the electrical cross-talk is minimised. It is likely that the signal to noise ratio

could be increased by optimising the design of the electronics circuitry and/or by improving the electrical shielding. The Q-factor of the amplitude response shown in Figure 5.23 was ascertained by fitting a curve to the data and found to be 9660 ± 50 at a cavity pressure of 10 Pa. This Q-factor is lower than that of the lateral resonator given in the previous section. The reason for this discrepancy is thought to be due to the internal losses caused the additional layer of aluminium deposited onto the resonator to increase its electrical conductivity [5.2].

5.7 Conclusions

In this chapter the basic operation of the lateral resonant pressure sensor has been demonstrated. Preliminary measurements, obtained via optical observation of the lateral resonator, show that the pressure sensor has a relative pressure sensitivity of 0.54 - 3.44 ppm/Pa, a range of at least 4×10^5 Pa and a maximum over-pressure of at least 3 times the range. The experimental and theoretical relative pressure sensitivities were found to be in good agreement. The temperature sensitivity of a pressure sensitive lateral resonator (type 'B') was measured to be -240 ppm/^{o}C, whilst that of an identical reference resonator was measured to be -114 ppm/^{o}C.

It was found that the high drive voltages needed to excite the resonator in air led to a breakdown in the dielectric insulation layer, especially when electrical connections to the contact pads were made via wire bonds. Moreover, a low electrical impedance between the drive and sense comb resulted in a high level of cross talk that obscured the motional sense current, even in vacuum when lower drive voltages were employed. To overcome these problems the resonator was excited using an indirect piezoelectric drive scheme that allowed an electrical shield to be introduced, and so the level of cross-talk greatly reduced. This piezoelectric drive scheme was employed together with a new optical technique to measure the Q-factor variation of the lateral resonator with cavity pressure. Using this technique, the Q-factor of the lateral resonator was measured to be 51 in air at atmospheric pressure and 26 000 in high vacuum, slightly lower than other resonant pressure sensors. The transition from a linear to a non-linear response was found to occur when the amplitude of vibration of the unloaded (type 'A') resonator exceeded $\approx 2 \mu$m. In the lateral resonator design this limitation on the amplitude of vibration is a disadvantages because it limits the magnitude of the motional sense current.

Finally, the first stages of the integration of the lateral resonator into a self-oscillating circuit were described. The resonator was excited using the indirect piezoelectric drive scheme and its motion detected by measuring the motional sense current with a precision high gain amplifier. The measured linear response function demonstrates that the operation of the lateral resonator is feasible when cross-talk is minimised. This subject is covered further in the concluding chapter.

References

[5.1]   Pratt R. I., Johnson G. C., Howe R. T. and Chang J. C., Micromechanical structures for thin film characterisation, *6th Int. Conf. Solid State Sensors and Actuators*, *(Transducers '91)* (1991) 204-207.

[5.2]   Gopel W., Hesse J. and Zemel J. N. (eds.), *Sensors a comprehensive survey, Mechanical sensors*, Vol. 7, Weinham, New York, (1994) 513-556.

[5.3]   Brignell J. and White N., *Intelligent sensor systems*, IOP Publishing, (1994).

[5.4]   Biebl M., Brandl G., and Howe R. T., Youngs's modulus of *in situ* phosphorus-doped polysilicon, *8th Int. Conf. Solid State Sensors and Actuators*, *(Transducers '95)* (1991) 251-PA8.

[5.5]   Tang W. C.-K., Electrostatic comb drive for resonant sensor and actuator applications, *PhD Thesis*, University of California, Berkeley, (1990).

[5.6]   Blom F. R., Bouwstra S., Elwenospoek M. and Fluitman J. H. J., Dependence of the quality factor of micromachined silicon beam resonators on pressure and geometry, *J. Vac. Sci. Technol.,* Vol. B10 No. 1 (1992) 19-26.

[5.7]   Kirman R., Druck Ltd., personal communication.

[5.8]   van Mullem C., Micromachined silicon integrated resonant sensors, *PhD Thesis*, University of Twente, Enschede, The Netherlands, (1993).

[5.9]   Gardner F. M., *Phaselock techniques*, second edition, John Wiley & Sons, New York, (1979).

Chapter 6

Conclusions and future research

This final chapter concludes the research presented in this thesis and proposes future work. The limitations of the current lateral resonant pressure sensor design are discussed and a new fabrication route, designed to bypass these limitations, is presented.

6.1 General conclusions

Currently, there is an increasing demand for resonant pressure sensors because they are capable of providing highly accurate pressure measurements that are extremely stable over time, so meeting the stringent requirements of high performance applications, e.g., in the calibration of pneumatically driven avionic systems and in precision metrology. Silicon micromachining has played an important part in the development of the modern pressure sensor and, over the last ten years, this technology has been applied to produce resonant pressure sensors with the aim of replacing conventional precision machined devices.

Some benefits of silicon micromachining are the ability to fabricate low-cost micron-sized mechanical structures with precise control of material properties and dimensions. However, the development of current silicon based resonant pressure sensors is restricted by the use of bulk micromachining processes used in fabrication. In this research, these restrictions have been bypassed by employing surface micromachining technology and a new type of resonant pressure sensor has been realised.

The design of the pressure sensor was presented in chapter 2. The pressure sensor is based upon a laterally driven resonant strain-gauge that is ≈ 450 μm long by ≈ 150 μm wide, with minimum feature width of 3 μm. The resonator consists of an inertial mass

supported by a hammock flexure, and is located centrally on a $\approx$ 1 mm^2 bulk-etched single crystal silicon (SCS) diaphragm.

There are several advantages of the lateral resonator design over resonant (pressure) sensors that oscillate in a mode that is perpendicular to the substrate. First, in the lateral resonator design, the relative amplitudes and frequencies of spurious modes can be controlled by adjusting the dimension of the supporting flexure and the inertial mass. Second, the fundamental mode of oscillation of the resonator and diaphragm are perpendicular, so that the possibility of mode coupling between the resonator and the diaphragm is reduced. One spurious mode that may prove problematic is a fundamental vertical mode, because of the vertical force created by charge imaging on the ground plane. However, in my resonator design the potential for mode coupling between the lateral and vertical modes was reduced by employing a hammock flexure of rectangular cross-section, so that the two modes were widely spaced in the frequency domain. Finally, the lateral mode of oscillation means that the Q-factor of the resonator should be less sensitive to changes in cavity gas levels that may occur over the lifetime of the sensor which should lead to better long term stability.

Expressions for the fundamental lateral resonant frequency and gauge factor of the lateral resonator were derived using Rayleigh's method. The theory showed that the gauge factor of the lateral resonator is maximised when the inertial mass is supported by long thin flexures that possess a low residual strain, preferably below 10^{-4} ε. An additional term included in the analysis showed that of the stretching of the flexure under a lateral displacement resulted in a non-linear (cubic) term in the force-deflection relationship.

The relative pressure sensitivity of the pressure sensor was determined by using linear elastic theory to model the relationship between the pressure applied to the diaphragm and the strain applied to the lateral resonator. The theory showed that the pressure sensitivity is determined by the gauge factor of the lateral resonator, and thereafter the diaphragm side-length to thickness ratio, which is selected for the required pressure range. Using an assumed frequency resolution of 2 ppm, the pressure resolution of the lateral resonant pressure sensor when operated in a closed loop mode was predicted to be $\approx$ 0.82 Pa.

In Chapter 3 the operation and response of the lateral resonator was investigated, beginning with a review of microresonator excitation and detection mechanisms. Of the

various excitation and detection mechanisms available, an electrostatic excitation and capacitive detection scheme based upon interdigitised comb capacitors was employed to operate the lateral resonator. Some resonators also possessed an integrated piezoresistive pick-up. These mechanisms were used because they integrated well with the with the fabrication scheme. The piezoresistive pick-up also offers the potential for higher signal amplitudes because it is based on the modulation of an external energy flow and so should be less susceptible to electrical cross-talk.

One characteristic of resonant strain gauges is that they possess a non-linear spring rate. The non-linearity is due to deflection induced axial strain, and is commonly known as the hard spring effect. The hard spring effect accounts for the bias induced frequency shift and the non-linear frequency response of a resonator, the latter of which is seen when the resonator is over-modulated. To avoid the frequency shift associated with this non-linearity, a stable bias voltage should be used and the vibration amplitude restricted to avoid deflection induced axial strain.

The linear response of the lateral resonator, when operated with an electrostatic excitation and capacitive detection scheme, was modelled using an energy approach. The analysis showed that in the one-port mode the response is similar to a quartz crystal resonator, while in the two port mode it is similar to that of a second order (bandpass) electromechanical filter. The analysis also showed how, in the one-port mode, the measured resonant frequency is shifted by the presence of external parallel capacitive loads, an effect well known as parallel resonance. It was concluded that because these loads may change, the resonant frequency should be measured by monitoring a motional sense current rather than a motional sense voltage. It was also concluded that the operation of the resonator in the one-port mode would be problematic because the motional admittance was very small (≈ 3.5 nS) and so likely to be obscured by parallel parasitic capacitance. The alternative mode of operation, the two port mode, has the advantage that the energy of the drive and sense signals are separated. This implies that detection signal should be easier to monitor than in the one port mode, although the response can still be degraded by electrical coupling, or cross-talk, especially when the amplitude of the motional sense signal is small.

In Chapter 4 the fabrication of the pressure sensor was described. The lateral resonator was fabricated using surface micromachining, while the diaphragm was formed using a conventional anisotropic KOH etch. The critical materials used in the production

of the pressure sensor were low stress silicon nitride and low-stress mechanical-grade structural polysilicon. The critical process steps were the control of the polysilicon residual strain, the dry etching of the microstructures and stiction. The residual strain was controlled by proper control of the deposition conditions and the use of a post deposition annealing step. The dry etching of the microstructures was optimised by controlling the gas chemistry and etch time. The potential problem of stiction was successfully avoided by freeze drying the microstructures. Unfortunately, the resistivity of the polysilicon was found to be rather high at $\approx 260 \text{ k}\Omega/$. It is thought that this was due an incorrect gas flow during processing. However, this problem was overcome by depositing a thin (≈ 40 nm) film of aluminium onto the surface of the resonator.

An array of test microstructures was integrated onto the wafer to help characterise the fabrication process and measure the mechanical properties of the structural polysilicon layer. The residual strain was calculated to be $\approx 3.5 \times 10^{-5} \varepsilon$, which is in the expected range, while Young's modulus of polysilicon was calculated to be ≈ 94 GPa, which is somewhat lower than the expect values of 130 - 175 GPa. The reason is thought to be a variation in the dimensions of the flexures cause by a variation in the RIE process. The test structures integrated onto wafer suggest that the processing envelope can be expanded to give longer and thicker flexures, which will result in a higher capacitance gradient and a lower spring rate. Further processing, using a comprehensive array of tests structures, is required to determine the limitation of the fabrication process, so that the optimum pressure sensor can be designed and successfully commercialised.

The evaluation of the pressure sensor was described in Chapter 5. Preliminary results, obtained via visual observation of the vibrating strain gauge, show that the resonant pressure sensor possesses a relative pressure sensitivity of 0.5 - 3.4 ppm/Pa, range of up to 4×10^{5} Pa and a maximum over pressure that is at least 3 times the range. The experimental relative pressure sensitivities were shown to be in good agreement with the theoretical values. The linear temperature sensitivity of the pressure sensor over a temperature range from 19 $^{\circ}$C to 92°C was found to be -240 ppm/$^{\circ}$C, whilst that of a reference resonator, that has possible uses for temperature compensation, was found to be -114 ppm/$^{\circ}$C.

The variation of the Q-factor of the lateral resonator with cavity pressure was measured using a novel optical technique that is based on the modulation of an image of

resonator. Experimental results show that the lateral resonator has a Q-factor in air of 51 rising to 26 000 in high vacuum. A higher Q-factor would be advantageous in terms of an improved performance. As a comparison, most of the resonant pressure sensors reviewed in Table 1.1 of chapter 1 have a Q-factor in excess of 26 000. Further work is required to determined whether the relatively low Q-factor of the lateral resonator in high vacuum is a result of excessive energy loss at the supports of the resonator, due to the unbalanced mode of oscillation, or simply a high intrinsic loss in the polysilicon itself.

In practice it was found that the level of cross-talk in the lateral resonator was high enough to obscure the motional sense current, which was predicted to be in the sub-nA range in chapter 3. It is concluded then, that small motional current and high level of cross-talk present a disadvantage for this resonator design. Significantly increasing the motional sense current is difficult with the lateral resonator design for two reasons. First, the amplitude of oscillation is restricted by the need to avoid a deflection induced frequency shift. In the lateral resonator design types 'A' and 'B' a deflection induced frequency shift was observed when the vibration amplitudes exceeded ≈ 2 μm. Second, the fabrication process limits the thickness of the resonator to a few microns. This limits the magnitude of the capacitance gradient dC/dx, and consequently the motional sense current. The high level of cross-talk seen in the lateral resonator is thought to be due, in part, to the additional layer of aluminium that was deposited over the wafer to increase the electrical conductivity of the structural polysilicon. Unfortunately this layer also shorted the piezoresistive pick-up so that its uses as an alternative means of avoiding electrical cross-talk could not be tested.

To overcome the problem of electrical cross-talk an indirect drive scheme was employed that allowed effective shielding of the drive signal. This demonstrated that the motional sense current can be measured provided the level of cross-talk can be sufficiently reduced. Whilst the use of an indirect drive scheme was not ideal, it avoided the necessity of a further process run that was required to allow the shield to be integrated into the sensor chip itself. Using this technique, a linear transfer function of the lateral resonator was measured using a precision amplifier with a current to voltage gain of $1 \times 10^{8\Omega}$. Further work should enable the sensor to be operated in a closed loop mode and so allow the long term stability of the pressure sensor to be assessed.

6.2 Future research

In summary the objectives of this research have been fulfilled: a new type of surface micromachined pressure sensor has been designed, successfully fabricated and exhibits an impressive relative pressure sensitivity over a wide pressure range. This pressure sensor offers a viable alternative to current devices, provided the long term stability of the pressure sensor is comparable. A comprehensive literature research reveals that little is known about the long term stability of polysilicon resonators. It is probable that the intrinsic stability of polysilicon is lower than SCS, given its less ideal crystal structure. However, further work is needed to confirm this. In my research this interesting topic was not investigated due to the difficulty encountered in operating the resonator in a closed loop mode, because of the high level of cross-talk and the small motional sense current. Thus, further work is needed to reduce the level of cross-talk reduced and/or increase the magnitude of the sense signal.

As is mentioned previously, other researchers have demonstrated that an integrated electrostatic shield is effective in significantly reducing electrical cross-talk. A second generation device should incorporate such a shield. However, a significant increase in the magnitude of the motional sense current (by at least factor of 100) is impractical using surface micromachining. One solution is to use an on-chip amplifier to measure the motional sense current. Whilst this is possibly the best technological solution, the use of an integrated amplifier is only economically viable where the sensor is to be sold in high volume, e.g. in the automotive sector, because of the additional processing costs. Another option is to use a more efficient detection mechanism, such as piezoresistive detection, which offers the potential for generating higher motional sense signals, and greater immunity to electrical cross-talk. Perhaps the best way forward is to combine the advantages of a piezoresistive pick-up with a new etching technology, known as deep reactive ion etching, that allows the fabrication of truly 3-dimensional SCS microstructures.

Deep reactive ion etching is a relatively new etching process that enables SCS to be etched to depths from 20 µm to over 300 µm, whilst retaining an anisotropic profile, i.e. vertical side-walls. This means that the thickness of the lateral resonator can be increased by at least an order of magnitude, leading to an increased separation of the vertical and lateral modes and, in the case of capacitive detection, an increase in the

motional sense current of at least two orders of magnitude. Furthermore, it enables the microstructure to be fabricated from SCS, so the question of the suitability of polysilicon as a resonator material is bypassed. A further benefit of SCS is that it is inherently stress free, unlike LPCVD polysilicon, where proper control of deposition conditions and further post processing annealing is required to control the residual strain.

One method of fabricating a free standing microstructure is to create a buried cavity, by etching a recess in a SCS substrate and then fusion bonding this substrate to another. One substrate is then thinned (using chemical mechanical polishing, for example) to the desired thickness of the microstructure, between 20 μm and 300 μm depending on the microstructure design. The thinned substrate is then patterned so that the microstructure is located over the buried cavity. Etching through to the buried cavity releases the microstructure in the same way as the removal of the sacrificial oxide layer in micromachining [6.10], see Figure 6.1.
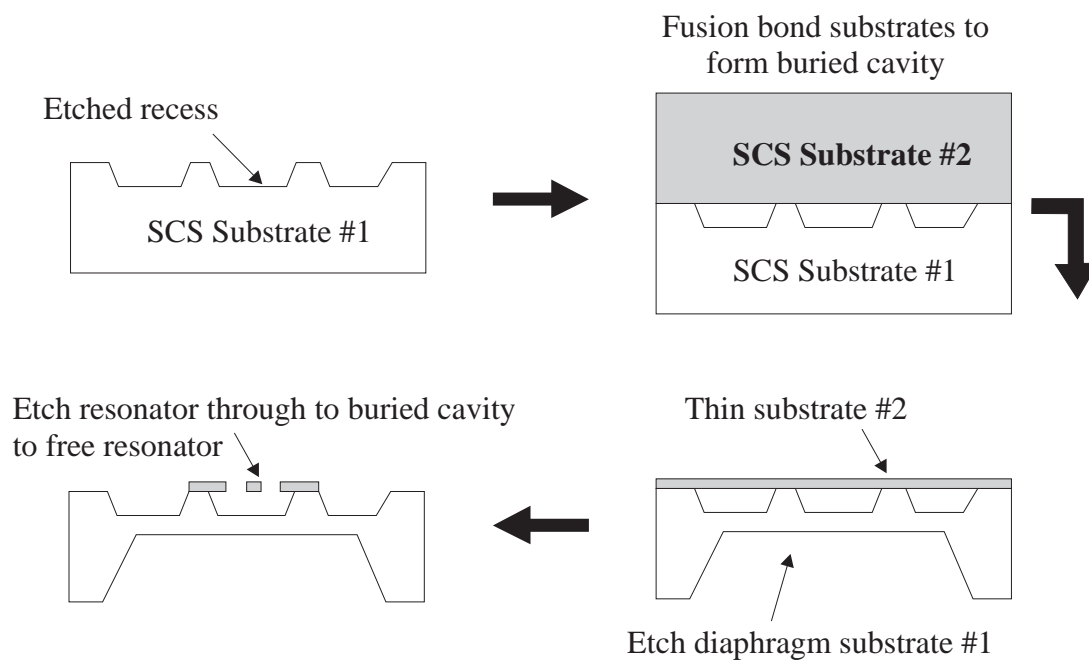

Figure 6.1 Proposed lateral resonant pressure sensor fabrication scheme employing deep reactive ion etching and silicon fusion bonding.

This process is currently being developed at Druck Ltd. Its progress is beyond the scope of this thesis, but the author hopes to fabricate second generation lateral resonant pressure sensors using this new technology.

References

[6.10] Klaassen E. H., Peterson K., Nowonlski M., Logn J., Maluf N., Brown J., Storrment C., McCulley W., and Kovacs G. T. A., Silicon fusion bonding and deep reactive ion etching, a new technology for microstructures, *Proc. 8th Int. Conf. Solid State Sensors and Actuators*, (*Transducers '95),* Stockholm (1995) 139-C3.

Appendix 1

Process flow: lateral resonant pressure sensor

Wafers: *P*-type ⟨100⟩ double sided polished resistivity 3-4 Ωcm

1. Measure and mark
Objective: To measure the variation in thickness of the wafer
Equipment: HDM thickness measuring meter

2. Ultrasonic clean in DIW
Objective: To remove particulates from wafer before standard clean
Equipment: Ultrasonic bath

3. Standard clean
Objective: To remove organic (fuming nitric) and metallic components (hot nitric)
Equipment: Standard cleaning station
Fuming nitric bath 1 > 5 min
Fuming nitric bath 2 > 5 min
Quick dump rinse (QDR) until conductivity < 0.1 μS
Heated (70 $^{\mathrm{O}}$C) nitric > 15 min
Quick dump rinse (QDR) until conductivity < 0.1 μS
Spin dry

4. Solid state boron diffusion
Objective: Diffusion of boron ground plane
Equipment: Tempress Omega junior furnace for solid source boron diffusion
N_2-1l/min
Temperature -1135 $^{\mathrm{O}}$C
Time - 4 h

5. LPCVD low stress silicon rich nitride
Objective: To deposit 250 nm of LPCVD low stress nitride
Equipment: Tempress LPCVD system for silicon(oxy) nitride
Pressure - 200 mTorr
Temperature - 850 $^{\mathrm{O}}$C
Dichlorosilane (DCS) - 70 sccm
NH_3 - 18 sccm
Time 60 min

6. Photolithography backside
Objective: Pattern backside nitride with mask DA
Equipment: Electronic Visions double sided mask aligner, single sided mode.
De-hydrate 200 $^{\mathrm{O}}$C > 30 min
0_2 - plasma 300 $^{\mathrm{O}}$C (high humidity)

HMDS 30 s 4000 rpm
Positive S1813 photoresist spin on for 30 s at 4000 rpm
Prebake 30 min 90 °C
Exposure hard contact mode 0.5 bar N_2 pressure nominal 6.5 s with light integration
Develop Shipley MIF 319 developer 45 s
QDR < 0.1 µS
Spin dry
Post bake 120 °C 30 min

7. Reactive ion etch (RIE) backside
Objective: RIE Backside
Equipment: Elektrotech PF 340 (in combination with PECVD system)
Gas Flow CHF_3 25 sccm, O_2 5 sccm
Pressure: 10 mTorr
Power 75 W
Target TiO_2
Target Temperature 25 °C
Time 3.5 - min (5 min nominal 700 nm)

8. Photoresist Strip
Objective: To remove photoresist
Equipment: Oxygen plasma stripper (in house)
Time > 20 min
KOH timed etch

9. Anisotropic diaphragm etch
Objective: to etch diaphragms
Equipment: KOH etch bath
HF dip 45 s
QDR < 0.1 µS
KOH 1500 ml DI 500 g KOH 74 °C.
Etch Rate (new solution) 0.95 µm/min
Time *ca.* 360 min depending on rate and wafer thickness

10. RCA cleaning
Objective: To remove potassium ions
Equipment: General
Solution: 1:1:5; H_2SO_4:H_2O_2:H_2O
Add H_2SO_4 to H_2O heat to 80 °C
Add H_2O_2 heat to 80 °C
Clean for 20 min
Repeat if necessary
QDR < 0.1 µS
Spin dry

11. Photolithography frontside

Objective: Pattern frontside nitride with mask ON
Equipment: Electronic Visions double sided mask aligner, single sided mode
De-hydrate 200 °C > 30 min
0_2 - plasma 300 °C (high humidity)
HMDS 30 s 4000 rpm
Positive S1813 photoresist spin on for 30 s at 4000 rpm
Prebake 30 min 90 °C
Exposure hard contact mode 0.5 bar N_2 pressure nominal 6.5 s with light integration
Develop Shipley MIF 319 developer 45 s
QDR < 0.1 µS
Spin dry
Post bake 120 °C 30 min

12. Reactive ion etch (RIE) frontside
Objective: RIE frontside
Equipment: Elektrotech PF 340 (in combination with PECVD system)
Gas Flow CHF_3 25 sccm, O_2 5 sccm
Pressure: 10 mTorr
Power 75 W
Target TiO_2
Target temperature 25 °C
Time 3.5 - min (5 min nominal 700 nm)

13. Photoresist strip
Objective: Remove photoresist
Equipment: UT oxygen plasma stripper
Time > 20 min
PECVD 2 µm oxide

14. PECVD sacrificial oxide
Objective: To deposit 2 µm of sacrificial oxide
Equipment: Elektrotech PF 340 (in combination with PECVD system)
Standard clean
Gas Flow: SiH_4 200 sccm, N_2O 710 sccm
Pressure 650 mTorr
Power 60 W
Temperature 300 °C
Time 66 min

15. Densify oxide
Objective: To densify and de-gas hydrogen from oxide
Equipment: Tempress Omega junior furnace
Gas N_2 1*l⁄*min
Temperature 800 °C
Time 30 min

16. Photolithography oxide
Objective: To pattern frontside with mask SA

Equipment: Electronic Visions double sided mask aligner, single sided mode
De-hydrate 200 °C > 30 min
0_2 - plasma 300 °C (high humidity)
HMDS 30 s 4000 rpm
Positive S1813 photoresist spin on for 30 s at 4000 rpm
Prebake 30 min 90 °C
Exposure hard contact mode 0.5 bar N_2 pressure nominal 6.5 s with light integration
Develop Shipley MIF 319 developer 45 s
QDR < 0.1 µS
Spin dry
Post bake 120 °C 30 min

17. Etch oxide
Objective: To etch oxide
Equipment: General
Etch in BHF until clear
BHF rate ≈ 60 nm/min
Time *ca.* 30 min
QDR < 0.1 µS
Spin dry

18. LPCVD (poly)silicon
Objective: To deposit 2 µm LPCVD polysilicon
Equipment: Tempress LPCVD system for silicon(oxy)nitride
Standard clean
BHF dip 45 s to remove native oxide
QDR <0.1 µS
Spin dry
load furnace
Gas flow SiH_4 50 sccm
Pressure 250 mTorr
Temperature 590 °C
Time 360 min

19. SILOX BSG
Objective: To deposit a dopant layer
Equipment: UT Atmospheric Pressure (APCVD) system for (doped) silox
Gas flows N_2 85 top ball, O_2 65 top ball, SiH_4 85 top ball B_2H_6 high 50 bottom ball
HF dip 45 s
QDR ,0.1 µS
Spin dry
Heater 425 °C
N_2 20 s
B_2H_6 80 s
SiH_4 260 s
Densify 650 °C N_2 1*l/*min

20. Diffusion and anneal
Objective: To diffuse boron into polysilicon and anneal polysilicon
Equipment: Tempress Omega junior furnace

Gas flow N_2 1l/min
Temperature 1000 ^oC
Time 60 min
Removal of dopant layer
HF dip until cleared (48% HF 10 min)
QDR < O.1 µS
Spin dry

21. Photolithography
Objective: To pattern a lift-off mask for the chrome/gold contact pads
Equipment: Electronic Visions double sided mask aligner, single sided mode
De-hydrate 200 ^oC > 30 min
0_2 - plasma 300 ^oC (high humidity)
HMDS 30 s 4000 rpm
Positive S1813 photoresist spin on for 30 s at 4000 rpm
Exposure hard contact mode 0.5 bar N_2 pressure nominal 6.5 s with light integration
Chlorobenzine 5 min
Spin dry
QDR <0.1 µS
Spin dry
Develop Shipley MIF 319 60 s

22. Evaporation of chrome/gold contact pads
Objective: To deposit 10 nm chrome and 150 nm gold onto a lift-off mask
Equipment: Balzers resistive evaporator
HF dip 45 s to remove native oxide
QDR <0.1 µS
Spin dry
Evaporate 10 nm chrome
Evaporate 150 nm gold
Lift-off chrome/gold with acetone. Ultrasonics will remove diaphragms!
QDR <0.1 µS
Spin dry

23. Photolithography
Objective: To pattern polysilicon with mask PO
Equipment: Electronic Visions double sided mask aligner, single sided mode
De-hydrate 200 ^oC > 30 min
0_2 - plasma 300 ^oC (high humidity)
HMDS 30 s 4000 rpm
Positive S1813 photoresist spin on for 30 s at 4000 rpm
Prebake 30 min 90 ^oC
Exposure hard contact mode 0.5 bar N_2 pressure nominal 6.5 s with light integration
Develop Shipley MIF 319 developer 45 s
QDR < 0.1 µS
Spin dry
Post bake 90 ^oC 15 min

24. RIE polysilicon

Objective: To define the resonators in Polysilicon
Equipment: Elektrotech PF 340 (in combination with PECVD system)
Gas flow SF_6 54 sccm O_2 5 sccm
Pressure 100 mTorr
Power 75 W
Target 6" silicon with vacuum grease for good thermal contact
Time until cleared $\approx$ 9 min. Additional over etch 15 s to clear combs

25. Resist strip
Objective: To remove photoresist mask
Equipment : General
Remove resist with acetone
QDR <0.1µS
Spin dry

26. HF sacrificial etch and freeze dry
Objective: To free the microstructures by etching the sacrificial oxide
Equipment. General and freeze dryer
Immerse in HF for 29 min at room temperature
Dilute HF, without removing wafer from beaker, with DI water until PH is neutral
Remove excess water
Add IPA
Remove wafer from IPA/DI water solution in to pure IPA
Rinse 3/4 times in IPA
Rinse 3/4 times in cyclohexane
Freeze dry @ -10 ^{O}C for at least 30 min
Heat to 25 ^{O}C and remove wafer